Multiscale solar wind turbulence : from theory to observations

Vincent David

université PARIS-SACLAY

Multiscale solar wind turbulence: from theory to observations

Turbulence multi-échelle dans le vent solaire: de la théorie aux observations

Thèse de doctorat de l'université Paris-Saclay

École doctorale n°572 Ondes et Matière (EDOM)
Spécialité de doctorat: Physique
Graduate School : Physique
Référent : faculté des sciences d'Orsay

Thèse préparée au **Laboratoire de Physique des Plasmas**, (Université Paris-Saclay, CNRS, École polytechnique), sous la direction de **Sébastien GALTIER**, professeur, le co-encadrement de **Fouad SAHRAOUI**, directeur de recherche.

Thèse soutenue à Palaiseau, le 21/09/2023, par

Vincent DAVID

Composition du jury

Membres du jury avec voix délibérative

Sergio CHIBBARO Professeur, Université Paris-Saclay	Président
Raffaele MARINO Chargé de recherche, HDR, CNRS, École Centrale de Lyon	Rapporteur
Sergey NAZARENKO Directeur de recherche, CNRS, Université Côte d'Azur	Rapporteur & Examinateur
Christopher CHEN Chargé de recherche, Queen Mary University of London	Examinateur
Bérengère DUBRULLE Directrice de Recherche, CNRS, Université Paris-Saclay	Examinatrice

THESE DE DOCTORAT
NNT : 2023UPASP102

université PARIS-SACLAY | ÉCOLE DOCTORALE Ondes et matière (EDOM)

Titre: Turbulence multi-échelle dans le vent solaire: de la théorie aux observations

Mots clés: Plasma, Turbulence, Vent solaire

Résumé: Le vent solaire, plasma turbulent, est mesuré *in situ* par de nombreuses sondes spatiales. Les mesures révèlent des fluctuations du champ magnétique sur une large gamme de fréquences, avec une rupture de pente à environ 1 Hz, marquant une transition du comportement MHD mono-fluide vers un état où ions et électrons agissent différemment. Une seconde transition survient vers 50 Hz, où le spectre magnétique s'accentue davantage, indiquant un changement lié à l'inertie des électrons. Cette turbulence est étroitement liée à l'origine du chauffage, caractérisé par la décroissance progressive de la température ionique avec la distance héliosphérique. Cela est interprété comme le résultat du transfert d'énergie de grandes à petites échelles par la turbulence. Notre objectif est d'étudier cette turbulence du vent solaire, couvrant des échelles allant de la MHD aux échelles inertielles électroniques. Premièrement, nous utilisons la loi zéro de la turbulence qui révèle une dissipation d'énergie, dite anomale anomale, lorsque les viscosité/résistivité diminuent. L'utilisation de la dissipation anomale, basée sur une forme locale de la loi de Kolmogorov dans les données THEMIS et PSP, montre que le chauffage calculé dépasse considérablement la moyenne de la MHD. En outre, elle permet également de prouver la loi zéro dans un modèle simplifié de la MHD, et son application aux données Voyager 2 révèle que le chauffage généré par les chocs présents aux abords de Jupiter domine celui provenant des fluctuations turbulentes. Deuxièmement, nous nous intéressons aux échelles sous-MHD. Les mesures révèlent un comportement monofractal des fluctuations magnétiques, contrairement aux échelles MHD qui présentent un comportement multifractal. Pour comprendre cette différence, nous effectuons des simulations numériques directes 3D des équations de l'électron MHD réduite dans des régimes de turbulence d'ondes faible et forte. Ces simulations montrent que seule la turbulence faible peut reproduire la monofractalité, suggèrant qu'aux échelles électroniques, le vent solaire évolue dans un régime de turbulence d'ondes d'Alfvén cinétique faible et sans collision. Enfin, une théorie de la turbulence d'ondes faible pour la MHD électronique inertielle est développée. Nous donnons les solutions exactes, prouvons que la cascade d'énergie est directe et évaluons la constante de Kolmogorov. De manière remarquable, ces équations sont identiques (à une constante près) à celles décrivant la turbulence d'ondes inertielles dans les fluides non ionisés en rotation rapide. Ce fort lien souligne l'importance des investigations en laboratoire pour étudier la turbulence à ces échelles, difficilement accessibles aux satellites. Ces études permettent d'obtenir une vision globale du comportement turbulent du vent solaire d'un point de vue observationnel, numérique et théorique.

Title: Multiscale solar wind turbulence: from theory to observations

Keywords: Plasma, Turbulence, Solar wind

Abstract: The solar wind is a turbulent plasma that can be measured in situ by spacecraft such as Voyager/NASA, THEMIS/ESA, or PSP/NASA. Measurements reveal magnetic field fluctuations over a wide range of frequencies, with a change in slope around 1 Hz, indicating a transition from the single-fluid MHD behavior of the plasma to a state where ions and electrons have distinct dynamics. A second transition is observed around 50 Hz, beyond which the magnetic spectrum becomes steeper, marking a change in physics where the inertia effects of electrons become significant. The study of this turbulence is closely linked to understanding the origin of local heating, characterized by a slow decrease in ion temperature with increasing heliospheric distance. This decrease is interpreted as a signature of heating resulting from the transfer of energy from large to small scales by turbulence. The objective of this thesis is to study solar wind turbulence from MHD scales to electron inertial scales.

In the first part, we use the Zeroth law of turbulence to measure energy dissipation at MHD scales. This law states that energy dissipation per unit mass approaches a non-zero limit, known as anomalous dissipation, as viscosity/resistivity decreases. A local form of Kolmogorov's exact law is used with THEMIS and PSP data to show that heating calculated using anomalous dissipation can be significantly higher than the average heating predicted by the exact MHD law. Furthermore, the application of anomalous dissipation proves the Zeroth law in a simplified MHD model. Its application to Voyager 2 data reveals that heating generated by shocks near Jupiter is dominant compared to that from turbulent fluctuations.

In the second part, we focus on sub-MHD scales (frequencies between 1 and 50 Hz). In situ measurements show a monofractal behavior of magnetic fluctuations, whereas at MHD scales a (standard) multifractal behavior is observed. To study this difference, high-resolution 3D direct numerical simulations of the electron reduced MHD equations are conducted in weak and strong wave turbulence regimes. These simulations reveal that only weak turbulence can reproduce the monofractality. Combined with recent work, this result suggests that at electron scales, the solar wind is in a regime of weak kinetic Alfvén wave turbulence without collisions.

Finally, a theory of (weak) wave turbulence for inertial electron MHD in the presence of a strong external magnetic field is developed. Exact solutions (Kolmogorov-Zakharov spectrum) are provided, and it is shown that the cascade is direct. The importance of considering electron mass in this regime is highlighted. Remarkably, these equations are identical (up to a constant) to those describing inertial wave turbulence in rapidly rotating non-ionized fluids. This connection underscores the importance of laboratory investigations to study turbulence at these scales, which are currently challenging to access by satellites.

These studies provide a comprehensive understanding of the turbulent behavior of the solar wind from observational, numerical, and theoretical perspectives.


ÉCOLE
POLYTECHNIQUE
UNIVERSITÉ PARIS-SACLAY


LPP

À mes frères et sœur.

Même s'ils n'en font qu'un cale-porte.

Acknowledgements

Je ne saurais commencer par autre que toi, Florian, jeune chimiste qui sut me donner goût à cette si belle discipline qu'est la Physique — le comble de l'ironie. Ton passage dans ma vie fut bref, mais son impact démesuré. Je ne peux t'exprimer cela de vive voix, alors j'utilise ces lignes pour te remercier.

Quelques années plus tard, je croisai le chemin de Sébastien. À l'époque, je ne le savais pas encore mais, derrière ce professeur qui maniait avec aisance des concepts qui me semblaient alors abstraits, mais que je percevais tout de même comme empreints d'une certaine élégance, se cachait la personne qui, jusqu'alors, m'apporterait professionnellement plus que quiconque. C'est avec lui que je compris que la recherche est un luxe : chaque détail compte. L'intégralité de nos travaux se doit d'être réfléchie, soignée, et irréprochable. En d'autres termes, l'à peut près n'y a pas sa place et il ne peut en être autrement.

À l'instar de Starsky & Hutch, il est difficile de dissocier Sébastien de Fouad. Son approche complémentaire me fit prendre conscience des enjeux observationnels qui se cachaient derrière la théorie que j'apprenais à manier avec Sébastien. Nos conversations furent riches, mais si je devais ne retenir qu'une phrase, qu'un mantra, ce serait celui-ci : "L'excellence réside dans les détails. Et une bière fraîche aide à garder les idées claires." C'est donc grâce à l'encadrement et sous les regards bienveillants de ces deux hommes que je réussis à décrocher ce doctorat. Pour tout cela, je souhaitais les remercier à nouveau.

Je tiens également à remercier Romain pour sa générosité et sa disponibilité. Ses outils me permirent d'aboutir au Chapitre 4 de ce manuscrit et nos échanges m'apprirent beaucoup. Continue d'être un meilleur plasmicien que je ne serai jamais.

J'omets certains collègues tels qu'Alexis, Benoît, Clément, Davide, Gérard ou Nicolas. Mais des remerciements interminables sont quelque peu ennuyeux. Je conclurai donc par celle qui eut la plus grande importance et qui écoutait (?) mes monologues turbulents et incompréhensibles pour le profane du couloir voisin : Léa. Sans toi, ces trois années n'auraient pas été aussi douces.

Contents

List of Figures

List of Tables

Chapter 1

General introduction

1.1 Turbulence

Here we are... The sempiternal question of How to define turbulence? The funny paradox is that turbulence is ubiquitous, but there is not a universally agreed-upon definition (it is, to say, how hard it is to work on turbulence). I think the fairest definition is: "You know it when you see it". Instead of giving a clear and formal definition, I rather prefer to discuss some characteristics of turbulence through examples so that you know it when you see it.

1.1.1 Unpredictability

Turbulent flow is a mess. It is by definition chaotic, meaning it is significantly dependent on initial conditions. This property gave rise to the so-called butterfly effect, which states that a butterfly flapping its wings can potentially lead to the formation of a storm. What we need to understand is that chaos roughly means that even if the equations are deterministic, a minuscule difference in the initial states can lead to vastly different behavior over a sufficiently long time. This makes it impossible to precisely describe turbulent motion because the outcome is highly dependent on the initial conditions. All you can do is to speak about it statistically.

This short anecdote demonstrates the concept of chaos and how a tiny error made by a meteorologist in the 1960s led to its revolutionary discovery. In 1963, Edward Lorenz, a meteorologist at the Massachusetts Institute of Technology, was studying the equations used to understand the dynamics of air in the atmosphere. Up until now, nothing surprising. However, to gain a deeper understanding of the equations, he simplified them as much as possible, distilling only the essential elements of the underlying physics that gave rise to what is now known as the Lorenz system [16]. Lorenz attempted to solve these equations using a supercomputer of the time. To do this, he inputted his equations with a precision of up to six decimal places and ran the computations twice for each set of parameters. Legend has it that on one occasion, Lorenz was in a rush and wanted to save time, so he entered the parameters with only three decimal places. When he returned from a coffee break, he noticed that his data was drastically different from what he had obtained using six decimal places. He repeated the experiment, this time using four and then five decimal places, but the conclusion remained unchanged: they were entirely different from those of the reference simulation. Lorenz had unknowingly discovered chaos. Almost a decade later, this inspired him to give a talk entitled "*Predictability: Does the Flap of a Butterfly's Wings in Brazil Set Off a Tornado in Texas?*" [17]... The butterfly effect was born.

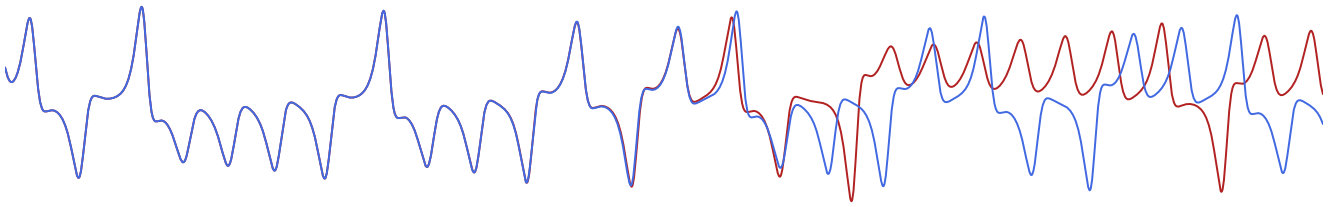

Figure 1.1: Illustration of the divergence between two predictions using the Lorenz model.

1.1.2 Multiscale

Turbulence is arguably the most ubiquitous physical phenomenon, appearing at nearly all scales of the universe. We find it from the subatomic world of the quantum vortex [2] to the vastness of interstellar dust and nebula [11], such as the Orion Nebula, which spans more than 20 million light-years across. It can also be found in the human body, such as the blood flowing through your aorta [26], and in the atmosphere, where it plays a crucial role in the formation of rain clouds [27]. Even solar cells, –with a France-sized surface area – are turbulent. And let us not forget about the great Jupiter vortex, with a size larger than that of Earth, and exhibits turbulent behavior [30]. Although not an exhaustive list, these examples provide a glimpse into the ubiquitous nature of turbulence in the universe. As we will see in the following paragraphs, the propensity for turbulence is not surprising, given that it arises from the nonlinearities inherent in the equations describing physical systems. Since nature itself is nonlinear, it is natural to find turbulence occurring at all scales of the universe. Lastly, it is worth noting that a turbulent flow is multiscale. For instance, consider the eruption plume depicted in Figure 1.2. The gas movement emerging from the crater is turbulent, and as you zoom in, you will notice finer details and structures. To emphasize the significance of this property, Alexander Smits [29] humorously remarked, "*You can tell how high budget a Hollywood movie is based on how many scales are in their turbulent explosions.*"

1.1.3 Diffusive

Turbulence mixes things. It is easy to imagine that if a drop of dye is introduced into a turbulent flow, it will be distorted and blended with the surrounding fluid until it is fully incorporated, thereby making it impossible to discern between regions with or without the dye. One approach to illustrate this point is to describe what turbulence is not: laminar flow. This term stems from the same Latin word that *lamination* does: 'lamina', meaning a thin layer of a material, and it refers to smooth flow in a fluid, where the moving particles stay largely confined to distinct layers, that move at different speeds with no mixing to each other.

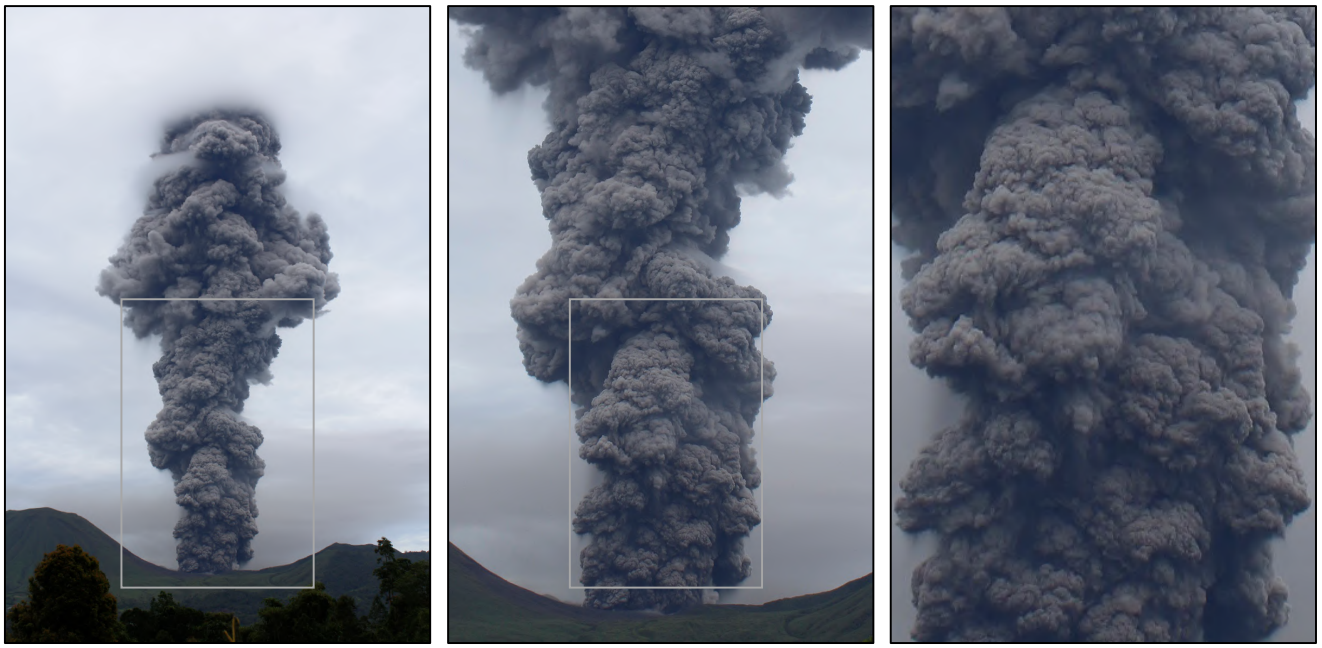

Figure 1.2: Tompualan crater, mount Lokon-Empung, Indonesia. The eruption plume is reaching its peak height, as it reaches the cloud base. 10 September, 7.01 AM local time. Credits: David Pyle.

It is particularly satisfying to look at because it is so smooth that one can ask whether they are looking at a glass or a flowing fluid. Moreover, analytical solutions for laminar flows are relatively easy to find, but this type of flow is rare in nature. Turbulent flows are all contrary to what I just described.

1.1.4 High Reynolds number

It is now the time to introduce the incompressible Navier-Stokes equations since they are the fundamental equations governing the motion of fluids, and they are the equivalent of Newton's second law.

$$\boldsymbol{\nabla} \cdot \boldsymbol{u} = 0, \tag{1.1a}$$

$$\frac{\partial \boldsymbol{u}}{\partial t} + \boldsymbol{u} \cdot \boldsymbol{\nabla} \boldsymbol{u} = -\frac{1}{\rho} \boldsymbol{\nabla} P + \nu \nabla^2 \boldsymbol{u}. \tag{1.1b}$$

The first equation verifies the incompressibility of the flow, indicating that a fixed number of fluid particles consistently occupy a constant volume within the fluid. This holds for water and many liquids, but is not realistic for gases. The second equation describes how the velocity will change in space and time under the influence of the pressure P and the viscosity ν. To be more specific, the first term describes the time evolution of the velocity field, while the second term on the left-hand side describes the nonlinear advection. The first term on the right-hand side models the impact of the pressure, while the last one stands for the

energy dissipation due to molecular collisions. The Reynolds number is defined as the ratio between the nonlinear advection and the viscous terms [24, 31]:

$$\left|\frac{\boldsymbol{u}\cdot\boldsymbol{\nabla}\boldsymbol{u}}{\nu\nabla^2\boldsymbol{u}}\right| \sim \frac{U^2/L}{U\nu/L^2} = \frac{LU}{\nu} \equiv Re, \tag{1.2}$$

where U and L are respectively the characteristic velocity and size of the flow. When $Re \gg 1$, the flow is dominated by the advection and the viscous dissipation becomes negligible. This type of flow is turbulent (typically when $Re > 10^3$). On the contrary, if the advection term is negligible compared to the viscous one, the flow is laminar.

It could be interesting to explain why these two terms are modeled like this. Let us begin with the viscous one. The classical example is the one-dimensional linear diffusion equation:

$$\frac{\partial u(x,t)}{\partial t} = \nu\frac{\partial^2 u(x,t)}{\partial x^2}, \tag{1.3a}$$

$$u(x,t=0) = u_0(x). \tag{1.3b}$$

The curvature of the velocity profile, whether it is concave or convex, is represented by the second derivative in space. Therefore, the equations preceding this statement establish a connection between the evolution of the velocity profile over time and its curvature, with the viscosity ν serving as a coefficient that either enhances ($\nu > 1$) or reduces ($\nu < 1$) this curvature modification – note that a time renormalization can absorb this coefficient. A solution of this diffusion equation is

$$u(x,t) = \frac{1}{\sqrt{4\pi\nu t}}\int_{-\infty}^{+\infty}\exp\left[-\frac{(y-x)^2}{4\nu t}\right]u_0(y)\mathrm{d}y. \tag{1.4}$$

As one can see in this expression, as time passes, on the one hand, the exponential in the convolution product becomes increasingly widespread and then smooths the function $u_0(x)$; and on the other hand, the amplitude of the velocity field decreases, as can be observed in the prefactor of the integral (cf., top panel of Figure 1.3 for a visual representation). Both effects are accentuated with the viscosity that only appears in a product of νt – which is not surprising since, as said before, ν can be absorbed by a time renormalization.

On the contrary, the nonlinear advection term will increase the velocity shear. We can begin with a

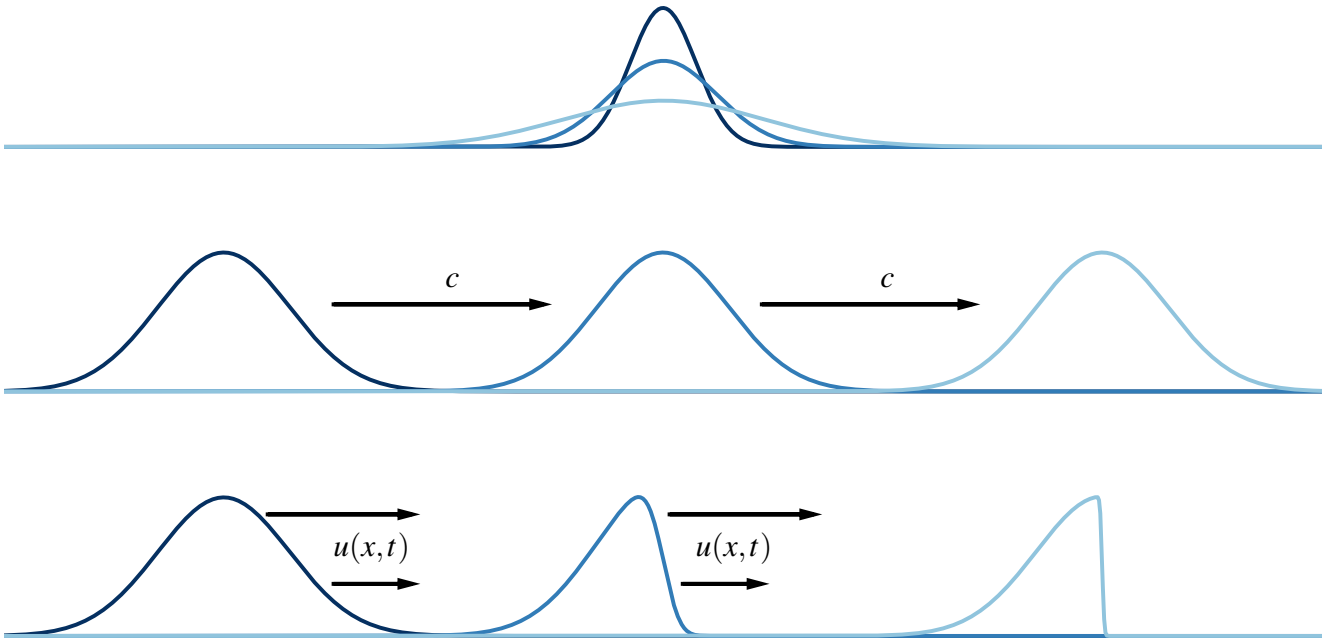

Figure 1.3: From top to bottom: linear diffusion, linear advection, and nonlinear advection sketches. The shades of blue from dark to light indicate the progression in time.

simpler equation, such as the linear advection equation,

$$\frac{\partial u(x,t)}{\partial t} = c\frac{\partial u(x,t)}{\partial x}, \tag{1.5a}$$

$$u(x,t=0) = u_0(x). \tag{1.5b}$$

The solution is the initial velocity profile $u_0(x)$ traveling at a constant velocity c. Now, in the nonlinear case, we have

$$\frac{\partial u(x,t)}{\partial t} = u(x,t)\frac{\partial u(x,t)}{\partial x}. \tag{1.6}$$

This implies that the original wave is no longer traveling at a constant velocity; rather, the higher the value of $u(x,t)$, the faster the wave speed, leading to a steepening of the wave and ultimately the formation of a shock (cf., middle and bottom panels of Figure 1.3). Such a phenomenon is described by the Burgers equation, which serves as a one-dimensional representation of turbulence.

These simplified one-dimensional examples help us understand the physical impact of the two factors that determine the Reynolds number and how they interact. Turbulent flows exhibit a stronger nonlinear advection effect than the viscous effect, resulting in a more complex dynamics than laminar flows with a low Reynolds number and no mixing.

1.2 Plasma

1.2.1 Definition

Plasma is considered the fourth state of matter: heating a solid makes a liquid, heating a liquid makes a gas, and heating a gas makes a plasma. This state of matter is created when a gas is partially or fully ionized, resulting in a mixture of positively charged ions and negatively charged electrons with approximately equal densities. This ionization can be achieved through a variety of methods, including high temperatures, such as those found in stars or flames, or through constant bombardment by other particles, as is the case in the Earth's ionosphere. Although plasmas are not natural on Earth, they have many industrial uses, ranging from fluorescent lights and high-voltage circuit breakers to space propulsion systems and tokamaks for nuclear fusion experiments. Despite being discovered experimentally in 1879, the first theoretical descriptions of plasmas did not emerge until 1929 in a study on the dynamics of electrons and ions in an arc-type discharge [32].

Plasmas, although similar to neutral gases on a macroscopic level, exhibit unique microscopic behaviors. They maintain overall electrical *quasi-neutrality*, but can experience significant variations in charge density within small regions. This distinct characteristic gives rise to various properties of plasmas, which will be explored in this manuscript. Moreover, they can be categorized based on their particle interactions. Collisional ones are governed by the macroscopic electromagnetic field and Coulomb forces between neighboring particles, while collisionless plasmas are diluted and have few interactions between charged particles and can behave differently depending on whether we look at individual particles or the plasma as a whole. To study such plasmas, different models exist. The kinetic approach examines a group of particles whose velocities follow a distribution function f and studies the change of this function over space and time. The fluid approach, on the other hand, disregards individual particles and studies the macroscopic behavior of the plasma by looking at different moments of the distribution function f. For instance, magnetohydrodynamics (MHD) is the simplest fluid description and can deal with complex phenomena such as plasma turbulence, but more advanced descriptions like Hall-MHD consider electron-ion separation, and the bi-fluid approach treats species as distinct interacting fluids. To summarize, there are different perspectives one can take depending on what aspect of the plasma we want to investigate. Now, in the upcoming paragraphs, I plan to delve into greater detail about the two primary frameworks through which we study plasmas: the kinetic and the fluid descriptions.

Clearly, any definition of plasma must be accompanied by parameters, of which one is the dimensionless

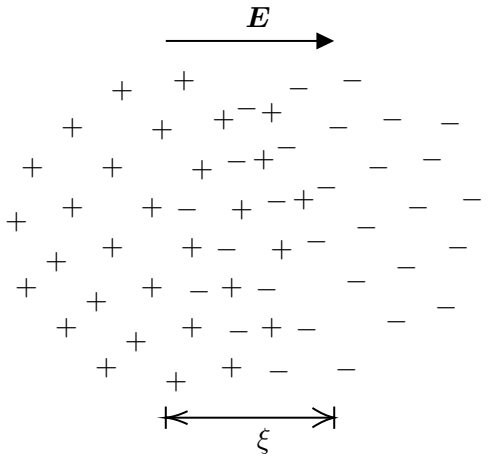

Figure 1.4: Illustration of a shift of all the electrons slightly to the right by a distance ξ to perturb the uniform, quasi-neutral plasma and highlight the plasma pulsation.

plasma parameter,

$$\Lambda \equiv n_e \lambda_D^3, \tag{1.7}$$

where n_e represents the electron density. The Debye length, denoted as λ_D, plays a crucial role as it serves as the characteristic length scale over which the Coulomb potential of an individual charged particle is exponentially weakened or "screened". This screening effect arises due to the preferential accumulation or exclusion of oppositely or like-charged particles in the vicinity of the charged particle. Mathematically, the Debye length is defined as [8]:

$$\boxed{\lambda_D \equiv \sqrt{\frac{\varepsilon_0 k_B T}{n_e e^2}}}, \tag{1.8}$$

with ε_0 represents the vacuum permittivity, k_B is the Boltzmann constant, T denotes the temperature, and e stands for the elementary charge. When $\Lambda \gg 1$, collective electrostatic interactions outweigh binary particle-particle collisions, indicating a weakly coupled plasma. It is precisely this type of plasma that will be the main focus of our investigation in this manuscript. Furthermore, as $\Lambda \to \infty$, the charges in the plasma become uniformly distributed, leading to quasi-neutrality. Beyond the Debye sphere, the positive and negative charges balance each other out. One might naturally wonder about the characteristic timescale associated with the Debye length. Let us imagine a uniformly distributed quasi-neutral plasma with well-equilibrated Debye clouds. Now, let us introduce a slight shift of all the electrons to the right by a distance ξ, as depicted in Figure 1.4. Due to this displacement, an electric field arises, pointing from the ions to the displaced electrons, with a magnitude of $E = en_e\xi/\varepsilon_0$. The equation of motion for the electrons

can then be expressed as follows:

$$m_e \frac{\mathrm{d}^2\xi}{\mathrm{d}t^2} = -eE \quad \Longrightarrow \quad \frac{\mathrm{d}^2\xi}{\mathrm{d}t^2} = -\omega_{\mathrm{pe}}^2 \xi, \quad \text{with} \quad \omega_{\mathrm{pe}} \equiv \sqrt{\frac{n_e e^2}{\epsilon_0 m_e}}. \tag{1.9}$$

where ω_{pe} denotes the pulsation of a simple harmonic oscillator, commonly called plasma pulsation. Hence, even small displacements between the positively and negatively charged species give rise to plasma oscillations, commonly known as *Langmuir waves* [32]. This collective phenomenon emerges as the plasma endeavors to restore quasi-neutrality in response to a disturbance.

1.2.2 Kinetic description

In this section, we draw inspiration from the insightful work of Dwight R. Nicholson, as presented in his notable book on plasma physics [23].

Plasma kinetic theory is a theory that considers the movements of all particles in a plasma. To describe how they all evolve over time and space, we first need to determine the precise trajectories of each one. One helpful way to do this is to consider their positions and velocities as independent variables in a hypothetical six-dimensional space with $(\boldsymbol{x}, \boldsymbol{v})$ axes, which is referred to as the phase space and where the vector $\boldsymbol{x}$ represents the real space position (x, y, z) of a particle, and the vector $\boldsymbol{v}$ represents its velocity components (v_x, v_y, v_z). To begin with, we can model the density of the N_0 particles of the species s of the plasma as

$$N_s(\boldsymbol{x}, \boldsymbol{v}, t) = \sum_{i=1}^{N_0} \delta(\boldsymbol{x} - \boldsymbol{x}_i)\delta(\boldsymbol{v} - \boldsymbol{v}_i), \tag{1.10}$$

where $\delta(\boldsymbol{x} - \boldsymbol{x}_i)$ is the Dirac distribution – which is zero if $\boldsymbol{x} \neq \boldsymbol{x}_i$ and one if $\boldsymbol{x} = \boldsymbol{x}_i$. Taking into account all the species s forming the plasma, we obtain the total density

$$N(\boldsymbol{x}, \boldsymbol{v}, t) = \sum_s N_s(\boldsymbol{x}, \boldsymbol{v}, t). \tag{1.11}$$

Since the number of particles does not change, thus one has

$$\frac{\mathrm{d}N(\boldsymbol{x}, \boldsymbol{v}, t)}{\mathrm{d}t} = 0, \tag{1.12}$$

where $\mathrm{d}/\mathrm{d}t$ stands for the total derivative. Developing this expression leads to

$$\frac{\partial N}{\partial t} + \boldsymbol{v} \cdot \boldsymbol{\nabla}_{\boldsymbol{x}} N + \boldsymbol{a} \cdot \boldsymbol{\nabla}_{\boldsymbol{v}} N = 0, \tag{1.13}$$

where $\boldsymbol{a}$ is the acceleration. The velocity $\boldsymbol{v}_i$ of a particle i satisfies the Lorentz force equation,

$$m_s \frac{\mathrm{d}\boldsymbol{v}_i(t)}{\mathrm{d}t} = q_s \boldsymbol{E}^{(m)}[\boldsymbol{x}_i(t), t] + q_s \boldsymbol{v}_i(t) \times \boldsymbol{B}^{(m)}[\boldsymbol{x}_i(t), t], \tag{1.14}$$

where $\boldsymbol{E}$ and $\boldsymbol{B}$ are respectively the electric and magnetic fields. The superscript (m) refers to the electromagnetic fields at a microscopic scale that are generated by the particles themselves, together with externally applied fields. These microscopic fields are ruled by the Maxwell equations that describe the time and space evolution of the electric and magnetic fields

$$\text{Maxwell-Gauss:} \quad \boldsymbol{\nabla} \cdot \boldsymbol{E}^{(m)} = \frac{\rho_c^{(m)}}{\varepsilon_0}, \tag{1.15a}$$

$$\text{Maxwell-Thomson:} \quad \boldsymbol{\nabla} \cdot \boldsymbol{B}^{(m)} = 0, \tag{1.15b}$$

$$\text{Maxwell-Faraday:} \quad \boldsymbol{\nabla} \times \boldsymbol{E}^{(m)} = -\frac{\partial \boldsymbol{B}^{(m)}}{\partial t}, \tag{1.15c}$$

$$\text{Maxwell-Ampère:} \quad \boldsymbol{\nabla} \times \boldsymbol{B}^{(m)} = \mu_0 \boldsymbol{J}^{(m)} + \frac{1}{c^2} \frac{\partial \boldsymbol{E}^{(m)}}{\partial t}, \tag{1.15d}$$

with ε_0 the vacuum dielectric permittivity, μ_0 the vacuum magnetic permeability and $c = 1/\sqrt{\epsilon_0 \mu_0}$ the speed of light in vacuum. We define the microscopic charge density $\rho_c^{(m)}$ and the microscopic current $\boldsymbol{J}^{(m)}$ as

$$\rho^{(m)}(\boldsymbol{x}, t) = \sum_s q_s \int_{\mathbb{R}^3} N_s(\boldsymbol{x}, \boldsymbol{v}, t) \mathrm{d}\boldsymbol{v}, \tag{1.16a}$$

$$\boldsymbol{J}^{(m)}(\boldsymbol{x}, t) = \sum_s q_s \int_{\mathbb{R}^3} \boldsymbol{v} N_s(\boldsymbol{x}, \boldsymbol{v}, t) \mathrm{d}\boldsymbol{v}. \tag{1.16b}$$

According to Newton's second law, the acceleration $\boldsymbol{a}$ can be replaced by the Lorentz force and one obtains

$$\boxed{\frac{\partial N_s(\boldsymbol{x}, \boldsymbol{v}, t)}{\partial t} + \boldsymbol{v} \cdot \boldsymbol{\nabla}_{\boldsymbol{x}} N_s + \frac{q_s}{m_s} \left(\boldsymbol{E}^{(m)} + \boldsymbol{v} \times \boldsymbol{B}^{(m)} \right) \cdot \boldsymbol{\nabla}_{\boldsymbol{v}} N_s = 0}, \tag{1.17}$$

which is the *Klimontovitch equation* that tells us whether there is a particle with infinite density at a given point [12]. While this equation is exact and provides a precise description of all the orbits of the particles

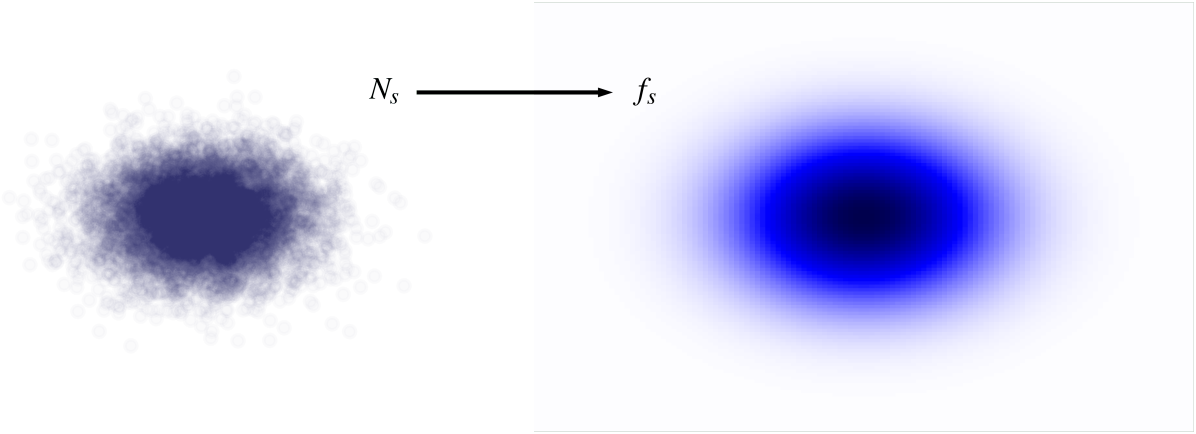

Figure 1.5: Illustration of the ensemble average operation.

composing the plasma, we are not particularly interested in the exact solutions of it because they would be far too detailed for practical purposes. What we are really interested in is how many particles are likely to be found in a small volume $\Delta\boldsymbol{x}\Delta\boldsymbol{v}$ in the phase-space centered at $(\boldsymbol{x}, \boldsymbol{v})$. So, we want to know the smooth function $f(\boldsymbol{x}, \boldsymbol{v}, t) = \langle N_s(\boldsymbol{x}, \boldsymbol{v}, t)\rangle$, which is the average number of particles of species s per unit of phase space. Suppose we are studying long-range electric and magnetic fields that span distances much larger than the Debye length. In this case, we can consider a box centered around the point $\boldsymbol{x}$ in phase space. This box should be significantly larger than the mean interparticle spacing but still much smaller than the Debye length. We can now count the number of particles of species s in the box at time t with velocities in the range $\boldsymbol{v}$ to $\boldsymbol{v} + \Delta\boldsymbol{v}$, divide by the size of the box (multiplied by $\Delta v_x \Delta v_y \Delta v_z$), and refer to the result as $f_s(\boldsymbol{x}, \boldsymbol{v}, t)$ – cf., Figure 1.5 for an illustration of this process. This smooth function $f_s(\boldsymbol{x}, \boldsymbol{v}, t)$ is commonly known as the distribution function. Although this number will fluctuate over time, the fluctuations will be small if there are numerous particles in the box (enough to verify the plasma parameter $\Lambda \gg 1$). An equation for the time evolution of the distribution function can be obtained from the Klimontovitch equation by ensemble averaging. Let us define the perturbations δN_S, $\delta\boldsymbol{B}$ and $\delta\boldsymbol{E}$ as

$$N_s = f_s + \delta N_s, \tag{1.18a}$$

$$\boldsymbol{B}^{(m)} = \boldsymbol{B} + \delta\boldsymbol{B}, \tag{1.18b}$$

$$\boldsymbol{E}^{(m)} = \boldsymbol{E} + \delta\boldsymbol{E}, \tag{1.18c}$$

where $\boldsymbol{B} = \langle \boldsymbol{B}^{(m)}\rangle$, $\boldsymbol{E} = \langle \boldsymbol{E}^{(m)}\rangle$, $\langle \delta\boldsymbol{E}\rangle = \langle \delta\boldsymbol{B}\rangle = \boldsymbol{0}$, and $\langle \delta N_s\rangle = 0$. Using these definitions and ensemble

averaging, one obtains

$$\boxed{\frac{\partial f_s(\boldsymbol{x},\boldsymbol{v},t)}{\partial t} + \boldsymbol{v}\cdot\boldsymbol{\nabla}_{\boldsymbol{x}} f_s + \frac{q_s}{m_s}\left(\boldsymbol{E}+\boldsymbol{v}\times\boldsymbol{B}\right)\cdot\boldsymbol{\nabla}_{\boldsymbol{v}} f_s = -\frac{q_s}{m_s}\left\langle\left(\delta\boldsymbol{E}+\boldsymbol{v}\times\delta\boldsymbol{B}\right)\cdot\boldsymbol{\nabla}_{\boldsymbol{v}}\delta N_s\right\rangle}, \tag{1.19}$$

which is the *Boltzmann equation* that models the kinetic description of the plasma [4]. The left-hand side changes gradually in phase space and represents plasma collective behavior. The right-hand side is the average of products involving peakly quantities, such as $\delta\boldsymbol{E}$ or δN_s, and is very sensitive to the discrete nature of the particles. Thus, it represents discrete particle effects, including collisions. This term is particularly difficult to model accurately, as it is highly dependent on the nature of the plasma under consideration. For instance, we must carefully consider whether we are dealing with collisions between two, three, or even more particles at a time. Moreover, we must determine whether these collisions are elastic or inelastic and what the corresponding cross-sections are. Additionally, we must account for the possibility of collisions between neutral and charged particles, which introduces an additional level of complexity. Consequently, a vast amount of research is dedicated to modeling this term, taking into account the specific characteristics of the plasma being studied [25, 28]. If collisions are negligible because, for instance, the plasma is very diluted, then we are left with the *Vlasov equation* [33]:

$$\frac{\partial f_s(\boldsymbol{x},\boldsymbol{v},t)}{\partial t} + \boldsymbol{v}\cdot\boldsymbol{\nabla}_{\boldsymbol{x}} f_s + \frac{q_s}{m_s}\left(\boldsymbol{E}+\boldsymbol{v}\times\boldsymbol{B}\right)\cdot\boldsymbol{\nabla}_{\boldsymbol{v}} f_s = 0. \tag{1.20}$$

1.2.3 Fluid description

Most of the time, plasmas can be considered as two interpenetrating fluids, one made up of electrons and the other of positive ions. This simplifies the equations because we do not have to worry about the different velocities of each particle in the fluids. Instead of the seven-dimensional phase-space of the kinetic theory, we can use a set of equations that describe the behavior of each fluid as a whole, using just three spatial dimensions and time. However, this approach has a drawback: it ignores the details of the velocity distribution function such as Landau damping, which can be important in certain cases [13].

We start with the Vlasov equation and use it to derive the *continuity equation,* which tells us that the fluid density of a species s, denoted by $n_s(\boldsymbol{x},t)$, does not change at a point $\boldsymbol{x}$ unless there is a net amount of fluid entering or leaving a small volume that includes that point. In other words, the fluid is neither created nor destroyed – its density can only change if it flows in or out of a given region. We use the

normalization

$$n_s(\boldsymbol{x},t) = \int_{\mathbb{R}^3} f_s(\boldsymbol{x},\boldsymbol{v},t)\mathrm{d}\boldsymbol{v}, \tag{1.21}$$

and note the fluid velocity $\boldsymbol{u}_s$

$$\boldsymbol{u}_s(\boldsymbol{x},t) = \frac{1}{n_s}\int_{\mathbb{R}^3} \boldsymbol{v} f_s(\boldsymbol{x},\boldsymbol{v},t)\mathrm{d}\boldsymbol{v}. \tag{1.22}$$

Integrating the Vlasov equation (1.20) over the velocity $\boldsymbol{v}$, the third and fourth terms vanish and one obtains

$$\boxed{\frac{\partial n_s(\boldsymbol{x},t)}{\partial t} + \boldsymbol{\nabla}\cdot(n_s\boldsymbol{u}_s) = 0}, \tag{1.23}$$

where $\boldsymbol{\nabla}$ stands for $\boldsymbol{\nabla}_{\boldsymbol{x}}$ in the fluid description.

The *momentum equation*, which describes how this quantity changes over time, is obtained by multiplying the Vlasov equation by $m_s\boldsymbol{v}$ before integrating over the same variable. This yields

$$\frac{\partial}{\partial t}\left(\int_{\mathbb{R}^3} m_s\boldsymbol{v} f_s \mathrm{d}\boldsymbol{v}\right) + \int_{\mathbb{R}^3} m_s\boldsymbol{v}\boldsymbol{v}\cdot\boldsymbol{\nabla}_{\boldsymbol{x}} f_s \mathrm{d}\boldsymbol{v} + q_s\int_{\mathbb{R}^3} \boldsymbol{v}\left(\boldsymbol{E}+\boldsymbol{v}\times\boldsymbol{B}\right)\cdot\boldsymbol{\nabla}_{\boldsymbol{v}} f_s \mathrm{d}\boldsymbol{v} = 0. \tag{1.24}$$

The first term is by definition $\partial_t(n_s m_s \boldsymbol{u}_s)$. For the second term, we can use the relation $\boldsymbol{v}\boldsymbol{v}\cdot\boldsymbol{\nabla}_{\boldsymbol{x}} f_s = \boldsymbol{\nabla}_{\boldsymbol{x}}\cdot(\boldsymbol{v}\boldsymbol{v} f_s)$. Since f_s is a probability distribution, the ensemble average of any quantity is $\langle g\rangle = n_s^{-1}\int_{\mathbb{R}^3} g f_s \mathrm{d}\boldsymbol{v}$. Thus, the second term is equal to $\boldsymbol{\nabla}_{\boldsymbol{x}}\cdot(n_s m_s\langle\boldsymbol{v}\boldsymbol{v}\rangle)$. The third term is, by integration by parts, equal to $-q_s n_s \boldsymbol{E}$. In the last term, it is useful to move the $\boldsymbol{\nabla}_{\boldsymbol{v}}$ operator to the left to obtain $\boldsymbol{\nabla}_{\boldsymbol{v}}\cdot[(\boldsymbol{v}\times\boldsymbol{B})f_s]$. Integration by parts then yields $-q_s n_s \boldsymbol{u}_s\times\boldsymbol{B}$. Combining all terms, the momentum equation becomes,

$$\boxed{\frac{\partial}{\partial t}\left(n_s m_s \boldsymbol{u}_s\right) + \boldsymbol{\nabla}\cdot\left(n_s m_s\langle\boldsymbol{v}\boldsymbol{v}\rangle\right) = q_s n_s\left(\boldsymbol{E}+\boldsymbol{u}_s\times\boldsymbol{B}\right)}. \tag{1.25}$$

However, there is a problem with the fluid approach. The continuity equation, which tells us how the density evolves, involves the function $\boldsymbol{u}_s$, while the momentum equation involves the function $\langle\boldsymbol{v}\boldsymbol{v}\rangle$. To solve the equation that describes the i-th factor of $\boldsymbol{v}$, we need to take into account a term that involves the $(i+1)$-th factor of $\boldsymbol{v}$. This means that a complete description of plasma would require an infinite number of moment equations derived from the Vlasov equation. In essence, we would need to replace the seven-dimensional Vlasov equation with an infinite number of four-dimensional fluid equations... In practice, we truncate this series of equations by using a physical argument to model the term with $i+1$ factor of $\boldsymbol{v}$. Generally, and it is the case in the solar wind, we have a net velocity $\boldsymbol{u}_s$ in a direction. So, in a first approximation, one can assume that all particles have the same macroscopic velocity and

$f_s(\boldsymbol{x}, \boldsymbol{v}, t) = n_s(\boldsymbol{x}, t)\delta(\boldsymbol{v} - \boldsymbol{u}_s)$, thus

$$\langle \boldsymbol{v}\boldsymbol{v} \rangle = \frac{1}{n_s} \int_{\mathbb{R}^3} \boldsymbol{v}\boldsymbol{v} n_s \delta(\boldsymbol{v} - \boldsymbol{u}_s) \, \mathrm{d}\boldsymbol{v} = \boldsymbol{u}_s \boldsymbol{u}_s. \tag{1.26}$$

But to be more realistic, let us consider a distribution that exhibits a net velocity $\boldsymbol{u}_s$ in a specific direction and has a velocity distribution when viewed from the frame moving with the velocity $\boldsymbol{u}_s$. Therefore, we can model this as follows

$$\langle \boldsymbol{v}\boldsymbol{v} \rangle = \frac{1}{n_s} \int_{\mathbb{R}^3} n_s \boldsymbol{v}\boldsymbol{v} \delta(\boldsymbol{v} - \boldsymbol{u}_s) \, \mathrm{d}\boldsymbol{v} + \frac{1}{n_s} \int_{\mathbb{R}^3} (\boldsymbol{v} - \boldsymbol{u}_s)(\boldsymbol{v} - \boldsymbol{u}_s) f_s \mathrm{d}\boldsymbol{v} = \boldsymbol{u}_s \boldsymbol{u}_s + \frac{\mathbf{P}_s}{n_s m_s}, \tag{1.27}$$

where $\mathbf{P}_s$ is, by definition, the pressure tensor. We end up with

$$\boldsymbol{\nabla} \cdot (n_s m_s \langle \boldsymbol{v}\boldsymbol{v} \rangle) = (\boldsymbol{\nabla} \cdot \boldsymbol{u}_s)(n_s m_s \boldsymbol{u}_s) + (\boldsymbol{u}_s \cdot \boldsymbol{\nabla})(n_s m_s \boldsymbol{u}_s) + \boldsymbol{\nabla} \cdot \mathbf{P}_s, \tag{1.28}$$

and the momentum equation becomes

$$\frac{\partial}{\partial t}(m_s n_s \boldsymbol{u}_s) + (\boldsymbol{\nabla} \cdot \boldsymbol{u}_s)(m_s n_s \boldsymbol{u}_s) + (\boldsymbol{u}_s \cdot \boldsymbol{\nabla})(m_s n_s \boldsymbol{u}_s) = -\boldsymbol{\nabla} \cdot \mathbf{P}_s + q_s n_s (\boldsymbol{E} + \boldsymbol{u}_s \times \boldsymbol{B}). \tag{1.29}$$

Subtracting the continuity equation multiplied by $\boldsymbol{u}_s$ from the left side, we find

$$\boxed{m_s n_s \left(\frac{\partial \boldsymbol{u}_s}{\partial t} + \boldsymbol{u}_s \cdot \boldsymbol{\nabla} \boldsymbol{u}_s \right) = -\boldsymbol{\nabla} \cdot \mathbf{P}_s + q_s n_s (\boldsymbol{E} + \boldsymbol{u}_s \times \boldsymbol{B})}. \tag{1.30}$$

When coupled with the Maxwell equations and a closure (which heuristically describes the pressure tensor [3]), this provides a fluid description for each species forming the plasma.

1.2.4 Magnetohydrodynamics approach

If we think of the solar wind as a fluid, one can use the previous equations derived for each species of plasma. Since it is mainly composed of electrons and protons, we assume that a *bi-fluid* description is appropriate. Now we wish to combine the electrons and ions equations to obtain a *single-fluid* equation also known as the equation of *magnetohydrodynamics* (MHD). By defining the single fluid mass density,

charge density, velocity, current density, and pressure tensor as follows

$$\rho_M(\boldsymbol{x},t) = \sum_s n_s m_s, \tag{1.31a}$$

$$\rho_c(\boldsymbol{x},t) = \sum_s n_s q_s, \tag{1.31b}$$

$$\boldsymbol{u}(\boldsymbol{x},t) = \frac{1}{\rho_M}\sum_s n_s m_s \boldsymbol{u}_s, \tag{1.31c}$$

$$\boldsymbol{J}(\boldsymbol{x},t) = \sum_s q_s n_s \boldsymbol{u}_s, \tag{1.31d}$$

$$\mathbf{P} = \sum_s \mathbf{P}_s, \tag{1.31e}$$

we want to derive the *mass conservation*, the *charge conservation*, the *momentum conservation* equations, and the *generalized Ohm's law* to obtain a complete set of equations.

The mass conservation law is obtained by multiplying the ion mass conservation by m_i, the electron mass conservation by m_e and then adding the two equations together to obtain

$$\boxed{\frac{\partial \rho_M}{\partial t} + \boldsymbol{\nabla}\cdot(\rho_M \boldsymbol{u}) = 0}. \tag{1.32}$$

The charge conservation law is obtained by using the same algebra but replacing the mass with the charges

$$\boxed{\frac{\partial \rho_c}{\partial t} + \boldsymbol{\nabla}\cdot\boldsymbol{J} = 0}. \tag{1.33}$$

Now, regarding $\partial_t n_s$ and $\boldsymbol{u}_s$ as small quantities, we add the momentum equations for ions and electrons and keep only the leading order terms to obtain

$$\boxed{\rho_M\left(\frac{\partial \boldsymbol{u}}{\partial t} + \boldsymbol{u}\cdot\boldsymbol{\nabla}\boldsymbol{u}\right) = -\boldsymbol{\nabla}\cdot\mathbf{P} + \rho_c\boldsymbol{E} + \boldsymbol{J}\times\boldsymbol{B}}, \tag{1.34}$$

which is the single-fluid *momentum equation*. Note that $\rho_c\boldsymbol{E}$ is negligible with respect to the other terms, but we keep it for the subsequent analysis. Finally, we need a relation that describes the time derivative of the current, also called *generalized Ohm's law*. Multiplying (1.30) by q_s/m_s, adding the ion version to the electron one, neglecting the quadratic terms in the small quantities $\partial_t n_s$ and $\boldsymbol{u}_s$ we find

$$\frac{\partial \boldsymbol{J}}{\partial t} = -\sum_s\left[\frac{q_s}{m_s}\boldsymbol{\nabla}\cdot\mathbf{P}_s + \frac{q_s^2 n_s}{m_s}\left(\boldsymbol{E}+\boldsymbol{u}_s\times\boldsymbol{B}\right)\right]. \tag{1.35}$$

We note that

$$\frac{n_e e^2}{m_e}\boldsymbol{u}_e = -\frac{e}{m_e}\boldsymbol{J} + \frac{e^2}{m_e m_i}\rho_M \boldsymbol{V} - \frac{m_e n_e e^2}{m_i n_i}\boldsymbol{u}_e. \tag{1.36}$$

Then, neglecting $1/m_i \ll 1/m_e$ whenever possible and assuming $n_e \simeq n_i \simeq n$, we find

$$\frac{\partial \boldsymbol{J}}{\partial t} = \frac{e}{m_e}\boldsymbol{\nabla}\cdot\mathbf{P}_e + \frac{ne^2}{m_e}\left(\boldsymbol{E} + \boldsymbol{u}\times\boldsymbol{B}\right) - \frac{e}{m_e}\boldsymbol{J}\times\boldsymbol{B}. \tag{1.37}$$

Multiplying the previous relation by $m_e/(ne^2)$ leads to the generalized Ohm's law

$$\boxed{\frac{m_e}{ne^2}\frac{\partial \boldsymbol{J}}{\partial t} = \frac{1}{ne}\boldsymbol{\nabla}\cdot\mathbf{P}_e + \boldsymbol{E} + \boldsymbol{u}\times\boldsymbol{B} - \frac{1}{ne}\boldsymbol{J}\times\boldsymbol{B}}. \tag{1.38}$$

Coupled with the Maxwell equations, we obtain a complete set of equations – if we assume the pressure term can be expressed in terms of mass density. For cold electrons, the gradient pressure is negligible and the first term of the right-hand side can be ignored whereas at low frequency (i.e., lower than the ion cyclotron frequency), the left-hand side is negligible. In addition, when the current is small the $\boldsymbol{J}\times\boldsymbol{B}$ term, also known as the *Hall term*, can be ignored[1]. Under these assumptions, Ohm's law becomes

$$\boldsymbol{E} = -\boldsymbol{u}\times\boldsymbol{B}, \tag{1.39}$$

and we finally obtain the non-relativistic equations of the *ideal MHD* that model a collisionless plasma as a fluid

$$\begin{aligned}
\frac{\partial \rho_M}{\partial t} + \boldsymbol{\nabla}\cdot(\rho_M \boldsymbol{u}) &= 0, && \text{(1.40a)}\\
\rho_M\left(\frac{\partial \boldsymbol{u}}{\partial t} + \boldsymbol{u}\cdot\boldsymbol{\nabla}\boldsymbol{u}\right) &= -\boldsymbol{\nabla}\cdot\mathbf{P} + \boldsymbol{J}\times\boldsymbol{B}, && \text{(1.40b)}\\
\frac{\partial \boldsymbol{B}}{\partial t} &= \boldsymbol{\nabla}\times(\boldsymbol{u}\times\boldsymbol{B}), && \text{(1.40c)}\\
\boldsymbol{\nabla}\times\boldsymbol{B} &= \mu_0\boldsymbol{J}, && \text{(1.40d)}
\end{aligned}$$

where the term involving $1/c^2$ in the Maxwell-Faraday equation (1.15c) is considered negligible, in particular due to the low-frequency assumption (i.e., non-relativistic plasma).

[1] By scaling the magnetic field in velocity units, $\boldsymbol{B} \to \boldsymbol{B}/\sqrt{\mu_0\rho_M}$, it appears that the Hall term is also negligible when modeling plasma dynamics at scales ℓ larger than the ion inertial length $d_i \equiv c/\omega_{\rm pi}$.

1.2.5 MHD Waves and linear theory

Waves play a central role in turbulence. They are the fundamental bricks on which many features and models of turbulence rely. In the context of ideal MHD, the plasma obeys the following equations

$$\begin{aligned}
\frac{\partial \rho}{\partial t} + \boldsymbol{\nabla} \cdot (\rho \boldsymbol{u}) &= 0, && \text{(1.41a)}\\
\frac{\partial P}{\partial t} &= -\gamma \frac{P}{\rho} \boldsymbol{\nabla} \cdot (\rho \boldsymbol{u}), && \text{(1.41b)}\\
\rho \left(\frac{\partial \boldsymbol{u}}{\partial t} + \boldsymbol{u} \cdot \boldsymbol{\nabla} \boldsymbol{u} \right) &= -\boldsymbol{\nabla} \left(P + \frac{B^2}{2\mu_0} \right) + \frac{1}{\mu_0} \boldsymbol{B} \cdot \nabla \boldsymbol{B}, && \text{(1.41c)}\\
\frac{\partial \boldsymbol{B}}{\partial t} + \boldsymbol{u} \cdot \boldsymbol{\nabla} \boldsymbol{B} &= \boldsymbol{B} \cdot \boldsymbol{\nabla} \boldsymbol{u}, && \text{(1.41d)}
\end{aligned}$$

where $\rho = \rho_M$ – we will adopt this notation for the rest of the manuscript – and we use a polytropic closure to link the pressure to the mass density with γ the polytropic index ($P \propto \rho^\gamma$).

Now, let us consider a uniform, stationary MHD fluid, threaded by a uniform magnetic field $\boldsymbol{B_0} = B_0 \boldsymbol{e}_\parallel$, where $\boldsymbol{e}_\parallel$ represents a unit vector. To orient the coordinate system, we will use $\boldsymbol{e}_\parallel = \boldsymbol{e}_z$ and, the perpendicular directions being $\boldsymbol{e}_x$ and $\boldsymbol{e}_y$. We perturb the fluid with small displacements, which we take to be sinusoidal:

$$\begin{aligned}
\rho &= \rho_0 + \rho_1 \mathrm{e}^{i(\boldsymbol{k}\cdot\boldsymbol{x} - \omega t)}, && \text{(1.42a)}\\
P &= P_0 + P_1 \mathrm{e}^{i(\boldsymbol{k}\cdot\boldsymbol{x} - \omega t)}, && \text{(1.42b)}\\
\boldsymbol{u} &= \boldsymbol{u_1} \mathrm{e}^{i(\boldsymbol{k}\cdot\boldsymbol{x} - \omega t)}, && \text{(1.42c)}\\
\boldsymbol{B} &= \boldsymbol{B_0} + \boldsymbol{B_1} \mathrm{e}^{i(\boldsymbol{k}\cdot\boldsymbol{x} - \omega t)}. && \text{(1.42d)}
\end{aligned}$$

By small displacement, we mean that nonlinearities are neglected. This results in *linear theory*. Our linearized MHD equations, projected along the perpendicular and the parallel directions, are then

$$\begin{aligned}
\omega \rho_1 &= \rho_0 \boldsymbol{k} \cdot \boldsymbol{u_1}, && \text{(1.43a)}\\
\omega P_1 &= \rho_0 c_s^2 \boldsymbol{k} \cdot \boldsymbol{u_1}, && \text{(1.43b)}\\
\omega \boldsymbol{u_1} &= \boldsymbol{k}_\perp \left(\frac{P_1}{\rho_0} + \frac{\boldsymbol{B_0} \cdot \boldsymbol{B_1}}{2\mu_0 \rho_0} \right) - \frac{\boldsymbol{B_0} \cdot \boldsymbol{k}}{\mu_0 \rho_0} \boldsymbol{B_1}, && \text{(1.43c)}\\
\omega \boldsymbol{B_1} &= -\left(\boldsymbol{B_0} \cdot \boldsymbol{k} \right) \boldsymbol{u_1} + \boldsymbol{B_0} \left(\boldsymbol{k} \cdot \boldsymbol{u_1} \right), && \text{(1.43d)}
\end{aligned}$$

where $c_s^2 = \gamma P_0 / \rho_0$ is the sound speed. Now, we establish the general wavevector $\boldsymbol{k} = k_\perp \boldsymbol{e}_\perp + k_\parallel \boldsymbol{e}_\parallel$ where $\boldsymbol{e}_\perp$

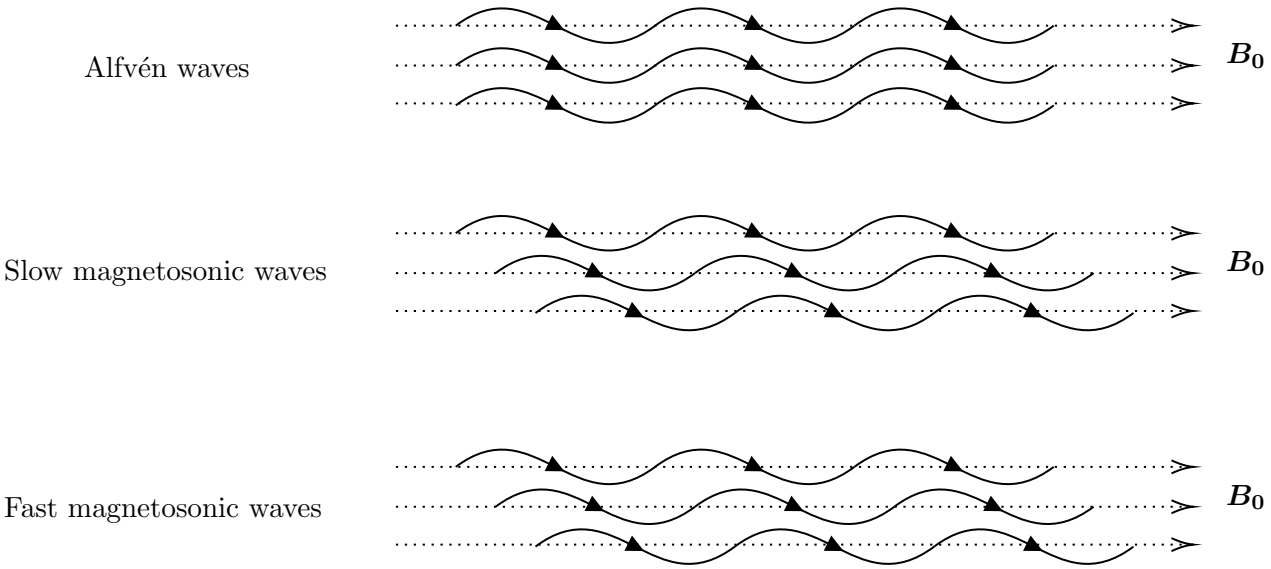

Figure 1.6: Illustration of the three distinct wave types, characterized within the framework of MHD. The dotted lines depict the local mean magnetic field, while the solid lines represent the perturbed magnetic field lines. The color gradient indicates the thermal pressure variations in the plasma. It is noteworthy that the direction of pressure variations does not always align with the local mean magnetic field. This peculiar case was chosen for illustrative purposes.

and $\boldsymbol{e}_\parallel$ are defined to be mutually perpendicular. By substituting Equations (1.43b – 1.43d) into Equation (1.43c), one obtains,

$$\begin{pmatrix} \omega^2 - k_\parallel^2 b_0^2 & 0 & 0 \\ 0 & \omega^2 - k_\perp^2 c_s^2 - k^2 b_0^2 & -k_\perp k_\parallel c_s^2 \\ 0 & -k_\perp k_\parallel c_s^2 & \omega^2 - k_\parallel^2 c_s^2 \end{pmatrix} \begin{pmatrix} u_{1x} \\ u_{1y} \\ u_{1z} \end{pmatrix} = 0, \tag{1.44}$$

where we have introduced the Alfvén velocity $b_0 \equiv B_0/\sqrt{\mu_0 \rho_0}$ for convenience. A non-trivial solution arises in this system when the determinant of the matrix is equal to zero. This condition leads to the following dispersion relation:

$$\left(\omega^2 - k_\parallel^2 b_0^2\right) \left[\omega^4 - \left(c_s^2 + b_0^2\right) k^2 \omega^2 + k^2 k_\parallel^2 c_s^2 b_0^2\right] = 0. \tag{1.45}$$

From this general relation, three distinct limits can be identified. First, in the incompressible case where $c_s \to \infty$, the first factor in the preceding expression must be zero. This yields the so-called Alfvén waves characterized by the dispersion relation:

$$\boxed{\omega_{\mathrm{A}} = \pm b_0 k_\parallel}. \tag{1.46}$$

They were analytically predicted by Hannes Alfvén [1] in 1942 who was awarded the prestigious Nobel Prize in 1970 "*for fundamental work and discoveries in magnetohydrodynamics with fruitful applications in different parts of plasma physics*" [22]. These are transverse waves ($\boldsymbol{u}_k$ and $\boldsymbol{b}_k$ are perpendicular to $\boldsymbol{k}$) propagating at the group velocity $\boldsymbol{b_0}$, also known as the Alfvén speed. The phase velocity v_ϕ of these waves can be expressed as $v_\phi = b_0 k_\parallel / k$, indicating their semi-dispersive nature. Essentially, these waves exhibit anisotropic behavior. As shown in the top panel of Figure 1.6, Alfvén waves are magnetic field perturbations and act on the field like you will pluck a string. The initial experimental attempts to detect them were conducted in a magnetized mercury bath [18] and later in ionized helium gas [5]. The first irrefutable evidence of their existence was provided by Lehnert [15] in 1954 using liquid sodium. Subsequently, Alfvén waves were observed in the interplanetary space by the Pioneer and Explorer probes [7]. It was not until 2008 that the initial indications of Alfvén waves on the Sun were obtained through the data collected by the Hinode/JAXA space telescope [21].

We have two additional solutions known as the fast and slow magnetosonic waves, which correspondingly follow the dispersion relations:

$$\omega_{\mathrm{F}} = \pm\frac{c_s k}{\sqrt{2}}\left[1+\frac{b_0^2}{c_s^2}+\sqrt{\left(1+\frac{b_0^2}{c_s^2}\right)^2-4\frac{b_0^2}{c_s^2}\frac{k_\parallel^2}{k^2}}\right]^{1/2}, \tag{1.47a}$$

$$\omega_{\mathrm{S}} = \pm\frac{c_s k}{\sqrt{2}}\left[1+\frac{b_0^2}{c_s^2}-\sqrt{\left(1+\frac{b_0^2}{c_s^2}\right)^2-4\frac{b_0^2}{c_s^2}\frac{k_\parallel^2}{k^2}}\right]^{1/2}. \tag{1.47b}$$

It is readily apparent that these waves emerge as natural extensions of the classical sound waves in the context of a magnetic field. In the absence of such a field, the Alfvén waves cease to exist and the MHD equations revert to their hydrodynamic form. Consequently, the discernment between fast and slow waves becomes impossible, and they assimilate into the isotropic sound waves. The key distinction between the slow and fast waves lies in the positioning of the pressure perturbations relative to the magnetic field lines. In the case of fast waves, compression regions align with regions where the magnetic field lines are closely packed, while rarefaction regions correspond to regions where the magnetic field lines are more spread apart. The fundamental difference is that for fast waves, there are two restoring forces working in unison: the thermal pressure, which tends to expand the plasma, and the magnetic field, which resists compression. In contrast, slow waves exhibit an anti-correlation between thermal pressure and changes in field strength, resulting in a scenario where the combined effect of thermal and magnetic pressure is relatively small. The

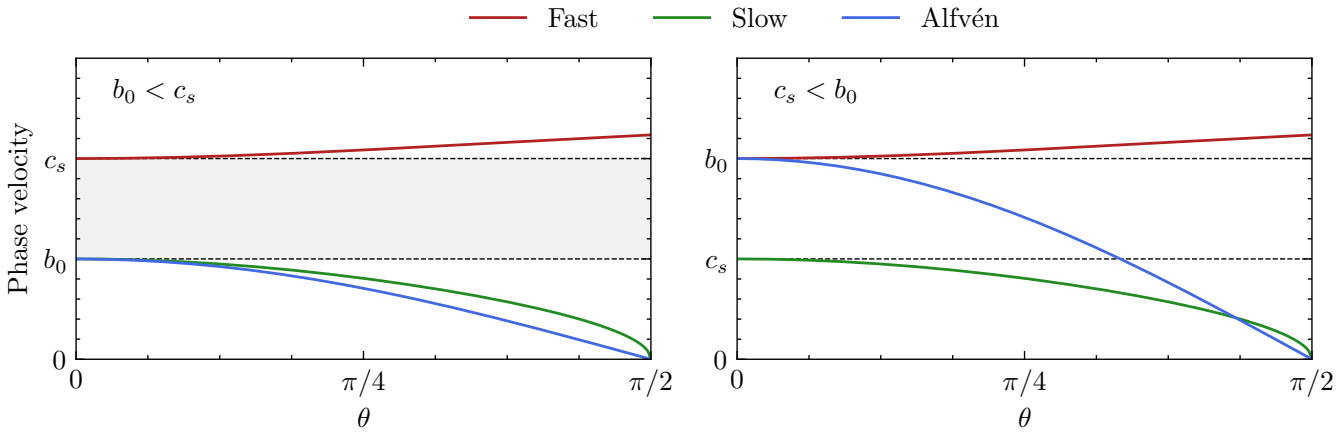

Figure 1.7: The phase diagrams depict the behavior of fast, slow, and Alfvén waves with respect to the angle θ between the mean magnetic field $\boldsymbol{B_0}$ and the wavevector $\boldsymbol{k}$. In the case where thermal pressure dominates over magnetic pressure ($b_0 < c_s$), shown on the left, a distinct region emerges where no waves occur within the phase velocity range of $v_\phi \in [b_0, c_s]$. Conversely, in the case where magnetic pressure dominates over thermal pressure ($c_s < b_0$), depicted on the right, there is no forbidden region.

distinction is illustrated in the middle and bottom panels of Figure 1.6.

Another intriguing aspect concealed within these magnetosonic waves is the regime of high thermal pressure relative to the magnetic pressure. In this scenario, where $b_0 \ll c_s$, the fast waves exhibit a dispersion relation approximately given by $\omega_{\rm F} \simeq \pm c_s k$, while the dispersion relation for the slow wave tends to $\omega_{\rm S} \simeq \pm b_0 k_\parallel$. These correspond, respectively, to the classical sound waves and the Alfvén-like waves. Notably, in this regime, the two types of waves become decoupled, coexisting without any interplay or exchange. Two last intriguing limits worth noting are when $k = k_\parallel$ and $k = k_\perp$. In the former case, one of the waves can be identified as a sound wave propagating along the mean magnetic field ($\omega_{\rm F} \simeq \pm c_s k_\parallel$), while the other wave can be identified as the classical Alfvén wave ($\omega_{\rm S} \simeq \pm b_0 k_\parallel$). In the latter case, only the fast wave persists, which takes the form of a longitudinal wave resembling a modified sound wave: $\omega_{\rm F} \simeq \pm c_s^2 k^2 \sqrt{1 + b_0^2/c_s^2}$. Figure 1.7 displays the phase diagram of the magnetosonic waves, encompassing all of these scenarios. To summarize, in ideal MHD, we encounter two significant types of waves: Alfvén waves and magnetosonic waves.

1.3 Solar wind

1.3.1 What is it?

Each second, approximately 10^{36} particles escape from the Sun, forming what we call the solar wind. These particles (mainly electrons, protons, and α-particles) have an exceptionally large mean free path, which is

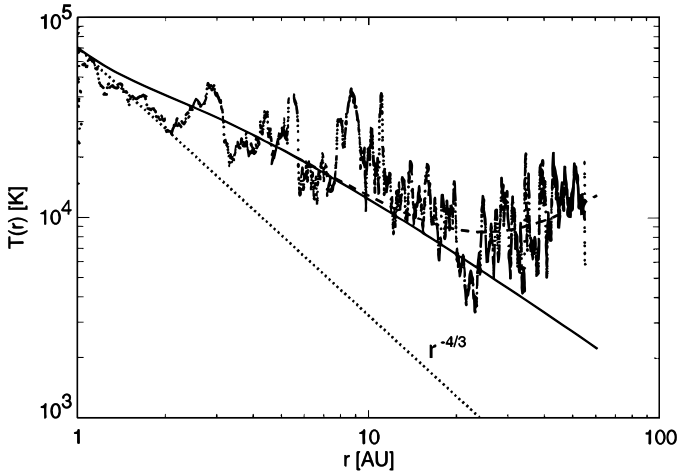

Figure 1.8: Proton temperature data from Voyager 2 plasma instrument, from 1 au to about, 50 au. Credits: Matthaeus *et al.* [19].

the average distance between two collisions. In fact, it is estimated that a particle in the solar wind will only collide (Coulomb collisions) with another particle approximately once every Sun-Earth distance. This characteristic renders the solar wind a collisionless plasma, resulting in a highly diluted environment with only about 10^7 particles per cubic meter at one astronomical unit (au) from the Sun, in contrast to the approximately 10^{25} particles per cubic meter in the air we breathe at sea level. The solar wind presents a plethora of intriguing questions, such as the mechanisms behind its acceleration, the temperature evolution resulting from the absence of collisions, and the presence of two distinct winds, one being approximately twice as fast as the other [6]. As an illustrative instance where turbulence might play a role, we present in Figure 1.8 the radial variation of the temperature of solar wind protons. The intriguing aspect here lies in the quest to precisely identify and quantify the elusive mechanisms responsible for shaping this temperature profile. These are all important questions that drive active research, including in the field of turbulence. However, I do not want to limit the study of plasma turbulence to just these questions. In my view, the solar wind is a fundamental object that can offer insights that go far beyond its own properties.

1.3.2 Why use it?

When it comes to the fundamentals of physics, our goal is to describe nature using mathematical models that explain measurements. However, in astrophysics, we face a unique challenge as the phenomena and objects we seek to understand are often located far away from us. As a result, we can only rely on a magnifying glass (however large and sophisticated) to infer properties from the light we receive. The main issue is that light has been traveling over very (very) long distances, crossing various media, and

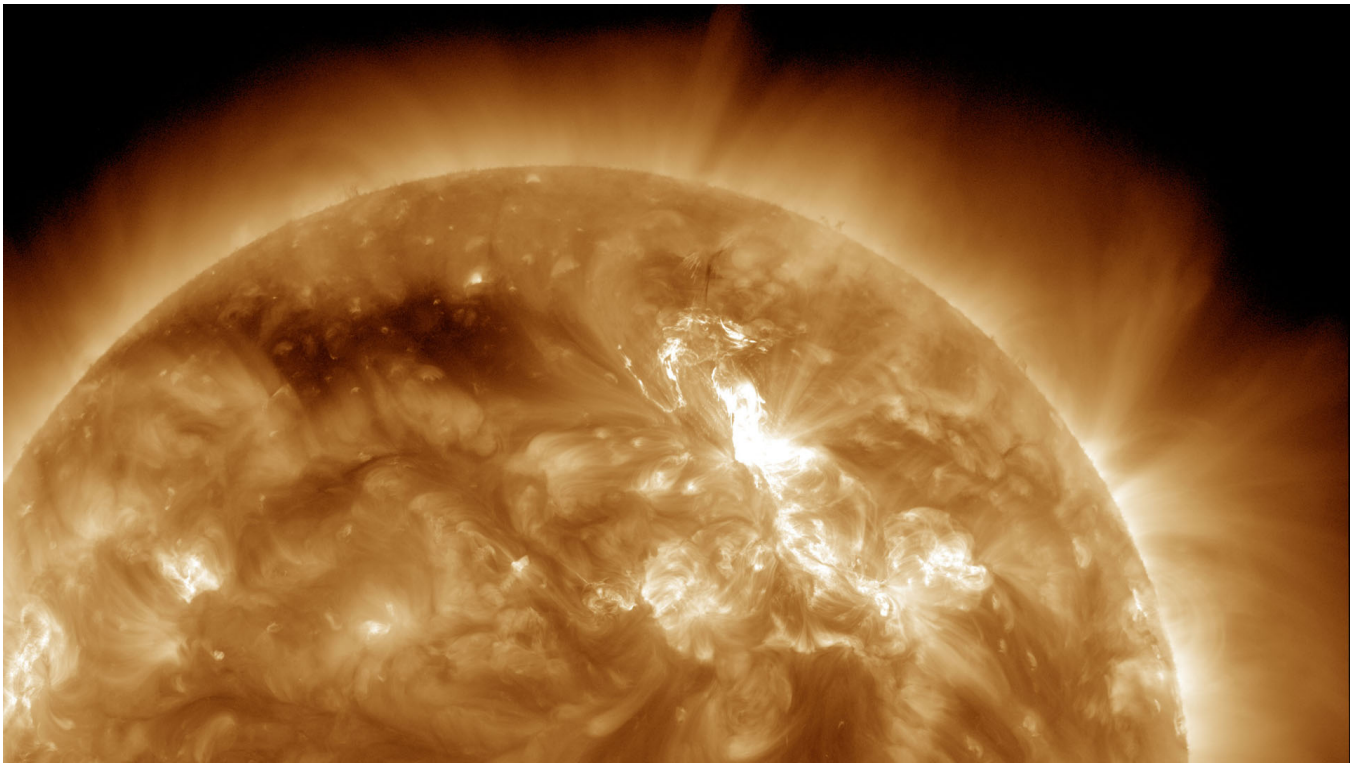

Figure 1.9: Photo taken January 22, 2012, at the wavelength 17.1 nm (Fe IX line): the Sun erupted with a solar flare leading to a coronal mass ejection and a burst of highly energetic protons known as solar energetic particles. Credits: NASA/SDO/AIA.

has a significant chance of interacting with them, potentially falsifying our deductions. Thankfully, the plasma turbulence community enjoys a unique advantage in the form of solar wind, as illustrated in Figure 1.9. This archetypal plasma with no boundary condition is located at $\sim 100,000$km from Earth – to be understood as two steps away from home – presents an ideal opportunity for launching spacecraft and obtaining in situ measurements to test the validity of our theories and making detailed predictions. As we assume that physical laws remain constant in time and space [20], we have verified that, out of the countless stars identified in the visible universe, our sun is a prototypical middle-aged star [14]. This allows us to reasonably assume that our findings on the solar wind are likely applicable to a multitude of other stars. By leveraging this universal character, we can attempt to model plasma turbulence in its essence and gain a profound understanding of this ubiquitous phenomenon.

1.3.3 What about turbulence in the solar wind?

In this thesis, I will focus on turbulence through the fluid approach, using the solar wind to discuss with nature. The fluid approach can seem out of context since this medium is collisionless but because it is

collisionless its Reynolds number is huge and turbulence may play an essential role in the dynamics, acting as a unifying force, linking scales through a cascade process, and enhancing the cohesion of the plasma. This cohesion not only enables the description of the large-scale solar wind with MHD, but also makes the fluid approach relevant even at scales where kinetic effects would be expected to dominate [10]. The most common refinement to probe turbulence beyond MHD scales is the Hall-MHD that takes into account the Hall term in the generalized Ohm's law we derived above. The idea is since a proton is more than 1800 times heavier than an electron, the mass ratio between the two species is roughly equivalent to that between an African bush elephant and a newborn baby. It goes without saying that if you apply the same amount of force to push the elephant and the baby, one will move a little faster than the other... This is precisely what the Hall effect describes: due to the mass difference between ions and electrons, the two species exhibit different dynamics. Ions move more slowly than electrons, which results in a separation of electric charge and the creation of a (Hall) current. Further refinements are possible by playing with Ohm's law, but for the solar wind, the collisionless nature implies some kinetic effects that are no longer negligible as we model plasma at scales smaller and smaller. One can always use the fluid framework to probe peculiar effects, but it will be complicated to arrive at a complete understanding of the plasma properties at small scales/high frequencies.

In this manuscript, I will explore the intriguing world of turbulence across various scales of plasma. My focus will be on investigating two distinct regimes: the weak and strong turbulence. We will delve into the details of these two approaches in the upcoming chapters, but the key difference between them lies in the impact of nonlinear terms in the equations. In summary, weak turbulence consists of interacting waves that are distorted over a much longer timescale than linear waves due to weak nonlinearities in the equations. After numerous interactions, we can make detailed predictions of how the plasma energy will evolve and at which scale, both quantitatively and qualitatively. Although powerful, this approach is somewhat limiting because it only models a specific type of plasma, and as time progresses, the turbulence cannot remain weak. The strong turbulence approach does not have a theory that is as rigorous and predictive as the weak turbulence approach, but we can still make analytical predictions. These are based on what is known as the Zeroth law of turbulence, which is considered to be an axiom. The Zeroth law of turbulence states that "*If in an experiment on turbulent flow, all control parameters are fixed, except for the viscosity, which is lowered as much as possible, the energy dissipation per unit mass ε approaches a nonzero limit.*" [9]. I will discuss this milestone in more detail in the next chapter, but this unique property that the energy dissipation of a turbulent flow is independent of viscosity has sparked investigations that have led to the

discovery of the only law that we are currently capable of predicting in strong turbulence.

There is another important aspect of turbulence theory that I have not mentioned yet, but it plays a central role. If you are a mathematician, you can skip this part and go directly to the next section. Physicists often rely on dimensional analysis to make predictions using hand calculations before delving into more sophisticated analyses (and potentially seeking help from mathematicians). The turbulence community is no exception to this approach. Moreover, due to the inherent complexity of the equations that model turbulence, there are predictions based solely on what is known as phenomenology, which is a jargon used to refer to a refined dimensional analysis in the context of turbulence. Although approximate, phenomenology enables us to make predictions that have been validated through direct numerical simulations (DNS) and in situ observations. It remains a valuable tool to consider, even though it can never replace rigorous theories.

1.4 Overview

This manuscript is divided into six chapters (excluded this one). In Chapter 2, I present an MHD low-dimensional model, for which I prove the Zeroth law of turbulence. Chapter 3 extends the findings from the preceding chapter to the three-dimensional case, allowing us to apply these theoretical insights to estimate the energy dissipation in solar wind turbulence using in situ data. In Chapter 4, we venture into sub-MHD scales, where ions are too heavy to follow the electron dynamics, to explore the differences between weak and strong turbulence regimes. By conducting direct numerical simulations, we investigate whether either of these regimes can capture the features of solar wind turbulence at such scales. We then continue to descent into the depths of plasma dynamics in Chapter 5. Here, we delve into the intricate world of even smaller scales, where the influence of electron inertia cannot be overlooked. By developing a weak turbulence theory, we aim to predict the energy spectrum at these scales, taking into account the perturbations induced by electron inertia that were previously neglected. We finally discuss, in Chapter 6, an elegant connection between the equations governing the prediction of the energy spectrum and the world of autonomous dynamical systems. This intriguing link allows us to accurately measure the power law of the energy spectrum in the absence of dissipative processes, thus overcoming the limitations encountered in previous chapters. In Chapter 7, we bring this expedition to its end, offering a succinct recapitulation and perspectives that highlights the necessity of a collaborative effort, intertwining theoretical investigations, numerical simulations, and the scrutiny of observational data.

In summary, this manuscript provides an overview of three years' worth of research on hot and chaotic space gas.

References

[1] H. Alfvén, "Existence of electromagnetic-hydrodynamic waves," *Nature*, vol. 150, no. 3805, pp. 405–406, Oct. 1942.

[2] C. F. Barenghi, L. Skrbek, and K. R. Sreenivasan, "Introduction to quantum turbulence," *Proceedings of the National Academy of Sciences*, vol. 111, no. supplement_1, pp. 4647–4652, 2014.

[3] G. Belmont, L. Rezeau, C. Riconda, and A. Zaslavsky, *Introduction to Plasma Physics*. Science Direct, 2019.

[4] L. Boltzmann, "Weitere studien über das wärmegleichgewicht unter gasmolekülen," *Sitzungsberichte Akademie der Wissenschaften*, vol. 66, pp. 275–370, 1872.

[5] W. H. Bostick and M. A. Levine, "Experimental demonstration in the laboratory of the existence of magneto-hydrodynamic waves in ionized helium," *Phys. Rev.*, vol. 87, pp. 671–671, 4 Aug. 1952.

[6] R. Bruno and V. Carbone, "The solar wind as a turbulence laboratory," *Living Reviews in Solar Physics*, vol. 10, no. 1, p. 2, May 2013.

[7] P. J. Coleman Jr., C. P. Sonett, D. L. Judge, and E. J. Smith, "Some preliminary results of the pioneer v magnetometer experiment," *Journal of Geophysical Research (1896-1977)*, vol. 65, no. 6, pp. 1856–1857, 1960.

[8] P. Debye and E. Hückel, "Zur theorie der elektrolyte. i. gefrierpunktserniedrigung und verwandte erscheinungen," *Physikalische Zeitschrift*, vol. 24, pp. 185–206, 1923.

[9] U. Frisch, *Turbulence: The Legacy of A. N. Kolmogorov*. Cambridge University Press, 1995.

[10] S. Galtier, *Introduction to modern magnetohydrodynamics*. Cambridge University Press, 2016, p. 288.

[11] P. Hennebelle and E. Falgarone, "Turbulent molecular clouds," *The Astronomy and Astrophysics Review*, vol. 20, no. 1, p. 55, Nov. 2012.

[12] Y. L. Klimontovich, "On the method of 'second quantization'in phase space," *Sov. Phys. JETP*, vol. 6, no. 33, p. 4, 1958.

[13] L. D. Landau, *Oscillations of an electron plasma*. US Atomic Energy Commission, 1946.

[14] R. Langendorf, S. Schneider, and P. Klein, "Extracting information from the hertzsprung-russell diagram: An eye-tracking study," *Phys. Rev. Phys. Educ. Res.*, vol. 18, p. 020 121, 2 Sep. 2022.

[15] B. Lehnert, "Magneto-hydrodynamic waves in liquid sodium," *Phys. Rev.*, vol. 94, pp. 815–824, 4 May 1954.

[16] E. N. Lorenz, "Deterministic nonperiodic flow," *Journal of Atmospheric Sciences*, vol. 20, no. 2, pp. 130–141, 1963.

[17] E. N. Lorenz, "Predictability: Does the flap of a butterfly's wings in brazil set off a tornado in texas?" American Association for the Advancement of Science, Dec. 1972.

[18] S. Lundquist, "Experimental investigations of magneto-hydrodynamic waves," *Phys. Rev.*, vol. 76, pp. 1805–1809, 12 Dec. 1949.

[19] W. H. Matthaeus, G. P. Zank, C. W. Smith, and S. Oughton, "Turbulence, spatial transport, and heating of the solar wind," *Phys. Rev. Lett.*, vol. 82, pp. 3444–3447, 17 Apr. 1999.

[20] E. Noether, "Invariante variationsprobleme," ger, *Nachrichten von der Gesellschaft der Wissenschaften zu Göttingen, Mathematisch-Physikalische Klasse*, vol. 1918, pp. 235–257, 1918.

[21] B. D. Pontieu *et al.*, "Chromospheric alfvénic waves strong enough to power the solar wind," *Science*, vol. 318, no. 5856, pp. 1574–1577, 2007.

[22] N. Prize, *The nobel prize in physics 1970*, Jun. 2023.

[23] N. D. R., *Introduction to Plasma Theory*. Wiley, 1983.

[24] O. Reynolds, "Xxix. an experimental investigation of the circumstances which determine whether the motion of water shall be direct or sinuous, and of the law of resistance in parallel channels," *Philosophical Transactions of the Royal Society of London*, vol. 174, pp. 935–982, 1883.

[25] R. Robson, *Introductory Transport Theory for Charged Particles in Gases*. World Scientific, 2006.

[26] K. M. Saqr *et al.*, "Physiologic blood flow is turbulent," *Scientific Reports*, vol. 10, no. 1, p. 15 492, Sep. 2020.

[27] R. A. Shaw, "Particle-turbulence interactions in atmospheric clouds," *Annual Review of Fluid Mechanics*, vol. 35, no. 1, pp. 183–227, 2003.

[28] I. P. Shkarofsky, T. W. Johnston, M. P. Bachynski, and J. L. Hirshfield, "The Particle Kinetics of Plasmas," *American Journal of Physics*, vol. 35, no. 6, pp. 551–552, Jun. 1967.

[29] A. Smits, *Viscous flows and turbulence*, Sep. 2009.

[30] J. Sommeria, S. D. Meyers, and H. L. Swinney, "Laboratory simulation of jupiter's great red spot," *Nature*, vol. 331, no. 6158, pp. 689–693, Feb. 1988.

[31] G. G. Stokes, *On the Effect of the Internal Friction of Fluids on the Motion of Pendulums* (Cambridge Library Collection - Mathematics). Cambridge University Press, 1851, vol. 3, pp. 1–.

[32] L. Tonks and I. Langmuir, "Oscillations in ionized gases," *Phys. Rev.*, vol. 33, pp. 195–210, 2 Feb. 1929.

[33] A. A. Vlasov, "The vibrational properties of an electron gas," *Usp. Fiz. Nauk*, vol. 93, no. 11, pp. 444–470, 1967.

Chapter 2

The Yanase model

This study is published in:

V. David & S. Galtier., "Proof of the Zeroth Law of Turbulence in 1D Compressible MHD and Shock Heating", *Phys. Rev. E*, **103**, 063217, 2021.

2.1 Introduction

The Yanase model is to MHD what the Burgers equation is to hydrodynamics. One might question the value of studying a simplified model, but as Kadanoff has pointed out: *"The strategy of studying physical questions by using highly simplified models is made rewarding by a characteristic of physical systems called "universality", in that many systems may show the very same qualitative features, and sometimes even the same quantitative ones. To study a given qualitative feature, it often pays to look for the simplest possible example."* [27]. Following this principle, we will demonstrate the Zeroth law of turbulence by examining it through the framework of the Yanase model. But before presenting the novel insights that the Yanase model brings to turbulence theory, I must take a brief detour to introduce an older method that has been employed for many years and has provided valuable insights into the behavior of turbulent systems. Despite the advent of newer techniques, it remains a valuable tool for understanding the fundamental aspects of turbulence. In reality, the upcoming presentation is an extension of the older approach, which was extensively utilized but necessitates restrictive assumptions to be applied.

2.1.1 The elementary brick

Turbulence has an interesting property known as the *Zeroth law of turbulence*, which is regarded as an axiom. In hydrodynamics, as the viscosity ν approaches zero, the total energy of the system continues to decrease at a constant rate ε, regardless of the value of the viscosity. This observation is somewhat surprising, but it turns out that this behavior is consistent with a key principle named *anomalous dissipation*

$$\lim_{\nu \to 0} \frac{\mathrm{d}E}{\mathrm{d}t} = -\varepsilon < 0. \tag{2.1}$$

This property is something that is a bit counter-intuitive and raises interesting questions. For instance, is the limit of $\nu \to 0$ the same as having $\nu = 0$? And assuming that statement is true, how can a conservative system dissipate energy? Before considering these questions, I have to follow the historical storytelling and present what was for a long time the only theoretical result we had concerning the strong turbulence.

2.1.2 The exact law of turbulence

In the 1940s, a Russian mathematician named Kolmogorov tackled this problem and made a groundbreaking contribution to the field of hydrodynamic turbulence, leaving behind a remarkable legacy. While I will not

delve into the derivation of his result, as numerous textbooks, books, reviews, and articles have already covered it, I will describe the key idea, hypotheses on which this result is based, and its implications.

Starting with the incompressible Navier-stokes equations (1.1), the idea was to derive an equation describing the time evolution of the velocity correlation tensor $R_{ij}(\boldsymbol{x}, \boldsymbol{r}, t) \equiv \langle u_i(\boldsymbol{x}, t) u_j(\boldsymbol{x} + \boldsymbol{r}, t) \rangle$, where $\langle \cdot \rangle$ is the ensemble average. This is the fundamental quantity upon which all statistical theories of turbulence are built, and measures how much two distinct points separated from a distance $\boldsymbol{r}$ are dependent on each other. Based on this tool, one can distinguish three peculiar cases:

- If $R_{ij}(\boldsymbol{x}, \boldsymbol{r}, \cancel{t})$, then the turbulence is stationary.
- If $R_{ij}(\cancel{\boldsymbol{x}}, \boldsymbol{r}, t)$, then the turbulence is statistically homogeneous.
- If $R_{ij}(\boldsymbol{x}, |\boldsymbol{r}|, t)$, then the turbulence is isotropic, meaning that the ensemble averages possess mirror symmetry and are invariant under rotation of the reference frame.

Here, we must take note that the definition of R_{ij} involves the fluctuating velocity field, which has a zero mean. The correlation tensor measures the disparity between the velocity field at two distinct points, let us say M and M' (cf. Figure 2.1). It is important to stress that fluid flow does not undergo sudden changes in an instant. Even in turbulent situations, there is a form of memory within the flow, and it requires a certain duration for the observed fluid parcel to undergo significant transformations from its initial state. Thus, for large separations r, we expect the velocity correlation tensor $R_{ij}(\boldsymbol{r})$ to approach zero, while in the limit of $r \to 0$, R_{ij} only gives us information about the kinetic energy at a single point $\boldsymbol{x}$, and does not reveal anything about the distribution of energy concerning the size of turbulent structures. To address this, we introduce the velocity increment $\delta \boldsymbol{u} \equiv \boldsymbol{u}(\boldsymbol{x} + \boldsymbol{r}) - \boldsymbol{u}(\boldsymbol{x})$, which acts as a statistical spatial filter, extracting information about the distribution of velocity with respect to separation scales $\boldsymbol{r}$.

With the help of these mathematical tools, the earliest prediction for turbulent flow was made in 1941 by Kolmogorov [28] which is now known as the four-fifths law due to a particular constant that appears in the equation. The path to this result involved tensor analysis, which can make the formalism cumbersome. In this section, we will follow a more direct approach to derive this law in a different form: the four-thirds law, which was only discovered in 1997 by Antonia *et al.* [4]. Both laws relate the third-order structure functions — representing the velocity field's increment moment — to the separation distance between two points in homogeneous, isotropic, stationary, and three-dimensional incompressible turbulence.

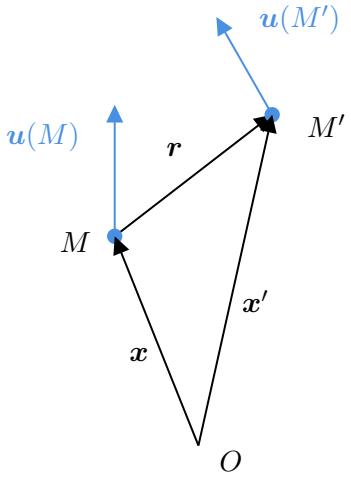

Figure 2.1: In homogeneous turbulence, only the relative difference in position between the points M and M' is relevant.

Let us write the incompressible Navier-Stokes equations at points $\boldsymbol{x}$ and $\boldsymbol{x'}$

$$\partial_t u_i + \partial_k \left(u_k u_i\right) = -\partial_i P_i + \nu \partial_{kk} u_i + f_i, \tag{2.2a}$$

$$\partial_t u'_j + \partial'_k \left(u'_k u'_j\right) = -\partial'_j P'_j + + \nu \partial'_{kk} u'_j + f'_j, \tag{2.2b}$$

where Einstein's notations are used, $\boldsymbol{f}$ represents the external large scale forcing, and the prime symbol in the derivatives and pressure term signifies that they are with respect to the variable $\boldsymbol{x'}$. Multiply the first equation by u'_j and the second by u_i, and the addition of these two equations gives us, on taking the ensemble average, a dynamic equation for the second-order correlation tensor

$$\begin{aligned}\partial_t \left\langle u_i u'_j \right\rangle + \left\langle \partial_k \left(u_k u_i u'_j\right) + \partial'_k \left(u'_k u_i u'_j\right) \right\rangle = &- \left\langle \partial_i \left(P_i u'_j\right) + \partial'_j \left(P'_j u_i\right) \right\rangle + \nu \left\langle \partial_{kk} \left(u_i u'_j\right) + \partial'_{kk} \left(u_i u'_j\right) \right\rangle \\ &+ \left\langle f_i u'_j + f_j u_i \right\rangle .\end{aligned} \tag{2.3}$$

Assuming homogeneity and after a few calculations (see e.g Galtier [21]) one can rewrite the previous relation as follows

$$\frac{\partial}{\partial t} \left\langle \frac{u_i u'_i}{2} \right\rangle = \frac{1}{4} \boldsymbol{\nabla}_{\boldsymbol{r}} \cdot \left\langle \left(\delta \boldsymbol{u} \cdot \delta \boldsymbol{u}\right) \delta \boldsymbol{u} \right\rangle + 2\nu \nabla_r^2 \left\langle \frac{u_i u'_i}{2} \right\rangle + \mathcal{F}, \tag{2.4}$$

where $\mathcal{F}(\boldsymbol{r})$ is a correlator as well. We now define the mean rate of total energy injection as $\mathcal{F} = \varepsilon$. The final expression of the exact law is valid in the inertial range, where the corresponding scales are much smaller than the forcing scales but much larger than the dissipation scales. By using the stationarity

assumption, we find

$$\varepsilon = -\frac{1}{4}\boldsymbol{\nabla}_{\boldsymbol{r}} \cdot \langle (\delta \boldsymbol{u} \cdot \delta \boldsymbol{u})\, \delta \boldsymbol{u} \rangle \,. \tag{2.5}$$

Assuming isotropy, one can integrate this expression and obtain the *four-third law*

$$\boxed{-\frac{4}{3}\varepsilon r = \langle (\delta \boldsymbol{u} \cdot \delta \boldsymbol{u})\, \delta u_r \rangle}, \tag{2.6}$$

where u_r is the longitudinal component of the velocity, i.e., that along the direction of separation $\boldsymbol{r}$. This expression provides an estimate of the energy flux in the inertial range, which is far from the forcing and dissipation ranges. At the time of its discovery, it was the only theoretical result that did not require perturbative development, hence it is referred to as an exact law. Since, it has been generalized to more complex systems such as both incompressible and compressible MHD [2, 6, 38, 40], Hall-MHD [1, 7, 20, 22, 26] and even gravitoturbulence [8, 9]. However, the applicability of exact laws is quite restrictive since several approximations are needed to derive them. Specifically, an external force is required to reach a stationary state, and the flow must be homogeneous (and isotropic). In the next sections, we will explore an alternative approach that relaxes some of these assumptions by working with weak solutions.

Inspired by the Leray [29] idea that turbulent solutions of the Navier-Stokes equations might be irregular, Onsager [35] suggested examining the Euler equation to shed light on this intriguing phenomenon. He states that the absence of viscosity in the Euler equation causes the flow to evolve into a turbulent state, leading to sharp gradients, irregularities and this lack of smoothness can result in energy dissipation. More recently, two French mathematicians, Jean Duchon, and Raoul Robert [18], made a big leap forward in support of Leray and Onsager. First, they proved that the answer to the earlier question is yes, the same phenomenon occurs in the Euler equations, and then the Zeroth law is still valid when $\nu = 0$. They also devised a method based on *weak solutions* for calculating anomalous dissipation in both Euler and Navier-Stokes equations and provided an expression for it.

In this chapter, we will focus on Onsager's conjecture using a low-dimensional model of MHD called the *Yanase model*. By following the approach of Duchon & Robert, we will prove the Zeroth law of turbulence in this model, and thus get a good feeling for how to estimate the energy dissipation rate ε defined in Equation (2.1).

2.2 Mathematical prerequisites

2.2.1 What is a weak solution?

It is not superfluous to introduce the concept of weak solutions mathematically before delving into calculations. First, let me introduce the Hölder continuity. A function f defined on a segment $I \in \mathbb{R}$ is α-Hölder continuous, where $\alpha \in \mathbb{R}_+^*$, if there exists a positive constant C_α such that for any pair of points $x, y \in I$

$$|f(x) - f(y)| \leq C_\alpha |x - y|^\alpha . \tag{2.7}$$

For $\alpha = 1$, we recognize the Lipschitz continuity. Now, if $\alpha > 1$, $f(x)$ is constant. To prove it, we can rearrange the terms as

$$\left| \frac{f(x) - f(y)}{x - y} \right| \leq C_\alpha |x - y|^{\alpha - 1}$$

and by taking the limit as $(x-y) \to 0$, we can identify $f'(x)$ on the left-hand side of the equation, while the right-hand side approaches zero. Thus, $f(x)$ is constant if $\alpha > 1$. In considering the case of $\alpha < 1$, we find that according to the definition (2.7), the function f is still uniformly continuous, but its derivative may diverge and therefore cannot be defined in the usual sense. This leads to the introduction of the concept of a *weak derivative*, which is more general than the (strong) derivative and is applicable to functions that are not differentiable but still integrable. When dealing with weak derivatives, it can be useful to employ the notion of generalized functions – also named distributions. Specifically, we can move the derivatives onto a suitable test function, which enables us to work with weak solutions of the equations. This test function should be an infinitely differentiable function with compact support, even, non-negative, and having an integral of 1.

2.2.2 An example of the use of weak solutions

When we solve ordinary or partial differential equations, we usually assume that the solution is smooth and has all its derivatives well-defined. But sometimes, equations do not have nice, smooth solutions that we can differentiate. In these cases, we can use the concept of *weak solutions,* which allows us to find solutions to equations even when we cannot differentiate them. The idea is to rewrite the equation in a way that does not require differentiating the solution, and then find functions that satisfy this new weak formulation. These are important because they allow us to solve equations that we would not be able to otherwise and are encountered in many real-world phenomena such as conservation laws.

As an example, one can take the linear diffusion equation seen in the previous chapter. Let us assume that the diffusion coefficient $\nu = 1$, then

$$\frac{\partial u(x,t)}{\partial t} = \frac{\partial^2 u(x,t)}{\partial x^2}. \tag{2.8}$$

To get an idea of the properties of a hypothetical solution $u(x,t)$ without directly solving the equation, one can integrate it with a test function $\varphi(x,t)$.

$$\int_{-\infty}^{+\infty}\int_{-\infty}^{+\infty} \frac{\partial u(x,t)}{\partial t}\varphi(x,t)\mathrm{d}x\mathrm{d}t = \int_{-\infty}^{+\infty}\int_{-\infty}^{+\infty} \frac{\partial^2 u(x,t)}{\partial x^2}\varphi(x,t)\mathrm{d}x\mathrm{d}t.$$

Performing an integration by parts, the boundary terms vanish because of the compact support of $\varphi(x,t)$ and we find

$$\int_{-\infty}^{+\infty}\int_{-\infty}^{+\infty} u(x,t)\frac{\partial \varphi(x,t)}{\partial t}\mathrm{d}x\mathrm{d}t = -\int_{-\infty}^{+\infty}\int_{-\infty}^{+\infty} u(x,t)\frac{\partial^2 \varphi(x,t)}{\partial x^2}\mathrm{d}x\mathrm{d}t. \tag{2.9}$$

So, if $u(x,t)$ is continuously differentiable, then equation (2.8) implies equation (2.9). But there are functions $u(x,t)$ that can satisfy equation (2.9) for any $\varphi(x,t)$, even though they might not be differentiable and therefore cannot satisfy equation (2.8). This is where the concept of weak solutions comes in. It allows us to deal with these types of functions and still make sense of the equation. In the subsequent analysis, we assume that weak solutions are primarily concerned with resolving spatial irregularities rather than temporal ones. Then, the test function φ will depend solely on the spatial variable x.

2.3 The Yanase model

2.3.1 Derivation of the model

We start from the 3D compressible MHD equations (with $\boldsymbol{\nabla}\cdot\boldsymbol{B} = 0$)

$$\frac{\partial \rho}{\partial t} + \boldsymbol{\nabla}\cdot(\rho\boldsymbol{u}) = 0, \tag{2.10a}$$

$$\rho\left(\frac{\partial \boldsymbol{u}}{\partial t} + \boldsymbol{u}\cdot\boldsymbol{\nabla}\boldsymbol{u}\right) = -\boldsymbol{\nabla}P + \frac{1}{\mu_0}(\boldsymbol{\nabla}\times\boldsymbol{B})\times\boldsymbol{B} + \mathbf{d}_{\tilde{\nu}}, \tag{2.10b}$$

$$\frac{\partial \boldsymbol{B}}{\partial t} = \boldsymbol{\nabla}\times(\boldsymbol{u}\times\boldsymbol{B}) + \mathbf{d}_{\eta}, \tag{2.10c}$$

where ρ is the mass density, $\boldsymbol{u}$ the velocity, $\boldsymbol{B}$ the magnetic field, P the pressure, μ_0 the magnetic permeability of the vacuum, $\mathbf{d}_{\tilde{\nu}} = \tilde{\nu}\nabla^2\boldsymbol{u} + (\tilde{\nu}/3)\boldsymbol{\nabla}(\boldsymbol{\nabla}\cdot\boldsymbol{u})$ and $\mathbf{d}_{\eta} = \eta\nabla^2\boldsymbol{B}$ are the dissipative terms, $\tilde{\nu}$ the

dynamic viscosity and η the magnetic diffusivity. Yanase [46] reduces this system by making the following assumptions: $\boldsymbol{u}$ and $\boldsymbol{B}$ depend only on the one-dimensional space variable x and time t such that $\boldsymbol{u}(x,t) = u(x,t)\hat{\boldsymbol{e}}_x$ and $\boldsymbol{B}(x,t) = B_y(x,t)\hat{\boldsymbol{e}}_y + B_z(x,t)\hat{\boldsymbol{e}}_z$. The pressure term is neglected compared to the magnetic pressure; the density ρ is put constant and equal to ρ_0 in the equations for the velocity and magnetic fields. All this leads to the Yanase equations

$$\frac{\partial u}{\partial t} + \frac{\partial}{\partial x}\left(\frac{u^2 + b_y^2 + b_z^2}{2}\right) = \nu\frac{\partial^2 u}{\partial x^2}, \tag{2.11a}$$

$$\frac{\partial b_y}{\partial t} + \frac{\partial}{\partial x}\left(ub_y\right) = \eta\frac{\partial^2 b_y}{\partial x^2}, \tag{2.11b}$$

$$\frac{\partial b_z}{\partial t} + \frac{\partial}{\partial x}\left(ub_z\right) = \eta\frac{\partial^2 b_z}{\partial x^2}, \tag{2.11c}$$

where by definition $b_j \equiv B_j/\sqrt{\rho_0\mu_0}$ with $j = y, z$ and $\nu \equiv 4\tilde{\nu}/(3\rho_0)$. It is straightforward to show that the total energy, $E = (u^2+b_y^2+b_z^2)/2$, and the modified cross-helicity, ub with b the magnetic field modulus, are conserved when $\nu = \eta = 0$. Although this one-dimensional system mimics the compressible MHD equations with two similar invariants [21], it is generally not fully consistent with it because of the assumption of constant density (in space and time), which, according to Equation (2.10a), leads necessarily to a constant velocity u. There is, however, one exception to this (considered here): when the velocity derivative is constant in space, the mass density will remain constant in space (but not in time) if it is initially so.

2.3.2 Anomalous dissipation

In the classical picture of turbulence, the fields u, b_y, and b_z are assumed to remain smooth at all scales. If it is not the case, one needs to regularize Equations (2.11). To do this, we introduce φ an infinitely differentiable function with compact support on $\mathbb{R}$, even, non-negative with integral 1 [18]. We also define $\varphi^\ell(\xi) \equiv \varphi(\xi/\ell)/\ell$, where $\xi \in \mathbb{R}$ and $\ell \in \mathbb{R}_+^*$. Denoting $u^\ell = \varphi^\ell * u$, $b_y^\ell = \varphi^\ell * b_y$ and $b_z^\ell = \varphi^\ell * b_z$, with $*$ the convolution product, one obtains (we consider a periodic domain)

$$\frac{\partial u^\ell}{\partial t} + \frac{\partial}{\partial x}\left(\frac{(u^2)^\ell + (b_y^2)^\ell + (b_z^2)^\ell}{2} - \nu\frac{\partial u^\ell}{\partial x}\right) = 0, \tag{2.12a}$$

$$\frac{\partial b_y^\ell}{\partial t} + \frac{\partial}{\partial x}\left((ub_y)^\ell - \eta\frac{\partial b_y^\ell}{\partial x}\right) = 0, \tag{2.12b}$$

$$\frac{\partial b_z^\ell}{\partial t} + \frac{\partial}{\partial x}\left((ub_z)^\ell - \eta\frac{\partial b_z^\ell}{\partial x}\right) = 0, \tag{2.12c}$$

from which we can deduce

$$\begin{aligned}\frac{\partial}{\partial t}\left(\frac{uu^\ell+b_yb_y^\ell+b_zb_z^\ell}{2}\right)+\frac{u^\ell}{4}\frac{\partial}{\partial x}\left(u^2+b_y^2+b_z^2\right)+\frac{u}{4}\frac{\partial}{\partial x}\left(u^2+b_y^2+b_z^2\right)^\ell+\frac{b_y^\ell}{2}\frac{\partial}{\partial x}\left(ub_y\right)\\+\frac{b_y}{2}\frac{\partial}{\partial x}(ub_y)^\ell+\frac{b_z^\ell}{2}\frac{\partial}{\partial x}\left(ub_z\right)+\frac{b_z}{2}\frac{\partial}{\partial x}(ub_z)^\ell-\frac{\partial^2}{\partial x^2}\left(\nu uu^\ell+\eta b_yb_y^\ell+\eta b_zb_z^\ell\right)=-\mathcal{D}_{\nu,\eta}^\ell,\end{aligned}\tag{2.13}$$

where by definition

$$\mathcal{D}_{\nu,\eta}^\ell\equiv\nu\frac{\partial u}{\partial x}\frac{\partial u^\ell}{\partial x}+\eta\frac{\partial b_y}{\partial x}\frac{\partial b_y^\ell}{\partial x}+\eta\frac{\partial b_z}{\partial x}\frac{\partial b_z^\ell}{\partial x},\tag{2.14}$$

is the viscous/resistive dissipative term. The third-order structure functions are introduced in the following manner,

$$\mathcal{D}_a^\ell\equiv\frac{1}{12}\int\frac{\mathrm{d}\varphi^\ell}{\mathrm{d}\xi}\left[(\delta u)^3+3\left((\delta b_y)^2+(\delta b_z)^2\right)\delta u\right]\mathrm{d}\xi,\tag{2.15}$$

where $\delta u\equiv u(x+\xi)-u(x)$, $\delta b_y\equiv b_y(x+\xi)-b_y(x)$ and $\delta b_z\equiv b_z(x+\xi)-b_z(x)$. After integration by parts and development, one finds

$$\begin{aligned}\mathcal{D}_a^\ell=-\frac{1}{12}\left[\frac{\partial}{\partial x}\left(u^3\right)^\ell-3u\frac{\partial}{\partial x}\left(u^2+b_y^2+b_z^2\right)^\ell+3\left(u^2+b_y^2+b_z^2\right)\frac{\partial u^\ell}{\partial x}+6u\left(b_y\frac{\partial b_y^\ell}{\partial x}+b_z\frac{\partial b_z^\ell}{\partial x}\right)\right.\\\left.+3\frac{\partial}{\partial x}\left(ub_y^2+ub_z^2\right)^\ell-6b_y\frac{\partial}{\partial x}\left(ub_y\right)^\ell-6b_z\frac{\partial}{\partial x}\left(ub_z\right)^\ell\right].\end{aligned}$$

Introducing the previous expression into the local expression of energy conservation (2.13) leads to the point-splitting energy conservation equation,

$$\begin{aligned}\frac{\partial}{\partial t}\left(\frac{uu^\ell+b_yb_y^\ell+b_zb_z^\ell}{2}\right)+\frac{\partial}{\partial x}\left[\frac{(u^3)^\ell}{12}+\frac{\left(ub_y^2+ub_z^2\right)^\ell}{4}+\frac{u^\ell\left(u^2+b_y^2+b_z^2\right)}{4}+\frac{u\left(b_yb_y^\ell+b_zb_z^\ell\right)}{2}\right]\\-\nu\frac{\partial^2}{\partial x^2}\left(uu^\ell\right)-\eta\frac{\partial^2}{\partial x^2}\left(b_yb_y^\ell+b_zb_z^\ell\right)=-\mathcal{D}_a^\ell-\mathcal{D}_{\nu,\eta}^\ell.\end{aligned}\tag{2.16}$$

The limit $\ell\to0$ leads to the first main result

$$\boxed{\frac{\partial E}{\partial t}+\frac{\partial\Pi}{\partial x}=-\mathcal{D}_a-\mathcal{D}_{\nu,\eta}},\tag{2.17}$$

with by definition

$$\Pi = \frac{u^3}{3} + ub^2 - \frac{\partial}{\partial x}\left(\nu u^2 + \eta b^2\right), \tag{2.18a}$$

$$\mathcal{D}_a = \lim_{\ell \to 0} \mathcal{D}_a^\ell, \tag{2.18b}$$

$$\mathcal{D}_{\nu,\eta} = \nu \left(\frac{\partial u}{\partial x}\right)^2 + \eta \left(\frac{\partial b_y}{\partial x}\right)^2 + \eta \left(\frac{\partial b_z}{\partial x}\right)^2, \tag{2.18c}$$

where Π is the energy flux. Expression (2.17) is particularly relevant in the inviscid/ideal limit, *i.e.,* when $\nu = \eta = 0$. In this case, there is still a channel to dissipate energy through the anomalous dissipation $\mathcal{D}_a$ which happens because of the lack of smoothness of the fields. On the contrary, if the fields are regular enough, by using a Taylor expansion it is straightforward to show that $\mathcal{D}_a^\ell \to 0$ when $\ell \to 0$. Finally, note that we recover the well-known result on Burgers' equation in the absence of a magnetic field [17, 19].

2.3.3 Analytical solutions

Let us define the velocity $u(x,t)$ and the magnetic field components $b_{y\pm}(x,t)$ and $b_{z\pm}(x,t)$ in the interval $x \in [-L,+L]$, with $L \in \mathbb{R}_+$ and $t \in \mathbb{R}_+^*$. If the dissipative coefficients $\nu = \eta \in \mathbb{R}_+^*$, then the Yanase equations admit the following analytical solutions

$$u(x,t) = \frac{x}{t} - \frac{L}{t}\tanh\left(\frac{xL}{\nu t}\right), \tag{2.19a}$$

$$b_{y\pm}(x,t) = \pm b_{y,0}\frac{L}{t}\tanh\left(\frac{xL}{\nu t}\right), \tag{2.19b}$$

$$b_{z\pm}(x,t) = \pm b_{z,0}\frac{L}{t}\tanh\left(\frac{xL}{\nu t}\right), \tag{2.19c}$$

where by definition

$$b_{y,0} = \frac{1}{\sqrt{1+c^2}}, \quad b_{z,0} = \frac{c}{\sqrt{1+c^2}},$$

and $c \in \mathbb{R}$ is a constant. In the limit $\nu \to 0^+$, the solutions (2.19) tend to the following inviscid profiles corresponding to discontinuities

$$u(x,t) \xrightarrow{\nu\to 0^+} \begin{cases} (x+L)/t, & \text{if } x<0 \\ (x-L)/t, & \text{if } x>0 \end{cases}, \tag{2.20a}$$

$$b_{y\pm}(x,t) \xrightarrow{\nu\to 0^+} \pm \begin{cases} b_{y,0}L/t, & \text{if } x<0 \\ -b_{y,0}L/t, & \text{if } x>0 \end{cases}, \tag{2.20b}$$

$$b_{z\pm}(x,t) \xrightarrow{\nu\to 0^+} \pm \begin{cases} b_{z,0}L/t, & \text{if } x<0 \\ -b_{z,0}L/t, & \text{if } x>0 \end{cases}. \tag{2.20c}$$

These are stationary shocks of amplitude $\Delta = 2L/t$ for the velocity, $\Delta_y = b_{y,0}\Delta$ for the y-component and $\Delta_z = b_{z,0}\Delta$ for the z-component of the magnetic field, localized at point $x = 0$ for all time (see Figure 2.2). These inviscid solutions are the MHD version of the Khokhlov sawtooth solution for Burgers' equation [41].

It is interesting to note that the analytical solutions (2.20) are fully consistent with the three-dimensional compressible MHD equations since the velocity derivative is constant in space. Indeed, from the Yanase equations completed with the density equation (so far left out of our one-dimensional model), it is possible to find, in the inviscid limit, an exact solution for the mass density, which remains constant (in a given interval) in space but evolves in time as

$$\rho(x,t) = \frac{1}{t}[C_+ H(x) + C_- H(-x)], \tag{2.21}$$

where H is the Heaviside function and $C_\pm \in \mathbb{R}_+^*$.

A direct numerical simulation of Equations (2.11) was performed to check if (and how) the analytical solutions (2.19) are generated. We use a spatial resolution of 8192 grid points and $-L \le x \le L$, with $L = 1$. A fourth-order Runge-Kutta numerical scheme was implemented in time and the spatial derivatives are performed using fast Fourier transforms with periodic boundary conditions. The initial conditions correspond to plane waves and are $u(x, t = 0) = \sin(2\pi x)$, $b_y(x, t = 0) = \sin(\pi x)$ and $b_z(x, t = 0) = 2\sin(\pi x)$. (See [46] for random initial conditions.) The time step and the viscosity are computed automatically using CFL conditions [16]. The time evolution of the fields is shown in Figure 2.2 from $t = 0$ (blue) to $t = 1.1$ (red). After an initial phase during which the amplitude of the magnetic field increases locally at the expense of the velocity (with $\max|b_{j_+}(x, t > 0)| > \max|b_{j_+}(x, t = 0)|$ and $\max|u(x, t = 0)| > \max|u(x, t > 0)|$),

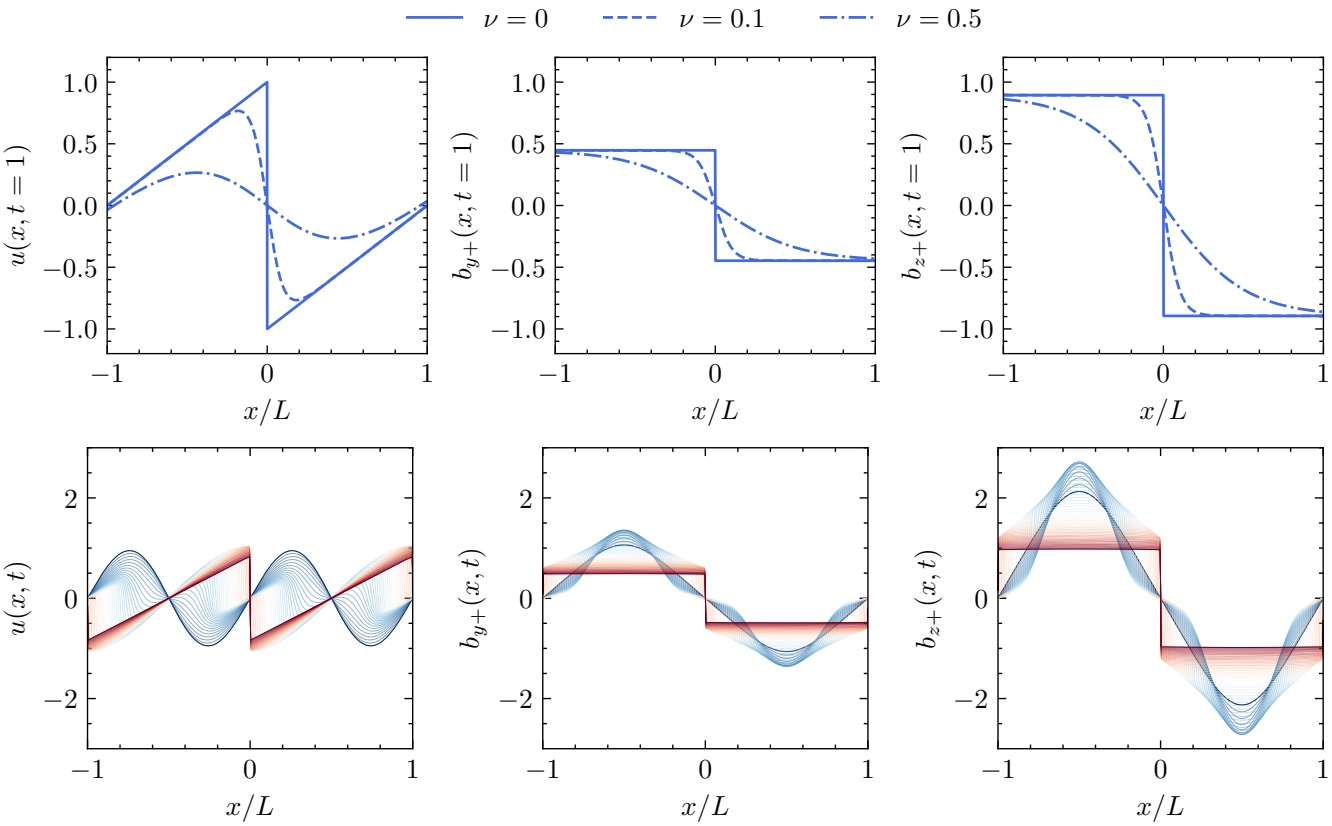

Figure 2.2: Top line: analytical solutions u (left), b_{y+} (center) and b_{z+} (right) at $t = 1$, for $\nu = 0$, 0.1 and 0.5 (solid, dashed and dashed-dotted lines, respectively), in a domain of size $2L = 2$. We take $c = 2$ and thus the amplitude of the shocks are $\Delta = 2$, $\Delta_y = 2/\sqrt{5}$ and $\Delta_z = 4/\sqrt{5}$. Bottom line: direct numerical solution of Yanase's equations with the time evolution (from blue to red) of the velocity (left) and the magnetic field components (center and right).

which can be interpreted as a kind of dynamo effect, the analytical solutions $(u, b_{j\pm})$ are eventually formed at positions $x = 0$ and $\pm L$ after the merger of shocks.

With the analytical formula in hand, we can now predict the intermittency profile, which is defined as the moments of the ensemble average of the increments of velocity denoted as $\delta u \equiv u(x+\ell) - u(x)$ and increments of the magnetic fields denoted as $\delta b \equiv b(x+\ell) - b(x)$. These are calculated as follows:

$$\delta u = \begin{cases} (\ell - 2L)/t & \text{if } x \le 0 \le x + \ell, \\ \ell/t & \text{else.} \end{cases} \tag{2.22a}$$

$$\delta b = \begin{cases} -2L/t & \text{if } x \le 0 \le x + \ell, \\ 0 & \text{else.} \end{cases} \tag{2.22b}$$

We respectively define the structure functions for the velocity field $S_p^u = \langle |\delta u|^p \rangle$ and for the magnetic field $S_p^b = \langle |\delta b|^p \rangle$, where $\langle f \rangle = (2L)^{-1} \int_{-L}^{+L} f(x) \mathrm{d}x$. In the limit $\ell \ll L$ and at the main order, one has

$$S_p^u = \frac{1}{2L} \left(\int_{-L}^{-\ell} \left| \frac{\ell}{t} \right|^p \mathrm{d}x + \int_{-\ell}^{0} \left| \frac{\ell - 2L}{t} \right|^p \mathrm{d}x + \int_{0}^{+L} \left| \frac{\ell}{t} \right|^p \mathrm{d}x \right) \simeq \Delta^p \left[\left| \frac{\ell}{2L} \right|^p + \frac{\ell}{2L} \right], \tag{2.23a}$$

$$S_p^b = \frac{1}{2L} \int_{-\ell}^{0} \left| \frac{-2L}{t} \right|^p \mathrm{d}x = \Delta^p \frac{\ell}{2L}. \tag{2.23b}$$

Distinguishing the cases $p < 1$ and $p \ge 1$, we finally find

$$S_p^u \simeq \Delta^p \begin{cases} (\ell/2L)^p & \text{if } 0 < p < 1, \\ \ell/2L & \text{if } p \ge 1. \end{cases} \tag{2.24a}$$

$$S_p^b = \Delta^p \frac{\ell}{2L}. \tag{2.24b}$$

Thus, S_p^u and S_p^b exponents are

$$\zeta_p^u = \begin{cases} p & \text{if } 0 < p < 1, \\ 1 & \text{if } p \ge 1. \end{cases} \tag{2.25a}$$

$$\zeta_p^b = 1. \tag{2.25b}$$

It is worth noting that even this simple model presents a challenge to a theory à la Kolmogorov in the one-dimensional case. While the naive extension of the exact laws predicts mono-fractal behavior characterized by a linear dependence between ζ and p, as shown in Figure 2.3, this is not observed here. A comparison

between the Burgers equation and the four-fifth law can be found in Eyink [19], but the conclusion remains the same.

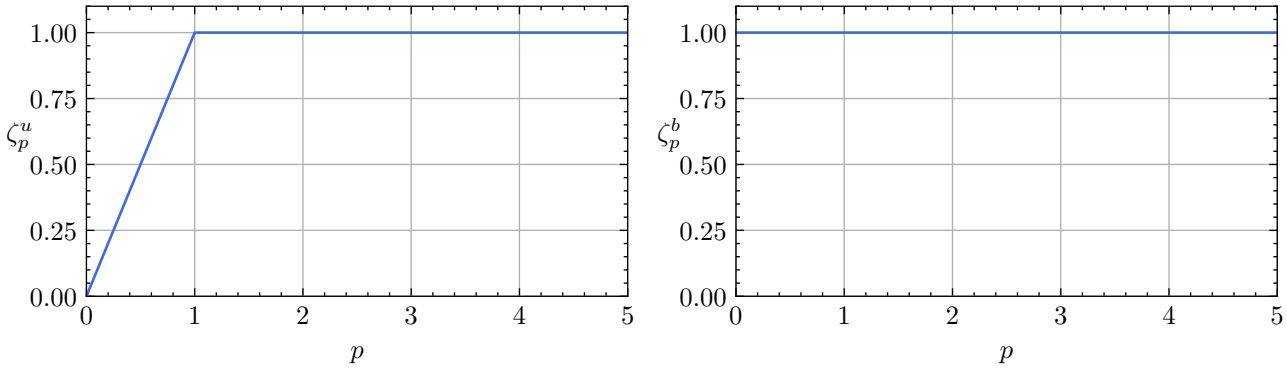

Figure 2.3: Structure function exponents ζ_p^u and ζ_p^b as a function of p.

2.3.4 Mean dissipation rates

We shall compute the mean rate of energy dissipation. From the analytical solutions (2.19) one can find the mean rate of viscous dissipation $\varepsilon \equiv \langle \mathcal{D}_{\nu,\nu}(x,t) \rangle$. In the limit of small viscosity, a simple calculation gives

$$\lim_{\nu\to 0^+} \varepsilon = \lim_{\nu\to 0^+} \frac{\nu}{2L} \int_{-L}^{+L} \left\{ \left[\frac{1}{t} - \frac{L^2}{\nu t^2} \operatorname{sech}^2\left(\frac{xL}{\nu t}\right) \right]^2 + \left(b_{y,0}^2 + b_{z,0}^2\right) \frac{L^4}{t^4 \nu^2} \operatorname{sech}^4\left(\frac{xL}{\nu t}\right) \right\} \mathrm{d}x. \tag{2.26}$$

In the main order, one finds

$$\lim_{\nu\to 0} \varepsilon = \lim_{\nu\to 0} \frac{L^3}{\nu t^4} \int_{-L}^{+L} \operatorname{sech}^4\left(\frac{xL}{\nu t}\right) \mathrm{d}x = \frac{\Delta^3}{6L}, \tag{2.27}$$

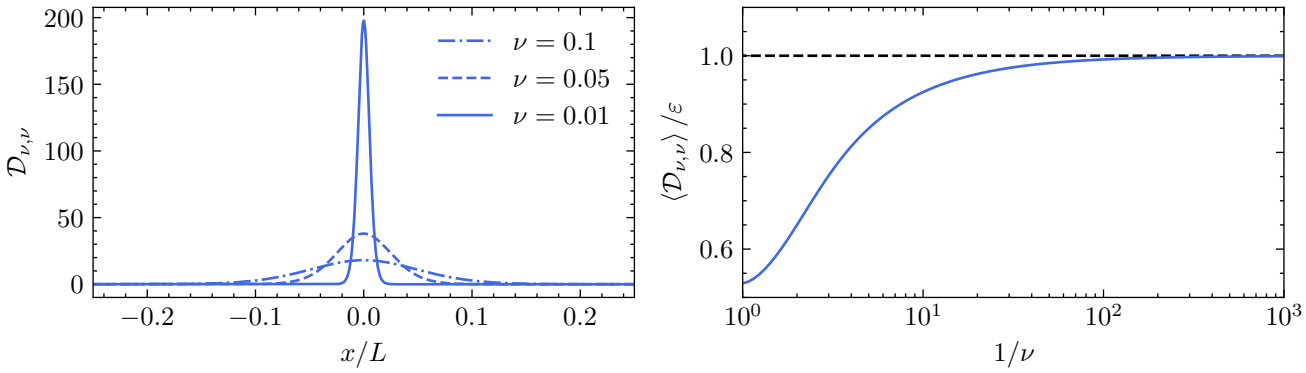

Figure 2.4: Left: viscous dissipation in the analytical solutions for various viscosities. Right: ratio of the mean rate of viscous dissipation and its main order estimation.

which is positive and independent of ν. As depicted in the left panel of Figure 2.4, the dissipation phenomenon is concentrated near the shock location at $x = 0$. Remarkably, as the viscosity decreases, the dissipation becomes more prominent and localized in that region. In the right panel of Figure 2.4, we validate this trend by confirming that as the viscosity decreases, the mean rate of viscous dissipation converges towards the expression (2.27). Taking now the inviscid/ideal solutions (2.20), one finds for the variation of total energy $dE/dt = -\Delta^3/(6L)$, which is compatible with expression (2.27). However, when $\nu = \eta = 0$ the only way to dissipate energy is through the mean anomalous dissipation $\langle \mathcal{D}_a \rangle$. In the inviscid/ideal case, one has (with expressions (2.20)),

$$\boxed{\mathcal{D}_a = \lim_{\ell \to 0} \mathcal{D}_a^\ell = \frac{\Delta^3}{3}\delta(x)}, \tag{2.28}$$

hence we find the exact relation

$$\langle \mathcal{D}_a \rangle = \frac{1}{2L}\int_{-L}^{+L} \frac{\delta(x)}{12}\left[1 + 3\left(b_{y,0}^2 + b_{z,0}^2\right)\right]\Delta^3 \mathrm{d}x = \frac{\Delta^3}{6L},$$

which is equal to ε in the limit of small viscosity. Therefore, the viscous dissipation can be substituted exactly by the anomalous dissipation in the absence of viscosity. In other words, the loss of energy in Yanase's equations is then produced by the loss of regularity of the velocity and magnetic field. These results prove the Zeroth law of turbulence in this particular case. Note that shocks are often considered as a part of the structures produced by turbulence (for Burgers' equation see [10]) in addition to fluctuations, as one can see in supersonic hydrodynamic turbulence (see e.g., [20]). Therefore, the Zeroth law of turbulence can be applied to one-dimensional equations too, which are characterized by shock steepening. The particularity of our approach is that the computation of anomalous dissipation does not require a statistical treatment and can be applied to a single nonlinear event. The discrepancy between the viscous (2.19) and the inviscid (2.20) solutions can be investigated numerically with expression (2.15). The latter is computed with a convolution product based on FFT and a normalized Gaussian function is chosen for φ. One might object that a Gaussian function does not satisfy all the requirements to be a test function, particularly the condition of compact support. However, from a numerical standpoint, the Gaussian kernel demonstrates the most favorable behavior for obtaining accurate analytical predictions (cf. Figure 2.5). Simulations are made on a spatial domain of size $2L = 2$ with spatial increment $dx = 10^{-4}$. The term $\mathcal{D}_a^\ell$ is computed over the entire simulation domain for 10^2 values of ℓ ranging from 2×10^{-4} to 2×10^{-1}. Figure 2.5 (top) shows

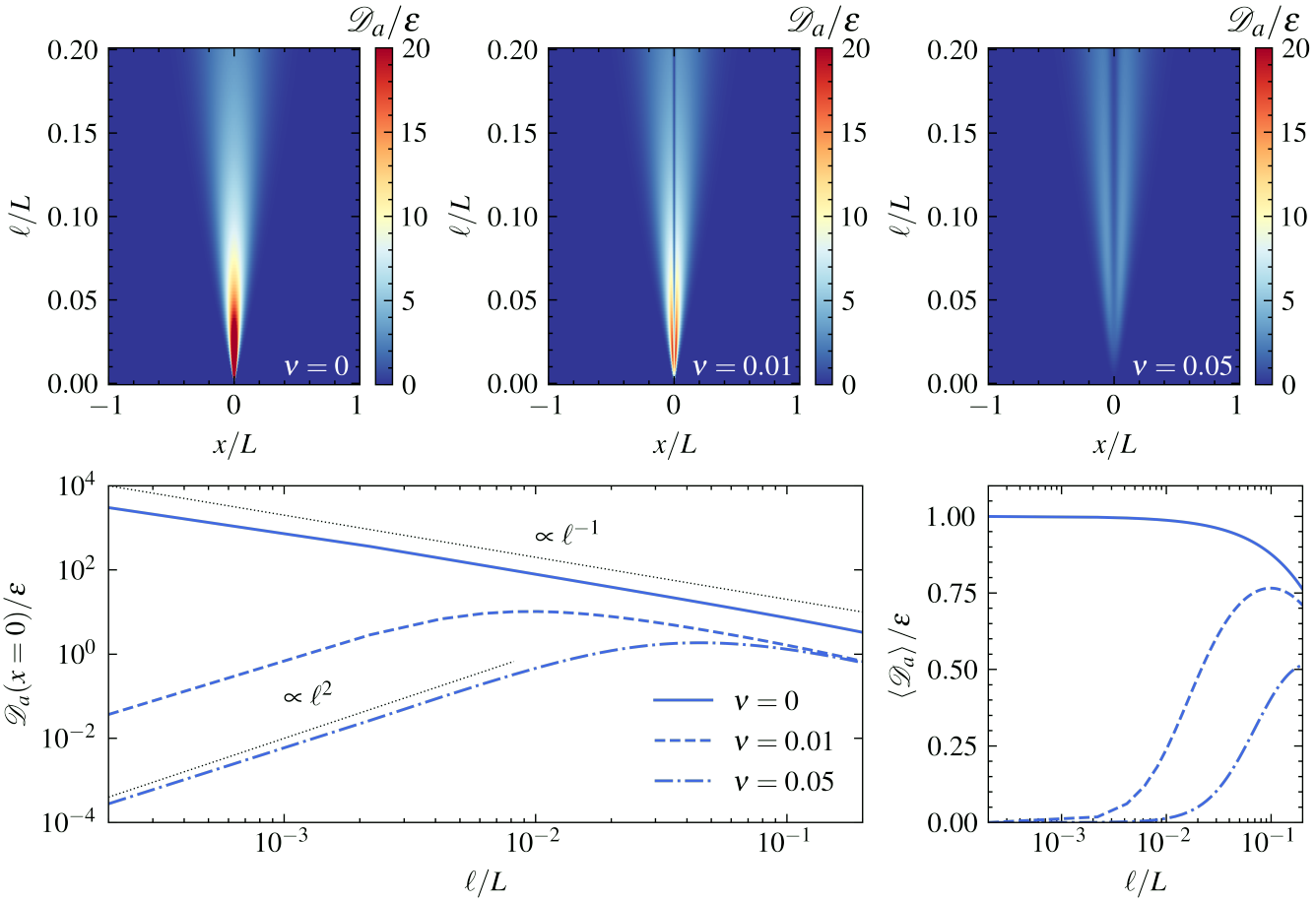

Figure 2.5: Top: space/scale diagram of the normalized local energy transfer $\mathcal{D}_a^\ell/\varepsilon$ for the inviscid (left) and viscous (center and right) analytical solutions of Yanase's equations. The intensity of $\mathcal{D}_a^\ell/\varepsilon$ is given by the colorbar. Bottom: variation with ℓ of the normalized local energy transfer at $x = 0$ (left) and averaged over $[-L, +L]$ (right), in the inviscid and viscous cases.

the evolution of the anomalous dissipation as a function of two parameters: the position in the simulation domain (x-axis) and the width (or scale) of φ (y-axis). Both the inviscid (left) and viscous (center and right) solutions lead to a map where the intensity of $\mathcal{D}_a^\ell$ is relatively low far from the shock (localized at $x = 0$). It becomes relatively high close to $x = 0$ with, however, a difference between the two types of solution: while the inviscid solution continues to increase and forms a true singularity, the viscous one converges to zero at small ℓ, meaning that it is a quasi-singularity. Therefore, this map tells us at first glance what kind of solution leads to a non-zero anomalous dissipation.

A more precise analysis can be done by observing how $\mathcal{D}_a^\ell$ evolves with ℓ. Figure 2.5 (bottom left) shows this (normalized) evolution on the shock for the inviscid case and two viscous cases. We see that the inviscid solution follows a power law in ℓ^{-1} at all scales, while the viscous solutions follow mainly (at small scales) a power law in ℓ^2. These behaviors can be understood by simple dimensional arguments. In the inviscid case, $\delta u \sim \delta b \sim \Delta$ and we find $\mathcal{D}_a^\ell \sim \Delta^3/\ell$, whereas with the viscosity effect we have $\delta u \sim \delta b \sim \ell$; plugging this into (2.15) gives $\mathcal{D}_a^\ell \sim \ell^2$. Figure 2.5 (bottom right) confirms this behavior when the (normalized) mean value $\langle \mathcal{D}_a^\ell \rangle$ is taken. We can conclude that the lower the viscosity, the better the power law ℓ^{-1} will be followed by the viscous solution, but one always reaches a scale in ℓ below which the viscous solution becomes attractive.

2.4 Application to shocks in the solar wind

2.4.1 From time to space measurements

In our previous analysis, we focused on the spatial characteristics of anomalous dissipation. However, since the available spacecraft data primarily consists of time measurements, we must devise an appropriate method to translate these temporal observations into meaningful spatial measurements. The Taylor hypothesis suggests that the measurements taken aboard a spacecraft can be considered as samples from a one-dimensional spatial profile [44]. In other words, we assume that the timescale over which the wave characteristics change is much larger than the duration it takes for the spacecraft to traverse through them. This hypothesis allows us to relate the frequency of waves in the plasma rest frame to the observed frequency measured onboard the spacecraft. One might question the relevance of considering the wave frequency as ω_{plas}, given the nonlinear nature of the solar wind and the fact that we can only theoretically derive a dispersion relation for linear waves. As we will discuss in Chapter 4, the nonlinear behavior of the plasma and its modeling requires a separation of timescales between linear and nonlinear effects. However,

the outcome reveals that the linear timescale is the most rapid, making it the safest choice to regard $\omega_{\rm plas}$ as the linear wave timescale. The equation that connects $\omega_{\rm plas}$ to the observed frequency onboard the spacecraft $\omega_{\rm sc}$ can be expressed in the following manner:

$$\omega_{\rm sc} = \omega_{\rm plas} + \boldsymbol{k} \cdot (\boldsymbol{V} + \boldsymbol{V}_{\rm sc}) \,. \tag{2.29}$$

Here, $\boldsymbol{k}$ represents the wavevector, $\boldsymbol{V}$ denotes the velocity of the solar wind, and $\boldsymbol{V}_{\rm sc}$ represents the spacecraft velocity. In typical space plasma scenarios, we have $V_{\rm sc} \ll V$, yielding a simplified expression:

$$\omega_{\rm sc} = \omega_{\rm plas} + \boldsymbol{k} \cdot \boldsymbol{V} = \omega_{\rm plas} + kV \cos\theta_{kV}, \tag{2.30}$$

where θ_{kV} corresponds to the angle between the wavevector and the solar wind velocity. The second term on the right-hand side arises from the Doppler shift. What Taylor proposed is a method to determine the dominance of the Doppler shift. The practical implementation involves assessing whether the phase speed of the wave, denoted as $V_\phi = \omega/k$, is significantly smaller than the flow speed represented by V. In simpler terms, we aim to ensure that $V_\phi \ll V$. Considering the wind supersonic and super-Alfvénic nature, we find that the Taylor hypothesis holds remarkably well. However, it becomes evident that not only the wind speed but also the angle formed between the wavevector and the flow, plays a role. When dealing with waves having an angle $\theta_{\rm kV}$ approaches $\pm\pi/2$, it becomes necessary to scrutinize the validity of the Taylor hypothesis for wave propagation. Secondly, in situations of strong anisotropy ($k_\parallel \ll k_\perp$) like in the solar wind, the expression for $\omega_{\rm sc}$ for Alfvénic turbulence becomes:

$$\omega_{\rm sc} = k_\parallel V_A + kV = kV\cos\theta_{\rm kV}\left(1 + \frac{k_\parallel V_A}{kV\cos\theta_{\rm kV}}\right). \tag{2.31}$$

Therefore, if $|\theta_{\rm kV}| \ll \pi/2$, the Taylor hypothesis still holds its ground at MHD scales. Lastly, when examining fluctuations at scales smaller than MHD ones, the significance of the wave phase speed can become prominent. Consequently, it is imperative to meticulously verify the validity of the Taylor hypothesis, since the assumption $V_\phi \ll V$ is no longer evident. In this context, as we focus on the solar wind at extremely low frequencies, there is no need for concern when employing this hypothesis.

2.4.2 The application

As an illustration, we will study the outer solar wind around 5 au (near Jupiter), where sawtooth and battlement structures are observed. For the following, let us be a bit loose with our language and say that anomalous dissipation can be used as a proxy to estimate the amount of energy that will eventually be converted into heat via kinetic processes in the solar wind, on time (and space) scales much smaller than the resolution of the data we are currently working with. Then, as we will see, the expression of anomalous dissipation provides a simple and concise formula to estimate the heating produced by collisionless shocks.

For $r > 10$ au cosmic particles are the main source of heating of the solar wind [36, 37], while for $r < 2$ au turbulent fluctuations are omnipresent. On the other hand, at 2–10 au collisionless shocks have been clearly detected by Voyager 1 & 2 [11, 39] (relatively weak field fluctuations are also present with possibly non-trivial dynamics [31]). Although these events are known for years and are believed to have a strong impact on the local heating [24], to the best of my knowledge, so far no theory with an exact, concise, and directly applicable formula for estimating the heating rate has been proposed. As we can see in Figure 2.6, the velocity profile shows shocks on which turbulent fluctuations are superposed. For the magnetic field and density, we also observe large-scale structures as well as fluctuations. The study of these fluctuations has already been done by Pine *et al.* [37] to deduce the turbulent heating. Here, we only consider the large-scale variations of the fields where the fluctuations are filtered. Our theory may be applied precisely in this region where the radial direction is identified with the x-direction. Then, u is the main component of the velocity: we have verified in the data that the perpendicular (to the radial direction) components of the velocity are at most equal to 5% (in modulus) of the radial component. Knowing that Parker's spiral angle is close to 80^o at 5 au, the transverse (to the radial direction) components of the magnetic field are dominant, and B_x can be neglected. We use the shock profiles (2.20)–(2.21) which are exact solutions of the one-dimensional compressible MHD equations (Yanase's equations completed by the density equation). Although limited, it is believed that this one-dimensional MHD approach can provide an estimate of the shock heating in the outer solar wind. The hypothesis that the dissipation finds its origin in the lack of regularity of the fields is a useful mathematical model for obtaining predictions, but in reality, dissipation is physically produced by kinetic effects at sub-MHD scales. Therefore, the heating rate found must be seen as an approximation of the actual dissipation.

In Figure 2.6 an example of such shocks (one can easily verify that these are not contact discontinuities for which only the mass density varies, nor rotational discontinuities for which $|B|$ does not vary [21])

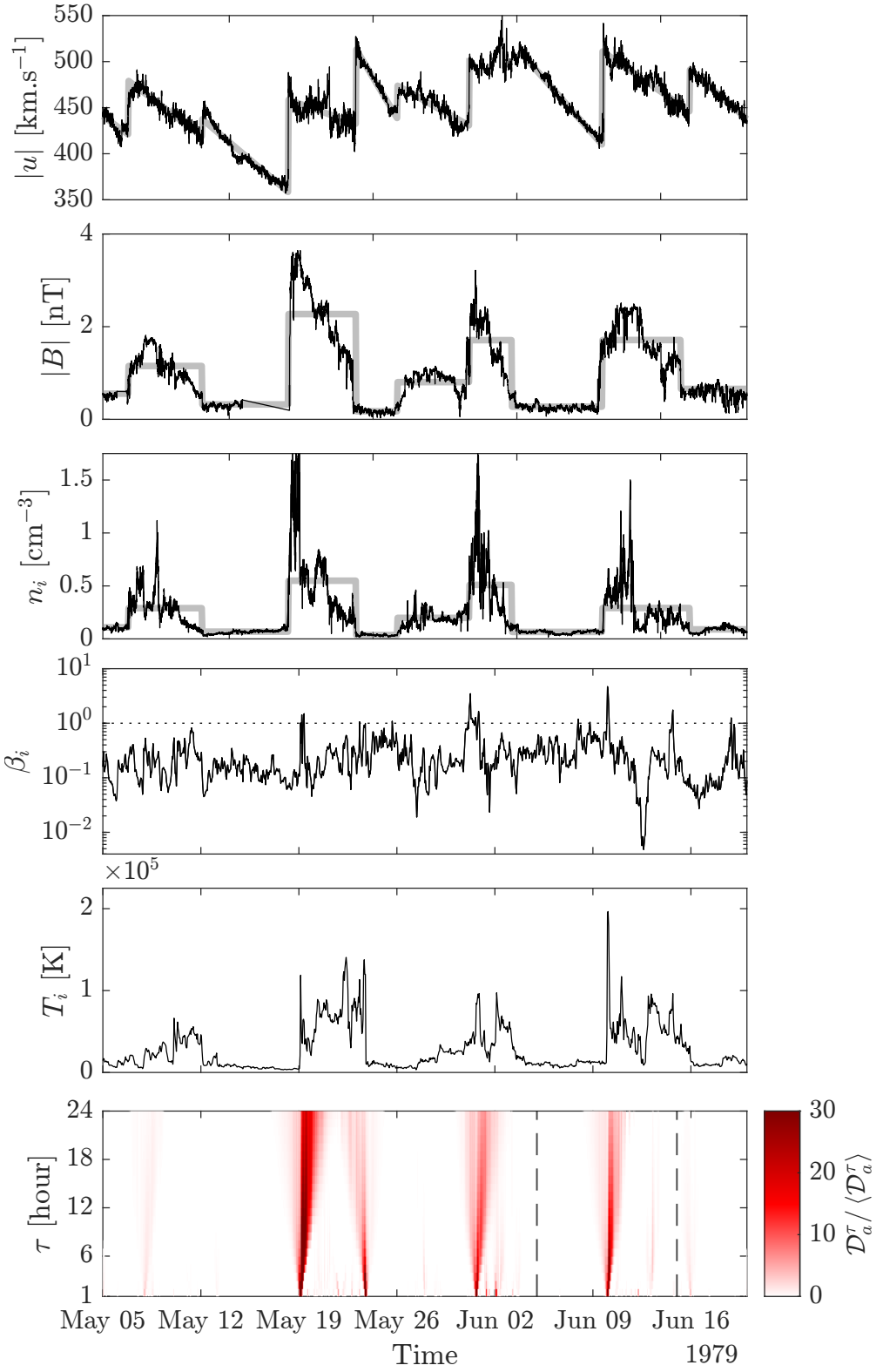

Figure 2.6: From top to bottom: modulus of the proton velocity and magnetic field, the proton density, proton plasma beta, proton temperature, and time/scale diagram of the normalized local anomalous dissipation (vertical dashed lines delimit the area studied in Figure 2.7, where a compressible shock arises at time $t_\star$). Data measured by Voyager 2 into the solar wind from May 5 to June 20, 1979, at ~ 5.1 au. Theoretical fits (thick gray lines) are superposed to emphasize the sawtooth and crenelated nature of the basic fields.

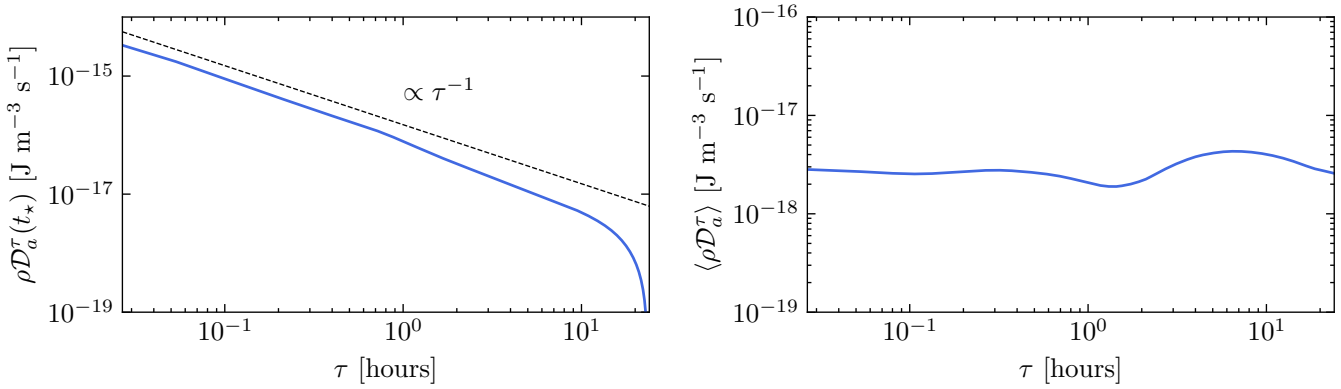

Figure 2.7: Left: $\rho\mathcal{D}_a^\tau(t_\star)$ as a function of scale τ; note that $t_\star$ corresponds to the shock's location. Right: variation with τ of $\rho\mathcal{D}_a^\tau$ averaged over a time interval of 10 days centered at the shock position $t_\star$.

is reported and fitted with a sawtooth velocity (in modulus), a crenelated magnetic field (in modulus) and density. The magnetic field data and plasma moments (density, velocity, temperature) were measured respectively by the Flux Gate Magnetometer (MAG) and the Plasma Spectrometer (PLS) onboard Voyager 2. Data have between 48 s and 96 s time resolution [33]. A moving median window of length 5 points is used to fill small data gaps, and linear interpolation fills the remaining gaps. After using the Taylor hypothesis ($t = -x/U_{SW}$, with U_{SW} the solar wind velocity), the velocity antishocks can be interpreted as a succession of shocks. Therefore, the profiles of the basic fields ($|u|$, $|B|$, n_i) are roughly compatible with the inviscid solutions (with possibly the absolute value and normalization for the magnetic field) discussed above. The one-dimensional MHD model assumes a small plasma beta, a condition satisfied with a (proton) $\beta_i = 2\mu_0 n_i k_B T_i/B^2$ (k_B the Boltzmann constant) usually smaller than 1 (see also [36]) except on some shock locations (which shows the limitation of our model). The ion temperature reveals very often the presence of large peaks at the discontinuities (e.g., May 19, May 24, or June 10), but it is not systematically the case. A possible explanation is that the energy from the shock may be converted into another form than heating (e.g., radiation), hence a possible slight overestimation of the heating. Note that we are in the same situation as for the estimation of the heating rate from the turbulent fluctuations at MHD scales, for which it is implicitly assumed that ε is entirely converted into plasma heating. The other smaller peaks observed at any time may be the consequence of turbulent heating. Finally, the time/scale diagram (τ is used instead of ℓ) of the normalized local anomalous dissipation reveals the position of the main discontinuities, which are characterized by a scaling $\mathcal{D}_a^\tau \sim 1/\tau$ (see Figure 2.7). It is actually from this signal we were able to define (most of) the positions of the singularities in the basic fields (thick gray lines). We see that the heating coincides well with peaks in temperature.

It is straightforward to deduce the heating rate produced by such discontinuities. For the velocity, we find a typical amplitude $\Delta \simeq 10^5 \mathrm{m\,s^{-1}}$ and a duration $\tau \simeq 5$ days which is consistent with the integral scale of the f^{-2} spectra measured in this region [12, 13]. With $U_{SW} \simeq 4.5 \times 10^5 \mathrm{m\,s^{-1}}$, we obtain $L = \tau U_{SW} \simeq 10^{11}\mathrm{m}$. The mass density being $n_i \simeq 10^5 \mathrm{m^3}$, we eventually obtain the mean rate of energy dissipation (or heating rate)

$$\rho \langle \mathcal{D}_a \rangle = \frac{\rho \Delta^3}{6L} \sim 10^{-18} \mathrm{J\,m^{-3}\,s^{-1}}. \tag{2.32}$$

We can easily verify that the amplitude and duration of the magnetic events (after normalization) are approximately the same, confirming the relevance of our MHD solutions.

Expression (2.32) is used to evaluate the local heating produced by a compressible shock localized at $t_\star$, which is the center of the time interval of 10 days (from June 5 to June 15) defined with the two vertical dashed lines in Figure 2.6. First, the presence of a shock at $t_\star$ is clearly confirmed in Figure 2.7 (top) with a clear scaling $\rho \mathcal{D}_a^\tau \sim 1/\tau$. Then, the local heating can be directly deduced from the anomalous dissipation averaged over this time interval of 10 days centered around $t_\star$ (bottom). Within the limit of small τ, a value $\langle \rho \mathcal{D}_a^\tau \rangle \simeq 3 \times 10^{-18} \mathrm{J\,m^{-3}\,s^{-1}}$ is obtained, which confirms the previous evaluation. Note that the overall behavior found here should be compared to Figure 2.5 (bottom). The heating rate found is smaller than that commonly obtained at 1 au from turbulent fluctuations, with $\rho\varepsilon > 10^{-17} \mathrm{J\,m^{-3}\,s^{-1}}$ [3, 5, 14, 15, 25, 30, 32, 42, 43, 45]. However, the value (2.32) is more than one order of magnitude larger than the values recently reported from the turbulent fluctuations at the same heliocentric distance [37]. This suggests that in the outer solar wind, discontinuities if they exist, can be the main source of local heating.

2.5 Conclusion

The Zeroth law of turbulence is one of the oldest conjectures in turbulence that is still unproven in general. In this chapter, we considered weak solutions of a low-dimensional model of compressible MHD named the Yanase model. It provides an example where this law can be proven and reinforces Onsager's conjecture, which assumed that the lack of smoothness of the fields could be the cause of the energy dissipation in the limit of infinite Reynolds numbers [35].

We employed this model and its anomalous dissipation expression to approximate the heating generated by a collisionless shock. To be precise, we assumed that the anomalous dissipation observed at the larger scales would transform into heat through kinetic processes taking place at sub-MHD scales. The dissipation of energy in collisionless plasmas is an important topic in space physics, astrophysics, and laboratory

plasmas. Although plasma heating involves kinetic effects at sub-ion scales, it has been increasingly recognized in recent years that the exact laws of turbulence in MHD [5, 25, 42] provide means of estimating the mean rate of heating through the measure of the mean rate of energy transfer (assuming that the MHD energy transfer is mainly converted into small-scale heating). For space plasmas, this method has been used in homogeneous regions (solar wind and Earth's magnetosheath) where turbulent fluctuations are dominant. However, in the presence of collisionless shocks, the assumption of statistical homogeneity is broken and the exact laws of turbulence become unusable [23]. Our application to the solar wind of the low-dimensional MHD solutions, which are by nature intrinsically limited, reveals that the heating produced by a discontinuity is much higher than the values obtained from turbulent fluctuations at the same heliocentric distance [37], suggesting that collisionless shocks can be a dominant source of heating in the outer solar wind. Given the importance of collisionless shocks in astrophysics and laboratory plasmas [34], it is believed that this study may be useful in a number of other situations.

In summary, our investigation of the Yanase model provides a promising insight into the relationship between anomalous dissipation and the Onsager conjecture. However, it is important to note that a complete proof of this connection at the level of the full three-dimensional equations is a huge challenge. But we can still do something that goes in that way...

References

[1] N. Andrés, S. Galtier, and F. Sahraoui, "Exact law for homogeneous compressible hall magnetohydrodynamics turbulence," *Phys. Rev. E*, vol. 97, p. 013 204, 1 Jan. 2018.

[2] N. Andrés and F. Sahraoui, "Alternative derivation of exact law for compressible and isothermal magnetohydrodynamics turbulence," *Phys. Rev. E*, vol. 96, p. 053 205, 5 Nov. 2017.

[3] N. Andrés, F. Sahraoui, S. Galtier, L. Z. Hadid, R. Ferrand, and S. Y. Huang, "Energy cascade rate measured in a collisionless space plasma with mms data and compressible hall magnetohydrodynamic turbulence theory," *Phys. Rev. Lett.*, vol. 123, p. 245 101, 24 Dec. 2019.

[4] R. A. Antonia, M. Ould-Rouis, F. Anselmet, and Y. Zhu, "Analogy between predictions of kolmogorov and yaglom," *Journal of Fluid Mechanics*, vol. 332, pp. 395–409, 1997.

[5] S. Banerjee, L. Z. Hadid, F. Sahraoui, and S. Galtier, "Scaling of Compressible Magnetohydrodynamic Turbulence in the Fast Solar Wind," *Astrophys. J. Lett.*, vol. 829, no. 2, p. L27, 2016.

[6] S. Banerjee and S. Galtier, "Exact relation with two-point correlation functions and phenomenological approach for compressible magnetohydrodynamic turbulence," *Phys. Rev. E*, vol. 87, p. 013 019, 1 Jan. 2013.

[7] S. Banerjee and S. Galtier, "Chiral exact relations for helicities in hall magnetohydrodynamic turbulence," *Phys. Rev. E*, vol. 93, p. 033 120, 3 Mar. 2016.

[8] S. Banerjee and A. G. Kritsuk, "Exact relations for energy transfer in self-gravitating isothermal turbulence," *Phys. Rev. E*, vol. 96, p. 053 116, 5 Nov. 2017.

[9] S. Banerjee and A. G. Kritsuk, "Energy transfer in compressible magnetohydrodynamic turbulence for isothermal self-gravitating fluids," *Phys. Rev. E*, vol. 97, p. 023 107, 2 Feb. 2018.

[10] J. Bec and K. Khanin, "Burgers turbulence," *Physics Reports*, vol. 447, no. 1, pp. 1–66, 2007.

[11] L. F. Burlaga and M. L. Goldstein, "Radial variations of large-scale magnetohydrodynamic fluctuations in the solar wind," *Journal of Geophysical Research: Space Physics*, vol. 89, no. A8, pp. 6813–6817, 1984.

[12] L. F. Burlaga and W. H. Mish, "Large-scale fluctuations in the interplanetary medium," *J. Geophys. Res.*, vol. 92, no. A2, pp. 1261–1266, 1987.

[13] L. F. Burlaga, N. F. Ness, and F. B. McDonald, "Large-scale fluctuations between 13 AU and 25 AU and their effects on cosmic rays," *J. Geophys. Res.*, vol. 92, no. A12, pp. 13 647–13 652, 1987.

[14] V. Carbone, R. Marino, L. Sorriso-Valvo, A. Noullez, and R. Bruno, "Scaling laws of turbulence and heating of fast solar wind: The role of density fluctuations," *Phys. Rev. Lett.*, vol. 103, p. 061 102, 6 Aug. 2009.

[15] J. T. Coburn, M. A. Forman, C. W. Smith, B. J. Vasquez, and J. E. Stawarz, "Third-moment descriptions of the interplanetary turbulent cascade, intermittency and back transfer," *Philosophical Transactions of the Royal Society A: Mathematical, Physical and Engineering Sciences*, vol. 373, no. 2041, p. 20 140 150, 2015.

[16] R. Courant, K. Friedrichs, and H. Lewy, "Über die partiellen Differenzengleichungen der mathematischen Physik.," German, *Math. Ann.*, vol. 100, pp. 32–74, 1928.

[17] B. Dubrulle, "Beyond kolmogorov cascades," *Journal of Fluid Mechanics*, vol. 867, P1, 2019.

[18] J. Duchon and R. Robert, "Inertial energy dissipation for weak solutions of incompressible euler and navier-stokes equations," *Nonlinearity*, vol. 13, no. 1, pp. 249–255, Dec. 2000.

[19] G. Eyink, *Small-scale intermittency and anomalous scaling*, 2019.

[20] R. Ferrand, S. Galtier, F. Sahraoui, and C. Federrath, "Compressible turbulence in the interstellar medium: New insights from a high-resolution supersonic turbulence simulation," *The Astrophysical Journal*, vol. 904, no. 2, p. 160, 2020.

[21] S. Galtier, *Introduction to modern magnetohydrodynamics*. Cambridge University Press, 2016, p. 288.

[22] S. Galtier, "Von kármán–howarth equations for hall magnetohydrodynamic flows," *Phys. Rev. E*, vol. 77, 015302(R), 1 Jan. 2008.

[23] S. Galtier, "On the origin of the energy dissipation anomaly in (hall) magnetohydrodynamics," *Journal of Physics A: Mathematical and Theoretical*, vol. 51, no. 20, p. 205 501, Apr. 2018.

[24] P. R. Gazis and A. J. Lazarus, "Voyager observations of solar wind proton temperature: 1-10au," *Geophysical Research Letters*, vol. 9, no. 4, pp. 431–434, 1982.

[25] L. Z. Hadid, F. Sahraoui, S. Galtier, and S. Y. Huang, "Compressible magnetohydrodynamic turbulence in the earth's magnetosheath: Estimation of the energy cascade rate using in situ spacecraft data," *Phys. Rev. Lett.*, vol. 120, p. 055 102, 5 Jan. 2018.

[26] P. Hellinger, A. Verdini, S. Landi, L. Franci, and L. Matteini, "von Kármán-Howarth Equation for Hall Magnetohydrodynamics: Hybrid Simulations," *apjl*, vol. 857, no. 2, L19, p. L19, Apr. 2018.

[27] L. P. Kadanoff, "More is the same; phase transitions and mean field theories," *Journal of Statistical Physics*, vol. 137, no. 5, pp. 777–797, Dec. 2009.

[28] A. N. Kolmogorov, "Dissipation of energy in locally isotropic turbulence," *Dokl Akad Nauk SSSR*, vol. 32, pp. 16–18, 1941.

[29] J. Leray, "Sur le mouvement d'un liquide visqueux emplissant l'espace," *Acta Math.*, vol. 63, pp. 193–248, 1934.

[30] B. T. MacBride, C. W. Smith, and M. A. Forman, "The turbulent cascade at 1 AU: Energy transfer and the third-order scaling for MHD," *The Astrophysical Journal*, vol. 679, no. 2, pp. 1644–1660, Jun. 2008.

[31] F. Malara, L. Primavera, and P. Veltri, "Effects of entropy inhomogeneity on density-temperature correlation in solar wind," *Phys. Rev. E*, vol. 59, no. 5, pp. 6023–6031, 1999.

[32] R. Marino, L. Sorriso-Valvo, V. Carbone, A. Noullez, R. Bruno, and B. Bavassano, "Heating the solar wind by a magnetohydrodynamic turbulent energy cascade," *The Astrophysical Journal*, vol. 677, no. 1, pp. L71–L74, Mar. 2008.

[33] W. H. Matthaeus and M. L. Goldstein, "Measurement of the rugged invariants of magnetohydrodynamic turbulence in the solar wind," *J. Geophys. Res.*, vol. 87, no. A8, pp. 6011–6028, 1982.

[34] M. Miceli *et al.*, "Collisionless shock heating of heavy ions in SN 1987A," *Nature Astronomy*, vol. 3, pp. 236–241, 2019.

[35] L. Onsager, "Statistical hydrodynamics," *Il Nuovo Cimento*, vol. 6, 2 1949.

[36] Z. B. Pine *et al.*, "Solar Wind Turbulence from 1 to 45 au. II. Analysis of Inertial-range Fluctuations Using Voyager and ACE Observations," *Astrophys. J.*, vol. 900, no. 2, p. 92, 2020.

[37] Z. B. Pine *et al.*, "Solar Wind Turbulence from 1 to 45 au. IV. Turbulent Transport and Heating of the Solar Wind Using Voyager Observations," *apj*, vol. 900, no. 2, 94, p. 94, Sep. 2020.

[38] H. Politano and A. Pouquet, "Von kármán–howarth equation for magnetohydrodynamics and its consequences on third-order longitudinal structure and correlation functions," *Phys. Rev. E*, vol. 57, R21–R24, 1 Jan. 1998.

[39] D. A. Roberts and M. L. Goldstein, "Spectral signatures of jumps and turbulence in interplanetary speed and magnetic field data," *J. Geophys. Res*, vol. 92, no. A9, pp. 10 105–10 110, 1987.

[40] P. Simon and F. Sahraoui, "General Exact Law of Compressible Isentropic Magnetohydrodynamic Flows: Theory and Spacecraft Observations in the Solar Wind," *apj*, vol. 916, no. 1, 49, p. 49, Jul. 2021.

[41] S. Soluyan and R. Khokhlov, "Propagation of acoustic waves of finite amplitude in a dissipative medium.," *Vestnik Moscow State Univ., Phys. Astron*, vol. 3, pp. 52–61, 1961.

[42] L. Sorriso-Valvo *et al.*, "Observation of inertial energy cascade in interplanetary space plasma," *Phys. Rev. Lett.*, vol. 99, p. 115 001, 11 Sep. 2007.

[43] J. E. Stawarz, C. W. Smith, B. J. Vasquez, M. A. Forman, and B. T. MacBride, "The turbulent cascade and proton heating in the solar wind at 1 au," *The Astrophysical Journal*, vol. 697, no. 2, pp. 1119–1127, May 2009.

[44] G. I. Taylor, "The spectrum of turbulence," *Proceedings of the Royal Society of London. Series A – Mathematical and Physical Sciences*, vol. 164, no. 919, pp. 476–490, 1938.

[45] B. J. Vasquez, C. W. Smith, K. Hamilton, B. T. MacBride, and R. J. Leamon, "Evaluation of the turbulent energy cascade rates from the upper inertial range in the solar wind at 1 au," *Journal of Geophysical Research: Space Physics*, vol. 112, no. A7, 2007.

[46] S. Yanase, "New one-dimensional model equations of magnetohydrodynamic turbulence," *Physics of Plasmas*, vol. 4, no. 4, pp. 1010–1017, 1997.

Chapter 3

Weak solutions of magnetohydrodynamics

This study is published in:
V. David, S. Galtier, F. Sahraoui & L. Z. Hadid., "Energy Transfer, Discontinuities, and Heating in the Inner Heliosphere Measured with a Weak and Local Formulation of the Politano-Pouquet Law", *Astrophys. J.* **927**, 200, 2022.

3.1 Introduction

Now that we have tackled the Yanase model, let us turn our attention to the more general problem of three-dimensional incompressible MHD. Unlike the low-dimensional model, exact solutions and Zeroth law proofs are not feasible in the general case. Nevertheless, we can derive an exact law and an expression of anomalous dissipation.

To put our findings to the test, we have the advantage of numerous missions that measure solar wind turbulence in situ (the one I spoke about in the Section 1.3). In particular, we will use data from two spacecraft: Parker Solar Probe, which is roaming around the Sun, and THEMIS-B, which is close to Earth. By comparing the two datasets, we will determine which tool between the exact law and the anomalous dissipation is more suitable for estimating turbulent dissipation in the solar wind at MHD scales.

3.2 Incompressible MHD theory

3.2.1 Waves and structures

To begin with the incompressible MHD theory, let us explore the linear case. Assuming the presence of a mean magnetic field, we can study its perturbations and simplify the equations to their linear form. As discussed in Chapter 1, in this context, we encounter the Alfvén wave which propagates along the magnetic field lines at a constant velocity known as the Alfvén velocity. These waves exhibit a characteristic motion, where the particles and the perturbation of the magnetic field are transverse to the direction of propagation. Now, when we consider the complete equations, we encounter nonlinearities. These nonlinear effects can distort the original Alfvén waves, causing modifications to their wavenumber. This phenomenon, known as turbulent cascade, will be extensively discussed in the next chapters. In addition to distortion, the waves can also exhibit phase coherence, giving rise to the formation of coherent structures such as vortices.

As we delve into the subsequent sections, we will explore, inter alia, how certain inhomogeneous structures named switchbacks, measured in the solar wind, exhibit distinct alfvénic characteristics. Therefore, the incompressible assumption does not hinder our ability to study and understand these types of events.

3.2.2 Exact law

In the previous chapter, we mentioned that the four-thirds law derived by Antonia *et al.* [2] has many generalizations. One such extension was developed in 1998 by Politano and Pouquet [22] for incompressible

MHD (hereafter called the PP98 law). Let me give you a rough idea of how they did it. Let $\boldsymbol{u}$ be the fluid velocity, $\boldsymbol{b} \equiv \boldsymbol{B}/(\mu_0\rho_0)$ the magnetic field normalized to a velocity, with ρ_0 the (constant) plasma density and μ_0 the vacuum permeability, $P_\star = P + b^2/2$ the sum of the thermal and magnetic pressures, ν the kinematic viscosity, and η the magnetic diffusivity. Then, the incompressible MHD equations read [8]:

$$\frac{\partial \boldsymbol{u}}{\partial t} = -\boldsymbol{\nabla} P_\star - \boldsymbol{\nabla}\cdot(\boldsymbol{u}\otimes\boldsymbol{u} - \boldsymbol{b}\otimes\boldsymbol{b}) + \nu\nabla^2\boldsymbol{u}, \tag{3.1a}$$

$$\frac{\partial \boldsymbol{b}}{\partial t} = -\boldsymbol{\nabla}\cdot(\boldsymbol{u}\otimes\boldsymbol{b} - \boldsymbol{b}\otimes\boldsymbol{u}) + \eta\nabla^2\boldsymbol{b}, \tag{3.1b}$$

$$\boldsymbol{\nabla}\cdot\boldsymbol{u} = 0, \tag{3.1c}$$

$$\boldsymbol{\nabla}\cdot\boldsymbol{b} = 0, \tag{3.1d}$$

where $\otimes$ denotes the tensor product operation. To derive these equations, the following Ohm's law is used:

$$\boldsymbol{e} = \eta\boldsymbol{j} - \boldsymbol{u}\times\boldsymbol{b}, \tag{3.2}$$

where $\boldsymbol{e}$ is the normalized electric field and $\boldsymbol{j} = \boldsymbol{\nabla}\times\boldsymbol{b}$ is the normalized electric current density. To obtain the PP98 law, we assume that we are dealing with asymptotically large values of both magnetic and kinetic Reynolds numbers, as well as with stationary, homogeneous turbulence. After a standard calculation, one obtains a primitive form of the PP98 exact law:

$$-4\varepsilon = \boldsymbol{\nabla}_{\boldsymbol{r}}\cdot\langle\boldsymbol{\mathcal{S}}_{\rm MHD}\rangle\,, \tag{3.3a}$$

$$\boldsymbol{\mathcal{S}}_{\rm MHD} = (\delta\boldsymbol{u}\cdot\delta\boldsymbol{u} + \delta\boldsymbol{b}\cdot\delta\boldsymbol{b})\,\delta\boldsymbol{u} - 2\,(\delta\boldsymbol{u}\cdot\delta\boldsymbol{b})\,\delta\boldsymbol{b}. \tag{3.3b}$$

In this equation, ε is the mean rate of energy transfer / dissipation / forcing, the equivalence between the three definitions being due to the stationarity assumption. The previous expression can be reduced to the PP98 law when the statistical isotropy is further assumed:

$$-\frac{4}{3}\varepsilon r = \langle(\delta\boldsymbol{u}\cdot\delta\boldsymbol{u} + \delta\boldsymbol{b}\cdot\delta\boldsymbol{b})\,\delta u_r - 2\,(\delta\boldsymbol{u}\cdot\delta\boldsymbol{b})\,\delta b_r\rangle\,. \tag{3.4}$$

Here, $\delta u_r = \delta\boldsymbol{u}\cdot(\boldsymbol{r}/r)$ and $\delta b_r = \delta\boldsymbol{b}\cdot(\boldsymbol{r}/r)$ with r the norm of the vector $\boldsymbol{r}$. The PP98 law is valid in the inertial range of incompressible MHD turbulence, and a basic assumption made to use it is that the fields are regular (i.e., differentiable). To characterize the behavior of the fluctuations in the velocity $\boldsymbol{u}$ and the

magnetic field $\boldsymbol{b}$, we can define Hölder exponents $(p, q) \in \mathbb{Q}_*^+$ such that the following inequalities hold:

$$|\langle \delta u \rangle| \leq \langle |\delta u| \rangle \quad ; \quad |\langle \delta b \rangle| \leq \langle |\delta b| \rangle \,, \tag{3.5a}$$

$$|\delta u| \leq C_u r^p \quad ; \quad |\delta b| \leq C_b r^q, \tag{3.5b}$$

where C_u and C_b are some positive constants. By applying these inequalities to the PP98 law, we find that this theory is valid if the following conditions on the Hölder exponents are fulfilled:

$$p = 1/3 \quad ; \quad q = (1-p)/2. \tag{3.6}$$

Two crucial points warrant discussion. Firstly, if $p < 1/3$ and/or $q < (1-p)/2$, the right-hand side of Equation (3.3a) scales as r^{3p-1} or r^{p+2q-1}, and exhibits a potential blow-up as $r \to 0$. To overcome this limitation, a weak formulation must be introduced. The second point arises when $p > 1/3$ and/or $q > (1-p)/2$. In this scenario, as $r \to 0$, the right-hand side of Equation (3.3a) decreases faster than r, ultimately converging to zero. This result implies $\varepsilon = 0$, which contradicts the assumption of a nonzero value for ε and, consequently, the existence of an inertial range in the energy cascade.

3.2.3 Anomalous dissipation

As before, the weak formalism is based on smoothing of a field with some kernel $\varphi \in \mathbb{C}^\infty$ with compact support on $\mathbb{R}^3$, even, non-negative and with integral 1. To formalize the notion of scale, we define a family of test functions φ^ℓ such that $\varphi^\ell(\boldsymbol{\xi}) \equiv \varphi(\boldsymbol{\xi}/\ell)/\ell^3$. Note that there is no unique solution for the test function. However, with this definition, the anomalous dissipation does not depend on the test function in the limit $\ell \to 0$ because in this case, the test function tends to a Dirac distribution [7]. Note also that this filtering process consists in smoothing the fields in a space defined by a sphere of radius ℓ centered at the point $\boldsymbol{\xi}$ (cf. Figure 3.1). The regularized fields at scale ℓ are defined by taking the convolution product of the fields with φ^ℓ

$$\boldsymbol{u}^\ell(\boldsymbol{x}, t) \equiv \ \varphi^\ell * \boldsymbol{u} = \int \varphi^\ell(\boldsymbol{\xi}) \boldsymbol{u}(\boldsymbol{x} + \boldsymbol{\xi}, t) \mathrm{d}\boldsymbol{\xi}, \tag{3.7}$$

which tends to $\boldsymbol{u}(\boldsymbol{x}, t)$ when $\ell \to 0$. The other regularized quantities are defined in the same way. Under

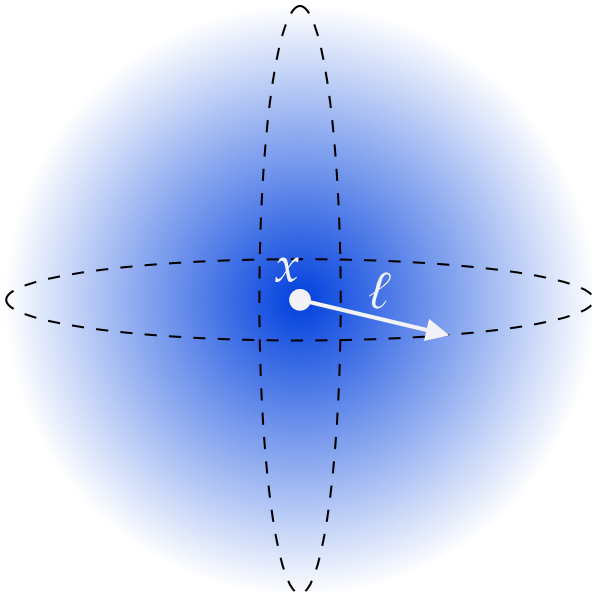

Figure 3.1: Scheme of the filtering process. The color reflects the intensity of the smoothing. ℓ can be seen as the typical scale beyond which the contribution to the integral (see Equation (3.7)) is mainly negligible.

these considerations, the kinetic, and magnetic energies read

$$E_u^\ell(\boldsymbol{x},t) \equiv \frac{\boldsymbol{u}\cdot\boldsymbol{u}^\ell}{2} = \int \varphi^\ell(\boldsymbol{\xi})\frac{\boldsymbol{u}(\boldsymbol{x},t)\cdot\boldsymbol{u}(\boldsymbol{x}+\boldsymbol{\xi},t)}{2}\mathrm{d}\boldsymbol{\xi}, \tag{3.8a}$$

$$E_b^\ell(\boldsymbol{x},t) \equiv \frac{\boldsymbol{b}\cdot\boldsymbol{b}^\ell}{2} = \int \varphi^\ell(\boldsymbol{\xi})\frac{\boldsymbol{b}(\boldsymbol{x},t)\cdot\boldsymbol{b}(\boldsymbol{x}+\boldsymbol{\xi},t)}{2}\mathrm{d}\boldsymbol{\xi}. \tag{3.8b}$$

The previous expressions can also be interpreted as the local equivalents of a correlation function, where the ensemble average is replaced by a local average over scale. Now, if we assume that $(\boldsymbol{u},\boldsymbol{b})$ are weak solutions of the incompressible MHD equations (3.1) over a periodic domain $\mathbb{T}^3$ and that $(\boldsymbol{u},\boldsymbol{b}) \in L^3\left([0,T]\times\mathbb{T}^3\right)$, with the above definitions and using a point-splitting regularization, one can derive the following weak formulation (valid for individual realizations) of the local energy conservation at position $\boldsymbol{x}$:

$$\frac{\partial}{\partial t}E^\ell(\boldsymbol{x},t) + \boldsymbol{\nabla}\cdot\boldsymbol{\Pi}^\ell(\boldsymbol{x},t) = -\mathcal{D}^\ell_{\nu,\eta}(\boldsymbol{x},t) - \mathcal{D}^\ell_a(\boldsymbol{x},t), \tag{3.9}$$

with $E^\ell = E_u^\ell + E_b^\ell$ the total energy. $\boldsymbol{\Pi}^\ell$ is the spatial flux whose heavy form is not given explicitly here; this is a purely local term that describes how energy is transported across the flow, and it vanishes after integration over space with the appropriate boundary conditions. We also have the energy dissipation by

viscous and resistive effects (that includes the vorticity $\boldsymbol{\omega} = \boldsymbol{\nabla} \times \boldsymbol{u}$ and the electric current $\boldsymbol{j} = \boldsymbol{\nabla} \times \boldsymbol{b}$),

$$\mathcal{D}_{\nu,\eta} = \nu\omega^2 + \eta j^2 \tag{3.10}$$

and the anomalous dissipation,

$$\mathcal{D}_a(\boldsymbol{x},t) = \lim_{\ell\to 0} \frac{1}{4} \int_{\mathbb{T}^3} \boldsymbol{\nabla}\varphi^\ell(\boldsymbol{\xi}) \cdot \boldsymbol{\mathcal{S}}_{\mathrm{MHD}}(\boldsymbol{x},\boldsymbol{\xi},t)\,\mathrm{d}\boldsymbol{\xi}, \tag{3.11}$$

where the third-order structure function reads

$$\boldsymbol{\mathcal{S}}_{\mathrm{MHD}}(\boldsymbol{x},\boldsymbol{\xi},t) = (\delta\boldsymbol{u}\cdot\delta\boldsymbol{u} + \delta\boldsymbol{b}\cdot\delta\boldsymbol{b})\,\delta\boldsymbol{u} - 2\,(\delta\boldsymbol{u}\cdot\delta\boldsymbol{b})\,\delta\boldsymbol{b}. \tag{3.12}$$

The approach to derive these equations follows a similar path to the one we used for the Yanase model, and for a detailed derivation, one may refer to Galtier [9]. Expression (3.8) must be seen as a generalization of the PP98 law (or more precisely of the Kármán–Howarth MHD equation [22]) that we can recover for regular fields and homogeneous turbulence (see below). Note that in the limit $\ell \to 0$, the two dissipative terms are mutually exclusive: the presence of any viscosity/resistivity should prevent the formation of singularities. Thus, in this limit, only one of them can appear in the equation. Another physical relevance of the weak formulation is revealed when performing an integration over space. The absence of an energy source at the boundary is formally equivalent to assuming periodicity (or homogeneity); therefore, the notation $\langle\cdot\rangle$ will be used for integration in space. We find

$$\frac{\partial}{\partial t}\left\langle E^\ell \right\rangle = -\left\langle \mathcal{D}_a^\ell \right\rangle - \left\langle \mathcal{D}_{\nu,\eta}^\ell \right\rangle, \tag{3.13a}$$

$$\left\langle \mathcal{D}_a^\ell \right\rangle = \frac{1}{4} \int_{\mathbb{T}^3} \boldsymbol{\nabla}\varphi^\ell(\boldsymbol{\xi}) \cdot \langle \boldsymbol{\mathcal{S}}_{\mathrm{MHD}} \rangle\,\mathrm{d}\boldsymbol{\xi}. \tag{3.13b}$$

In the small-scale limit, we find for a viscous/resistive flow

$$\lim_{\ell\to 0} \left\langle \mathcal{D}_{\nu,\eta}^\ell \right\rangle \equiv \langle \mathcal{D}_{\nu,\eta} \rangle = \varepsilon. \tag{3.14}$$

Therefore, $\mathcal{D}_{\nu,\eta}^\ell$ can be used to trace, locally and across scales, the rate of viscous/resistive energy dissipation [17]. On the other hand, expression (3.13b) has a strong similarity with the right-hand side term of the exact law (3.4), especially if one performs an integration by part, assuming the fields to be regular, and

takes the small scale limit

$$\mathcal{D}_a\left(\boldsymbol{x},t\right) \equiv \lim_{\ell\to 0}\mathcal{D}_a^\ell = -\lim_{\ell\to 0}\frac{1}{4}\int_{\mathbb{T}^3}\varphi^\ell\left(\boldsymbol{\xi}\right)\boldsymbol{\nabla}\cdot\boldsymbol{\mathcal{S}}_{\mathrm{MHD}}(\boldsymbol{x},\boldsymbol{\xi},t)\mathrm{d}\boldsymbol{\xi}. \tag{3.15}$$

This relation directly connects $\mathcal{D}_a$ to the PP98 law, which leads to the remarkable equality $\langle\mathcal{D}_a\rangle = \varepsilon$. Therefore, $\mathcal{D}_a^\ell$ can also be used to trace, locally and across scales, the rate of energy transfer.

Other interpretations can be made based on the relation (3.15). In the presence of finite viscosity and resistivity, the fields are regular (because the Laplacian operator smooths the fields at small scales) and thus satisfy $\lim_{\boldsymbol{\xi}\to\mathbf{0}^+}\delta\boldsymbol{u} = \lim_{\boldsymbol{\xi}\to\mathbf{0}^+}\delta\boldsymbol{b} = \mathbf{0}$, which leads to $\mathcal{D}_a = 0$; this is the classical situation. On the contrary, if $\nu = \eta = 0$, non-regular fields can be produced and $\mathcal{D}_a$ can have a contribution. This contribution is however not systematic because the fields must satisfy the Hölder condition [6, 20]. Using a scaling analysis (at a fixed position $\boldsymbol{x}$), we can make three theoretical predictions of practical importance:

1. In the inertial range where the fields correspond to turbulent fluctuations that obey the PP98 law in the inertial range, we have $\delta u^3 \sim \delta b^3 \sim \ell$ and thus $\mathcal{D}_a^\ell(\boldsymbol{x}) \sim \ell^0$.

2. At small scales where viscous/resistive effects dominate, a Taylor expansion gives $\delta u \sim \delta b \sim \ell$ and thus $\mathcal{D}_a^\ell(\boldsymbol{x}) \sim \ell^2$.

3. However, when the fields are non-regular and act like discontinuities, the increments correspond to jumps $\delta u \sim \Delta_u$, $\delta b \sim \Delta_b$, and thus $\mathcal{D}_a^\ell(\boldsymbol{x}) \sim \ell^{-1}$.

Therefore, depending on the scaling that would be measured in the solar wind (see below) it will be possible to make a distinction between turbulence, viscous/resistive damping, and discontinuities (see Figure 3.2). Note, however, that other ℓ-dependence are possible for non-regular fields [15, 16, 18].

To conclude, we point out that $\mathcal{D}_a$ is a generalized function, and its analytic form (if it can be found) can lead to the appearance of a δ-function (see e.g., Chapter 2). This means that when the limit $\ell \to 0$ is taken, one expects to see the value of $\left|\mathcal{D}_a^\ell\right|$ increases without limit, however, in practice, the value $\ell = 0$ will never be reached (see below).

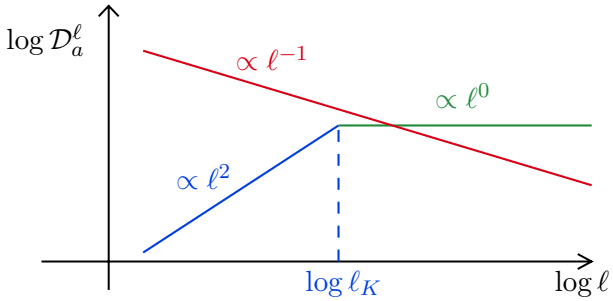

Figure 3.2: Variation (schematic) of the anomalous dissipation $\mathcal{D}_a^\ell(\boldsymbol{x})$ as a function of the scale ℓ for a discontinuity (red line), turbulent fluctuations (green line), and viscous/resistive damping (blue line). The intersection between the green and the blue lines defines the dissipative (i.e., Kolmogorov) scale and is noted ℓ_K. Similarly, the intersection between the green and the red line can define the discontinuity scale, below which discontinuities become dominant (see Figure 3.4).

3.3 Application to the solar wind

3.3.1 Data selection

In the remaining part of this chapter, our focus will shift toward the practical application of these two approaches in determining the rate of energy transfer within the solar wind. We will examine their effectiveness in capturing the turbulent plasma dynamics near Earth as well as in the proximity of the Sun. By comparing and contrasting the results obtained from these two distinct regions, we aim to gain valuable insights into the energy transfer processes operating within the solar wind.

In the first step, we used the THEMIS-B/ARTEMIS P1 spacecraft data during time intervals when it was traveling in the free-streaming solar wind. The magnetic field data and plasma moments (protons density and velocity) were measured respectively by the Flux Gate Magnetometer (FGM) and the Electrostatic Analyzer (ESA). All data are expressed in the Geocentric Solar Ecliptic (GSE) coordinate system, and have a time resolution $dt = 3\,\mathrm{s}$, which corresponds to the spacecraft spin period. We analyzed more than 180 h of data between 2008 and 2011 that cover both fast and slow solar winds. Fast winds are defined as having an average speed $U_{\mathrm{SW}} > 450\,\mathrm{km\,s^{-1}}$. The others are the slow winds. In the second step, we analyze PSP's data measured between 2018 and 2020 during the first and fifth approaches of the spacecraft to the Sun. We selected two subsets of a total duration of about 115 h corresponding roughly to radial distances of 17 and 13 solar radii (at perihelion) to which we refer respectively by subsets PSP1 and PSP5. The magnetic field and plasma moments (protons density and velocity) were measured respectively by the fluxgate magnetometer (MAG) and the Solar Probe Analyzer (SPAN). All data are expressed in the Radial Tangential Normal (RTN) coordinate system, and have a time resolution $dt = 1\,\mathrm{s}$.

For both spacecraft, the selected intervals are divided into samples of two hours, which correspond to a number of data points $N = 2400$ for THEMIS-B and $N = 7200$ for PSP. The data selection yielded :

- 51 samples (122,400 data points) in the slow solar wind.
- 46 samples (110,400 data points) in the fast solar wind.
- 61 samples (439,200 data points) for PSP1.
- 55 samples (396,000 data points) for PSP5.

Data gaps (when present) were interpolated linearly. For the selected time intervals, we compute the energy cascade rates ε estimated by PP98 and the anomalous dissipation $\mathcal{D}_a^\ell$ using Equations (3.4) and (3.11) respectively. The structure functions of $\boldsymbol{u}$ and $\boldsymbol{b}$ are calculated for different time lags $\tau \in [1,\ 100]\, dt$ to probe the scales of the inertial range. As usual (see e.g., Hadid *et al.* [11]), we use the Taylor hypothesis $\tau = -\xi/U_{\rm SW}$ with $U_{\rm SW}$ the mean solar wind speed on the interval, assuming that $\mathcal{D}_a = \mathcal{D}_a^{\ell_{\rm min}}$, with $\ell_{\rm min}$ the minimum accessible value, which is 3 s for THEMIS-B and 1 s for PSP data. We note $\left\langle \mathcal{D}_a^\ell \right\rangle$ the time average of the anomalous dissipation over the two hours sample.

Mathematically, the anomalous dissipation $\mathcal{D}_a^\ell$ can be interpreted as a continuous wavelet transform of the third-order structure function $\boldsymbol{\mathcal{S}}_{\rm MHD}$ with respect to the wavelet φ. The link between the weak formulation and the wavelet transform reveals several advantages of its application to rough turbulent fields. Indeed, a wavelet transform can be considered as a "local Fourier transform" and it is suitable for application to inhomogeneous fields. Thus, it will genuinely deal with the observed breaking of the spatial translation symmetry [6]. Therefore, we computed $\mathcal{D}_a^\ell$ on the entire time interval for 100 values of ℓ as a continuous one-dimensional wavelet transform based on fast Fourier transform – a MATLAB package provided by the toolbox YAWTB [14]. The test function φ^ℓ is a normalized Gaussian of width ℓ, which is convenient because its derivative is exact. Note that in the implementation of the anomalous dissipation, only the terms depending on ξ are computed because the convolution product is performed on this variable and, given the properties of φ^ℓ, it is obvious that the smoothing of a field independent of ξ leaves the result unchanged. To minimize the finite window size effects due to the non-periodicity of the data, we artificially extend each time series to twice its size to apply a Gaussian windowing before computing its Fourier transform. The final result is obtained in the time domain after an inverse Fourier transform, where only the information from the central part of the time series (i.e., the original one of interest) is considered.

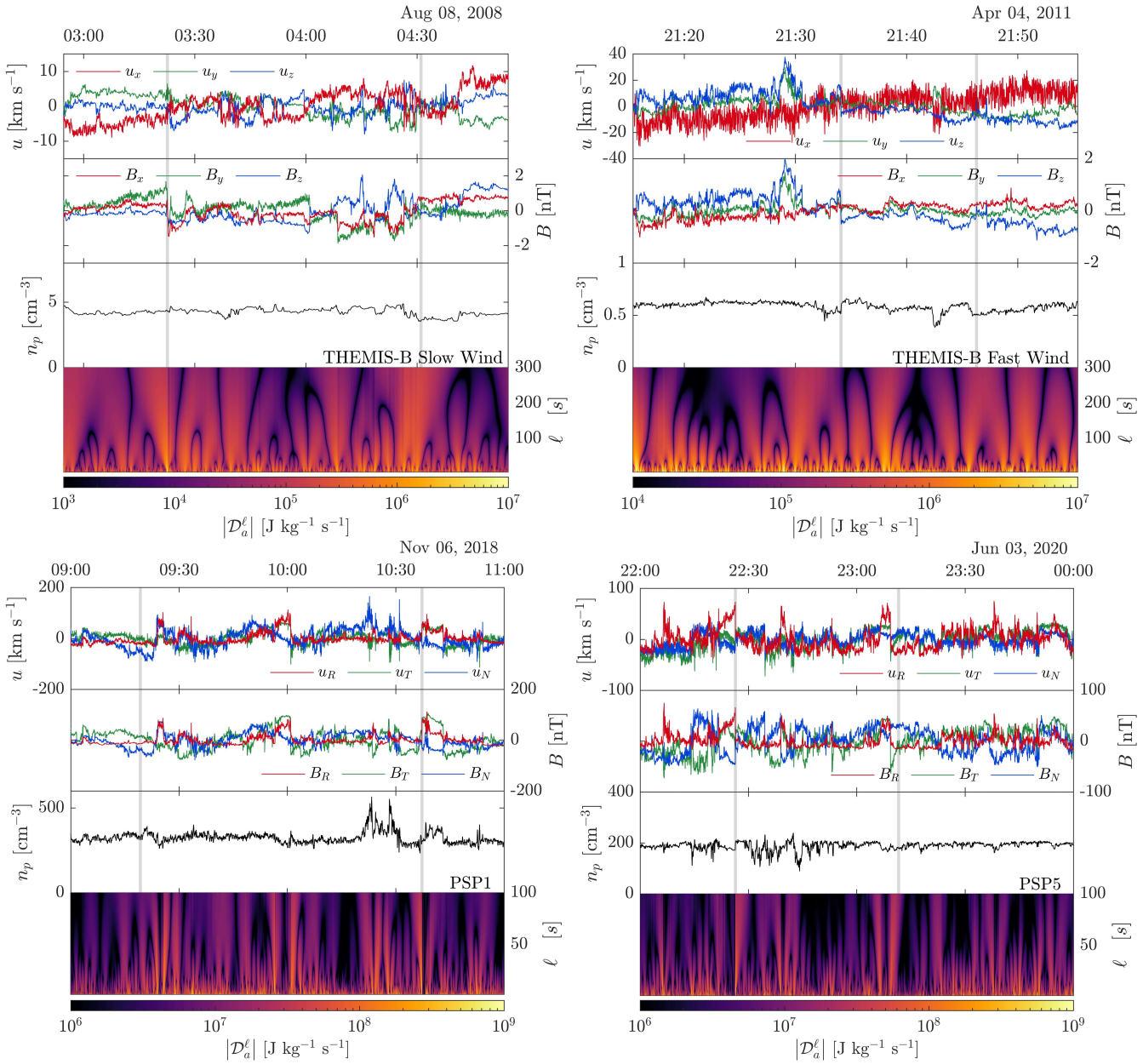

Figure 3.3: Top panels display the slow (left) and fast (right) winds measured with THEMIS-B. The bottom panels display PSP1 (left) and PSP5 (right). In each panel, from top to bottom, we find the fluctuations of the velocity components, fluctuations of the magnetic field components, proton density, and space-scale diagram (in modulus) of the anomalous dissipation. The red, blue, and green curves correspond respectively to the x, y, z components (GSE coordinates) for THEMIS-B and to the R, T, N components (RTN coordinates) for PSP. The vertical gray lines locate the instant for which $|\mathcal{D}_a|$ is extremal on the sample.

3.3.2 Inhomogeneous structures

We begin our data analysis with four examples where discontinuities are present. In Figure 3.3 we show (top left) a THEMIS-B slow wind interval on August 08, 2008, from 02:54:36 to 04:54:36, (top right) a THEMIS-B fast wind interval on April 04, 2011, from 21:15:23 to 23:15:23, (bottom left) a PSP1 interval on November 06, 2018, from 09:00:00 to 11:00:00, and (bottom right) a PSP5 interval on June 03, 2020, from 22:00:00 to June 04, 00:00:00. For each case study, the first two panels (top to bottom) show the three components of the protons velocity and the magnetic field, respectively. They highlight the presence of discontinuities, and thus the breaking of statistical homogeneity, which may jeopardize the use of exact laws. We find that for the PSP intervals that are closer to the Sun, the velocity and magnetic field components are strongly correlated (respectively 91%, 90%, and 91% for the radial, tangential, and normal components for the PSP1 interval, and 96%, 86%, and 80% for the PSP5 one), which can be interpreted as the signature of outward propagating Alfvén waves [5]. The third panel shows the proton density, which is relatively constant, and the last panel shows a space-scale diagram of the anomalous dissipation (in modulus): time is on the x-axis, the width ℓ of the test function on the y-axis and the intensity of $|\mathcal{D}_a^\ell|$ is in color. These maps illustrate the local energy transfer between different scales ℓ (at a given time t, or using the Taylor hypothesis, at a given position $x = -U_{SW}t$ with U_{SW} the solar wind speed). If we follow the evolution of the plasma from small to large scales, the dark areas delimit the impact of an event on the energy transfer: the larger the bright area in scale, the greater the impact of the event in scale and the smaller would be the local energy transfer. Conversely, when a region is mainly dark, this means that the energy transfer is local and the dynamic is driven by turbulent fluctuations.

A more precise analysis can be made by observing how $|\mathcal{D}_a^\ell|$ evolves according to the scale ℓ at given times $t_\star$ and t_f. We respectively chose $t_\star$ and t_f such that $|\mathcal{D}_a(t_\star)| = \max(|\mathcal{D}_a|)$ and $|\mathcal{D}_a^\ell(t_f)| = \min(|\mathcal{D}_a|)$ over the 2 h interval (see Figure 3.3). The top panels of Figure 3.4 reveals that when placed respectively on a discontinuity (at time $t_\star$) and on a turbulent fluctuation (at time t_f), the anomalous dissipation does follow the ℓ^{-1} and ℓ^0 power-laws, as theoretically expected. The third panel shows the evolution of the anomalous dissipation $|\langle \mathcal{D}_a^\ell \rangle|$, averaged over the entire intervals of 2 h, as a function of ℓ. The power laws found indicate the dominant type of energy transfer. For those coming from THEMIS-B (in blue), we observe mainly a flat profile, which means that the dominant mechanism is a turbulent cascade due to fluctuations. For PSP1 (dark red), a power law in ℓ^{-1} appears at small ℓ, showing the prevalence of discontinuities at small scales for this interval. For PSP5 (light red), an intermediate power law is observed,

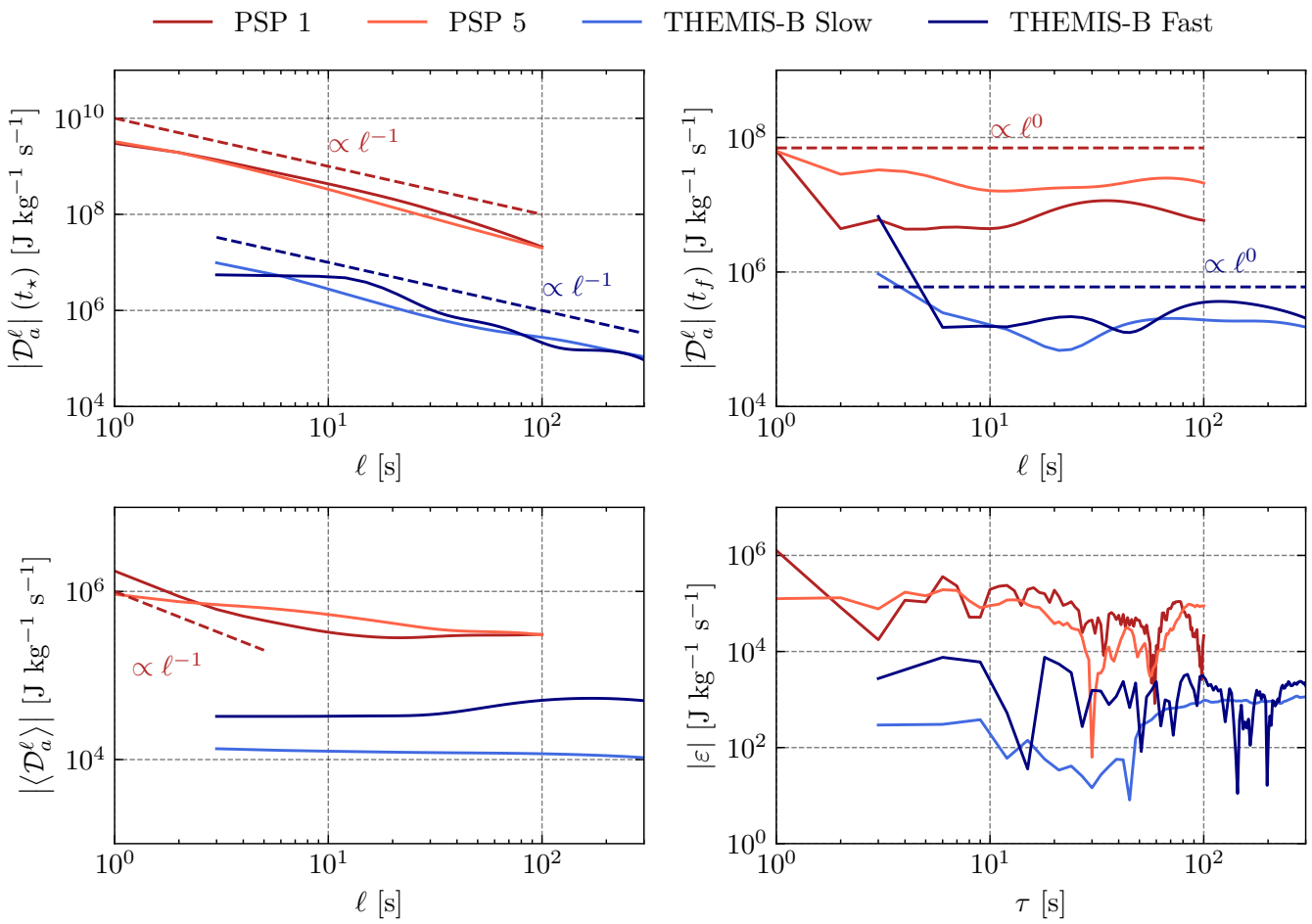

Figure 3.4: Top left: modulus of the anomalous dissipation at time $t_\star$ as a function of scale ℓ; top right: modulus of the anomalous dissipation at time t_f as a function of scale ℓ; bottom left: estimates of the mean anomalous dissipation as a function of ℓ; bottom right: modulus of the mean rate of energy cascade as a function of τ. Here, ℓ and τ vary approximately on the same interval.

suggesting that the effect of discontinuities is weaker. The last panel displays the value of $|\varepsilon|$ as a function of τ for the four intervals. We can see that the curves do not exhibit a clear plateau as theoretically expected; this might be due to the violation of one (or more) of the assumptions on which the exact law formalism is grounded. This is particularly the case for the statistical homogeneity, which is unlikely to be valid here because of the presence of discontinuities that distort the estimate of the mean rate of energy cascade [11]. Note that for the PSP intervals close to the Sun, both intervals give the same order of magnitude of the anomalous dissipation, but is larger than that from THEMIS-B data at 1 au, which overall remains true for the other intervals. This is consistent with the radial increase of the turbulent cascade rate ε as one approaches the Sun [1, 4]. Also, the anomalous dissipation is larger for fast than for slow solar winds, in agreement with previous results regarding the cascade rate ε [11].

3.3.3 Switchbacks

Switchbacks are defined as sudden reversals of the radial magnetic field component associated with sharp variations in the radial plasma flow [12, 13, 19]. Although they are actively studied, their origin remains an open question [3, 28] even if numerical simulations seem to show that many features of the observed turbulence (i.e., switchbacks) are reproduced by a spectrum of Alfvénic fluctuations advected by a radially expanding flow [26]. We propose here to estimate the anomalous dissipation produced by these peculiar structures in order to quantify their relative importance in the energy cascade.

We focus on a PSP1 interval on November 06, 2018, from 01:30 to 02:30 where switchbacks are numerous. The first two panels of Figure 3.5 again highlight a clear correlation between the velocity and the magnetic field (respectively 97%, 86%, and 90% for the radial, tangential and normal components), which testifies to the presence of outward Alfvén waves. By following the evolution of $|\mathcal{D}_a^\ell|$ as a function of ℓ on switchbacks located at times $t_\star$, a power-law close to $\ell^{-3/4}$ seems to emerge. This does not correspond to any scaling laws predicted analytically. Note that there is a zoology of non-regular fields, and the fact that we find empirically a $\ell^{-3/4}$-dependence could mean that a switchback is not strictly speaking a simple jump. However, as far as we know, the precise mathematical structure that could reproduce this ℓ-dependence is not known. The fifth panel shows mainly a flat curve for both the mean rate of energy cascade and the anomalous dissipation. We also see that the values coincide relatively well in the limit of small-scale ℓ. The fact that ε is relatively smooth and constant may come from the fact that the discontinuities are so large that they impose at all scales their jump (or amplitude) on the increments $\delta\boldsymbol{u}$ and $\delta\boldsymbol{b}$, which then would lead to a higher value of ε (compared to Figure 3.4). Although both estimates ($|\left\langle \mathcal{D}_a^\ell \right\rangle|$ and

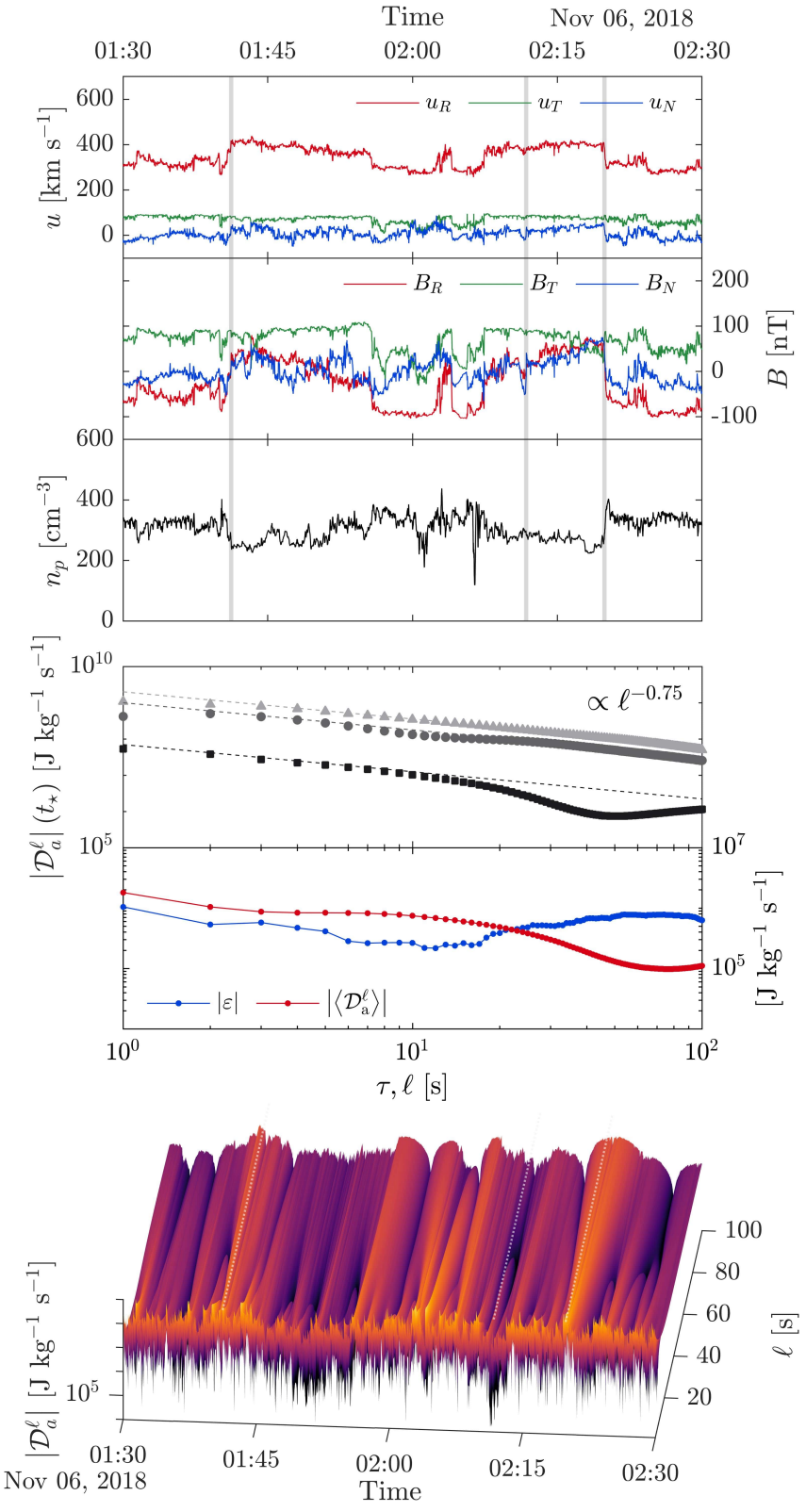

Figure 3.5: 1 h interval of PSP1 with switchbacks. From top to bottom: velocity components, magnetic field components, proton density, modulus of anomalous dissipation (at different times (see also the vertical gray lines in the first three panels and dotted white lines in the last one) $t_\star = \{01{:}41{:}13, 02{:}11{:}47, 02{:}19{:}53\}$ in gray, black and light gray, respectively) as a function of ℓ, modulus of 1h-averaged anomalous dissipation as a function of ℓ (red) and modulus of the mean rate of energy cascade as a function of τ (blue), and finally the three-dimensional map of the modulus of anomalous dissipation where the color is related to the intensity and thus to the height of $|\mathcal{D}_a^\ell|$. Velocity and magnetic fields are expressed in RTN coordinates.

$|\varepsilon|$) give a similar result, rigorously speaking, the exact law should not be applicable in this type of data. The last panel is a three-dimensional space-scale diagram of anomalous dissipation, which highlights that switchbacks make the main contribution to the energy cascade. Indeed, one can observe that the large-scale contribution of the anomalous dissipation comes from the locations where switchbacks occur and, we observe the same behavior as in Section 3.3.2: the dark areas mark the limit of the impact of a discontinuity on its vicinity. Overall, we observe that the values of $|\mathcal{D}_a^\ell|$ for switchbacks – in particular in the limit of small ℓ – are significantly higher than the values found for the other types of singularities, characterized by other power-laws, which suggests that switchbacks can contribute to stronger heating.

3.3.4 Statistical results

We conclude our data analysis with a statistical comparison between the mean anomalous dissipation and the mean rate of energy transfer as a function of the solar wind speed and the level of the magnetic field fluctuations. Note that the latter is estimated by the ratio between the root-mean-square $B_{\rm RMS}$ and the mean value B_0 of the magnetic field.

In Figure 3.6, we show $|\langle\mathcal{D}_a\rangle|$ as a function of $|\varepsilon|$ for each processed interval. The upper panels correspond to THEMIS-B intervals (triangles for slow wind and squares for fast wind) and the lower panels to PSP intervals (triangles for PSP1 and squares for PSP5). The dashed (diagonal) line obeys the equation $|\langle\mathcal{D}_a\rangle| = |\varepsilon|$. The colors in the left column reflect the mean solar wind velocity, while those in the right column correspond to the amplitude of the magnetic field fluctuations of each of the intervals. First, we notice that near the Sun (bottom panels), the values of $|\langle\mathcal{D}_a\rangle|$ and of $|\varepsilon|$ are higher than near the Earth (top panels). This property can be attributed primarily to the strength of the magnetic field which intensifies as one approaches the Sun, but also to the omnipresence of discontinuities near the Sun. Note that the decrease of the cascade rate with the heliocentric radial distance has already been measured from exact laws or turbulence transport models [1, 4], but the new observation regarding $|\langle\mathcal{D}_a\rangle|$ was achieved thanks to our anomalous model that applies in the presence of discontinuities. Second, a clear correlation with the wind speed is found at 1 au with the two methods: the faster the wind, the higher the mean rate of energy transfer. This property was also shown by [11] using exact (compressible and incompressible) laws. Note that only THEMIS-B data include fast winds (PSP orbits near the Sun remain mainly in the equatorial plane, where the wind is generally slow). Third, in the right column, no clear behavior emerges in the magnetic field fluctuations at 1 au while for the PSP intervals, even if these events are a few and thus statistically meaningless, large values of $B_{\rm RMS}/B_0$ tend to reduce the mean rate of energy transfer. Last,

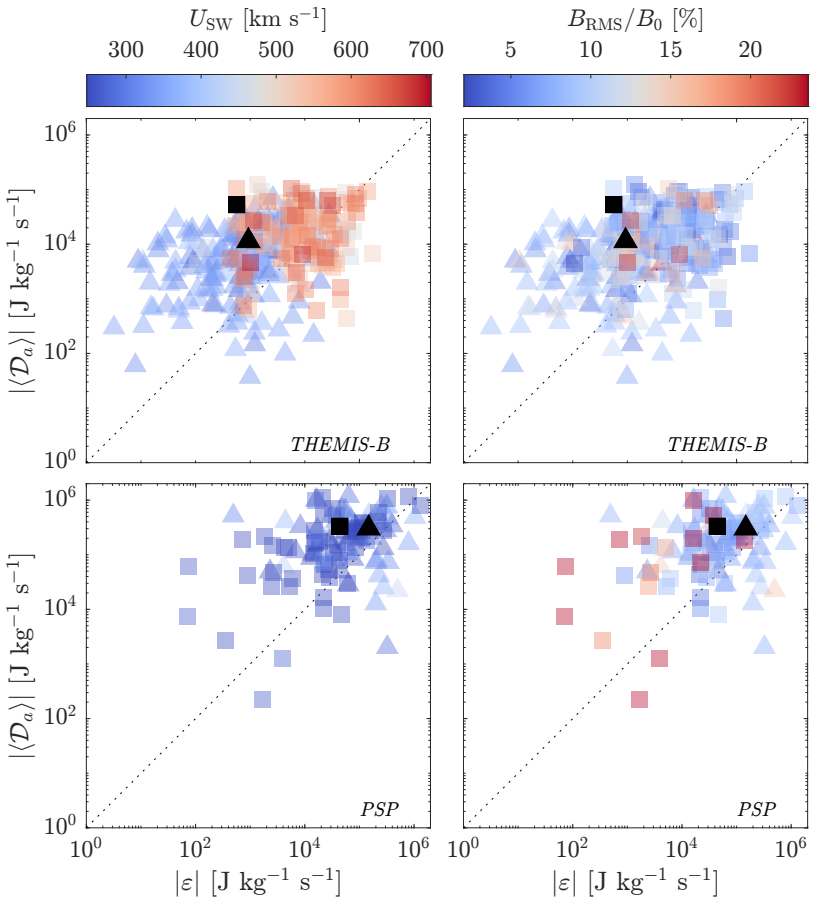

Figure 3.6: Anomalous dissipation as a function of the mean rate of energy transfer, measured via the PP98 law. The color scales correspond to the solar wind velocity (left) and to the magnetic field fluctuations (right). The triangle and square markers respectively refer to the slow and fast winds (THEMIS-B) in the upper panels and to PSP1 and PSP5 in the lower panels. The dashed (diagonal) lines correspond to $|\langle \mathcal{D}_a \rangle| = |\varepsilon|$ and black markers are the intervals studied in Figure 3.3.

the majority of the values lie above the diagonal, meaning that on average $|\langle \mathcal{D}_a \rangle| > |\varepsilon|$. This observation can be seen as a signature of inhomogeneities (discontinuities) that are not well captured by the method using the exact law. These inhomogeneities lead mainly to a non-local contribution visible at large ℓ (see Figures 3.3 and 3.5).

3.4 Conclusion

In this chapter, we have used two different methods to measure the rate of turbulent energy transfer at MHD scales. The first is the PP98 exact law applicable to stationary, homogeneous, and isotropic turbulence, and the second is the anomalous dissipation $\mathcal{D}_a^\ell$. Both laws have a similar form with the same combination of structure functions, but in the latter case, the stationarity and homogeneity assumptions

are not necessary for its derivation. Therefore, $\mathcal{D}_a^\ell$ can be considered as more general than the PP98 law since it is a local (exact) law allowing us to measure the energy transfer rate at each point of the turbulent flow even when discontinuities are present. Note that the weak formulation of the PP98 law provides a theoretical justification of the observational work of [23–25] who heuristically employed the PP98 law without ensemble average.

Theoretically, several scaling behaviors are expected for $\mathcal{D}_a^\ell$ depending on the type of signals. For pure turbulent fluctuations for which the PP98 applies well, a flat signal is expected for $\mathcal{D}_a^\ell$ and reported in our study. In the presence of discontinuities, a scaling in ℓ^{-1} is expected and indeed well observed over the whole available range of scales. However, no sign of a dissipation range in ℓ^2 is detected. These properties can be explained by the fact that the present study is limited to MHD scales. Therefore, a natural extension of this work would be to study sub-MHD scales using data that have the required high time resolution, such as those of the Magnetospheric Multiscale Mission (MMS), to see if a ℓ^2 dissipation can be detected. Unlike the viscous dissipation discussed in Section 3.2, in collisionless plasma, the dissipation involves complex physics at kinetic scales, and a variation different from ℓ^2 (but still with a positive slope) is likely. The method based on anomalous dissipation can offer an original diagnosis to characterize this dissipation.

Anomalous dissipation has many advantages over the exact law but its implementation on real data calls for some caution. This is because the dissipation formula is derived in the theoretical limit $\ell \to 0$, which is unattainable in real data. The smallest scale that can be used in spacecraft (or simulations) data is set by the available time (or grid) resolution. To what extent the anomalous dissipation estimated at this smallest *accessible* scale is representative of dissipation at the *actual* smallest scale of the system remains thus subject to caution.

The other limitation of the present study is that it is based on the MHD model. However, this limitation can (partly) be overcome by using the incompressible Hall-MHD model already derived by [10], which would allow probing finer scales and possibly highlight a correlation between the anomalous dissipation with temperature, or estimate the importance of the Hall effect in the energy cascade. A further potential improvement is to account for density fluctuations and see how they would impact the anomalous dissipation estimates in the solar wind. Such a model remains yet to be derived. However, even with such general models, there will always be a limitation imposed by the temporal resolution of the data that will prevent the strict application of $\ell \to 0$.

A final caveat that should be kept in mind when estimating both the anomalous dissipation and the cascade rate from the exact law, which is inherent to the use of single spacecraft data, is the validity of

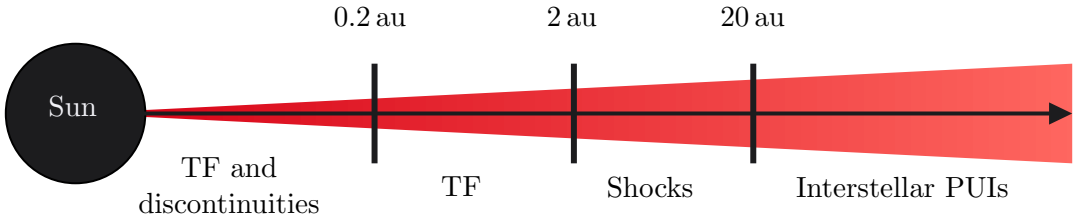

Figure 3.7: Overview of the observed predominant mechanisms that are responsible for the heliospheric turbulence's mean energy transfer rate. TF and PUIs stand for turbulent fluctuations and pickup ions, respectively. Note that this classification is made in terms of variations in the basic fields that enter the MHD equations. Therefore, this view is more rooted in the physics of turbulence than in the sources of turbulence of the solar wind.

the Taylor hypothesis and, *even when it is valid*, how its use would impact the measured quantities. In the case of anomalous dissipation, the use of the Taylor hypothesis implies that $\mathcal{D}_a$ only depends on a one-dimensional space variable. One can assume isotropy (as done in exact law studies) but this assumption is poorly verified in the solar wind.

Several heating mechanisms exist in the solar wind (see Figure 3.7) and their predominance seems to depend on the heliospheric radial distance as shown by the proton temperature measurements (cf., Figure 1.8). It is well known that around 1 au turbulent fluctuations are dominant, but closer to the Sun both discontinuities and strong turbulent fluctuations are important as now evidenced in PSP observations, while beyond 2 au we observe large-scale inhomogeneous structures such as interplanetary shocks, with relatively weak turbulent fluctuations. Beyond 20 au, the dominant heating mechanism is mainly pickup ions [21, 27]. Faced with such a variety of processes, it is interesting to have a tool that allows us to quantify the turbulent energy cascade rate at fluid scales, regardless of the dominant heating mechanism at work. The anomalous dissipation seems to be a good candidate for this purpose.

References

[1] N. Andrés *et al.*, "The evolution of compressible solar wind turbulence in the inner heliosphere: PSP, THEMIS, and MAVEN observations," vol. 919, no. 1, p. 19, Sep. 2021.

[2] R. A. Antonia, M. Ould-Rouis, F. Anselmet, and Y. Zhu, "Analogy between predictions of kolmogorov and yaglom," *Journal of Fluid Mechanics*, vol. 332, pp. 395–409, 1997.

[3] S. D. Bale *et al.*, "Highly structured slow solar wind emerging from an equatorial coronal hole," *Nature*, vol. 576, no. 7786, pp. 237–242, Dec. 2019.

[4] R. Bandyopadhyay *et al.*, "Enhanced energy transfer rate in solar wind turbulence observed near the sun from parker solar probe," vol. 246, no. 2, p. 48, Feb. 2020.

[5] J. W. Belcher and J. Davis Leverett, "Large-amplitude Alfvén waves in the interplanetary medium, 2," *J. Geophys. Res.*, vol. 76, no. 16, p. 3534, Jan. 1971.

[6] B. Dubrulle, "Beyond kolmogorov cascades," *Journal of Fluid Mechanics*, vol. 867, P1, 2019.

[7] J. Duchon and R. Robert, "Inertial energy dissipation for weak solutions of incompressible euler and navier-stokes equations," *Nonlinearity*, vol. 13, no. 1, pp. 249–255, Dec. 2000.

[8] S. Galtier, *Introduction to modern magnetohydrodynamics*. Cambridge University Press, 2016, p. 288.

[9] S. Galtier, "On the origin of the energy dissipation anomaly in (hall) magnetohydrodynamics," *Journal of Physics A: Mathematical and Theoretical*, vol. 51, no. 20, p. 205 501, Apr. 2018.

[10] S. Galtier, "On the origin of the energy dissipation anomaly in (hall) magnetohydrodynamics," *Journal of Physics A: Mathematical and Theoretical*, vol. 51, no. 20, p. 205 501, Apr. 2018.

[11] L. Z. Hadid, F. Sahraoui, and S. Galtier, "Energy cascade rate in compressible fast and slow solar wind turbulence," *The Astrophysical Journal*, vol. 838, no. 1, p. 9, Mar. 2017.

[12] T. S. Horbury, L. Matteini, and D. Stansby, "Short, large-amplitude speed enhancements in the near-Sunfast solar wind," *mnras*, vol. 478, no. 2, pp. 1980–1986, Aug. 2018.

[13] T. S. Horbury *et al.*, "Sharp Alfvénic Impulses in the Near-Sun Solar Wind," *apjs*, vol. 246, no. 2, 45, p. 45, Feb. 2020.

[14] L. Jacques, A. Coron, L. Demanet, A. Rivoldini, and P. Vandergheynst, *Yet another wavelet toolbox*, 2010.

[15] S. Jaffard, "Wavelet techniques for pointwise regularity," en, *Annales de la Faculté des sciences de Toulouse : Mathématiques*, vol. Ser. 6, 15, no. 1, pp. 3–33, 2006.

[16] S. Jaffard, P. Abry, and S. Roux, "Singularités oscillantes et coefficients d'ondelettes dominants," Jan. 2009.

[17] D. Kuzzay, O. Alexandrova, and L. Matteini, "Local approach to the study of energy transfers in incompressible magnetohydrodynamic turbulence," *Phys. Rev. E*, vol. 99, no. 5, p. 053 202, May 2019.

[18] B. Lashermes, S. G. Roux, P. Abry, and S. Jaffard, "Comprehensive multifractal analysis of turbulent velocity using the wavelet leaders," *European Physical Journal B*, vol. 61, no. 2, pp. 201–215, Jan. 2008.

[19] M. Neugebauer and B. E. Goldstein, "Double-proton beams and magnetic switchbacks in the solar wind," *AIP Conference Proceedings*, vol. 1539, no. 1, pp. 46–49, 2013.

[20] L. Onsager, "Statistical hydrodynamics," *Il Nuovo Cimento*, vol. 6, 2 1949.

[21] Z. B. Pine *et al.*, "Solar Wind Turbulence from 1 to 45 au. II. Analysis of Inertial-range Fluctuations Using Voyager and ACE Observations," *Astrophys. J.*, vol. 900, no. 2, p. 92, 2020.

[22] H. Politano and A. Pouquet, "Von kármán–howarth equation for magnetohydrodynamics and its consequences on third-order longitudinal structure and correlation functions," *Phys. Rev. E*, vol. 57, R21–R24, 1 Jan. 1998.

[23] L. Sorriso-Valvo, F. Carbone, S. Perri, A. Greco, R. Marino, and R. Bruno, "On the statistical properties of turbulent energy transfer rate in the inner heliosphere," *Solar Physics*, vol. 293, no. 1, p. 10, Jan. 2018.

[24] L. Sorriso-Valvo *et al.*, "Sign singularity of the local energy transfer in space plasma turbulence," *Frontiers in Physics*, vol. 7, p. 108, 2019.

[25] L. Sorriso-Valvo *et al.*, "Turbulence-driven ion beams in the magnetospheric kelvin-helmholtz instability," *Phys. Rev. Lett.*, vol. 122, p. 035 102, 3 Jan. 2019.

[26] J. Squire, B. D. G. Chandran, and R. Meyrand, "In-situ switchback formation in the expanding solar wind," *The Astrophysical Journal*, vol. 891, no. 1, p. L2, Feb. 2020.

[27] G. P. Zank, L. Adhikari, L.-L. Zhao, P. Mostafavi, E. J. Zirnstein, and D. J. McComas, "The pickup ion-mediated solar wind," *The Astrophysical Journal*, vol. 869, no. 1, p. 23, Dec. 2018.

[28] G. P. Zank, M. Nakanotani, L. .-. Zhao, L. Adhikari, and J. Kasper, "The Origin of Switchbacks in the Solar Corona: Linear Theory," *Astrophys. J.*, vol. 903, no. 1, p. 1, 2020.

Chapter 4

Intermittency in electron MHD

I must caution the reader that this chapter represents preliminary work and should be interpreted as such.

4.1 Introduction

Until now, our exploration of plasma turbulence has primarily focused on the scales governed by MHD. However, going beyond where the dynamics becomes more intricate demands further refinement. This occurs when we venture into scales smaller than the ion inertial length $d_i \equiv c/\omega_{\mathrm{pi}}$, where ω_{pi} represents the ion plasma pulsation. At such scales, the discrepancy in mass between ions and electrons becomes crucial (remember the baby and the elephant), and it is necessary to consider the behaviors of ions and electrons as distinct entities. To capture this distinction, we adopt an approach that applies to scales where $d_i \ll \ell \ll d_e$, with d_e representing the electron inertial length. In this range, the magnetic field is considered frozen into the electron flow $\boldsymbol{u}_e$, while the ions remain motionless ($\boldsymbol{u}_i = \mathbf{0}$). This approximation, known as electron magnetohydrodynamics (EMHD), allows us to delve into the dynamics of plasma at sub-proton scales with an accurate description. By incorporating anisotropy ($k_\parallel \ll k_\perp$) and considering small perturbations of the magnetic field, we arrive at the reduced EMHD (REMHD) formulation, which enables us to probe the characteristics of turbulent plasmas, like the solar wind, at such scales.

The motivation behind understanding the behavior of plasma turbulence at sub-proton scales in the solar wind remains an intriguing puzzle. Observations at these scales show a distribution of magnetic spectrum power law indices ranging from approximately -7/3 to -3, with a peak near -8/3 [55], which is the most commonly reported value [2, 3, 50, 54] - as depicted in Figure 4.1. This raises the fundamental question: what underlying physics accurately describes these observations? Several theoretical models have emerged as potential explanations for the observed magnetic spectra, namely weak wave turbulence, and strong wave turbulence with or without the presence of electronic Landau damping [68]. Each model presents a distinct perspective on the nature of plasma dynamics at sub-proton scales but is hardly differentiable through the lens of the energy spectrum power law. Thus, the question is: how to accurately distinguish them in the observational data?

In this chapter, we aim to go beyond the conventional diagnostic of the magnetic spectrum power law and propose a complementary approach by measuring their intermittency. This study is divided into four distinct sections. We begin by introducing the REMHD model, focusing on two regimes of particular interest: weak wave turbulence and strong wave turbulence in the absence of Landau damping[1]. Then we will present the numerical setup used to perform the experiments. Finally, after having analyzed the

[1]The accurate description of Landau damping goes beyond the scope of a fluid model, necessitating a kinetic model. However, according to the following results and DNS conducted by Zhou *et al.* [68], the nature of intermittency in strong wave turbulence appears to be independent of the presence or absence of Landau damping.

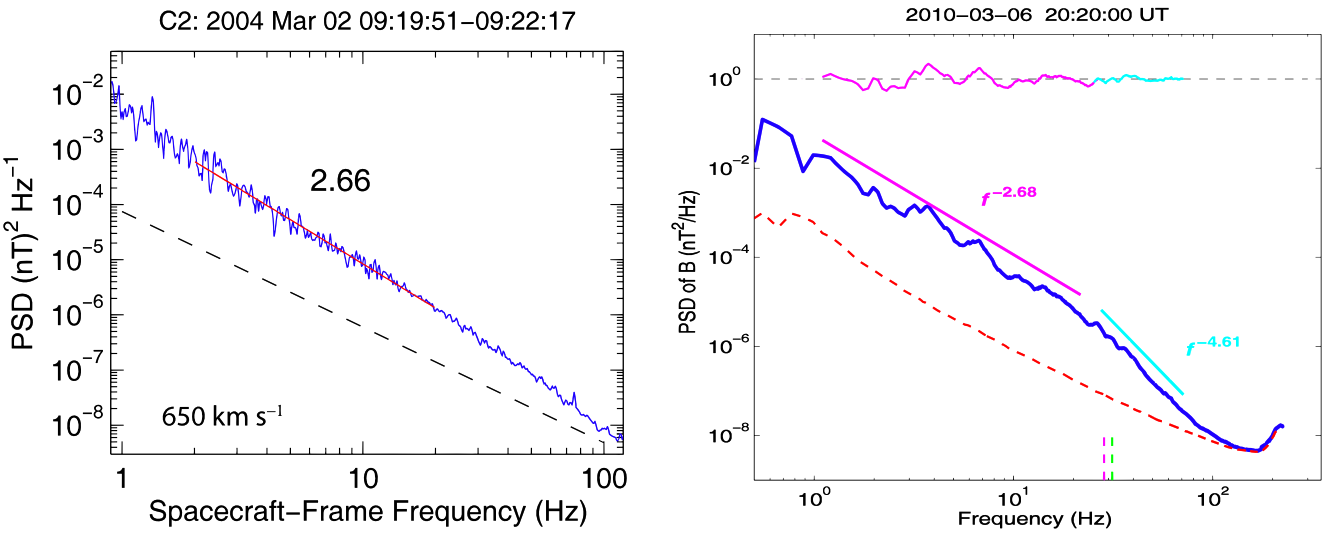

Figure 4.1: Examples of power spectral densities of magnetic field fluctuations in the solar wind at 1 au using data from the *Cluster* STAFF search-coil magnetometer. Left: plot from Podesta [50]. Right: plot from Sahraoui *et al.* [55].

numerical results, we will discuss their relevance and how one can transfer them to solar wind observations to better understand the underlying physics at play.

4.2 Theoretical framework

4.2.1 Derivation of the model

When examining sub-proton scales, one can assume that ions remain immobile on the timescales of interest and only electron dynamics is relevant. Consequently, we should adopt a bi-fluid approach, assuming massless electrons. Within this framework, Ohm's law, derived from Equation (1.30), takes the form:

$$\boldsymbol{E} = -\frac{1}{n_e e}\boldsymbol{\nabla} P_e - \boldsymbol{u}_e \times \boldsymbol{B}. \tag{4.1}$$

Here, $\boldsymbol{E}$ denotes the electric field, n_e represents the electronic density, e symbolizes the elementary charge, P_e designates the scalar pressure of the electrons (justified for isothermal electrons [58]), and $\boldsymbol{B}$ stands for the magnetic field. The electron velocity $\boldsymbol{u}_e$ can be expressed directly in terms of the magnetic field because in a plasma ($n_i = n_e$) with motionless protons and moving electrons, the current density $\boldsymbol{J}$ is given by $\boldsymbol{J} = en_e(\boldsymbol{u}_i - \boldsymbol{u}_e) \simeq -en_e\boldsymbol{u}_e$, and, at the same time, $\boldsymbol{J}$ is known through Maxwell-Ampère's law (1.15d). By expressing the magnetic field in velocity units $\boldsymbol{b} = \boldsymbol{B}/\sqrt{\mu_0\rho}$ and utilizing the Maxwell-Faraday

law (1.15c), we arrive at the self-consistent evolution equation for the magnetic field, namely the EMHD equation:

$$\boxed{\frac{\partial \boldsymbol{b}}{\partial t} = -d_i \boldsymbol{\nabla} \times [(\boldsymbol{\nabla} \times \ \boldsymbol{b}) \times \boldsymbol{b}]}. \tag{4.2}$$

This concept originated from the work of Kingsep *et al.* [35], but its roots can be traced back to the 1960s with early studies on semiconductor plasmas [14, 46]. In contrast to the MHD equations, the EMHD exhibits a dependence on the ion inertial scale, introducing a distinct length scale and a corresponding validity range. To investigate this further, we can consider normalizing the equation by characteristic quantities. It is natural to normalize length by d_i and magnetic field by its mean value b_0 in the context of studying turbulent fluctuations. Time is conveniently normalized by the ion cyclotron frequency $\Omega_i \equiv b_0/d_i$. By scaling time with Ω_i, spatial gradients with d_i, and magnetic field with b_0^{-1}, we adimensionalize the EMHD equation but also emphasize its validity range. Specifically, it is applicable when dealing with temporal and spatial fluctuations on timescales $t \ll \Omega_i^{-1}$ and spatial scales $\ell \ll d_i$, which precisely correspond to the scales of interest in our study. Additionally, this equation conserves two important quantities: the magnetic energy $E = 1/2 \int_{\mathbb{R}^3} b^2 \, \mathrm{d}\boldsymbol{x}$ that cascades directly (from large to small scales), and the magnetic helicity which is a measure of the linkage, twist, and writhe of the magnetic field $H = \int_{\mathbb{R}^3} \boldsymbol{a} \cdot \boldsymbol{b} \, \mathrm{d}\boldsymbol{x}$ such as $\boldsymbol{a} \equiv \boldsymbol{\nabla} \times \boldsymbol{b}$ represents the potential vector, which cascades inversely (from small to large scales) [10, 25, 58]

Now, let us consider a uniform and stationary magnetic field $\boldsymbol{b_0} = b_0 \boldsymbol{e}_\parallel$. By introducing small displacements and assuming sinusoidal perturbations, $\boldsymbol{b} = \boldsymbol{b_0} + \boldsymbol{b_1} \mathrm{e}^{i(\boldsymbol{k}\cdot\boldsymbol{x} - \omega t)}$, we obtain helical waves known as *whistler waves*. Their dispersion relation is given by:

$$\boxed{\omega = \pm d_i b_0 k_\parallel k}, \tag{4.3}$$

where the $\pm$ notation differentiates between the co-propagating and counter-propagating waves relative to the direction of the magnetic field. When $k_\parallel \ll k_\perp$, these dispersive waves become oblique [53] and are called hereafter *whistler Alfvén waves* (WAW). They experience changes in their phase speed based on the angle between the magnetic field and the direction of propagation (cf., Figure 4.2). As the waves deviate further from alignment with the magnetic field direction, their velocity decreases. Eventually, when they reach a completely perpendicular direction, they vanish.

Now, let us consider finite perturbations and establish the following ordering that allows linear and

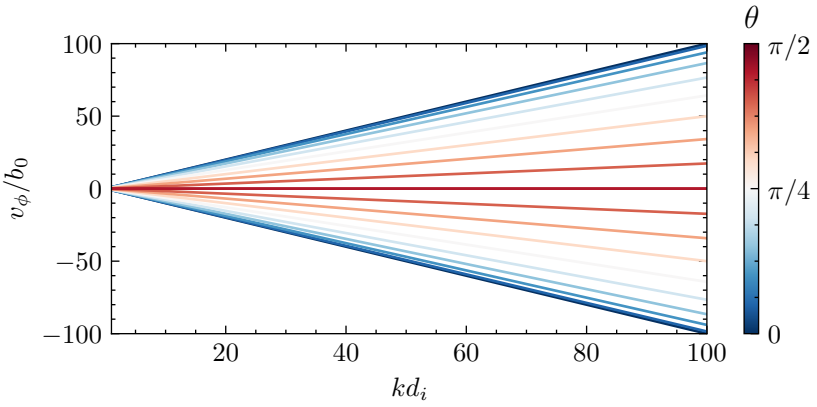

Figure 4.2: Phase velocity $v_\phi = \omega/k$ normalized to the Alfvén speed b_0 as a function of the normalized wavenumber kd_i.

nonlinear physics to coexist while keeping perturbations small [29, 58–60]:

$$\frac{b_1}{b_0} \sim \frac{k_\parallel}{k} \ll 1, \tag{4.4}$$

under which the magnetic field can be represented as $\boldsymbol{b_1} = \boldsymbol{e}_\parallel \times \boldsymbol{\nabla}_\perp \psi + b_z \boldsymbol{e}_\parallel$, where ψ is the stream function and b_z represents the perturbation along the guide field $\boldsymbol{b_0}$. From Equation (4.2), the evolution equations for ψ and b_z take the form [10, 27]:

$$\frac{\partial \psi}{\partial t} = d_i b_0 \nabla_\parallel b_z, \tag{4.5a}$$

$$\frac{\partial b_z}{\partial t} = -d_i b_0 \nabla_\parallel \nabla_\perp^2 \psi. \tag{4.5b}$$

Here, the parallel gradient operator $\nabla_\parallel \equiv \partial_z + b_0^{-1} \{\psi, \cdot\}$ comprises both a linear component, representing gradients along the guide field $\boldsymbol{b_0}$, and a nonlinear component, reflecting gradients along the local field $\boldsymbol{b} = \boldsymbol{b_0} + \boldsymbol{b_1}$. The notation $\{g, h\} \equiv \partial_x g \partial_y h - \partial_y g \partial_x h$ is the Poisson bracket of two scalar functions g and h. It is quite fascinating to observe that the chosen ordering restricts the nonlinear dynamics to occur solely within the planes perpendicular to the magnetic field $\boldsymbol{b_0}$. As a result, eddies and swirling motions are exclusively generated within these planes, while linear waves transmit information across them, leading to three-dimensional dynamics, as illustrated in Figure 4.3. The equations known as REMHD describe incompressible whistler Alfvén waves which can be generated by kinetic instabilities in the solar wind [28]. Interestingly, despite their incompressible nature, these waves share the same set of equations and then dispersion relation as the compressible version of REMHD called ERMHD (yes, the term “reduced” has simply been shifted one letter forward to make this distinction) [11, 58]. The ERMHD provides a framework

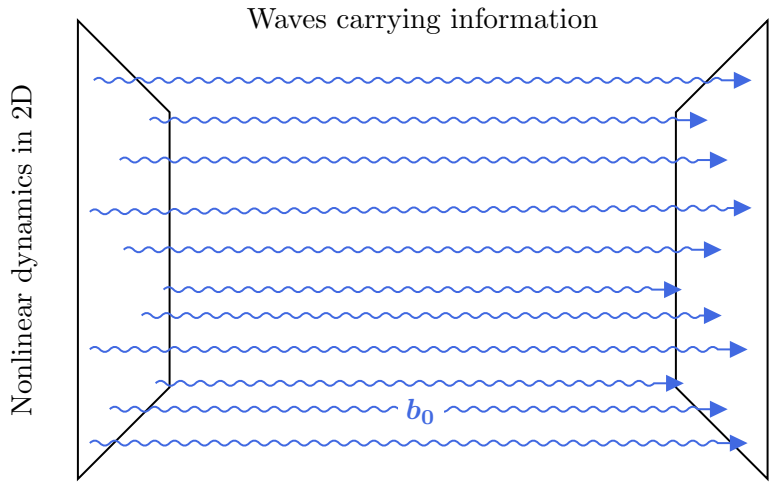

Figure 4.3: Three-dimensional reduced model supporting both nonlinearity and waves. Adapted from Schekochihin [59].

for understanding the dynamics of *kinetic Alfvén waves* (KAWs), which represent a natural extension of the Alfvén wave cascade. These KAWs can undergo damping due to the ionic Landau effect, resulting in plasma heating, while concurrently transferring energy to the KAW cascade [4, 6, 15, 39, 40, 45, 57, 58]. Although these waves may appear physically distinct, their dispersion relations are mathematically equivalent [27]. Hence, the forthcoming analysis and discussion apply to both whistler and kinetic Alfvén waves, as their turbulent characteristics are identical.

By utilizing REMHD (or ERMHD), we can classify the turbulent behavior into three regimes based on scale separation. This separation allows us to distinguish between the linear timescale, τ_{L}, associated with the motion of WAW/KAW, and the nonlinear timescale, τ_{NL}, arising from the nonlinear terms in the equations. These timescales are estimated through phenomenology and serve as a wet-finger approximation. Specifically, $\tau_{\mathrm{L}} \sim 1/(d_i b_0 k_\perp k_\parallel)$, while $\tau_{\mathrm{NL}} \sim 1/(d_i k_\perp^2 b)$. To compare the two timescales, we introduce the parameter χ, defined as $\chi \equiv \tau_{\mathrm{L}}/\tau_{\mathrm{NL}}$. The relation $b \sim \sqrt{2k_\perp k_\parallel E(k_\perp, k_\parallel)}$, gives

$$\chi \sim \sqrt{2E(k_\perp, k_\parallel) k_\perp^3 k_\parallel^{-1} b_0^{-2}}. \tag{4.6}$$

Based on this parameter, we can distinguish three regimes: when χ is negligible, of the order, or greater than unity. Those are referred to as the weak, strong, and supercritical regimes, respectively.

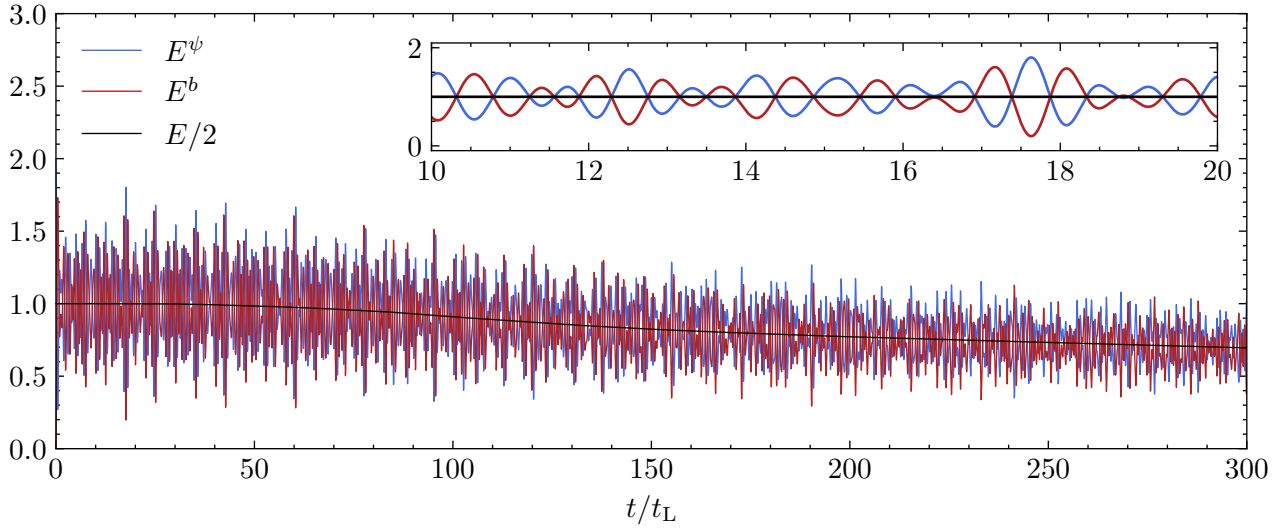

Figure 4.4: Temporal evolution of energies associated to Equations (4.5) as observed through direct numerical simulation of decaying turbulence. The inset provides a closer view of a shorter time interval, emphasizing the contrasting dynamics between the linear and nonlinear timescales.

4.2.2 Weak wave turbulence

In the weak regime, characterized by $\chi \ll 1$ for all wavenumbers, the nonlinearities are... weak. As a result, the distortions of wave packets occur over long timescales compared to the linear wave period, leading to a multi-timescale dynamics, as illustrated in Figure 4.4. The separation between linear and nonlinear dynamics allows for a rigorous analytical treatment incorporating a well-defined closure and accurate predictions under appropriate assumptions [7, 8, 51, 61]. This analytical approach reveals a magnetic energy spectrum $E(k_\perp, k_\parallel) \propto k_\perp^{-5/2} k_\parallel^{-1/2}$ [26]. A phenomenological approach can also yield similar results by considering the transfer time $\tau_\mathrm{tr} \sim \tau_\mathrm{NL}^2/\tau_\mathrm{L}$ and the magnetic energy flux $\varepsilon \sim b^2/\tau_\mathrm{tr}$. Calculations show that $E(k_\perp, k_\parallel) \sim (\varepsilon b_0/d_i)^{1/2}\, k_\perp^{-5/2} k_\parallel^{-1/2}$, consistent with the exact prediction for the weak regime. However, it is important to acknowledge that the weak regime cannot be sustained *ad vitam æternam*. Remarkably, even as the waves' $k_\parallel$ and, consequently, their frequency remain constant, the parameter $\chi \sim \left(d_i b_0^3/\varepsilon\right)^{-1/4} k_\perp^{1/4} k_\parallel^{-3/4}$ increases at higher values of k. Eventually, at a critical scale k_c, the condition $\chi \ll 1$ is violated, resulting in $\chi \sim 1$, prompting us to consider the implications of the strong regime.

4.2.3 Strong wave turbulence

The condition of $\chi \sim 1$ corresponds to the strong regime, also known as the *critical balance* assumption which conjectures that the linear and nonlinear effects operate on similar timescales [29, 30]. This regime

lacks a rigorous analytical description, then it has been investigated through numerical simulations to verify this phenomenology [9, 10, 18–20, 34]. The idea behind this can be pitched as follow. First, we assume that all electromagnetic perturbations exhibit strong anisotropy, meaning that their characteristic scales along the mean field are significantly larger than those across it, as expressed by the wavenumbers: $k_\parallel \ll k_\perp$. Second, we consider that the interactions between wave packets are strong, and as the turbulence reaches smaller scales, it naturally organizes itself in a manner where the linear timescale and the timescale for perpendicular nonlinear interactions become comparable to each other [29, 58]. These two key assumptions lay the foundation for our understanding of the strong regime. Through a phenomenological approach, similar to that used in the weak regime, we can make predictions by assuming $\tau_\mathrm{L} \sim \tau_\mathrm{NL}$. In this scenario, the magnetic energy spectrum is expected to follow $E(k_\perp, k_\parallel) \sim (\varepsilon/d_i)^{2/3}\, k_\perp^{-7/3} k_\parallel^{-1}$ [10, 58]. Interestingly, the power laws in this regime closely resemble those observed in weak wave turbulence, making it challenging to distinguish between the two based solely on this diagnostic.

4.2.4 Supercritical regime

When $\chi \gg 1$, the dynamics of the system undergoes a transition into an unsustainable two-dimensional regime. In this regime, the behavior of waves in the perpendicular planes becomes less significant. Surprisingly, an important quantity called anastrophy $A = \int_{\mathbb{R}^3} \boldsymbol{a} \cdot \boldsymbol{b}\, \mathrm{d}\boldsymbol{x}$ becomes an invariant [9], allowing for the emergence of an inverse cascade even when the magnetic helicity is zero. However, it is crucial to understand that this regime is not stable and cannot be sustained indefinitely – unless a forcing is applied to sustain it. The unsustainability of this regime can be attributed to two key factors. Firstly, in the REMHD, information propagates along the direction of the magnetic field $\boldsymbol{b_0}$ at the phase speed $v_\phi = d_i b_0 k_\parallel$. The structures within the system cannot remain coherent if their length exceeds a certain value, approximately given by $l_\parallel \sim v_\phi \tau_\mathrm{NL}$. Any structures longer than this characteristic length will inevitably break apart and lose their coherence. This limitation arises from the principle of causality, which governs the propagation of information in the system [47, 59]. Furthermore, as the value of χ increases, the planes perpendicular to $\boldsymbol{b}_0$ tend to lose their correlation over increasingly smaller distances, leading to the generation of higher parallel wavenumbers that decrease χ. In simpler terms, as χ increases, the system generates smaller scales that disrupt the overall coherence of the perpendicular planes. Consequently, the supercritical regime becomes unstable, and the system naturally relaxes towards the critical balance regime. Figure 4.5 illustrates the evolution of these three different regimes.

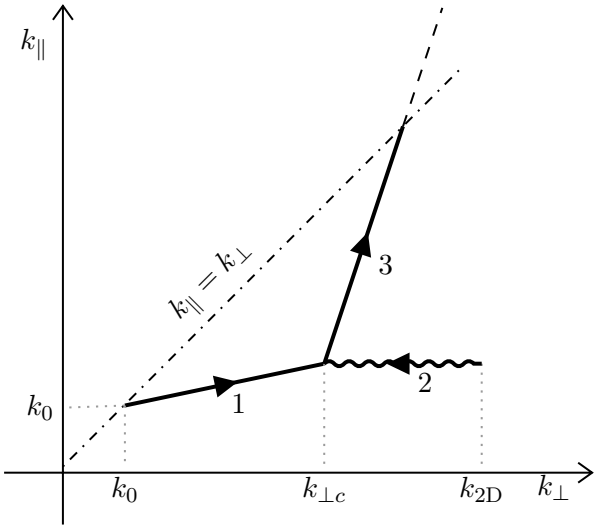

1: Weak turbulence $\left(\sim k_\perp^{-5/2} k_\parallel^{-1/2}\right)$

2: Supercritical

3: Critical balance $\left(\sim k_\perp^{-7/3} k_\parallel^{-1}\right)$

Figure 4.5: A sketch of cascade path and spectra for the EMHD turbulence: both the case of injection at $k_\perp = k_\parallel = k_0$ and that at $k_\parallel \ll k_\perp = k_{2\mathrm{D}}$ are shown. Adapted from Nazarenko and Schekochihin [47].

4.2.5 Intermittency

The challenge of distinguishing between weak and strong wave turbulences lies in their closely related spectra. However, we need not confine ourselves to this diagnostic alone. As introduced in the previous chapters, we can compute the increments of the magnetic field $\delta b = b(\boldsymbol{x} + \boldsymbol{r}) - b(\boldsymbol{x})$ and observe their evolution when they are raised to an arbitrary power $p \geq 1$. Based on this diagnostic, we can discern whether the energy, as it cascades towards smaller scales, becomes increasingly confined to sparse regions of space, giving rise to intermittent structures that emerge prominently from the fluctuations background. Consequently, we ascertain whether the statistics of magnetic field fluctuations exhibit a scale-dependent nature, indicative of the aforementioned energy concentration phenomena, or if a scale invariance prevails, with no particular region exhibiting a greater energy concentration over others [24, 42].

We propose that these two regimes display contrasting patterns of intermittency. In the case of weak wave turbulence, we anticipate monofractal intermittency, and by definition, the system exhibits a self-similar scaling behavior. This expectation is rooted in the predominance of waves in the dynamics, with no coherent structures formed[2]. Conversely, strong wave turbulence is expected to display intermittency and multifractal scaling, attributed to the emergence of swirling eddies, current sheets, and other coherent structures. Our objective is to elucidate these distinctions through direct numerical simulations (DNS) of REMHD.

[2]It is worth noting that our expectations may be overly simplistic, and it is not immediately apparent that weak regimes will be devoid of intermittency. In fact, direct numerical simulations of other systems such as MHD [43] or gravity waves [62] have demonstrated multifractal intermittency in weak regimes.

4.3 Direct numerical simulations

4.3.1 Numerical setup

To perform DNS, we employ a modified version of the pseudospectral code called `AsteriX` [44, 45], which is derived from the well-known code `TURBO` [66]. The simulations are conducted in a triple periodic cubic box of size $L = 2\pi$ and utilize $N_\perp^2 \times N_z$ Fourier modes. For time stepping, we make use of a third-order modified Williamson algorithm [67], which is a four-step, low-storage Runge-Kutta method. To ensure numerical stability and attain a turbulent stationary state, we introduce additional dissipative and forcing terms in the equations. The system we solve is represented by the following set of equations:

$$\frac{\partial \psi}{\partial t} = d_i b_0 \nabla_\parallel b_z + \eta \nabla^6 \psi + f^\psi, \tag{4.7a}$$

$$\frac{\partial b_z}{\partial t} = -d_i b_0 \nabla_\parallel \nabla_\perp^2 \psi + \eta \nabla^6 b_z + f^{b_z}. \tag{4.7b}$$

The dissipative terms take the form of collisional viscous damping, where the dissipative coefficient η is carefully chosen based on the numerical resolution. Its purpose is to facilitate a rapid fall-off of the energy spectrum before reaching the resolution cutoff. It is important to note that the hyper Laplacian operator is employed purely for numerical reasons and does not represent any physical phenomenon. It is used to achieve an extended inertial range and effectively dissipate energy without causing bottlenecks or reflections. To generate turbulence and regulate energy injection ε, we induce controlled fluctuations at large scales using forcing terms (f^ψ and f^{b_z}). These terms are selectively applied within the range $1.5 < k_\perp d_i < 2.5$ and adopt a negative damping form proportional to the large-scale modes of ψ and b_z. This technique allows us to precisely control the energy injection level while ensuring sufficiently chaotic motions to drive turbulent behavior. To optimize computational efficiency, we conduct simulations at various resolutions, employing a recursive refinement technique [44], with the highest resolution reaching up to $N_\perp = 1024$ and $N_z = 128$. Throughout all simulations, the values of (d_i, b_0) are consistently set as $(1, 1)$, serving as reference units alongside the size of the computational domain $L = 2\pi$. To mitigate aliasing effects in the nonlinear terms, a phase shift method is employed, enabling partial dealiasing [49]. Consequently, the total number of spectral modes is half the number of mesh points used. To investigate the two regimes of interest, we conducted two simulations of balanced turbulence, with the only distinction being the energy injection rate ε. Specifically, the latter was 500 times higher for the strong regime ($\varepsilon = 0.5$) compared to the weak one ($\varepsilon = 10^{-3}$). The top and middle panels of Figure 4.6 illustrate a three-dimensional depiction of the

electric current along the mean field and snapshots of the magnetic field modulus in a plane perpendicular to $\boldsymbol{b_0}$ for each regime. These visual representations reveal distinct dynamics between the two regimes.

4.3.2 Spectra

Before diving into the measurement of intermittency, it is crucial to verify whether we have indeed reached the regimes we are investigating. To do so, we can examine the values of the parameter χ. As depicted in Figure 4.7, both the weak and strong regimes adhere to this criterion. The weak regime exhibits a $\chi \ll 1$ across all wavenumbers, by the principles underlying the associated theory. On the other hand, the strong regime shows a noteworthy behavior, with the first parallel modes satisfying the condition $\chi \sim 1$. Then, as we ascend to higher parallel modes, χ diminishes, thus deviating from the critical balance hypothesis. But it is the low parallel modes that bear the greatest energy and hence exert a dominant influence on the turbulent dynamics (note that the $k_\parallel = 0$ mode corresponds to an average over $k_\parallel$ and is not considered in this analysis).

In Figure 4.8, we present the one-dimensional axisymmetric transverse magnetic spectra for both regimes. These spectra, obtained by integrating over a cylinder aligned with $\boldsymbol{b_0}$, exhibit power law behavior as predicted by theoretical expectations. The weak regime follows a power law index close to -5/2, while the strong regime follows a power law index of -7/3. This further validates our observation of these two distinct regimes.

The parallel spectra hold limited significance due to two primary factors. Firstly, the scarcity of Fourier modes in the parallel direction poses a challenge in establishing a distinct inertial range with a power law behavior in that specific dimension. Secondly, in both regimes, the parallel cascade exhibits a minimal energy transfer, necessitating an extensive amount of time for its occurrence (given that the parallel power law index is less than one, it would theoretically take an infinite amount of time for the parallel cascade to reach $k_\parallel \to \infty$). Due to these considerations, we set aside the parallel dynamics and focus our attention on the perpendicular counterpart. Fortunately, this does not impose significant limitations on our objective of reporting the observations of the solar wind at 1 au, since the in situ data collected by the roaming spacecraft predominantly captures the perpendicular dynamics. In comparison, the measurement of the parallel component remains less well-documented.

Additional confirmation of our findings involves investigating the wavenumber-frequency spectrum, a task that requires the simultaneous application of space and time Fourier transforms. In the case of weak wave turbulence, a distinct signal along the line defined by the dispersion relation should become

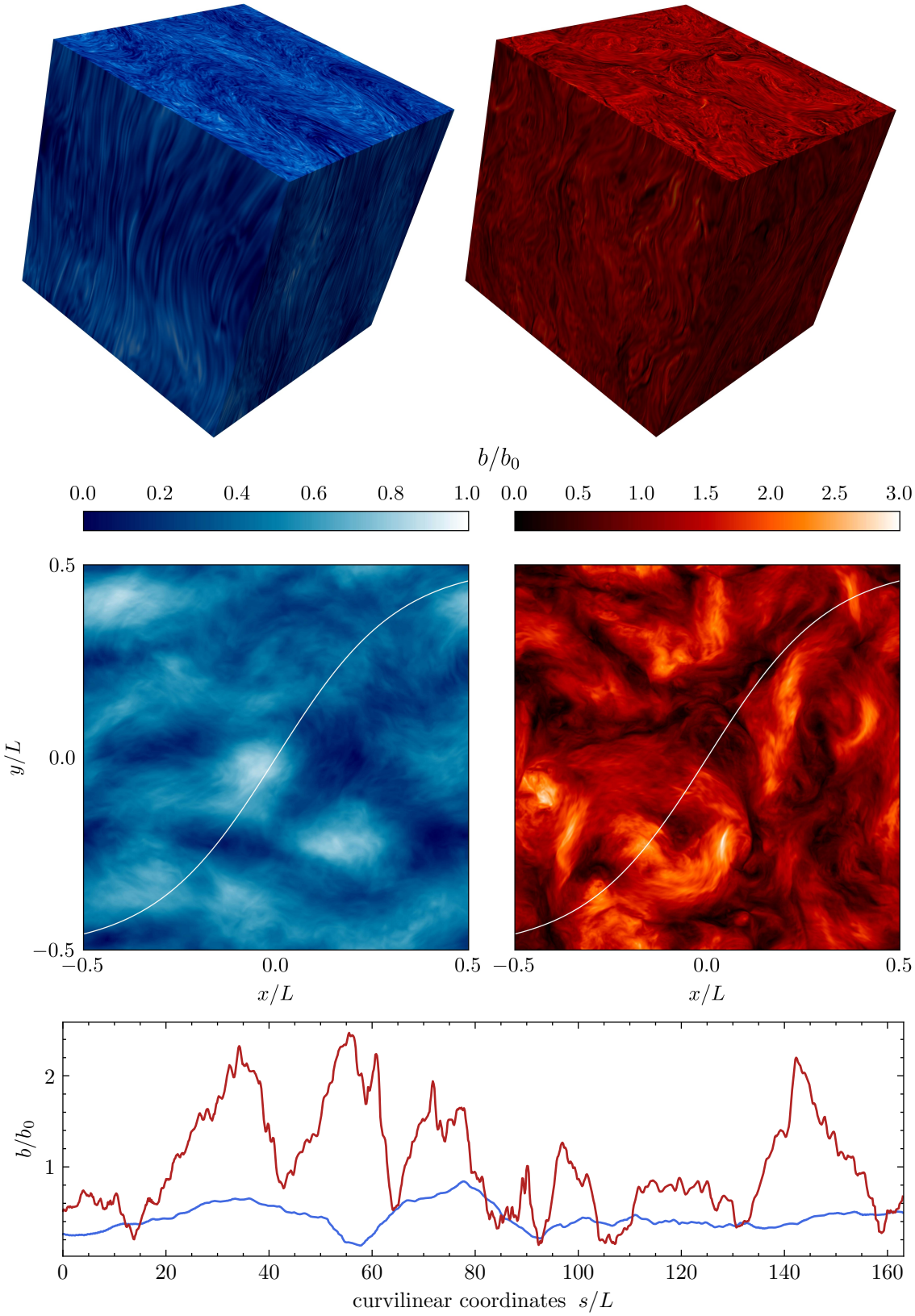

Figure 4.6: Top: Three-dimensional visualization of the electric current along the mean field, for weak (blue) and strong (red) wave turbulences. Middle: Snapshots of the magnetic field modulus, normalized by the mean field strength b_0, in a section perpendicular to $\boldsymbol{b_0}$ for weak (blue) and strong (red) wave turbulences. weak wave turbulence is characterized by the lack of coherent structures and lower magnetic fluctuations compared to strong wave turbulence. The white line represents the trajectory of a virtual spacecraft. Bottom: Detected magnetic field recorded by a virtual spacecraft following a specific path (white line in the upper panels) in both weak (blue line) and strong (red line) turbulence simulations.

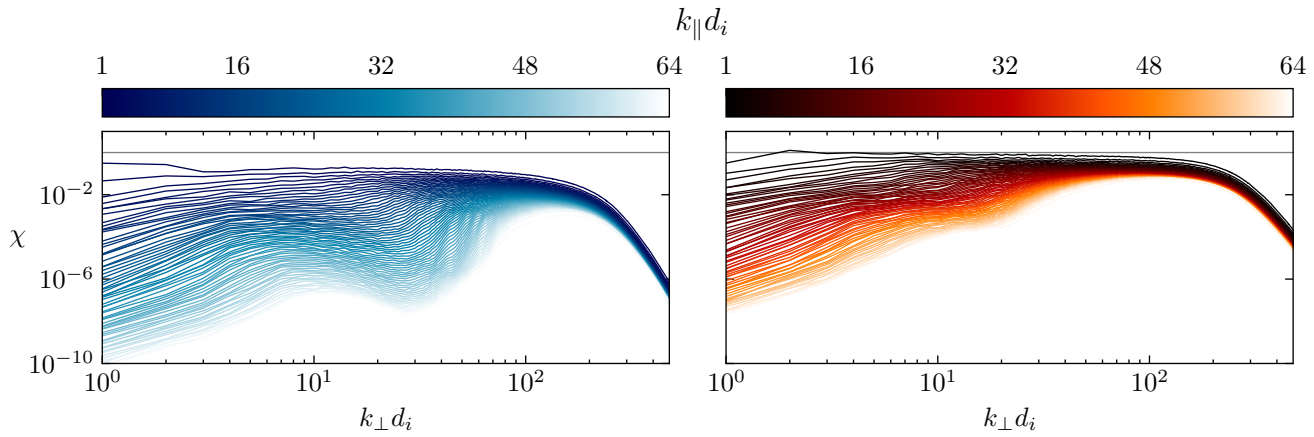

Figure 4.7: χ parameter for the weak (blue) and strong (red) turbulence regimes. The gray lines represent the value $\chi = 1$.

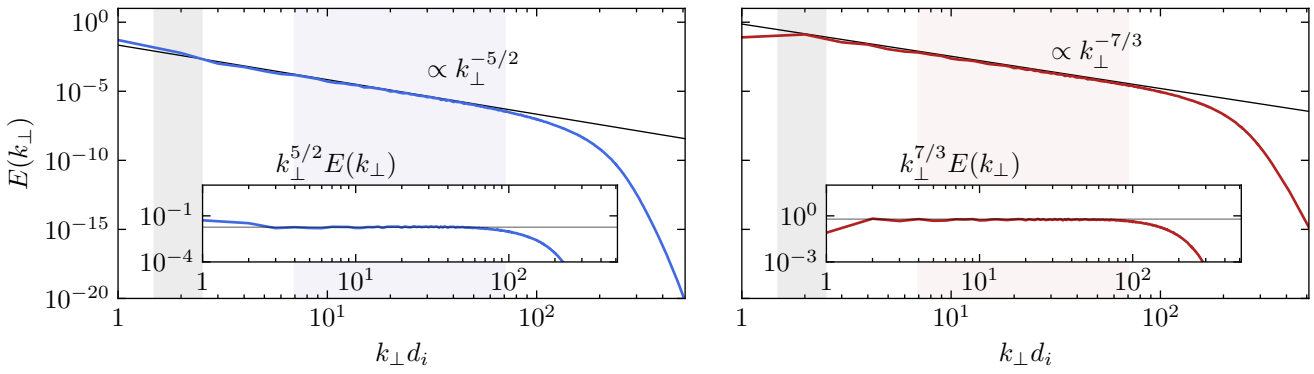

Figure 4.8: Transverse energy spectra of the weak (blue line) and strong (red line) regimes are presented in this figure. The grey column at low $k_\perp d_i$ represents the forcing scales, while the blue and red columns indicate the regions of the inertial range where intermittency will be evaluated for the two regimes (excluding the histograms). The insets provide compensated spectra for closer examination.

evident. Conversely, in the case of strong wave turbulence, where interactions lack preferential alignment, we would not anticipate the emergence of discernible patterns in this plot. To achieve this, we monitor the evolution of the diagonal $k_x = k_y$ within planes perpendicular to $\boldsymbol{b_0}$ over several linear wave periods. Through this approach, we reconstruct the wavenumber-frequency spectrum for both regimes, enabling us to ascertain whether the weak wave turbulence exhibits wave interactions, as expected. Figure 4.9 presents a visual representation of the space-time Fourier spectra for both regimes, considering values of $k_z = 4$, and $kz = \{1, 2, 4\}$ for the inset. A striking observation is that in the weak regime, wave interactions become apparent for $k_\perp d_i \gtrsim 20$ and follow the theoretical dispersion relation. One can identify three limitations to the observation of resonance at larger scales: (i) As we move towards larger scales, the influence of random forcing becomes increasingly prominent, leading to a randomization of the interactions. Consequently, a significant amount of time is required for resonant interactions to dominate, primarily manifesting at higher wavenumbers. (ii) For low values of ω, the diagnostic requires tracking the signal for extended periods. To resolve $\omega \simeq 0$, one would ultimately need to record data from the beginning of the DNS. However, in our case, we chose to save computational time by employing a recursive refinement technique, making such extended recordings unfeasible. (iii) The last limitation arises from finite box effects. In the weak regime, the nonlinear energy transfer occurs through the resonant interaction of three waves with different wavenumbers, primarily in close proximity (i.e., triadic interaction). As the wavenumber decreases, the number of possible configurations for wave resonance via triadic interactions diminishes, imposing a limiting factor. In stark contrast, the strong regime displays a distinct absence of discernible patterns. Instead, a broad range of frequencies becomes excited throughout the plasma scales, appearing to be confined within a domain where dynamically connected modes adhere to a power law resembling $k_\perp^{4/3}$. This characteristic aligns with the critical balanced assumption and signifies the existence of structures that are not primarily governed by resonances dictated by the dispersion relation. Furthermore, the presence of two-dimensional coherent structures becomes apparent through the distinct signal observed at low frequencies. These structures are likely to be stimulated by the perpendicular forcing at a large scale, coupled with the inherent propensity of the reduced model to generate nonlinear structures within the perpendicular planes. Lastly, at scales smaller than $k_\perp d_i \simeq 50$, the effects of dissipation become prominent in both regimes, and the noisy background overshadows the damped signal.

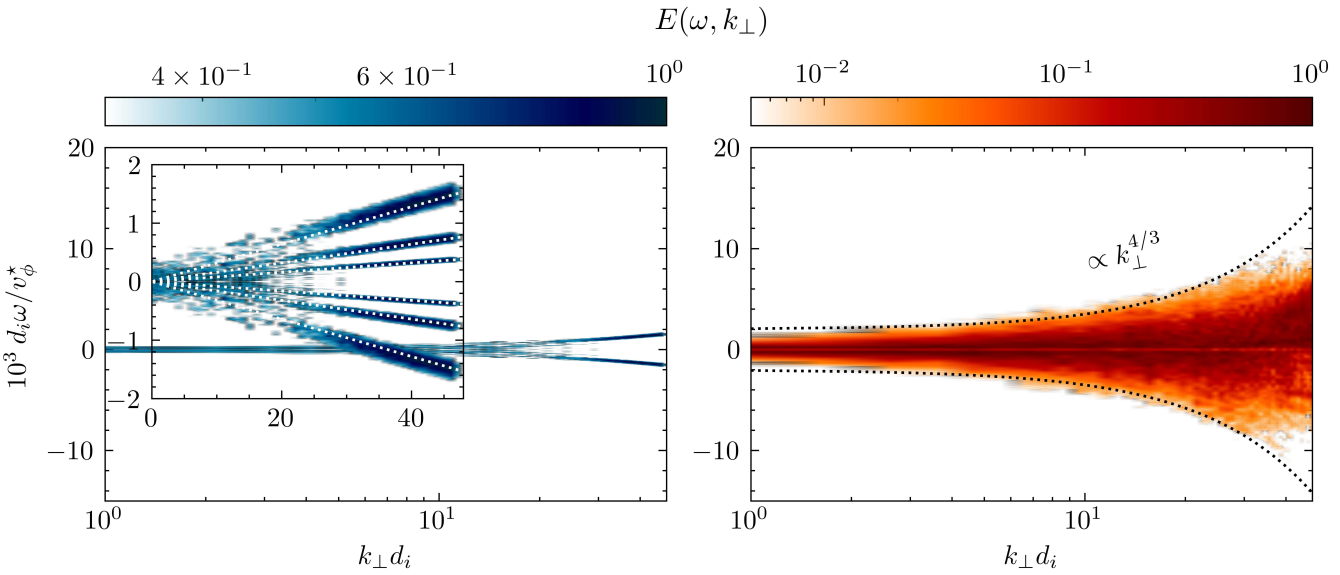

Figure 4.9: Space-time Fourier spectra of the magnetic energy in the weak (blue) and the strong regimes (red) in plane $k_z = 4$. The pulsation ω is normalized by $v_\phi^\star/d_i$, where $v_\phi^\star$ represents the phase speed defined as $v_\phi^\star \equiv d_i b_0 k_\perp^\star$, with $k_\perp^\star = \sqrt{2}$ being the lowest value considered for this diagnostic. The left panel includes an inset showing the superposition of the space-time Fourier spectra of the magnetic energy for planes $k_z = \{1, 2, 4\}$ in linear scales. The white dotted lines correspond to the theoretical dispersion relations of the WAW/KAW. The right panel exhibits a black dotted line illustrating the power law $k_\perp^{4/3}$, which serves as evidence for the presence of the critical balanced regime.

4.3.3 Structure functions

Intermittency is commonly quantified by examining the deviation from Gaussianity in the probability density function (PDF). Thus, a primary diagnostic involves computing the PDF of magnetic field increments $\delta b = b(\boldsymbol{x} + \boldsymbol{r}) - b(\boldsymbol{x})$ and observing its evolution as a function of increment size $\boldsymbol{r}$. Intuitively, we anticipate detecting non-Gaussianity for small increments, which should gradually converge to a Gaussian distribution as the increment size increases. This expectation arises from the notion that sufficiently distant points should exhibit decorrelation. However, we also anticipate the presence of fatter non-Gaussian tails as a result of the possible formation of coherent structures within this regime. This can be observed in the bottom panel of Figure 4.6, where the magnetic field modulus exhibits a higher level of intermittency compared to the weak regime.

In our analysis, we focus on increments within perpendicular planes, utilizing a total of $N_z = 128$ planes. The findings are depicted in Figure 4.10. It is noteworthy that the weak regime exhibits small non-Gaussian tails for lower values of the perpendicular increment distance, $r_\perp$, followed by a swift convergence towards a Gaussian-like distribution as $r_\perp$ increases. In contrast, the strong regime reveals pronounced non-Gaussian tails attributed to the presence of coherent structures such as eddies or current sheets. Furthermore, we

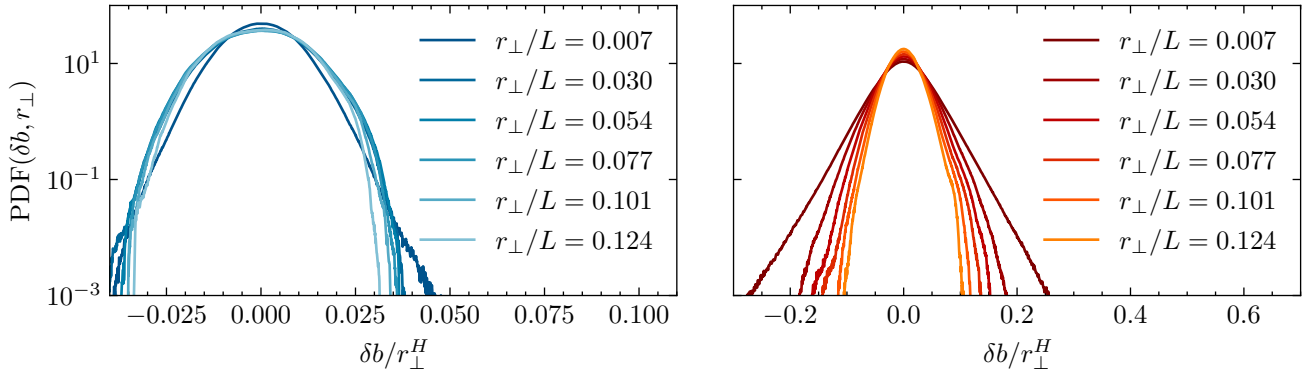

Figure 4.10: PDFs of the magnetic field increments δb for weak (blue) and strong (red) turbulence, and for six distances $r_\perp$.

have normalized the increments to the factor $r_\perp^H$, where $H = 0.75$ is determined through fitting analysis. This normalization allows us to examine the self-similar behavior of the PDFs. If self-similarity holds, they should collapse onto a single scaling function, at least for the majority of the distribution, according to the rescaling operation [36]:

$$P_s\left(\delta b/r_\perp^H\right) = r_\perp^H P_s\left(\delta b\right). \tag{4.8}$$

Remarkably, this normalization procedure yields a collapse of the different PDFs in the weak regime. However, it is worth noting that the lowest value of $r_\perp$ still exhibits coherence between the two points, preventing complete collapse (see Section 2.1.2). Interestingly, similar collapses with a rescaling using the value $H \sim 0.8$ have been documented in measurements of the solar wind's magnetic field PDF [37].

To obtain more precise results, we can investigate the behavior of higher-order structure functions. To do so, we introduce the p-order structure functions as

$$S_p \equiv \langle |\delta b|^p \rangle = C_p r^{\zeta(p)}, \tag{4.9}$$

where $\zeta(p)$ is the scaling exponents measured in the inertial range, and the coefficients C_p are constants. This process offers the opportunity to explore the behavior of the structure functions across smaller and smaller scales as we increase the value of p. Remarkably, as we elevate p, the structure function becomes more sensitive to small-scale gradients, allowing us to capture the occurrence of rare events in the PDFs. The theoretical predictions state that the energy spectrum follows a power law of $E(k_\perp) \propto k_\perp^{-5/2}$ and $E(k_\perp) \propto k_\perp^{-7/3}$ for the weak and strong turbulences respectively. Therefore, we should expect to observe $\zeta(2) = 3/2$ in the weak regime and $\zeta(2) = 4/3$ in the strong one and, under the assumption of self-similarity,

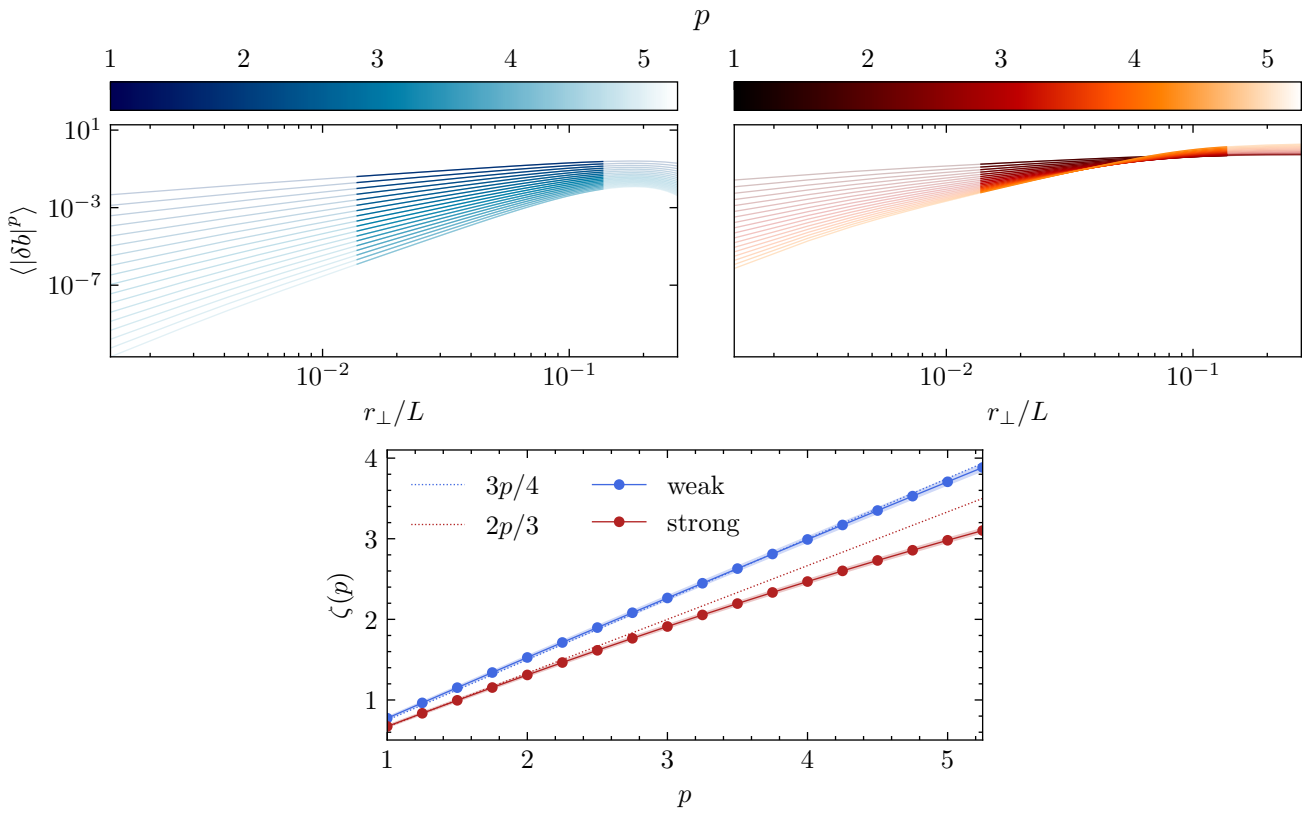

Figure 4.11: Top: Structure functions for both the weak (blue lines) and strong (red lines) turbulence regimes. The highlighted sections represent the specific data points utilized for fitting the scaling exponents $\zeta(p)$. Bottom: The corresponding scaling exponents $\zeta(p)$. The dotted lines represent the expected profiles based on self-similarity, while the shaded areas represent the fitting errors associated with the determined exponents.

the scaling exponents can be derived as $\zeta(p) = 3p/4$ and $\zeta(p) = 2p/3$ respectively. We can find another clue in the weak regime that lends support to this expectation. If intermittency is monofractal, then the coefficient H observed in the collapse of the PDFs should correspond to the coefficient of the function $\zeta(p)$. Theoretical predictions indicate that this coefficient should be $3/4$, which aligns with the fitted value of H. To investigate this further, we compute the structure functions for $p \in [1, 5]$, considering the limitations imposed by the available number of data points [22].

The top panels of Figure 4.11 present the behavior of the p-order structure function as a function of the scale separation $r_\perp$. The highlighted region indicates the specific locations where the scaling exponent $\zeta(p)$ will be determined through a fitting. This region corresponds to the shaded area within the inertial range in Figure 4.8 and spans a full decade for improved accuracy. The outcome is illustrated in the lower panel of Figure 4.11, where a distinct linear relationship emerges, in accordance with the self-similarity prediction for weak wave turbulence. In contrast, the strong regime exhibits multifractal intermittency,

deviating from the monofractal line as p increases. Notably, both regimes demonstrate the anticipated values for $\zeta(2)$. These observations suggest that, contrary to the strong regime which concentrates energy in sparse regions of the plasma to develop coherent structures like current sheets or vortices, in the weak regime, energy is distributed more evenly throughout the plasma which is consistent with the absence of strong nonlinearities and the lack of distinct structures.

4.4 Discussion

This preliminary investigation was initially driven by the challenge of distinguishing the turbulent regime prevailing in the solar wind at sub-proton scales. As depicted in Figure 4.1, in situ data revealed magnetic spectra close to the -8/3 scaling [3, 50, 55, 56]. A notable characteristic was the tendency to display self-similar behavior when examining the p-order structure functions [1, 16, 17, 31, 37, 38]. To investigate these features, we conducted two DNS: one focusing on the weak regime, characterized by small nonlinearities and weak interactions between wave packets, and another capturing the strong regime with significant wave packet interactions.

The numerical experiments yielded a clear distinction between the two regimes, particularly through the lens of intermittency. Contrary to the strong regime, the weak regime displayed monofractal intermittency. Interestingly, the characteristics observed in the latter regime closely aligned with those measured in the solar wind. We observed that the PDFs of magnetic field increments exhibited a universal collapse when appropriately rescaled by the factor $r_\perp^H$, with $H = 0.75$, closely resembling the values employed in analyzing in situ data [37]. On the other hand, the scaling exponents $\zeta(p)$ of the p-order structure functions exhibited a linear relationship, following the scaling law of $3p/4$, which is consistent with the estimation of the H value. This finding provides compelling evidence in support of the weak regime as an accurate description of the in situ measurements of the solar wind at sub-proton scales.

Two notable caveats arise in our investigation. The first issue concerns the observed power law in the solar wind, which closely aligns with a steep exponent close to -8/3 rather than the anticipated -5/2. Numerical simulations of the strong regime with Landau damping have revealed an exponent of -8/3, but also pronounced intermittency [68], which rules out this scenario to report the in situ data. I think that the key distinction lies in the fact that the solar wind represents a collisionless plasma, wherein dissipation is absent, preventing the attainment of a stationary solution. Hence, it is understandable to encounter a subtle difference among the theoretical predictions, which are based on assumptions of stationary turbulence, the

simulations incorporating viscous damping at small scales, and the actual observational data. In Chapter 6, we explore non-stationary solutions of the weak regime without introducing any additional dissipative processes. Intriguingly, we find that one solution closely resembles the in situ observations at sub-proton scales... The second objection that arises pertains to the sustainability of weak wave turbulence over an infinite range of scales, as discussed in Section 4.2.2. weak wave turbulence always gives way to strong turbulence beyond a critical scale k_c. Considering this, along with the fact that energy cascades begin at MHD scales in the solar wind, one might question why turbulence would appear in a weak regime at sub-proton scales. A clever solution emerges when you take your nose out of the grindstone and step back. When we shift our perspective from considering MHD scales and sub-proton scales as distinct entities to viewing them as part of a continuum, we can identify two conserved quantities: the total energy and the generalized helicity (which encompasses both cross and magnetic helicity) [5]. Additionally, a distinct category of waves known as ion cyclotron waves (ICWs) emerges near the ion inertial lengths [65]. These waves interact with particles efficiently, directly heating the plasma through resonant coupling to particle gyromotion [12, 28]. They present a potential avenue for turbulent dissipation and are enhanced by a concept called the "helicity barrier" [44]. This intriguing mechanism arises from the interaction between the inverse cascade of generalized helicity and the direct cascade of energy, resulting in an energy buildup within the inertial range [33]. Consequently, fluctuations with small parallel scales emerge, damping turbulence through cyclotron resonance and the helicity barrier selectively permits only a fraction of the flux from large scales to enter the sub-ion cascade [44, 64].

The presence of significant ICWs near the ion scale can induce notable drops in energy amount, leading to the weakening of nonlinearities at scales beyond the proton level [21, 32], and can potentially randomize turbulent fluctuations, renowned for their strong intermittency at MHD scales [17, 41]. Consequently, nonlinear interactions no longer give rise to highly intermittent fluctuations, thus suppressing the formation and occurrence of intermittent structures, especially those related to current sheets in the sub-proton scales [17, 23, 37, 48, 52, 63]. This leads us to the regime of weak wave turbulence.

Recent numerical investigations [44, 64] and observational studies [12, 13] have unequivocally substantiated and verified this scenario, thereby fortifying its profound relevance. The final piece of the puzzle lies in obtaining an analytical relationship that establishes a connection between the helicity level at MHD scales and the fraction of energy cascading to sub-proton scales. Such a relations holds great interest as it would shed light on the intricate interplay between helicity and energy transfer in turbulent plasmas. Furthermore, it would provide a theoretical validation of the helicity barrier, which currently remains confined

to observations from spacecraft and direct numerical simulations.

References

[1] T. Alberti, G. Consolini, V. Carbone, E. Yordanova, M. Marcucci, and P. De Michelis, "Multifractal and chaotic properties of solar wind at mhd and kinetic domains: An empirical mode decomposition approach," *Entropy*, vol. 21, no. 3, p. 320, Mar. 2019.

[2] O. Alexandrova, V. Carbone, P. Veltri, and L. Sorriso-Valvo, "Small-scale energy cascade of the solar wind turbulence," *The Astrophysical Journal*, vol. 674, no. 2, p. 1153, Feb. 2008.

[3] O. Alexandrova, C. Lacombe, A. Mangeney, R. Grappin, and M. Maksimovic, "Solar wind turbulent spectrum at plasma kinetic scales," *The Astrophysical Journal*, vol. 760, no. 2, p. 121, Nov. 2012.

[4] S. D. Bale, P. J. Kellogg, F. S. Mozer, T. S. Horbury, and H. Reme, "Measurement of the electric fluctuation spectrum of magnetohydrodynamic turbulence," *Phys. Rev. Lett.*, vol. 94, p. 215 002, 21 Jun. 2005.

[5] S. Banerjee and S. Galtier, "Chiral exact relations for helicities in hall magnetohydrodynamic turbulence," *Phys. Rev. E*, vol. 93, p. 033 120, 3 Mar. 2016.

[6] A. Barnes, "Collisionless Damping of Hydromagnetic Waves," *The Physics of Fluids*, vol. 9, no. 8, pp. 1483–1495, Aug. 1966.

[7] D. J. Benney and A. C. Newell, "The propagation of nonlinear wave envelopes," *Journal of Mathematics and Physics*, vol. 46, no. 1-4, pp. 133–139, 1967.

[8] D. Benney and P. Saffman, "Nonlinear Interactions of Random Waves in a Dispersive Medium," *Proc. R. Soc. Lond. A*, vol. 289, no. 1418, pp. 301–320, 1966.

[9] D. Biskamp, E. Schwarz, and J. F. Drake, "Two-Dimensional Electron Magnetohydrodynamic Turbulence," *Phys. Rev. Lett.*, vol. 76, no. 8, pp. 1264–1267, 1996.

[10] D. Biskamp, E. Schwarz, A. Zeiler, A. Celani, and J. F. Drake, "Electron magnetohydrodynamic turbulence," *Phys. Plasmas*, vol. 6, no. 3, pp. 751–758, 1999.

[11] S. Boldyrev, K. Horaites, Q. Xia, and J. C. Perez, "Toward a theory of astrophysical plasma turbulence at subproton scales," *The Astrophysical Journal*, vol. 777, no. 1, p. 41, Oct. 2013.

[12] T. A. Bowen *et al.*, "In situ signature of cyclotron resonant heating in the solar wind," *Phys. Rev. Lett.*, vol. 129, p. 165 101, 16 Oct. 2022.

[13] T. A. Bowen *et al.*, "Mediation of collisionless turbulent dissipation through cyclotron resonance," *arXiv*, 2023.

[14] V. I. Brzygalov and A. I. Morozov, "Stationary current in an axially symmetric conducting body with a strong hall effect," *Zh. Eksp. Teor. Fiz.*, vol. 49, pp. 1789–1795, Dec. 1965.

[15] C. H. K. Chen, S. Boldyrev, Q. Xia, and J. C. Perez, "Nature of subproton scale turbulence in the solar wind," *Phys. Rev. Lett.*, vol. 110, p. 225 002, 22 May 2013.

[16] C. H. K. Chen, L. Sorriso-Valvo, J. Šafránková, and Z. Němeček, "Intermittency of the solar wind density fluctuations from ion to electron scales," *The Astrophysical Journal Letters*, vol. 789, no. 1, p. L8, Jun. 2014.

[17] R. Chhiber, W. H. Matthaeus, T. A. Bowen, and S. D. Bale, "Subproton-scale intermittency in near-sun solar wind turbulence observed by the parker solar probe," *The Astrophysical Journal Letters*, vol. 911, no. 1, p. L7, Apr. 2021.

[18] J. Cho, "Magnetic Helicity Conservation and Inverse Energy Cascade in Electron Magnetohydrodynamic Wave Packets," *Phys. Rev. Lett.*, vol. 106, no. 19, p. 191 104, 2011.

[19] J. Cho and A. Lazarian, "The anisotropy of electron magnetohydrodynamic turbulence," *The Astrophysical Journal*, vol. 615, no. 1, p. L41, Sep. 2004.

[20] J. Cho and A. Lazarian, "Simulations of electron magnetohydrodynamic turbulence," *The Astrophysical Journal*, vol. 701, no. 1, p. 236, Jul. 2009.

[21] V. David and S. Galtier, "$k_\perp^{-8/3}$ Spectrum in kinetic alfvén wave turbulence: Implications for the solar wind," *The Astrophysical Journal*, vol. 880, no. 1, p. L10, Jul. 2019.

[22] T. Dudok de Wit, "Can high-order moments be meaningfully estimated from experimental turbulence measurements?" *Phys. Rev. E*, vol. 70, p. 055 302, 5 Nov. 2004.

[23] T. Dudok de Wit and V. V. Krasnosel'skikh, "Non-gaussian statistics in space plasma turbulence: Fractal properties and pitfalls," *Nonlinear Processes in Geophysics*, vol. 3, no. 4, pp. 262–273, 1996.

[24] U. Frisch, *Turbulence: The Legacy of A. N. Kolmogorov*. Cambridge University Press, 1995.

[25] S. Galtier, *Introduction to modern magnetohydrodynamics*. Cambridge University Press, 2016, p. 288.

[26] S. Galtier and A. Bhattacharjee, "Anisotropic weak whistler wave turbulence in electron magnetohydrodynamics," *Physics of Plasmas*, vol. 10, no. 8, pp. 3065–3076, 2003.

[27] S. Galtier and R. Meyrand, "Entanglement of helicity and energy in kinetic Alfvén wave/whistler turbulence," *J. Plasma Physics*, vol. 81, no. 1, p. 325 810 106, 2015.

[28] S. P. Gary, *Theory of Space Plasma Microinstabilities* (Cambridge Atmospheric and Space Science Series). Cambridge University Press, 1993.

[29] P. Goldreich and S. Sridhar, "Toward a Theory of Interstellar Turbulence. II. Strong Alfvenic Turbulence," *apj*, vol. 438, p. 763, Jan. 1995.

[30] P. Goldreich and S. Sridhar, "Magnetohydrodynamic turbulence revisited," *The Astrophysical Journal*, vol. 485, no. 2, p. 680, Aug. 1997.

[31] L. F. Gomes, T. F. P. Gomes, E. L. Rempel, and S. Gama, "Origin of multifractality in solar wind turbulence: the role of current sheets," *Monthly Notices of the Royal Astronomical Society*, vol. 519, no. 3, pp. 3623–3634, Dec. 2022.

[32] G. G. Howes *et al.*, "Gyrokinetic simulations of solar wind turbulence from ion to electron scales," *Phys. Rev. Lett.*, vol. 107, p. 035 004, 3 Jul. 2011.

[33] P. A. Isenberg and M. A. Lee, "A dispersive analysis of bispherical pickup ion distributions," *Journal of Geophysical Research: Space Physics*, vol. 101, no. A5, pp. 11 055–11 066, 1996.

[34] H. Kim and J. Cho, "Inverse Cascade in Imbalanced Electron Magnetohydrodynamic Turbulence," *Astrophys. J.*, vol. 801, no. 2, p. 75, 2015.

[35] A. Kingsep, K. Chukbar, and V. Yankov, "Reviews of plasma physics," *Electron Magnetohydrodynamics*, pp. 243–291, 1990.

[36] K. Kiyani, S. C. Chapman, and B. Hnat, "Extracting the scaling exponents of a self-affine, non-gaussian process from a finite-length time series," *Phys. Rev. E*, vol. 74, p. 051 122, 5 Nov. 2006.

[37] K. H. Kiyani, S. C. Chapman, Y. V. Khotyaintsev, M. W. Dunlop, and F. Sahraoui, "Global scale-invariant dissipation in collisionless plasma turbulence," *Phys. Rev. Lett.*, vol. 103, p. 075 006, 7 Aug. 2009.

[38] K. H. Kiyani, K. T. Osman, and S. C. Chapman, "Dissipation and heating in solar wind turbulence: From the macro to the micro and back again," *Philosophical Transactions of the Royal Society A: Mathematical, Physical and Engineering Sciences*, vol. 373, no. 2041, p. 20 140 155, 2015.

[39] Y. Lithwick and P. Goldreich, "Compressible magnetohydrodynamic turbulence in interstellar plasmas," *The Astrophysical Journal*, vol. 562, no. 1, p. 279, Nov. 2001.

[40] R. L. Lysak and W. Lotko, "On the kinetic dispersion relation for shear alfvén waves," *Journal of Geophysical Research: Space Physics*, vol. 101, no. A3, pp. 5085–5094, 1996.

[41] A. Mallet *et al.*, "Interplay between intermittency and dissipation in collisionless plasma turbulence," *Journal of Plasma Physics*, vol. 85, no. 3, p. 175 850 302, 2019.

[42] R. Marino and L. Sorriso-Valvo, "Scaling laws for the energy transfer in space plasma turbulence," *Physics Reports*, vol. 1006, pp. 1–144, 2023, Scaling laws for the energy transfer in space plasma turbulence.

[43] R. Meyrand, K. Kiyani, and S. Galtier, "Weak magnetohydrodynamic turbulence and intermittency," *J. Fluid Mech.*, vol. 770, R1, 2015.

[44] R. Meyrand, J. Squire, A. Schekochihin, and W. Dorland, "On the violation of the zeroth law of turbulence in space plasmas," *Journal of Plasma Physics*, vol. 87, no. 3, p. 535 870 301, 2021.

[45] R. Meyrand, A. Kanekar, W. Dorland, and A. A. Schekochihin, "Fluidization of collisionless plasma turbulence," *Proceedings of the National Academy of Sciences*, vol. 116, no. 4, pp. 1185–1194, 2019.

[46] A. I. Morozov, L. S. Solov'ev, K. V. Brushlinskii, V. F. D'yachenko, V. S. Imshennik, and S. V. Lebedev, *Reviews of Plasma Physics / Voprosy Teorii Plazmy*. Springer New York, NY, 1980.

[47] S. V. Nazarenko and A. A. Schekochihin, "Critical balance in magnetohydrodynamic, rotating and stratified turbulence: Towards a universal scaling conjecture," *Journal of Fluid Mechanics*, vol. 677, pp. 134–153, 2011.

[48] T. N. Parashar, C. Salem, R. T. Wicks, H. Karimabadi, S. P. Gary, and W. H. Matthaeus, "Turbulent dissipation challenge: A community-driven effort," *Journal of Plasma Physics*, vol. 81, no. 5, p. 905 810 513, 2015.

[49] J. Patterson G. S. and S. A. Orszag, "Spectral Calculations of Isotropic Turbulence: Efficient Removal of Aliasing Interactions," *The Physics of Fluids*, vol. 14, no. 11, pp. 2538–2541, Nov. 1971.

[50] J. J. Podesta, "Evidence of kinetic alfvén waves in the solar wind at 1 au," *Solar Physics*, vol. 286, no. 2, pp. 529–548, Sep. 2013.

[51] H. Poincaré, *Les méthodes nouvelles de la mécanique céleste, Volume 2*. Paris: Gauthier-Villars, 1893.

[52] O. W. Roberts *et al.*, "Scale-dependent kurtosis of magnetic field fluctuations in the solar wind: A multi-scale study with cluster 2003–2015," *Journal of Geophysical Research: Space Physics*, vol. 127, no. 9, e2021JA029483, 2022, e2021JA029483 2021JA029483.

[53] F. Sahraoui, G. Belmont, and M. L. Goldstein, "New insight into short-wavelength solar wind fluctuations from vlasov theory," *The Astrophysical Journal*, vol. 748, no. 2, p. 100, Mar. 2012.

[54] F. Sahraoui, M. L. Goldstein, P. Robert, and Y. V. Khotyaintsev, "Evidence of a cascade and dissipation of solar-wind turbulence at the electron gyroscale," *Phys. Rev. Lett.*, vol. 102, p. 231 102, 23 Jun. 2009.

[55] F. Sahraoui *et al.*, "Scaling of the electron dissipation range of solar wind turbulence," *Astrophys. J.*, vol. 777, no. 1, p. 15, Oct. 2013.

[56] F. Sahraoui, L. Hadid, and S. Huang, "Magnetohydrodynamic and kinetic scale turbulence in the near-earth space plasmas: A (short) biased review," *Reviews of Modern Plasma Physics*, vol. 4, no. 1, p. 4, Feb. 2020.

[57] C. S. Salem *et al.*, "Identification of kinetic alfvén wave turbulence in the solar wind," *The Astrophysical Journal Letters*, vol. 745, no. 1, p. L9, Jan. 2012.

[58] A. A. Schekochihin *et al.*, "Astrophysical gyrokinetics: Kinetic and fluid turbulent cascades in magnetized weakly collisional plasmas," *The Astrophysical Journal Supplement Series*, vol. 182, no. 1, p. 310, May 2009.

[59] A. A. Schekochihin, "Mhd turbulence: A biased review," *Journal of Plasma Physics*, vol. 88, no. 5, p. 155 880 501, 2022.

[60] A. A. Schekochihin and S. C. Cowley, "Turbulence and magnetic fields in astrophysical plasmas," in *Magnetohydrodynamics: Historical Evolution and Trends*. Dordrecht: Springer Netherlands, 2007, pp. 85–115.

[61] V. Shrira *et al.*, *Advances in Wave turbulence*. World Scientific, 2013, vol. 83.

[62] A. T. Skvortsov, C. Kirezci, D. Sgarioto, and A. V. Babanin, "Intermittency of gravity wave turbulence on the surface of an infinitely deep fluid: Numerical experiment," *Physics Letters A*, vol. 449, p. 128 337, 2022.

[63] L. Sorriso-Valvo, V. Carbone, P. Veltri, G. Consolini, and R. Bruno, "Intermittency in the solar wind turbulence through probability distribution functions of fluctuations," *Geophysical Research Letters*, vol. 26, no. 13, pp. 1801–1804, 1999.

[64] J. Squire, R. Meyrand, M. W. Kunz, L. Arzamasskiy, A. A. Schekochihin, and E. Quataert, "High-frequency heating of the solar wind triggered by low-frequency turbulence," *Nature Astronomy*, vol. 6, no. 6, pp. 715–723, Jun. 2022.

[65] T. H. Stix, *Waves in Plasmas*. American Institute of Physics Melville, NY, 1992.

[66] B. Teaca, M. K. Verma, B. Knaepen, and D. Carati, "Energy transfer in anisotropic magnetohydrodynamic turbulence," *Phys. Rev. E*, vol. 79, p. 046 312, 4 Apr. 2009.

[67] J. Williamson, "Low-storage runge-kutta schemes," *Journal of Computational Physics*, vol. 35, no. 1, pp. 48–56, 1980.

[68] M. Zhou, Z. Liu, and N. F. Loureiro, "Electron heating in kinetic-alfvén-wave turbulence," *Proceedings of the National Academy of Sciences*, vol. 120, no. 23, e2220927120, 2023.

Chapter 5

Wave turbulence in inertial EMHD

This study is published in:

V. David & S. Galtier., "Wave Turbulence in Inertial Electron MHD", *J. Plasma Physics*, **88**, 905880509, 2022.

V. David & S. Galtier., "Locality of Triad Interaction and Kolmogorov Constant in Inertial Wave Turbulence", *J. Fluid Mech. Rapids*, **955**, R2, 2023.

5.1 Introduction to wave turbulence

To understand the intricate process of energy transfer across various scales in a turbulent plasma, numerous approaches can be undertaken. However, there exists a remarkably rigorous one, rooted in systems consisting of numerous wave packets weakly interacting with each other: the theory of wave turbulence. The term "weakly interacting" arises from the assumptions that the nonlinearities are weak and only become significant after an extensively long time in comparison to the individual periods of the linear waves [30, 51]. The significance of wave turbulence theory is twofold. Firstly, it presents a natural mechanism for closure, ensuring consistency in the asymptotic evolution [5–7, 55]. Secondly, it provides a framework for obtaining exact analytical solutions, namely the thermodynamic equilibrium state and the Kolmogorov-Zakharov (KZ) spectra, representing stationary solutions of the wave kinetic equations [72]. These equations, reminiscent of Boltzmann-like equations, describe the temporal changes in wave packet density solely as a function of that density [34–36]. The thermodynamic equilibrium state represents the statistical energy distribution in isolated systems, maximizing entropy under energy constraints, and joint entropy in cases where multiple conserved quantities are involved [65]. While the Kolmogorov-Zakharov solution arises in nonequilibrium scenarios, specifically when nonisolated systems are subject to an external force and dissipation due to viscosity acting on various length scales, resulting in the Kolmogorov behavior of finite flux. In the range of motion where the kinetic equation holds, quantities such as energy are conserved. The flow of spectral densities can be visualized as moving from sources in the $\boldsymbol{k}$-space to sinks [70, 71]. These solutions, known as KZ solutions, bear resemblance to the well-known prediction of the Kolmogorov energy spectrum $E(k)$ in high Reynolds number hydrodynamics, denoted as $E(k) = c\Pi^{2/3}k^{-5/3}$ where Π is the energy flux, and c a constant. Additionally, the kinetic equation exhibits time-dependent solutions of a self-similar nature, providing insights into how the stationary solutions are reached. However, the analytical derivation of these solutions remains an open question.

Wave turbulence theory finds broad applicability in both natural and laboratory settings. One prominent example is the study of ocean gravity waves on a sea stirred by wind. Nonetheless, the theory's relevance extends beyond this specific case. In principle, its manifestations can also be observed, for instance, in: (i) Astrophysical environments, with Alfvén waves [26], fast magnetosonic waves [31, 42], kinetic Alfvén waves, and whistler waves [24]. (ii) The atmospheres of rotating planets, where Rossby-like waves are present [2–4]. (iii) The formation of Bose-Einstein condensates [52, 53]. (iv) The interface between air and a liquid, such as water, with capillary waves [71]. (v) Nonlinear optics, specifically the diffraction of

optical waves [21]. (vi) Acoustic waves [43, 54, 73]. (vii) The deformation of a material with elastic waves [20]. (viii) In the oceans due to the Coriolis effect with Kelvin waves [44]. (ix) Even the formation of the universe with gravitational waves [27, 33].

However, it is essential to question whether wave turbulence truly governs the behavior of ocean waves, capillary waves, and other relevant examples where we would expect the theory to apply. Despite notable achievements, the theory also encounters limitations. In essence, the story of wave turbulence remains far from complete, with our understanding still in its early stages of experimental investigation. Recent experimental observations in surface waves [22], gravity waves [18, 37], internal gravity waves [64], and inertial waves [48, 69] have provided supporting evidence for the theories developed in these areas, reinforcing the validity of the wave turbulence approach when the following conditions are met. To begin, we consider an infinite domain and assume that our physical fields have zero means, are *bounded* throughout, and possess sufficient smoothness, ensuring well-defined behavior described by the partial differential equations. Consequently, we reformulate the governing equations, employing a diagonalized set of Fourier amplitudes for the physical fields. It is important to recognize that these amplitudes, being associated with bounded fields rather than decaying ones, should be regarded as generalized functions rather than ordinary ones. Only statistical averages of the Fourier amplitudes hold significance in this context. Hence, we can identify at least three fundamental premises on which the wave turbulence closure is established [65]. We assume

1. spatial homogeneity for the fields, meaning that the ensemble averages of the fields, evaluated at points $\boldsymbol{x}$, $\boldsymbol{x}+\boldsymbol{r}_1$, $\boldsymbol{x}+\boldsymbol{r}_2$, ... depend only on the separations $\boldsymbol{r}_1$, $\boldsymbol{r}_2$, ...

2. that at an initial time, when the external driving force is introduced, the fields at distant points are uncorrelated. This implies that the cumulants in physical space initially exhibit a property where, as the separations $|r_j|$ become large, the cumulants decay rapidly enough, allowing their Fourier transforms to be treated as ordinary functions. Although this assumption is modest, it is necessary for evaluating the long-term behavior of integrals like $\int f(k)t\mathrm{sinc}(kt)\mathrm{d}k$, where we require the smoothness of $f(k)$ in wavenumber k to ensure that this integral behaves as $\pi\mathrm{sgn}(t)f(0)$ in a long time.

3. that different asymptotic expansions for the gradual evolution of two-point functions remain uniformly valid across all wavenumbers. In its most basic form, this requires that the ratio of linear to nonlinear timescales is small for every wavevector.

This chapter presents the wave turbulence theory for inertial kinetic Alfvén waves (IKAW) and inertial

whistler waves (IWW), governed by the inertial electron MHD (IEMHD) discussed in the next section. The structure of the chapter is as follows. After a quick (and therefore simplified) derivation of the equations that we will use for the theory of wave turbulence, we introduce the canonical variables and derive the dynamical equation describing the wave amplitude variation. In Section 5.4, a phenomenology of wave turbulence is developed to get a simple heuristic explanation for the solutions (Kolmogorov–Zakharov spectra) derived later. In the following Section 5.5, we derive the wave kinetic equations, from which we show the detailed conservation of invariants. The exact stationary solutions in the anisotropic limit $k_\parallel \ll k_\perp$ and the locality of these solutions is proved in Section 5.6. We then consider the limit of super-local interactions and derive the associated nonlinear diffusion equation for the energy in Section 5.7. Section 5.8 is dedicated to the computation of the sign of the energy flux, which gives the direction of the cascade, and to the determination of the Kolmogorov constant. Before concluding with a discussion of possible applications of our results, and ways in which these results can be extended, we discuss, in Section 5.9, the link between this plasma turbulence and the inertial waves turbulence arising in fast rotating non-ionized fluids.

5.2 Inertial electron magnetohydrodynamics

Here, the system in which we are interested in the plasma dynamics at scales where the electron inertia plays a non-negligible role. In our approach, the mass difference between ions and electrons is such that the ions will be considered static to form a neutralizing background. Therefore, at the timescale of interest, only the electron dynamics is relevant. This is the domain of EMHD (introduced in Chapter 4) and IEMHD which describe, respectively, the scales $d_e \ll \ell \ll d_i$ and $r_e \ll \ell \ll d_e$, where $r_e \equiv \sqrt{\beta_e} d_e$ is the electron Larmor radius. Remarkably, the IEMHD regime can only be observed when the magnetic pressure significantly exceeds the thermal pressure (i.e., when $\beta_e \ll 1$). Although it is difficult for current spacecraft to measure the plasma dynamics corresponding to the electron inertial scales, it is interesting to see what the theoretical description can predict. The EMHD and IEMHD approximations are widely used models to study, for example, magnetic reconnection or space plasma turbulence [8–10, 12–15, 39]. More information is given in [47] where an exhaustive list of plasmas driven by the IEMHD model is given with the parameter regimes. In this chapter, we present the theory of wave turbulence for IEMHD in the presence of a relatively strong and uniform external magnetic field $\boldsymbol{B_0}$. The equivalent theory for EMHD has already been published [24] but not yet for IEMHD. Strong IEMHD turbulence has recently received

new attention with the study of the weakly compressible case [11, 60]. The objective was to study the nature of plasma turbulence in the Earth's magnetosheath. The main prediction, phenomenological in nature, is a magnetic spectrum in $k_\perp^{-11/3}$ (see also [46]) which is less steep than the prediction we will derive here. In the meantime, a rigorous derivation (using systematic asymptotic expansions) based on a more general model including electron inertia and finite Larmor radius corrections has been proposed [57, 58]. This more general approach allows the study of several limits, and to recover in particular the model discussed previously [11]. In fact, these weakly compressible IEMHD equations have the same mathematical structure as the incompressible case when the ion β_i (the ratio between ion thermal pressure and magnetic pressure) is moderately small. Therefore, the physics of wave turbulence that we will describe in this chapter has a broader impact than strictly speaking the incompressible case and can be applied to both IWWs and IKAWs. As discussed in the previous chapter, a similar situation exists for scales larger than d_e: in the presence of a strong $\boldsymbol{B_0}$, the equations describing the nonlinear dynamics of kinetic Alfvén waves and whistler waves have exactly the same mathematical form, which means that the physics of wave turbulence is similar for both problems [25]. Although a fully kinetic approach is *a priori* required to describe plasma dynamics at electron inertial scales, all of these reduced fluid models can provide interesting insight when considering small fluctuations around a Maxwellian equilibrium state. In this chapter, we follow this precept and apply the powerful tool of wave turbulence to extract new properties useful for a better understanding of space plasmas.

The goal of this section is to quickly derive in a simplified way the set of equations describing the dynamics of non-relativistic electrons at inertial scales in a fully ionized plasma. For this reason, the assumption of incompressibility will be used. A complete derivation is found in [11] and in [58].

5.2.1 Governing equations

The basic fluid equations governing the electron dynamics in an incompressible (dissipationless) plasma are

$$\frac{\partial \boldsymbol{u}_e}{\partial t} + (\boldsymbol{u}_e \cdot \boldsymbol{\nabla})\, \boldsymbol{u}_e = -\frac{1}{\rho_e}\boldsymbol{\nabla} P_e - \frac{q_e}{m_e}\left(\boldsymbol{u}_e \times \boldsymbol{b} + \boldsymbol{E}\right), \tag{5.1a}$$

$$\frac{\partial \boldsymbol{B}}{\partial t} = -\boldsymbol{\nabla} \times \boldsymbol{E}, \tag{5.1b}$$

$$\boldsymbol{\nabla} \times \boldsymbol{B} = \mu_0 \boldsymbol{J}, \tag{5.1c}$$

$$\boldsymbol{\nabla} \cdot \boldsymbol{u}_e = 0, \tag{5.1d}$$

$$\boldsymbol{\nabla} \cdot \boldsymbol{B} = 0, \tag{5.1e}$$

where $\boldsymbol{u}_e(\boldsymbol{x}, t)$ is the electron velocity, $\rho_e(\boldsymbol{x}, t) = m_e n_0$ the constant electron mass density with m_e the electron mass and n_0 the density, $P_e(\boldsymbol{x}, t)$ the electron pressure, $q_e > 0$ the modulus of the electron charge, $\boldsymbol{b}(\boldsymbol{x}, t)$ the magnetic field, $\boldsymbol{E}(\boldsymbol{x}, t)$ the electric field, $\boldsymbol{J}(\boldsymbol{x}, t) = n_0 q_e\left(\boldsymbol{u}_i - \boldsymbol{u}_e\right)$ the electric current and $\boldsymbol{u}_i(\boldsymbol{x}, t)$ the ion velocity (assumed to be zero). Normalizing the magnetic field to the (electron) Alfvén velocity and then taking the rotational of equation (5.1a) combined with the Maxwell-Faraday law (5.1b), one obtains

$$\frac{\partial}{\partial t}\left(d_e^2 \nabla^2 - 1\right)\boldsymbol{b} + (\boldsymbol{u}_e \cdot \boldsymbol{\nabla})\,(d_e^2 \nabla^2 - 1)\boldsymbol{b} = \left(d_e^2 \nabla^2 - 1\right)\boldsymbol{b} \cdot \boldsymbol{\nabla} \boldsymbol{u}_e, \tag{5.2}$$

where $d_e = \sqrt{m_e/(n_0 q_e^2 \mu_0)}$ is the electron inertial length. Now, we introduce a relatively strong and uniform (normalized) magnetic field $\boldsymbol{b}_0 = b_0 \boldsymbol{e}_\parallel$ that defines the parallel direction. In the limit of IEMHD, the spatial variations of $\boldsymbol{b}$ are done on a characteristic length $L \ll d_e$ and mainly in the plane perpendicular to $\boldsymbol{e}_\parallel$. Thus, in the leading order, we have

$$\left(\frac{\partial}{\partial t} + \boldsymbol{u}_{e\perp} \cdot \boldsymbol{\nabla}_\perp\right) d_e^2 \nabla_\perp^2 \boldsymbol{b} = d_e^2 (\nabla_\perp^2 \boldsymbol{b}_\perp \cdot \boldsymbol{\nabla}_\perp)\boldsymbol{u}_e - (\boldsymbol{b}_0 \cdot \boldsymbol{\nabla})\boldsymbol{u}_e, \tag{5.3}$$

and also $\boldsymbol{J} = -n_0 q_e \boldsymbol{u}_e$, which can be written $d_e \boldsymbol{j} = -\boldsymbol{u}_e$ with the normalized electric current $\boldsymbol{j} \equiv \boldsymbol{\nabla} \times \boldsymbol{b}$. The magnetic field having a zero divergence, we define $\boldsymbol{b} \equiv \boldsymbol{b}_0 - \boldsymbol{\nabla} \times (g \boldsymbol{e}_x + \psi \boldsymbol{e}_z)$ where $\boldsymbol{e}_x$ and $\boldsymbol{e}_z$ are unit vectors (hereafter, we will assume $\boldsymbol{e}_z = \boldsymbol{e}_\parallel$ which is valid at leading order for a relatively strong uniform magnetic field $\boldsymbol{b}_0$), $\psi(\boldsymbol{x}, t)$ a stream function and $g(\boldsymbol{x}, t)$ a function satisfying the relation $\partial_y g \equiv b_\parallel$. We obtain the relation

$$\nabla_\perp^2 \boldsymbol{b} = \left(\boldsymbol{e}_\parallel \times \boldsymbol{\nabla}_\perp\right)(\nabla_\perp^2 \psi) + \nabla_\perp^2 b_\parallel \boldsymbol{e}_\parallel, \tag{5.4}$$

where, hereafter, the z-derivative is assumed to be negligible compared to the perpendicular derivative. Replacing $\boldsymbol{b}$ by its expression, the electron velocity can be expressed as a function of the magnetic field components

$$\boldsymbol{u}_e = d_e \left(\boldsymbol{e}_\parallel \times \boldsymbol{\nabla}_\perp b_\parallel - \nabla_\perp^2 \psi \boldsymbol{e}_\parallel \right). \tag{5.5}$$

Projecting equation (5.3) in the perpendicular plane to $\boldsymbol{e}_\parallel$, we find

$$\begin{aligned} \left(\boldsymbol{e}_\parallel \times \boldsymbol{\nabla}_\perp \right) \left[\frac{\partial}{\partial t} \left(d_e^2 \nabla_\perp^2 \psi \right) \right] + d_e^2 \left(\boldsymbol{u}_{e\perp} \cdot \boldsymbol{\nabla}_\perp \right) \left[\left(\boldsymbol{e}_\parallel \times \boldsymbol{\nabla}_\perp \right) \nabla_\perp^2 \psi \right] =& d_e^3 \left(\nabla_\perp^2 \boldsymbol{b} \cdot \boldsymbol{\nabla}_\perp \right) \left(\boldsymbol{e}_\parallel \times \boldsymbol{\nabla}_\perp b_\parallel \right) \\ & - d_e b_0 \partial_\parallel \left(\boldsymbol{e}_\parallel \times \boldsymbol{\nabla}_\perp \right) b_\parallel . \end{aligned} \tag{5.6}$$

The non-trivial relation

$$\left(\boldsymbol{u}_{e\perp} \cdot \boldsymbol{\nabla}_\perp \right) \left[\left(\boldsymbol{e}_\parallel \times \boldsymbol{\nabla}_\perp \right) \nabla_\perp^2 \psi \right] = \left(\boldsymbol{e}_\parallel \times \boldsymbol{\nabla}_\perp \right) \left[\left(\boldsymbol{u}_{e\perp} \cdot \boldsymbol{\nabla}_\perp \right) \nabla_\perp^2 \psi \right] + d_e \left(\nabla_\perp^2 \boldsymbol{b} \cdot \boldsymbol{\nabla}_\perp \right) \left(\boldsymbol{e}_\parallel \times \boldsymbol{\nabla}_\perp b_\parallel \right), \tag{5.7}$$

allows to simplify the previous equation and, by expressing $\boldsymbol{u}_e$ as a function of ψ, we obtain after some algebraic manipulations

$$\boxed{\frac{\partial}{\partial t} \left(\nabla_\perp^2 \psi \right) + d_e \left[\left(\boldsymbol{e}_\parallel \times \boldsymbol{\nabla}_\perp b_\parallel \right) \cdot \boldsymbol{\nabla}_\perp \right] \nabla_\perp^2 \psi = -\Omega_e \partial_\parallel b_\parallel}, \tag{5.8}$$

with $\Omega_e \equiv b_0 / d_e$ the cyclotron frequency of electrons (note that here, Ω_e is constant due to the assumption of incompressibility). Now, a projection of (5.3) in the $\boldsymbol{e}_\parallel$ direction gives directly

$$\frac{\partial}{\partial t} \left(d_e^2 \nabla_\perp^2 b_\parallel \right) + d_e^2 \left(\boldsymbol{u}_{e\perp} \cdot \boldsymbol{\nabla}_\perp \right) \nabla_\perp^2 b_\parallel = -d_e^3 \left(\nabla_\perp^2 \boldsymbol{b} \cdot \boldsymbol{\nabla}_\perp \right) \nabla_\perp^2 \psi + d_e b_0 \partial_\parallel \left(\nabla_\perp^2 \psi \right). \tag{5.9}$$

It is straightforward to show that the first term of the right-hand side is exactly zero. Then, by expressing $\boldsymbol{b}$ and $\boldsymbol{u}_e$ as functions of ψ and $b_\parallel$, we obtain

$$\boxed{\frac{\partial}{\partial t} \left(\nabla_\perp^2 b_\parallel \right) + d_e \left[\left(\boldsymbol{e}_\parallel \times \boldsymbol{\nabla}_\perp b_\parallel \right) \cdot \boldsymbol{\nabla}_\perp \right] \nabla_\perp^2 b_\parallel = \Omega_e \partial_\parallel \left(\nabla_\perp^2 \psi \right)}. \tag{5.10}$$

Equations (5.8) and (5.10) describe the dynamics of electrons at inertial scales. They have been derived in a more general framework and using kinetic arguments by [11] and [58]. Here, we have used the incompressibility condition to propose a (less accurate but more) fast derivation of a system that a priori describes only IWW. However, it is interesting to note that at inertial electron scales: (i) IKAW and IWW

can have the same dispersion relation and the only difference is that the transition to the inertial regime occurs at $k_\perp^2 d_e^2 \simeq 1$ for IWW rather than $k_\perp^2 d_e^2 \simeq 1 + 2/\beta_i$ for IKAW; (ii) the nonlinear equations governing the dynamics of IKAW and IWW are mathematically similar (up to a change of variable from b_z to ρ_e [11, 58]), which means that the physics of wave turbulence developed in this chapter applies to both waves. A similar situation is found at scales larger than d_e: in the presence of a strong $\boldsymbol{B_0}$, the equations describing the nonlinear dynamics of kinetic Alfvén waves and whistler waves have exactly the same mathematical form, which means that the physics of wave turbulence is similar for both problems [25].

5.2.2 Dispersion relation

In the linear regime, the Fourier transform of equations (5.8) and (5.10) gives

$$\frac{\partial \psi_k}{\partial t} = i\Omega_e k_\parallel k_\perp^{-2} b_k, \tag{5.11a}$$

$$\frac{\partial b_k}{\partial t} = i\Omega_e k_\parallel \psi_k, \tag{5.11b}$$

where the Fourier transform used is

$$\psi(\boldsymbol{k}, t) \equiv \psi_k = \int_{\mathbb{R}^3} \psi(\boldsymbol{x}, t) \mathrm{e}^{-i\boldsymbol{k}\cdot\boldsymbol{x}} \mathrm{d}\boldsymbol{x}, \tag{5.12}$$

and the notation $b_k \equiv b_{\parallel,k}$ as well. If the wavevector $\boldsymbol{k}$ is decomposed as $\boldsymbol{k} = k_\perp \boldsymbol{e}_\perp + k_\parallel \boldsymbol{e}_\parallel$, then the linear dispersion relation reads

$$\boxed{\left(\frac{\omega_k}{\Omega_e}\right)^2 = \left(\frac{k_\parallel}{k_\perp}\right)^2}. \tag{5.13}$$

One can find the following solutions to the linear IEMHD equations in Fourier space

$$\psi_k(k_\perp, t) = f(k_\perp)\cos(\omega_k t) + ig(k_\perp) k_\perp^{-1} \sin(\omega_k t), \tag{5.14a}$$

$$b_k(k_\perp, t) = g(k_\perp)\cos(\omega_k t) + if(k_\perp) k_\perp \sin(\omega_k t), \tag{5.14b}$$

with f and g two arbitrary functions.

5.2.3 Three-dimensional quadratic invariants

In the absence of forcing and dissipation, the system (5.8)–(5.10) has two quadratic invariants. The first invariant is the energy which is written at the leading order

$$E = d_e^2 \left\langle j^2 \right\rangle = E_\perp + E_\parallel = d_e^2 \left\langle \left(\nabla_\perp b_\parallel\right)^2 + \left(\nabla_\perp^2 \psi\right)^2 \right\rangle, \tag{5.15}$$

where $\langle\cdot\rangle$ is an ensemble average or, equivalently by ergodicity, a spatial average. E can also be interpreted as the kinetic energy of electrons. As shown hereafter, both $E_\perp$ and $E_\parallel$ are separately conserved at the nonlinear level, however, energy is exchanged between the two at the linear level, thanks to the presence of waves. This definition of energy is valid for both IWW and for IKAW in the limit of small β_i.

In Fourier space, the expressions of the energy density respectively in the directions parallel and perpendicular to the mean magnetic field are $|u_{\parallel,k}|^2 = d_e^2 k_\perp^4 |\psi_k|^2$ and $|u_{\perp,k}|^2 = d_e^2 k_\perp^2 |b_k|^2$. From the equations describing the temporal evolution of ψ and $b_\parallel$ in Fourier space, we obtain the evolution of the energy density (we used the properties $\psi_{-k}^* = \psi_k$ and $b_{-k}^* = b_k$)

$$\frac{\partial |u_{\parallel,k}|^2}{\partial t} - i d_e^2 \Omega_e k_\parallel k_\perp^2 b_k \psi_k^* + c.c. = d_e^3 \int_{(\mathbb{R}^3)^2} S_\parallel^u \left(k_\perp, p_\perp, q_\perp\right) \delta_{kpq} \mathrm{d}\boldsymbol{p}\mathrm{d}\boldsymbol{q} + c.c., \tag{5.16a}$$

$$\frac{\partial |u_{\perp,k}|^2}{\partial t} + i d_e^2 \Omega_e k_\parallel k_\perp^2 b_k \psi_k^* + c.c. = d_e^3 \int_{(\mathbb{R}^3)^2} S_\perp^u \left(k_\perp, p_\perp, q_\perp\right) \delta_{kpq} \mathrm{d}\boldsymbol{p}\mathrm{d}\boldsymbol{q} + c.c., \tag{5.16b}$$

with $S_\parallel^u \left(k_\perp, p_\perp, q_\perp\right)$ and $S_\perp^u \left(k_\perp, p_\perp, q_\perp\right)$ the nonlinear interaction coefficient defined as

$$S_\parallel^u \left(k_\perp, p_\perp, q_\perp\right) \equiv \sin\alpha_k k_\perp^2 p_\perp q_\perp \psi_k \left(q_\perp^2 \psi_q b_p - p_\perp^2 \psi_p b_q\right), \tag{5.17a}$$

$$S_\perp^u \left(k_\perp, p_\perp, q_\perp\right) \equiv \sin\alpha_k p_\perp q_\perp \left(q_\perp^2 - p_\perp^2\right) b_k b_p b_q, \tag{5.17b}$$

where we have used the relation $\boldsymbol{e}_\parallel \cdot (\boldsymbol{e}_{p_\perp} \times \boldsymbol{e}_{q_\perp}) = \sin\alpha_k$ and $c.c.$ denotes the complex conjugate. Parallel $E_\parallel^u$ and perpendicular $E_\perp^u$ energies being the sum of these quantities over all wavenumbers, we find

$$\frac{\partial E_\parallel^u}{\partial t} - i d_e^2 \Omega_e \int_{\mathbb{R}^3} k_\parallel k_\perp^2 b_k \psi_k^* \mathrm{d}\boldsymbol{k} + c.c. = d_e^3 \int_{(\mathbb{R}^3)^3} S_\parallel^u \left(k_\perp, p_\perp, q_\perp\right) \delta_{kpq} \mathrm{d}\boldsymbol{k}\mathrm{d}\boldsymbol{p}\mathrm{d}\boldsymbol{q} + c.c., \tag{5.18a}$$

$$\frac{\partial E_\perp^u}{\partial t} + i d_e^2 \Omega_e \int_{\mathbb{R}^3} k_\parallel k_\perp^2 b_k \psi_k^* \mathrm{d}\boldsymbol{k} + c.c. = d_e^3 \int_{(\mathbb{R}^3)^3} S_\perp^u \left(k_\perp, p_\perp, q_\perp\right) \delta_{kpq} \mathrm{d}\boldsymbol{k}\mathrm{d}\boldsymbol{p}\mathrm{d}\boldsymbol{q} + c.c.. \tag{5.18b}$$

The remarkable property is that the nonlinear contributions are both conserved over time since $S_\parallel^u \left(k_\perp, p_\perp, q_\perp\right)$

and $S^u_\perp(k_\perp, p_\perp, q_\perp)$ verify the following relations

$$S^u_\parallel(k_\perp, p_\perp, q_\perp) + S^u_\parallel(p_\perp, q_\perp, k_\perp) + S^u_\parallel(q_\perp, k_\perp, q_\perp) = 0, \tag{5.19a}$$

$$S^u_\perp(k_\perp, p_\perp, q_\perp) + S^u_\perp(p_\perp, q_\perp, k_\perp) + S^u_\perp(q_\perp, k_\perp, q_\perp) = 0. \tag{5.19b}$$

Then, as said before, the parallel and perpendicular components of the energy are conserved individually at the nonlinear level. The exchanges between the two are only done at the linear level.

The second quadratic invariant is the momentum that can be written in the leading order,

$$H = d_e^2 \left\langle (\nabla_\perp^2 \psi)(\nabla_\perp^2 b_\parallel) \right\rangle. \tag{5.20}$$

The quantity H can be understood as the kinetic helicity of electrons. Unlike energy, momentum is not positively defined. As we will see later, the wave kinetic equations conserve these two invariants on the resonant manifold, which will be introduced in the subsequent section.

5.3 Wave amplitude equation

In Fourier space, IEMHD equations (5.8) and (5.10) become,

$$k_\perp^2 \frac{\partial \psi_k}{\partial t} - i\Omega_e k_\parallel b_k = d_e \int_{(\mathbb{R}^3)^2} \boldsymbol{e}_\parallel \cdot (\boldsymbol{p}_\perp \times \boldsymbol{q}_\perp)\, q_\perp^2 b_p \psi_q \delta^k_{pq} \mathrm{d}\boldsymbol{p}\mathrm{d}\boldsymbol{q}, \tag{5.21a}$$

$$k_\perp^2 \frac{\partial b_k}{\partial t} - i\Omega_e k_\parallel k_\perp^2 \psi_k = d_e \int_{(\mathbb{R}^3)^2} \boldsymbol{e}_\parallel \cdot (\boldsymbol{p}_\perp \times \boldsymbol{q}_\perp)\, q_\perp^2 b_p b_q \delta^k_{pq} \mathrm{d}\boldsymbol{p}\mathrm{d}\boldsymbol{q}, \tag{5.21b}$$

with $\delta^k_{pq} \equiv \delta(\boldsymbol{k} - \boldsymbol{p} - \boldsymbol{q})$ the Dirac distribution coming from the Fourier transform of the nonlinear terms. We introduce the canonical variables as follows,

$$\psi_k \equiv -\frac{1}{2d_e k_\perp^2} \sum_{s_k} s_k A^{s_k}_{\boldsymbol{k}}, \qquad b_k \equiv \frac{1}{2d_e k_\perp} \sum_{s_k} A^{s_k}_{\boldsymbol{k}}, \tag{5.22}$$

where $s_k = \pm 1$ is the directional polarization that defines the direction of the wave propagation with $s_k k_\parallel \geq 0$. After a little calculation, we find

$$\left(\frac{\partial}{\partial t} + i s_k \omega_k\right) A^{s_k}_{\boldsymbol{k}} = \frac{1}{4} \sum_{s_p s_q} \int_{(\mathbb{R}^3)^2} \frac{\boldsymbol{e}_\parallel \cdot (\boldsymbol{p}_\perp \times \boldsymbol{q}_\perp)}{k_\perp p_\perp q_\perp} \left(q_\perp^2 + s_k s_q k_\perp q_\perp\right) A^{s_p}_{\boldsymbol{p}} A^{s_q}_{\boldsymbol{q}} \delta^k_{pq} \mathrm{d}\boldsymbol{p}\mathrm{d}\boldsymbol{q}. \tag{5.23}$$

By making the following change of variable $A_{\boldsymbol{k}}^{s_k} = \epsilon a_{\boldsymbol{k}}^{s_k} e^{-is_k\omega_k t}$, where $\epsilon \ll 1$ is a small positive parameter, the linear part of this equation vanishes and we obtain the fundamental equation describing the slow temporal evolution – thanks to ϵ – of the wave amplitude

$$\frac{\partial a_{\boldsymbol{k}}^{s_k}}{\partial t} = \frac{\epsilon}{4} \sum_{s_p s_q} \int_{(\mathbb{R}^3)^2} \mathcal{H}_{\boldsymbol{kpq}}^{s_k s_p s_q} a_{\boldsymbol{p}}^{s_p} a_{\boldsymbol{q}}^{s_q} \mathrm{e}^{i\Omega_{pq}^k t} \delta_{pq}^k \mathrm{d}\boldsymbol{p}\mathrm{d}\boldsymbol{q}, \tag{5.24}$$

with $\Omega_{pq}^k \equiv s_k\omega_k - s_p\omega_p - s_q\omega_q$ and $\mathcal{H}_{\boldsymbol{kpq}}^{s_k s_p s_q} \equiv \boldsymbol{e}_\parallel \cdot (\boldsymbol{p}_\perp \times \boldsymbol{q}_\perp) \left(q_\perp^2 + s_k s_q k_\perp q_\perp\right) / \left(k_\perp p_\perp q_\perp\right)$ the nonlinear interaction coefficient which depends on the nonlinearities of the system. The presence of the complex exponential is fundamental for the asymptotic closure: as we are interested in the long-time behavior with respect to the linear timescale $(1/\omega)$, the contribution of the exponential is mostly zero. Only (secular) terms for which $\Omega_{pq}^k = 0$ will survive [7, 55]. Adding to this the relation imposed by the Dirac distribution, we can obtain the following resonance condition (symmetries in $\boldsymbol{p}$ and $\boldsymbol{q}$ are used)

$$\boldsymbol{k} + \boldsymbol{p} + \boldsymbol{q} = \boldsymbol{0}, \tag{5.25a}$$

$$s_k\omega_k + s_p\omega_p + s_q\omega_q = 0. \tag{5.25b}$$

After a few manipulations, we find the anisotropic ($k_\parallel \ll k_\perp$) relationships

$$\frac{s_q q_\perp - s_p p_\perp}{s_k\omega_k} = \frac{s_k k_\perp - s_q q_\perp}{s_p\omega_p} = \frac{s_p p_\perp - s_k k_\perp}{s_q\omega_q}, \tag{5.26}$$

which will be useful to prove the conservation of the quadratic invariants. This is also useful to highlight the anisotropic character of the system, whereby it exhibits an inherent inclination to distribute its energy across higher perpendicular modes $k_\perp$ rather than parallel ones $k_\parallel$. Indeed, let us consider the particular case of super-local interactions which give, in general, a dominant contribution to the turbulent dynamics. In this case, we have $k_\perp \simeq p_\perp \simeq q_\perp$ and the resonance condition simplifies into

$$\frac{s_q - s_p}{s_k k_\parallel} \simeq \frac{s_k - s_q}{s_p p_\parallel} \simeq \frac{s_p - s_k}{s_q q_\parallel}. \tag{5.27}$$

If $k_\parallel$ is non-zero, the left-hand term will only give a non-negligible contribution when $s_p = -s_q$. We do not consider the case $s_p = s_q$ which is not relevant to the first order in the case of local interactions as can be seen in expression (5.24) which then becomes negligible (it is easier to see that in equations (5.29)–(5.30) after using the symmetry in $\boldsymbol{p}$ and $\boldsymbol{q}$). The immediate consequence is that either the middle or the right

term has its numerator canceling (to first order), which implies that the associated denominator must also cancel (to first order) to satisfy the equality: for example, if $s_k = s_p$ then $q_\parallel \simeq 0$. This condition means that the transfer in the parallel direction is negligible because the integration in the parallel direction of equation (5.24) is then reduced to a few modes (since $p_\parallel \simeq k_\parallel$) which strongly limits the transfer between the parallel modes. The cascade in the parallel direction is thus possible but relatively weak compared to the one in the perpendicular direction.

Before applying the spectral formalism of wave turbulence, it is necessary to symmetrize the fundamental equation (5.24) under the exchange of $\boldsymbol{p}$ and $\boldsymbol{q}$. To do this, we take advantage of the summation over the s_p and s_q polarizations and introduce

$$L^{s_k s_p s_q}_{\boldsymbol{kpq}} = \frac{1}{2}\left(\mathcal{H}^{s_k s_p s_q}_{\boldsymbol{kpq}} + \mathcal{H}^{s_k s_q s_p}_{\boldsymbol{kqp}}\right), \tag{5.28}$$

to finally obtain after a little calculation

$$\boxed{\frac{\partial a^{s_k}_{\boldsymbol{k}}}{\partial t} = \epsilon \sum_{s_p s_q} \int_{(\mathbb{R}^3)^2} L^{s_k s_p s_q}_{\boldsymbol{kpq}} a^{s_p}_{\boldsymbol{p}} a^{s_q}_{\boldsymbol{q}} \mathrm{e}^{i\Omega^k_{pq} t} \delta^k_{pq} \mathrm{d}\boldsymbol{p}\mathrm{d}\boldsymbol{q}}, \tag{5.29}$$

where

$$L^{s_k s_p s_q}_{\boldsymbol{kpq}} \equiv \frac{\boldsymbol{e}_\parallel \cdot (\boldsymbol{p}_\perp \times \boldsymbol{q}_\perp)}{8 k_\perp p_\perp q_\perp} \left(s_q q_\perp - s_p p_\perp\right)\left(s_k k_\perp + s_p p_\perp + s_q q_\perp\right). \tag{5.30}$$

This operator has, among others, the following symmetries

$$L^{s_k s_p s_q}_{\boldsymbol{kpq}} = L^{-s_k - s_p - s_q}_{\boldsymbol{kpq}} = L^{s_k s_p s_q}_{\boldsymbol{-k-p-q}} = L^{s_k s_p s_q}_{\boldsymbol{-kpq}} = L^{s_k s_p s_q}_{\boldsymbol{k-p-q}}, \tag{5.31a}$$

$$L^{s_k s_p s_q}_{\boldsymbol{kpq}} = L^{s_k s_q s_p}_{\boldsymbol{kqp}}, \tag{5.31b}$$

$$L^{s_k - s_p - s_q}_{\boldsymbol{kpq}} = L^{-s_k s_p s_q}_{\boldsymbol{kpq}}, \tag{5.31c}$$

$$L^{s_k s_p s_q}_{\boldsymbol{0pq}} = 0. \tag{5.31d}$$

Equation (5.29) is our fundamental equation, the starting point to derive the wave kinetic equations. Note that the nonlinear coupling associated with the wavevectors $\boldsymbol{p}$ and $\boldsymbol{q}$ vanishes when they are collinear ($k = 0$ is a particular case). Additionally, the nonlinear coupling vanishes whenever the wavenumbers $p_\perp$ and $q_\perp$ are equal if their associated polarities s_p and s_q are also equal. This was also observed in EMHD (for scales larger than d_e) and seems to be a general property of helical waves [24, 28, 40, 67, 68]. The nonlinear interaction, being a three-wave process, gives rise to eight potential resonant configurations when

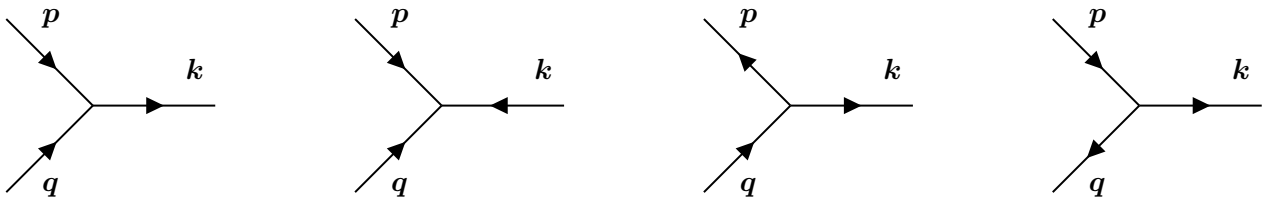

Figure 5.1: Diagram of the four fundamental interactions of the IWW/IKAW turbulence.

considering the polarities. However, by leveraging the symmetries of the nonlinear operator $L_{\boldsymbol{kpq}}^{s_k s_p s_q}$, we can simplify this to just four types of interactions encompassing all the possible polarities (cf. Figure 5.1).

5.4 Phenomenology of wave turbulence

Before going into the deep analysis of the wave turbulence regime, it is important to have a simple (phenomenological) picture in mind of the physical process that we are going to describe. According to the properties given in Section 5.3, if we assume that the nonlinear transfer is mainly driven by super-local interactions ($k \sim p \sim q$), which is a classical assumption in the turbulence phenomenology, then we can consider only stochastic collisions between counter-propagating waves ($s_p = -s_q$) to derive the form of the spectra. Note that non-local interactions (which include copropagating waves) also provide a contribution to the nonlinear dynamics but, as will be shown in Section 5.6.3 with the convergence study, their contributions are not dominant for the formation of a stationary spectrum.

To find the transfer time and then the energy spectrum, we first need to evaluate the modification of a wave produced by one collision. Starting from the momentum equation (for simplicity we write the wave amplitude as a_ℓ and assume anisotropy with $k \sim k_\perp$), we have

$$a_\ell(t+\tau_\mathrm{L}) \sim a_\ell(t) + \tau_\mathrm{L}\frac{\partial a}{\partial t} \sim a_\ell(t) + \tau_\mathrm{L}\frac{a_\ell^2}{\ell_\perp},$$

where τ_L is the duration of one collision; in other words, after a collision, the distortion of a wave is $\Delta_\mathrm{L} a_\ell \simeq a_\ell^2/\ell_\perp$. This distortion is going to increase with time in such a way that after N stochastic collisions, the cumulative effect may be evaluated like a random walk [23]

$$\sum_{i=1}^{N} \Delta_i a_\ell \sim \tau_\mathrm{L}\frac{a_\ell^2}{\ell_\perp}\sqrt{\frac{t}{\tau_\mathrm{L}}}.$$

The transfer time, $\tau_{\rm tr}$, that we are looking for is the time for which the cumulative distortion is of order one, i.e., of the order of the wave itself:

$$a_\ell \sim \tau_{\rm L} \frac{a_\ell^2}{\ell_\perp} \sqrt{\frac{\tau_{\rm tr}}{\tau_{\rm L}}}.$$

Then, we obtain

$$\tau_{\rm tr} \sim \frac{1}{\tau_{\rm L}} \frac{\ell_\perp^2}{a_\ell^2} \sim \frac{\tau_{\rm NL}^2}{\tau_{\rm L}},$$

where $\tau_{\rm NL} \equiv \ell_\perp / a_\ell$. This is basically the formula that we are going to use to evaluate the energy spectra. Let us consider IWW/IKAW for which $\tau_{\rm L} \sim 1/\omega_k \sim k_\perp / k_\parallel$. A classical calculation with a constant energy flux $\varepsilon \sim E_\ell / \tau_{\rm tr}$, leads finally to the bi-dimensional axisymmetric energy spectrum

$$E\left(k_\perp, k_\parallel\right) \sim \sqrt{\varepsilon \Omega_e} k_\perp^{-5/2} k_\parallel^{-1/2}. \tag{5.32}$$

As we will see in Section 5.6.2, this corresponds to the exact solution of the wave turbulence theory. The same calculation could be done for the momentum but, as we will see, it presents a more subtle behavior that phenomenology cannot describe.

5.5 Kinetic equations

5.5.1 Definition of the energy density tensor

We now move on to a statistical description. We use the ensemble average $\langle \cdot \rangle$ and define the following spectral correlators (cumulants) for homogeneous turbulence (we assume $\langle a_k^{s_k} \rangle = 0$)

$$\left\langle a_{\boldsymbol{k}}^{s_k} a_{\boldsymbol{k'}}^{s'_k} \right\rangle = e_{\boldsymbol{k'}}^{s'_k} \delta_{kk'} \delta_{s'_k}^{s_k}, \tag{5.33}$$

with $e^{s'_k}\left(\boldsymbol{k'}\right) = e_{\boldsymbol{k'}}^{s'_k}$. We observe the presence of the delta function $\delta_{s'_k}^{s_k}$ meaning that two-point correlations of opposite polarities have no long-time influence in the wave turbulence regime. The other delta function is the consequence of the statistical homogeneity assumption. The objective of the wave turbulence theory is to derive a self-consistent equation for the time evolution of this spectral correlator; this is the kinetic equation. In this development, we have to face the classical closure problem: a hierarchy of statistical equations of increasingly higher order emerges. In contrast to strong turbulence, in the weak wave turbulence regime we can use the timescale separation to achieve a natural closure of the system [7, 55]. We

start from (5.29) and write successively equations for the second- and third-order moments,

$$\frac{\partial}{\partial t}\left\langle a_{\boldsymbol{k}}^{s_k} a_{\boldsymbol{k'}}^{s'_k}\right\rangle = \epsilon \sum_{s_p s_q} \int_{(\mathbb{R}^3)^2} \left(L_{\boldsymbol{kpq}}^{s_k s_p s_q} \left\langle a_{\boldsymbol{k'}}^{s'_k} a_{\boldsymbol{p}}^{s_p} a_{\boldsymbol{q}}^{s_q}\right\rangle \mathrm{e}^{i\Omega_{pq}^{k} t} \delta_{pq}^{k} + L_{\boldsymbol{k'pq}}^{s'_k s_p s_q} \left\langle a_{\boldsymbol{k}}^{s_k} a_{\boldsymbol{p}}^{s_p} a_{\boldsymbol{q}}^{s_q}\right\rangle \mathrm{e}^{i\Omega_{pq}^{k'} t} \delta_{pq}^{k'} \right) \mathrm{d}\boldsymbol{p}\mathrm{d}\boldsymbol{q}, \tag{5.34}$$

and

$$\begin{aligned}\frac{\partial}{\partial t}\left\langle a_{\boldsymbol{k}}^{s_k} a_{\boldsymbol{k'}}^{s'_k} a_{\boldsymbol{k''}}^{s''_k}\right\rangle = \epsilon \sum_{s_p s_q} \int_{(\mathbb{R}^3)^2} \Big(& L_{\boldsymbol{kpq}}^{s_k s_p s_q} \left\langle a_{\boldsymbol{k'}}^{s'_k} a_{\boldsymbol{k''}}^{s''_k} a_{\boldsymbol{p}}^{s_p} a_{\boldsymbol{q}}^{s_q}\right\rangle \mathrm{e}^{i\Omega_{pq}^{k} t} \delta_{pq}^{k} + L_{\boldsymbol{k'pq}}^{s'_k s_p s_q} \left\langle a_{\boldsymbol{k}}^{s_k} a_{\boldsymbol{k''}}^{s''_k} a_{\boldsymbol{p}}^{s_p} a_{\boldsymbol{q}}^{s_q}\right\rangle \mathrm{e}^{i\Omega_{pq}^{k'} t} \delta_{pq}^{k'} \\ & + L_{\boldsymbol{k''pq}}^{s''_k s_p s_q} \left\langle a_{\boldsymbol{k}}^{s_k} a_{\boldsymbol{k'}}^{s'_k} a_{\boldsymbol{p}}^{s_p} a_{\boldsymbol{q}}^{s_q}\right\rangle \mathrm{e}^{i\Omega_{pq}^{k''} t} \delta_{pq}^{k''} \Big) \mathrm{d}\boldsymbol{p}\mathrm{d}\boldsymbol{q}.\end{aligned} \tag{5.35}$$

A natural closure arises for times asymptotically large compare to the linear wave timescale (see, e.g., [51, 55, 56]). An important aspect is the uniformity of the development, which was discussed first by [7]. In this case, the fourth-order moment does not contribute at large time and, therefore

$$\begin{aligned}\left\langle a_{\boldsymbol{k'}}^{s'_k} a_{\boldsymbol{k''}}^{s''_k} a_{\boldsymbol{p}}^{s_p} a_{\boldsymbol{q}}^{s_q}\right\rangle = & \left\langle a_{\boldsymbol{p}}^{s_p} a_{\boldsymbol{q}}^{s_q}\right\rangle \left\langle a_{\boldsymbol{k'}}^{s'_k} a_{\boldsymbol{k''}}^{s''_k}\right\rangle + \left\langle a_{\boldsymbol{p}}^{s_p} a_{\boldsymbol{k'}}^{s'_k}\right\rangle \left\langle a_{\boldsymbol{q}}^{s_q} a_{\boldsymbol{k''}}^{s''_k}\right\rangle + \left\langle a_{\boldsymbol{p}}^{s_p} a_{\boldsymbol{k''}}^{s''_k}\right\rangle \left\langle a_{\boldsymbol{q}}^{s_q} a_{\boldsymbol{k'}}^{s'_k}\right\rangle \\ & + \left\langle a_{\boldsymbol{p}}^{s_p} a_{\boldsymbol{q}}^{s_q} a_{\boldsymbol{k'}}^{s'_k}\right\rangle \left\langle a_{\boldsymbol{k''}}^{s''_k}\right\rangle + \left\langle a_{\boldsymbol{p}}^{s_p} a_{\boldsymbol{q}}^{s_q} a_{\boldsymbol{k''}}^{s''_k}\right\rangle \left\langle a_{\boldsymbol{k'}}^{s'_k}\right\rangle + \left\langle a_{\boldsymbol{p}}^{s_p} a_{\boldsymbol{k'}}^{s'_k} a_{\boldsymbol{k''}}^{s''_k}\right\rangle \left\langle a_{\boldsymbol{q}}^{s_q}\right\rangle + \left\langle a_{\boldsymbol{q}}^{s_q} a_{\boldsymbol{k'}}^{s'_k} a_{\boldsymbol{k''}}^{s''_k}\right\rangle \left\langle a_{\boldsymbol{p}}^{s_k}\right\rangle .\end{aligned} \tag{5.36}$$

Since, we assumed zero mean fields, the terms of the second line of the precedent relation are identically zero, and the nonlinear regeneration of third-order moments depends essentially on the products of second-order moments. Thanks to the integration on the dummy variables $\boldsymbol{p}$ and $\boldsymbol{q}$, to their symmetry and the symmetry between the polarizations s_p and s_q, we make the following simplification in advance

$$\left\langle a_{\boldsymbol{k'}}^{s'_k} a_{\boldsymbol{k''}}^{s''_k} a_{\boldsymbol{p}}^{s_p} a_{\boldsymbol{q}}^{s_q}\right\rangle = \left\langle a_{\boldsymbol{p}}^{s_p} a_{\boldsymbol{q}}^{s_q}\right\rangle \left\langle a_{\boldsymbol{k'}}^{s'_k} a_{\boldsymbol{k''}}^{s''_k}\right\rangle + 2 \left\langle a_{\boldsymbol{p}}^{s_p} a_{\boldsymbol{k'}}^{s'_k}\right\rangle \left\langle a_{\boldsymbol{q}}^{s_q} a_{\boldsymbol{k''}}^{s''_k}\right\rangle , \tag{5.37}$$

and also introduce the spectral energy density $e^{s'_k}(\boldsymbol{k'}) = e_{\boldsymbol{k'}}^{s'_k}$ such as

$$\left\langle a_{\boldsymbol{k}}^{s_k} a_{\boldsymbol{k'}}^{s'_k}\right\rangle = e_{\boldsymbol{k'}}^{s'_k} \delta_{kk'} \delta_{s'_k}^{s_k}, \tag{5.38}$$

where $\delta_{kk'} = \delta(\boldsymbol{k}+\boldsymbol{k'})$ and $\delta^{s_k}_{s'_k} = \delta(s_k - s'_k)$. The last delta condition ensures that the contribution is non-negligible over long times. We then write

$$\left\langle a^{s'_k}_{\boldsymbol{k'}} a^{s''_k}_{\boldsymbol{k''}} a^{s_p}_{\boldsymbol{p}} a^{s_q}_{\boldsymbol{q}} \right\rangle = e^{s_p}_{\boldsymbol{p}} \delta_{pq} \delta^{s_p}_{s_q} e^{s'_k}_{\boldsymbol{k'}} \delta_{k'k''} \delta^{s'_k}_{s''_k} + 2 e^{s_p}_{\boldsymbol{p}} \delta_{pk'} \delta^{s_p}_{s'_k} e^{s_q}_{\boldsymbol{q}} \delta_{qk''} \delta^{s_q}_{s''_k}, \tag{5.39a}$$

$$\left\langle a^{s_k}_{\boldsymbol{k}} a^{s''_k}_{\boldsymbol{k''}} a^{s_p}_{\boldsymbol{p}} a^{s_q}_{\boldsymbol{q}} \right\rangle = e^{s_p}_{\boldsymbol{p}} \delta_{pq} \delta^{s_p}_{s_q} e^{s_k}_{\boldsymbol{k}} \delta_{kk''} \delta^{s_k}_{s''_k} + 2 e^{s_p}_{\boldsymbol{p}} \delta_{pk} \delta^{s_p}_{s_k} e^{s_q}_{\boldsymbol{q}} \delta_{qk''} \delta^{s_q}_{s''_k}, \tag{5.39b}$$

$$\left\langle a^{s_k}_{\boldsymbol{k}} a^{s'_k}_{\boldsymbol{k'}} a^{s_p}_{\boldsymbol{p}} a^{s_q}_{\boldsymbol{q}} \right\rangle = e^{s_p}_{\boldsymbol{p}} \delta_{pq} \delta^{s_p}_{s_q} e^{s_k}_{\boldsymbol{k}} \delta_{kk'} \delta^{s_k}_{s'_k} + 2 e^{s_p}_{\boldsymbol{p}} \delta_{pk} \delta^{s_p}_{s_k} e^{s_q}_{\boldsymbol{q}} \delta_{qk'} \delta^{s_q}_{s'_k}. \tag{5.39c}$$

We note that, on the one hand, the δ_{pq} imposes $\boldsymbol{p} = -\boldsymbol{q}$ and, on the other hand, the δ^k_{pq} imposes $\boldsymbol{k} = \boldsymbol{p}+\boldsymbol{q}$. Thus, these two conditions lead to $\boldsymbol{k} = \boldsymbol{0}$. Since $L^{s_k s_p s_q}_{\boldsymbol{0pq}} = 0$, the first term on the right side hand side is zero, and we get

$$\begin{aligned}\frac{\partial}{\partial t}\left\langle a^{s_k}_{\boldsymbol{k}} a^{s'_k}_{\boldsymbol{k'}} a^{s''_k}_{\boldsymbol{k''}} \right\rangle = 2\epsilon \sum_{s_p s_q} \int_{(\mathbb{R}^3)^2} \Big(& L^{s_k s_p s_q}_{\boldsymbol{-kpq}} e^{s_p}_{\boldsymbol{p}} e^{s_q}_{\boldsymbol{q}} \mathrm{e}^{i\Omega^k_{pq} t} \delta^{s_p}_{s'_k} \delta^{s_q}_{s''_k} \delta_{pk'} \delta_{qk''} \delta^k_{pq} + L^{s'_k s_p s_q}_{\boldsymbol{-k'pq}} e^{s_p}_{\boldsymbol{p}} e^{s_q}_{\boldsymbol{q}} \mathrm{e}^{i\Omega^{k'}_{pq} t} \delta^{s_p}_{s_k} \delta^{s_q}_{s''_k} \delta_{pk} \delta_{qk''} \delta^{k'}_{pq} \\ & + L^{s''_k s_p s_q}_{\boldsymbol{-k''pq}} e^{s_p}_{\boldsymbol{p}} e^{s_q}_{\boldsymbol{q}} \mathrm{e}^{i\Omega^{k''}_{pq} t} \delta^{s_p}_{s_k} \delta^{s_q}_{s'_k} \delta_{pk} \delta_{qk'} \delta^{k''}_{pq} \Big) \mathrm{d}\boldsymbol{p} \mathrm{d}\boldsymbol{q}.\end{aligned} \tag{5.40}$$

After integration and summation of the polarizations, we obtain

$$\frac{\partial}{\partial t}\left\langle a^{s_k}_{\boldsymbol{k}} a^{s'_k}_{\boldsymbol{k'}} a^{s''_k}_{\boldsymbol{k''}} \right\rangle = 2\epsilon \mathrm{e}^{i\Omega_{kk'k''} t} \delta_{kk'k''} \left(L^{s_k s'_k s''_k}_{\boldsymbol{-k-k'-k''}} e^{s'_k}_{\boldsymbol{k'}} e^{s''_k}_{\boldsymbol{k''}} + L^{s'_k s_k s''_k}_{\boldsymbol{-k'-k-k''}} e^{s_k}_{\boldsymbol{k}} e^{s''_k}_{\boldsymbol{k''}} + L^{s''_k s_k s'_k}_{\boldsymbol{-k''-k-k'}} e^{s_k}_{\boldsymbol{k}} e^{s'_k}_{\boldsymbol{k'}} \right), \tag{5.41}$$

where $\Omega_{kk'k''} = s_k\omega_k + s'_k\omega'_k + s''_k\omega''_k$ and where we used the relation $e^{s_k}_{\boldsymbol{-k}} = e^{s_k}_{\boldsymbol{k}}$ due to the homogeneity of the turbulence. Further simplifications can be made. Firstly, the interaction coefficient has the following symmetry $L^{s_k s'_k s''_k}_{\boldsymbol{-k-k'-k''}} = L^{s_k s'_k s''_k}_{\boldsymbol{kk'k''}}$. Secondly, we introduce $L^{s_k s_p s_q}_{\boldsymbol{kpq}} \equiv (s_q q_\perp - s_p p_\perp) M^{s_k s_p s_q}_{\boldsymbol{kpq}}$ which is convenient for the calculations. We obtain

$$\begin{aligned}\frac{\partial}{\partial t}\left\langle a^{s_k}_{\boldsymbol{k}} a^{s'_k}_{\boldsymbol{k'}} a^{s''_k}_{\boldsymbol{k''}} \right\rangle = 2\epsilon \mathrm{e}^{i\Omega_{kk'k''} t} \delta_{kk'k''} \Big[& \left(s''_k k''_\perp - s'_k k'_\perp\right) M^{s_k s'_k s''_k}_{\boldsymbol{kk'k''}} e^{s'_k}_{\boldsymbol{k'}} e^{s''_k}_{\boldsymbol{k''}} + \left(s''_k k''_\perp - s_k k_\perp\right) M^{s'_k s_k s''_k}_{\boldsymbol{k'kk''}} e^{s_k}_{\boldsymbol{k}} e^{s''_k}_{\boldsymbol{k''}} \\ & + \left(s'_k k'_\perp - s_k k_\perp\right) M^{s''_k s_k s'_k}_{\boldsymbol{k''kk'}} e^{s_k}_{\boldsymbol{k}} e^{s'_k}_{\boldsymbol{k'}} \Big].\end{aligned} \tag{5.42}$$

We observe that $M^{s_k s'_k s''_k}_{\boldsymbol{kk'k''}} = M^{s''_k s_k s'_k}_{\boldsymbol{k''kk'}} = -M^{s'_k s_k s''_k}_{\boldsymbol{k'kk''}}$ thus the previous expression can be simplified

$$\begin{aligned}\frac{\partial}{\partial t}\left\langle a^{s_k}_{\boldsymbol{k}} a^{s'_k}_{\boldsymbol{k'}} a^{s''_k}_{\boldsymbol{k''}} \right\rangle = 2\epsilon \mathrm{e}^{i\Omega_{kk'k''} t} \delta_{kk'k''} M^{s_k s'_k s''_k}_{\boldsymbol{kk'k''}} \Big[& \left(s''_k k''_\perp - s'_k k'_\perp\right) e^{s'_k}_{\boldsymbol{k'}} e^{s''_k}_{\boldsymbol{k''}} - \left(s''_k k''_\perp - s_k k_\perp\right) e^{s_k}_{\boldsymbol{k}} e^{s''_k}_{\boldsymbol{k''}} \\ & + \left(s'_k k'_\perp - s_k k_\perp\right) e^{s_k}_{\boldsymbol{k}} e^{s'_k}_{\boldsymbol{k'}} \Big].\end{aligned} \tag{5.43}$$

We note that $s_k''k'' - s_k'k' = s_k''k'' - s_kk + s_kk - s_k'k'$, and thus

$$\begin{aligned}\frac{\partial}{\partial t}\left\langle a_{\boldsymbol{k}}^{s_k} a_{\boldsymbol{k'}}^{s_k'} a_{\boldsymbol{k''}}^{s_k''}\right\rangle = 2\epsilon \mathrm{e}^{i\Omega_{kk'k''}t}\delta_{kk'k''} M_{\boldsymbol{kk'k''}}^{s_k s_k' s_k''} \Big[&\left(s_k''k_\perp'' - s_kk_\perp\right)\left(e_{\boldsymbol{k'}}^{s_k'} e_{\boldsymbol{k''}}^{s_k''} - e_{\boldsymbol{k}}^{s_k} e_{\boldsymbol{k''}}^{s_k''}\right) \\ &+ \left(s_k'k_\perp' - s_kk_\perp\right)\left(e_{\boldsymbol{k}}^{s_k} e_{\boldsymbol{k'}}^{s_k'} - e_{\boldsymbol{k'}}^{s_k'} e_{\boldsymbol{k''}}^{s_k''}\right)\Big].\end{aligned} \tag{5.44}$$

After integration over time, one has

$$\begin{aligned}\left\langle a_{\boldsymbol{k}}^{s_k} a_{\boldsymbol{k'}}^{s_k'} a_{\boldsymbol{k''}}^{s_k''}\right\rangle = 2\epsilon\Delta\left(\Omega_{kk'k''}\right)\delta_{kk'k''} M_{\boldsymbol{kk'k''}}^{s_k s_k' s_k''} \Big[&\left(s_kk_\perp - s_k''k_\perp''\right) e_{\boldsymbol{k''}}^{s_k''}\left(e_{\boldsymbol{k}}^{s_k} - e_{\boldsymbol{k'}}^{s_k'}\right) \\ &+ \left(s_k'k_\perp' - s_kk_\perp\right) e_{\boldsymbol{k'}}^{s_k'}\left(e_{\boldsymbol{k}}^{s_k} - e_{\boldsymbol{k''}}^{s_k''}\right)\Big],\end{aligned} \tag{5.45}$$

with

$$\Delta\left(x\right) = \int_0^{t\gg 1/\omega} \mathrm{e}^{ix\tau}\mathrm{d}\tau = \frac{\mathrm{e}^{ixt}-1}{ix}. \tag{5.46}$$

Now, we can introduce expression (5.45) for the third-order moment into equation (5.34)

$$\begin{aligned}\frac{\partial}{\partial t}\left\langle a_{\boldsymbol{k}}^{s_k} a_{\boldsymbol{k'}}^{s_k'}\right\rangle &= \frac{\partial e_{\boldsymbol{k}}^{s_k}}{\partial t}\delta_{kk'}\delta_{s_k'}^{s_k} \\ &= \epsilon\sum_{s_ps_q}\int_{(\mathbb{R}^3)^2}\left(L_{\boldsymbol{-kpq}}^{s_k s_p s_q}\left\langle a_{\boldsymbol{k'}}^{s_k'} a_{\boldsymbol{p}}^{s_p} a_{\boldsymbol{q}}^{s_q}\right\rangle \mathrm{e}^{i\Omega_{pq}^k t}\delta_{pq}^k + L_{\boldsymbol{-k'pq}}^{s_k' s_p s_q}\left\langle a_{\boldsymbol{k}}^{s_k} a_{\boldsymbol{p}}^{s_p} a_{\boldsymbol{q}}^{s_q}\right\rangle \mathrm{e}^{i\Omega_{pq}^{k'} t}\delta_{pq}^{k'}\right)\delta_{s_k'}^{s_k}\delta_{kk'}\mathrm{d}\boldsymbol{p}\mathrm{d}\boldsymbol{q} \\ &= I_1 + I_2,\end{aligned} \tag{5.47}$$

where I_1 and I_2 are the two integrals involving the interaction coefficients $L_{\boldsymbol{-kpq}}^{s_k s_p s_q}$ and $L_{\boldsymbol{-k'pq}}^{s_k' s_p s_q}$, respectively. Expressing $L_{\boldsymbol{kpq}}^{s_k s_p s_q}$ as a function of $M_{\boldsymbol{kpq}}^{s_k s_p s_q}$, the first integral becomes

$$\begin{aligned}I_1 = 2\epsilon^2\sum_{s_ps_q}\int_{(\mathbb{R}^3)^2}&\left(s_qq_\perp - s_pp_\perp\right)\left|M_{\boldsymbol{-kpq}}^{s_k s_p s_q}\right|^2\Delta\left(\Omega_{-kpq}\right)\mathrm{e}^{i\Omega_{pq}^k t}\delta_{pq}^k \\ &\times\left[\left(s_kk_\perp - s_qq_\perp\right)e_{\boldsymbol{q}}^{s_q}\left(e_{\boldsymbol{k}}^{s_k} - e_{\boldsymbol{p}}^{s_p}\right) + \left(s_pp_\perp - s_kk_\perp\right)e_{\boldsymbol{p}}^{s_p}\left(e_{\boldsymbol{k}}^{s_k} - e_{\boldsymbol{q}}^{s_q}\right)\right]\mathrm{d}\boldsymbol{p}\mathrm{d}\boldsymbol{q}.\end{aligned} \tag{5.48}$$

We note that $\Delta\left(\Omega_{-kpq}\right)\mathrm{e}^{i\Omega_{pq}^k t} = \Delta\left(\Omega_{pq}^k\right)$. The long-time behavior is given by the Riemann-Lebesgue lemma

$$\Delta(x) \xrightarrow{t\to\infty} \pi\delta(x) + i\mathcal{P}\left(\frac{1}{x}\right). \tag{5.49}$$

After a last change of variable, we find $(\boldsymbol{p},\boldsymbol{q}) \to (-\boldsymbol{p},-\boldsymbol{q})$

$$\begin{aligned} I_1 =& 2\epsilon^2 \sum_{s_p s_q} \int_{(\mathbb{R}^3)^2} \left[(s_k k_\perp - s_q q_\perp)\, e_{\boldsymbol{q}}^{s_q} \left(e_{\boldsymbol{k}}^{s_k} - e_{\boldsymbol{p}}^{s_p} \right) + (s_p p_\perp - s_k k_\perp)\, e_{\boldsymbol{p}}^{s_p} \left(e_{\boldsymbol{k}}^{s_k} - e_{\boldsymbol{q}}^{s_q} \right) \right] \\ & \times (s_q q_\perp - s_p p_\perp) \left| M_{\boldsymbol{kpq}}^{s_k s_p s_q} \right|^2 \left[\pi \delta\left(\Omega_{kpq}\right) + i\mathcal{P}\left(\frac{1}{\Omega_{kpq}} \right) \right] \delta_{kpq} \mathrm{d}\boldsymbol{p} \mathrm{d}\boldsymbol{q}. \end{aligned} \tag{5.50}$$

The same manipulation with I_2 without performing the change of variable leads to

$$\begin{aligned} I_2 =& 2\epsilon^2 \sum_{s_p s_q} \int_{(\mathbb{R}^3)^2} \left[(s_k k_\perp - s_q q_\perp)\, e_{\boldsymbol{q}}^{s_q} \left(e_{\boldsymbol{k}}^{s_k} - e_{\boldsymbol{p}}^{s_p} \right) + (s_p p_\perp - s_k k_\perp)\, e_{\boldsymbol{p}}^{s_p} \left(e_{\boldsymbol{k}}^{s_k} - e_{\boldsymbol{q}}^{s_q} \right) \right] \\ & \times (s_q q_\perp - s_p p_\perp) \left| M_{\boldsymbol{kpq}}^{s_k s_p s_q} \right|^2 \left[\pi \delta\left(\Omega_{kpq}\right) - i\mathcal{P}\left(\frac{1}{\Omega_{kpq}} \right) \right] \delta_{kpq} \mathrm{d}\boldsymbol{p} \mathrm{d}\boldsymbol{q}, \end{aligned} \tag{5.51}$$

and the sum of these two integrals gives

$$\begin{aligned} \frac{\partial e_{\boldsymbol{k}}^{s_k}}{\partial t} =& 4\pi\epsilon^2 \sum_{s_p s_q} \int_{(\mathbb{R}^3)^2} \left[(s_k k_\perp - s_q q_\perp)\, e_{\boldsymbol{q}}^{s_q} \left(e_{\boldsymbol{k}}^{s_k} - e_{\boldsymbol{p}}^{s_p} \right) + (s_p p_\perp + s_k k_\perp)\, e_{\boldsymbol{p}}^{s_p} \left(e_{\boldsymbol{k}}^{s_k} - e_{\boldsymbol{q}}^{s_q} \right) \right] \\ & \times (s_q q_\perp - s_p p_\perp) \left| M_{\boldsymbol{kpq}}^{s_k s_p s_q} \right|^2 \delta\left(\Omega_{kpq}\right) \delta_{kpq} \mathrm{d}\boldsymbol{p} \mathrm{d}\boldsymbol{q}. \end{aligned} \tag{5.52}$$

Using the symmetries of the resonant conditions, we have

$$\begin{aligned} \frac{\partial e_{\boldsymbol{k}}^{s_k}}{\partial t} =& \frac{\pi\epsilon^2}{16} \sum_{s_p s_q} \int_{(\mathbb{R}^3)^2} \frac{(s_q q_\perp - s_p p_\perp)^2}{s_k \omega_k} \frac{\sin^2 \alpha_k}{k_\perp^2} \left(s_k k_\perp + s_p p_\perp + s_q q_\perp \right)^2 \\ & \times \left[s_p \omega_p e_{\boldsymbol{q}}^{s_q} \left(e_{\boldsymbol{k}}^{s_k} - e_{\boldsymbol{p}}^{s_p} \right) + s_q \omega_q e_{\boldsymbol{p}}^{s_p} \left(e_{\boldsymbol{k}}^{s_k} - e_{\boldsymbol{q}}^{s_q} \right) \right] \delta\left(\Omega_{kpq}\right) \delta_{kpq} \mathrm{d}\boldsymbol{p} \mathrm{d}\boldsymbol{q}. \end{aligned} \tag{5.53}$$

The $\delta\left(\Omega_{kpq}\right)$ allows us to finally rewrite the term in the second line as follows

$$\boxed{\frac{\partial e_{\boldsymbol{k}}^{s_k}}{\partial t} = \frac{\pi\epsilon^2}{16} \sum_{s_p s_q} \int_{(\mathbb{R}^3)^2} s_k \omega_k \left| \tilde{L}_{\boldsymbol{kpq}}^{s_k s_p s_q} \right|^2 \left(s_k \omega_k e_{\boldsymbol{p}}^{s_p} e_{\boldsymbol{q}}^{s_q} + s_p \omega_p e_{\boldsymbol{k}}^{s_k} e_{\boldsymbol{q}}^{s_q} + s_q \omega_q e_{\boldsymbol{k}}^{s_k} e_{\boldsymbol{p}}^{s_p} \right) \delta\left(\Omega_{kpq}\right) \delta_{kpq} \mathrm{d}\boldsymbol{p} \mathrm{d}\boldsymbol{q}}, \tag{5.54}$$

where

$$\tilde{L}_{\boldsymbol{kpq}}^{s_k s_p s_q} \equiv \frac{L_{\boldsymbol{kpq}}^{s_k s_p s_q}}{s_k \omega_k}, \tag{5.55}$$

$\Omega_{kpq} \equiv s_k\omega_k + s_p\omega_p + s_q\omega_q$ and $\delta_{kpq} = \delta\left(\boldsymbol{k}+\boldsymbol{p}+\boldsymbol{q}\right)$. This equation is the main result of the wave turbulence formalism. It describes the statistical properties of IWW or IKAW turbulence at the leading order, i.e., for three-wave interactions.

5.5.2 Detailed conservation of quadratic invariants

In Section 5.2.3 we introduced the three-dimensional invariants of IEMHD. The first test that the wave turbulence equations must pass is the detailed conservation – i.e., for each triad $(\boldsymbol{k},\boldsymbol{p},\boldsymbol{q})$ – of these invariants. Starting from the definitions (5.15) and (5.20), we define the energy and momentum spectra

$$E(\boldsymbol{k}) \equiv \sum_{s_k} e_{\boldsymbol{k}}^{s_k} = e_{\boldsymbol{k}}^{+} + e_{\boldsymbol{k}}^{-}, \tag{5.56a}$$

$$H(\boldsymbol{k}) \equiv \sum_{s_k} s_k k_\perp e_{\boldsymbol{k}}^{s_k} = k_\perp \left(e_{\boldsymbol{k}}^{+} - e_{\boldsymbol{k}}^{-}\right). \tag{5.56b}$$

Before checking the energy conservation, it is interesting to note that when one of the polarized energy density tensors $e_{\boldsymbol{k}}^{\pm}$ is zero, the other invariant is extremal and verifies the relation $H(\boldsymbol{k}) = \pm k_\perp E(\boldsymbol{k})$, which is in agreement with the realizability condition (Schwarz inequality) $|H(\boldsymbol{k})| \leq k_\perp E(\boldsymbol{k})$. From equation (5.54), we obtain the equation for the (total) energy

$$\begin{aligned}\frac{\partial E(t)}{\partial t} &\equiv \frac{\partial}{\partial t}\int_{\mathbb{R}^3}\sum_{s_k} e_{\boldsymbol{k}}^{s_k}\mathrm{d}\boldsymbol{k} \\ &= \frac{\pi\epsilon^2}{16}\sum_{s_k s_p s_q}\int_{(\mathbb{R}^3)^3} s_k\omega_k \left|\tilde{L}_{\boldsymbol{kpq}}^{s_k s_p s_q}\right|^2 \left(s_k\omega_k e_{\boldsymbol{p}}^{s_p} e_{\boldsymbol{q}}^{s_q} + s_p\omega_p e_{\boldsymbol{k}}^{s_k} e_{\boldsymbol{q}}^{s_q} + s_q\omega_q e_{\boldsymbol{k}}^{s_k} e_{\boldsymbol{p}}^{s_p}\right)\delta\left(\Omega_{kpq}\right)\delta_{kpq}\mathrm{d}\boldsymbol{k}\mathrm{d}\boldsymbol{p}\mathrm{d}\boldsymbol{q}.\end{aligned} \tag{5.57}$$

Without forcing and dissipation, energy must be conserved, and this conservation is done at the level of triadic interactions (detailed energy conservation). The demonstration is straightforward. By applying a cyclic permutation of wavevectors and polarizations, we find,

$$\begin{aligned}\frac{\partial E(t)}{\partial t} &= \frac{\pi\epsilon^2}{48}\sum_{s_k s_p s_q}\int_{(\mathbb{R}^3)^3} \Omega_{kpq} s_k\omega_k \left|\tilde{L}_{\boldsymbol{kpq}}^{s_k s_p s_q}\right|^2 \left(s_k\omega_k e_{\boldsymbol{p}}^{s_p} e_{\boldsymbol{q}}^{s_q} + s_p\omega_p e_{\boldsymbol{k}}^{s_k} e_{\boldsymbol{q}}^{s_q} + s_q\omega_q e_{\boldsymbol{k}}^{s_k} e_{\boldsymbol{p}}^{s_p}\right)\delta\left(\Omega_{kpq}\right)\delta_{kpq}\mathrm{d}\boldsymbol{k}\mathrm{d}\boldsymbol{p}\mathrm{d}\boldsymbol{q} \\ &= 0,\end{aligned} \tag{5.58}$$

which proves the conservation of (kinetic) energy on the resonant manifold for each triadic interaction.

For the second invariant $H(t)$, one has

$$\begin{aligned}\frac{\partial H(t)}{\partial t} &\equiv \frac{\partial}{\partial t}\int_{\mathbb{R}^3}\sum_{s_k} s_k k_\perp e^{s_k}_{\boldsymbol{k}}\,\mathrm{d}\boldsymbol{k}\\ &= \frac{\pi\epsilon^2\Omega_e}{16}\sum_{s_k s_p s_q}\int_{(\mathbb{R}^3)^3} k_\parallel \left|\tilde{L}^{s_k s_p s_q}_{\boldsymbol{kpq}}\right|^2 \left(s_k\omega_k e^{s_p}_{\boldsymbol{p}} e^{s_q}_{\boldsymbol{q}} + s_p\omega_p e^{s_k}_{\boldsymbol{k}} e^{s_q}_{\boldsymbol{q}} + s_q\omega_q e^{s_k}_{\boldsymbol{k}} e^{s_p}_{\boldsymbol{p}}\right)\delta\left(\Omega_{kpq}\right)\delta_{kpq}\mathrm{d}\boldsymbol{k}\mathrm{d}\boldsymbol{p}\mathrm{d}\boldsymbol{q}.\end{aligned} \tag{5.59}$$

The same manipulations as before lead immediately to

$$\begin{aligned}\frac{\partial H(t)}{\partial t} = \frac{\pi\epsilon^2\Omega_e}{48}\sum_{s_k s_p s_q}\int_{(\mathbb{R}^3)^3} &\left|\tilde{L}^{s_k s_p s_q}_{\boldsymbol{kpq}}\right|^2 \left(s_k\omega_k e^{s_p}_{\boldsymbol{p}} e^{s_q}_{\boldsymbol{q}} + s_p\omega_p e^{s_k}_{\boldsymbol{k}} e^{s_q}_{\boldsymbol{q}} + s_q\omega_q e^{s_k}_{\boldsymbol{k}} e^{s_p}_{\boldsymbol{p}}\right)\\ &\times\left(k_\parallel + p_\parallel + q_\parallel\right)\delta\left(\Omega_{kpq}\right)\delta_{kpq}\mathrm{d}\boldsymbol{k}\mathrm{d}\boldsymbol{p}\mathrm{d}\boldsymbol{q} = 0.\end{aligned} \tag{5.60}$$

This proves the conservation of momentum (kinetic helicity) on the resonant manifold for each triadic interaction.

5.5.3 Helical turbulence

From the wave turbulence equation (5.54), we can deduce several general properties. First, we observe that there is no coupling between the waves associated with the $\boldsymbol{p}$ and $\boldsymbol{q}$ wavevectors when these wavevectors are collinear. Second, the nonlinear coupling disappears whenever the wavenumbers $p_\perp$ and $q_\perp$ are equal if their associated polarities s_p and s_q are also equal. These properties are also observed in EMHD (for scales larger than d_e) and more generally for other helical waves [24, 28, 40, 67, 68]. Note that they can already be deduced directly from the fundamental equation (5.24). Third, the wave modes ($k_\parallel > 0$) are decoupled from the slow mode ($k_\parallel = 0$) which is not described by these wave kinetic equations. This situation is thus different from wave turbulence in incompressible MHD, where the slow mode has a profound influence on the nonlinear dynamics.

5.6 Turbulent spectra as exact solutions

5.6.1 Wave kinetic equations for the invariants

The objective of this section is to derive, in the stationary case, the exact power-law solutions of the kinetic equations for the two invariants, energy, and momentum. To do so, it is necessary to simplify the equations,

written for $E(\boldsymbol{k})$ and $H(\boldsymbol{k})$, using the axisymmetric assumption. First, we have

$$\begin{aligned}\frac{\partial}{\partial t}\begin{pmatrix}E(\boldsymbol{k})\\H(\boldsymbol{k})\end{pmatrix} = \frac{\pi\epsilon^2}{16}\sum_{s_k s_p s_q}\int_{(\mathbb{R}^3)^2} s_k\omega_k \left|\tilde{L}^{s_k s_p s_q}_{\boldsymbol{kpq}}\right|^2 \left(s_k\omega_k e^{s_p}_{\boldsymbol{p}} e^{s_q}_{\boldsymbol{q}} + s_p\omega_p e^{s_k}_{\boldsymbol{k}} e^{s_q}_{\boldsymbol{q}} + s_q\omega_q e^{s_k}_{\boldsymbol{k}} e^{s_p}_{\boldsymbol{p}}\right)\\ \times\begin{pmatrix}1\\ s_k k_\perp\end{pmatrix}\delta\left(\Omega_{kpq}\right)\delta_{kpq}\mathrm{d}\boldsymbol{p}\mathrm{d}\boldsymbol{q}.\end{aligned} \tag{5.61}$$

We now develop the energy density tensors inside the integral in terms of energy and momentum spectra. We note that only terms containing the products of two $E(\boldsymbol{k})$ or two $H(\boldsymbol{k})$ will survive for energy, whereas only the products of $E(\boldsymbol{k})H(\boldsymbol{k})$ will survive for helicity. After some algebra, we find for the energy

$$\begin{aligned}\frac{\partial E(\boldsymbol{k})}{\partial t} =& \frac{\pi\epsilon^2}{64}\sum_{s_k s_p s_q}\int_{(\mathbb{R}^3)^2} s_k\omega_k \left|\tilde{L}^{s_k s_p s_q}_{\boldsymbol{kpq}}\right|^2\\ &\times\left[s_k\omega_k E(\boldsymbol{p})E(\boldsymbol{q}) + s_p\omega_p E(\boldsymbol{k})E(\boldsymbol{q}) + s_q\omega_q E(\boldsymbol{k})E(\boldsymbol{p})\right.\\ &\left.+ s_k s_p s_q\left(\omega_k\frac{H(\boldsymbol{p})H(\boldsymbol{q})}{p_\perp q_\perp} + \omega_p\frac{H(\boldsymbol{k})H(\boldsymbol{q})}{k_\perp q_\perp} + \omega_q\frac{H(\boldsymbol{k})H(\boldsymbol{p})}{k_\perp p_\perp}\right)\right]\\ &\times\delta\left(\Omega_{kpq}\right)\delta_{kpq}\mathrm{d}\boldsymbol{p}\mathrm{d}\boldsymbol{q},\end{aligned} \tag{5.62}$$

and for the momentum

$$\begin{aligned}\frac{\partial H(\boldsymbol{k})}{\partial t} = \frac{\pi\epsilon^2}{64}\sum_{s_k s_p s_q}\int_{(\mathbb{R}^3)^2}\omega_k k_\perp \left|\tilde{L}^{s_k s_p s_q}_{\boldsymbol{kpq}}\right|^2 \left(s_k\omega_k\left[E(\boldsymbol{p})\frac{H(\boldsymbol{q})}{s_q q_\perp} + E(\boldsymbol{q})\frac{H(\boldsymbol{p})}{s_p p_\perp}\right]\right.\\ +s_p\omega_p\left[E(\boldsymbol{k})\frac{H(\boldsymbol{q})}{s_q q_\perp} + E(\boldsymbol{q})\frac{H(\boldsymbol{k})}{s_k k_\perp}\right]\\ \left.+s_q\omega_q\left[E(\boldsymbol{k})\frac{H(\boldsymbol{p})}{s_p p_\perp} + E(\boldsymbol{p})\frac{H(\boldsymbol{k})}{s_k k_\perp}\right]\right)\delta\left(\Omega_{kpq}\right)\delta_{kpq}\mathrm{d}\boldsymbol{p}\mathrm{d}\boldsymbol{q}.\end{aligned} \tag{5.63}$$

If we exchange in the integrand the dummy variables, $\boldsymbol{p}$ and $\boldsymbol{q}$, as well as s_p and s_q , we can simplify further the previous expressions to obtain

$$\frac{\partial}{\partial t}\begin{pmatrix}E(\boldsymbol{k})\\H(\boldsymbol{k})\end{pmatrix} = \frac{\pi\epsilon^2}{32}\sum_{s_k s_p s_q}\int_{(\mathbb{R}^3)^2}\left|\tilde{L}^{s_k s_p s_q}_{\boldsymbol{kpq}}\right|^2 s_k\omega_k s_p\omega_p\begin{pmatrix}X_E\\X_H\end{pmatrix}\delta\left(\Omega_{kpq}\right)\delta_{kpq}\mathrm{d}\boldsymbol{p}\mathrm{d}\boldsymbol{q}, \tag{5.64}$$

with

$$\begin{pmatrix}X_E\\X_H\end{pmatrix} = \begin{pmatrix}E(\boldsymbol{q})\left[E(\boldsymbol{k}) - E(\boldsymbol{p})\right] + \frac{H(\boldsymbol{q})}{s_q q_\perp}\left(\frac{H(\boldsymbol{k})}{s_k k_\perp} - \frac{H(\boldsymbol{p})}{s_p p_\perp}\right)\\ s_k k_\perp\left[E(\boldsymbol{q})\left(\frac{H(\boldsymbol{k})}{s_k k_\perp} - \frac{H(\boldsymbol{p})}{s_p p_\perp}\right) + \frac{H(\boldsymbol{q})}{s_q q_\perp}\left[E(\boldsymbol{k}) - E(\boldsymbol{p})\right]\right]\end{pmatrix}. \tag{5.65}$$

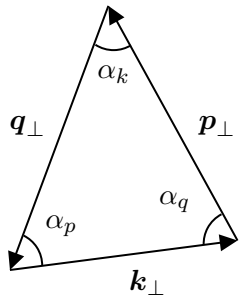

Figure 5.2: Triadic relation $\boldsymbol{k}_\perp + \boldsymbol{p}_\perp + \boldsymbol{q}_\perp = \boldsymbol{0}$.

To simplify the problem, we will consider an axial symmetry with respect to the external magnetic field and introduce the two-dimensional anisotropic spectra

$$E_k = E\left(k_\perp, k_\parallel\right) = 2\pi k_\perp E\left(\boldsymbol{k}_\perp, k_\parallel\right), \tag{5.66a}$$

$$H_k = H\left(k_\perp, k_\parallel\right) = 2\pi k_\perp H\left(\boldsymbol{k}_\perp, k_\parallel\right), \tag{5.66b}$$

which result from an integration over the angles in the plane perpendicular to the mean magnetic field (see Figure 5.2). In polar coordinates $\mathrm{d}\boldsymbol{p}\mathrm{d}\boldsymbol{q} = p_\perp \mathrm{d}\alpha_q \mathrm{d}p_\perp \mathrm{d}p_\parallel \mathrm{d}q_\parallel$ and, thanks to the Al-Kashi formula: $q_\perp^2 = k_\perp^2 + p_\perp^2 - 2k_\perp p_\perp \cos\alpha_q$, we find at fixed $k_\perp$ and $p_\perp$, $q_\perp \mathrm{d}q_\perp = k_\perp p_\perp \sin\alpha_q \mathrm{d}\alpha_q$. Using expression (5.55), we then obtain the kinetic equations

$$\begin{aligned}\frac{\partial}{\partial t}\begin{pmatrix} E_k \\ H_k \end{pmatrix} = \frac{\epsilon^2\Omega_e^2}{2^{12}} \sum_{s_k s_p s_q} \int_{\Delta_\perp} \frac{s_k s_p k_\parallel p_\parallel}{k_\perp^2 p_\perp^2 q_\perp^2} \left(\frac{s_q q_\perp - s_p p_\perp}{s_k \omega_k}\right)^2 \left(s_k k_\perp + s_p p_\perp + s_q q_\perp\right)^2 \sin\alpha_q \\ \times \begin{pmatrix} \tilde{X}_E \\ \tilde{X}_H \end{pmatrix} \delta\left(\Omega_{kpq}\right) \delta_{k_\parallel p_\parallel q_\parallel} \mathrm{d}p_\perp \mathrm{d}q_\perp \mathrm{d}p_\parallel \mathrm{d}q_\parallel,\end{aligned} \tag{5.67}$$

where $\Delta_\perp$ the integration domain verifies the resonance condition $\boldsymbol{k}_\perp + \boldsymbol{p}_\perp + \boldsymbol{q}_\perp = \boldsymbol{0}$ (cf., Figure 5.3) and

$$\begin{pmatrix} \tilde{X}_E \\ \tilde{X}_H \end{pmatrix} = \begin{pmatrix} E_q\left(p_\perp E_k - k_\perp E_p\right) + \frac{H_q}{s_q q_\perp}\left(\frac{p_\perp}{s_k k_\perp} H_k - \frac{k_\perp}{s_p p_\perp} H_p\right) \\ s_k k_\perp \left[E_q\left(\frac{p_\perp}{s_k k_\perp} H_k - \frac{k_\perp}{s_p p_\perp} H_p\right) + \frac{H_q}{s_q q_\perp}\left(p_\perp E_k - k_\perp E_p\right)\right] \end{pmatrix}, \tag{5.68}$$

with α_q the angle between $\boldsymbol{k}_\perp$ and $\boldsymbol{p}_\perp$ in the triangle defined by the triadic interaction $(\boldsymbol{k}_\perp, \boldsymbol{p}_\perp, \boldsymbol{q}_\perp)$ (see Figure 5.2). Equations (5.67) will be used to derive exact solutions also called Kolmogorov–Zakharov spectra.

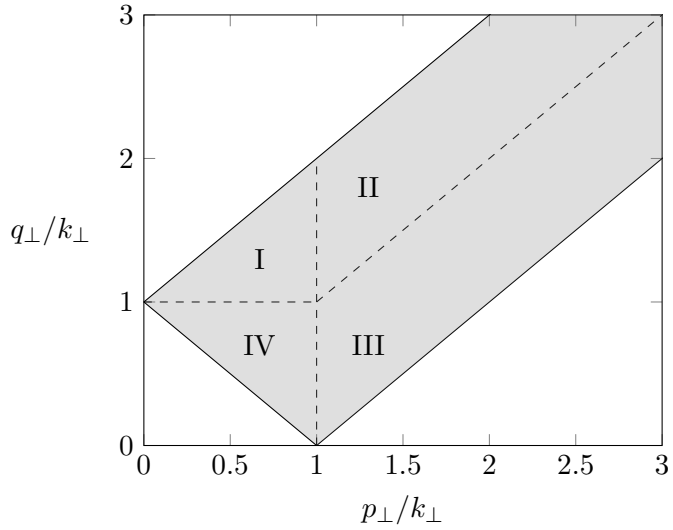

Figure 5.3: Illustration of the Kuznetsov–Zakharov transformation. It consists of swapping regions I and III with regions II and IV, respectively. We specify that the gray band is defined up to infinity and corresponds to the domain $\Delta_\perp$. The same manipulation is done on the parallel wavenumbers.

5.6.2 Kolmogorov–Zakharov spectra

Equations (5.67) have sufficient symmetry to apply the bi-homogeneous conformal Kuznetsov–Zakharov transformation [72]. This transformation has been applied to several problems involving anisotropy [28, 29, 42]. It is a generalization of the Zakharov transformation applied to isotropic turbulence (in the context of strong 2D HD turbulence, see also [41]). With such an operation, we are able to find the exact stationary solutions of the kinetic equations in power law form. The bihomogeneity of the integrals in the wavenumbers $k_\perp$ and $k_\parallel$ allows us to use the transformations (see Figure 5.3)

$$p_\perp \rightarrow k_\perp^2/p_\perp, \tag{5.69a}$$

$$q_\perp \rightarrow k_\perp q_\perp/p_\perp, \tag{5.69b}$$

$$p_\parallel \rightarrow k_\parallel^2/p_\parallel, \tag{5.69c}$$

$$q_\parallel \rightarrow k_\parallel q_\parallel/p_\parallel. \tag{5.69d}$$

We apply this transformation first on the energy equation (5.67) which means that we are looking for constant energy flux solutions. We seek stationary solutions in the power law form,

$$E\left(k_\perp, k_\parallel\right) = C_E k_\perp^{-x} \left|k_\parallel\right|^{-y}, \tag{5.70a}$$

$$H\left(k_\perp, k_\parallel\right) = C_H k_\perp^{-\tilde{x}} \left|k_\parallel\right|^{-\tilde{y}}, \tag{5.70b}$$

where C_E and C_H are two constants with $C_E \geq 0$. (We consider only positive parallel wavenumber since it is symmetric in $k_\parallel$.) The new form of the integral, resulting from the summation of the integrand in its primary form and after the Kuznetsov–Zakharov transformation, can be written as

$$\begin{aligned}\frac{\partial E_k}{\partial t} = \frac{\epsilon^2\Omega_e^2}{2^{13}} \sum_{s_k s_p s_q} \int_{\Delta_\perp} \frac{s_k s_p k_\parallel p_\parallel}{k_\perp^2 p_\perp q_\perp^2} \left(\frac{s_q q_\perp - s_p p_\perp}{s_k \omega_k}\right)^2 (s_k k_\perp + s_p p_\perp + s_q q_\perp)^2 \sin\alpha_q \\ \times \left(C_E^2 \Xi_E + s_k s_q C_H^2 \Xi_H\right) \delta\left(\Omega_{kpq}\right) \delta_{k_\parallel p_\parallel q_\parallel} \mathrm{d}p_\perp \mathrm{d}q_\perp \mathrm{d}p_\parallel \mathrm{d}q_\parallel,\end{aligned} \tag{5.71}$$

with the pure energy contribution

$$\Xi_E = k_\perp^{-x} \left|k_\parallel\right|^{-y} q_\perp^{-x} \left|q_\parallel\right|^{-y} \left[1 - \left(\frac{p_\perp}{k_\perp}\right)^{-1-x} \left|\frac{p_\parallel}{k_\parallel}\right|^{-y}\right] \left[1 - \left(\frac{p_\perp}{k_\perp}\right)^{-5+2x} \left|\frac{p_\parallel}{k_\parallel}\right|^{-1+2y}\right], \tag{5.72}$$

and the pure helicity contribution

$$\Xi_H = k_\perp^{-1-\tilde{x}} \left|k_\parallel\right|^{-\tilde{y}} q_\perp^{-1-\tilde{x}} \left|q_\parallel\right|^{-\tilde{y}} \left[1 - s_k s_p \left(\frac{p_\perp}{k_\perp}\right)^{-\tilde{x}-2} \left|\frac{p_\parallel}{k_\parallel}\right|^{-\tilde{y}}\right] \left[1 - \left(\frac{p_\perp}{k_\perp}\right)^{2\tilde{x}-3} \left|\frac{p_\parallel}{k_\parallel}\right|^{2\tilde{y}-1}\right]. \tag{5.73}$$

We can distinguish two different types of solutions. First, there are the thermodynamic equilibrium solutions, which correspond to the equipartition state for which the energy flux is zero. The power laws which verify this condition are,

$$\boxed{E\left(k_\perp, k_\parallel\right) = C_E k_\perp,} \tag{5.74a}$$

$$\boxed{H\left(k_\perp, k_\parallel\right) = C_H k_\perp^2.} \tag{5.74b}$$

These results can be easily verified by direct substitution in the original kinetic equations. In general, this stationary state cannot be reached in the presence of helicity because the value $s_k s_p = -1$ prevents the cancellation of the integral. There is, however, a particular case where the solutions exist: it is the state of maximal helicity for which either $e_{\boldsymbol{k}}^+ = 0$ or $e_{\boldsymbol{k}}^- = 0$. Then, we have the relation $H_k = \pm k_\perp E_k$. But this state is not viable as we can see in equation (5.54): for example, if $e_{\boldsymbol{k}}^- = 0$ at time $t = 0$, it will not remain zero at time $t > 0$. This means that this solution is only possible if there is an external mechanism that forces the system to remain in the maximal helicity state.

The most interesting solutions are those for which the energy flux is constant, non-zero, and finite. These exact solutions are called Kolmogorov–Zakharov (KZ) spectra and correspond to the values which

make the integral cancels in a non-trivial way and independently of the polarization. These spectra are

$$\boxed{E\left(k_\perp,k_\parallel\right)=C_E k_\perp^{-5/2}\left|k_\parallel\right|^{-1/2},} \tag{5.75a}$$

$$\boxed{H\left(k_\perp,k_\parallel\right)=C_H k_\perp^{-3/2}\left|k_\parallel\right|^{-1/2}.} \tag{5.75b}$$

They are not constrained by the polarization and can therefore be reached by the system even in the presence of helicity. For the helicity equation, using the same manipulations as before, we obtain

$$\begin{aligned}\frac{\partial H_k}{\partial t}=&\frac{\epsilon^2\Omega_e^2}{2^{13}}C_E C_H\sum_{s_k s_p s_q}\int_{\Delta_\perp}\frac{s_k s_p k_\parallel p_\parallel}{k_\perp^2 p_\perp q_\perp^2}\left(\frac{s_q q_\perp-s_p p_\perp}{s_k\omega_k}\right)^2\left(s_k k_\perp+s_p p_\perp+s_q q_\perp\right)^2\sin\alpha_q\\&\times k_\perp^{-x-\tilde{x}}\left|k_\parallel\right|^{-y-\tilde{y}}\left[1-s_k s_p\left(\frac{p_\perp}{k_\perp}\right)^{x+\tilde{x}-4}\left|\frac{p_\parallel}{k_\parallel}\right|^{y+\tilde{y}-1}\right]\\&\times\left[\left(\frac{q_\perp}{k_\perp}\right)^{-x}\left|\frac{q_\parallel}{k_\parallel}\right|^{-y}\left(1-s_k s_p\left(\frac{p_\perp}{k_\perp}\right)^{-\tilde{x}-2}\left|\frac{p_\parallel}{k_\parallel}\right|^{-\tilde{y}}\right)\right.\\&\left.+s_k s_q\left(\frac{q_\perp}{k_\perp}\right)^{-\tilde{x}-1}\left|\frac{q_\parallel}{k_\parallel}\right|^{-\tilde{y}}\left(1-\left(\frac{p_\perp}{k_\perp}\right)^{-x-1}\left|\frac{p_\parallel}{k_\parallel}\right|^{-y}\right)\right]\delta\left(\Omega_{kpq}\right)\delta_{k_\parallel p_\parallel q_\parallel}\mathrm{d}p_\perp\mathrm{d}q_\perp\mathrm{d}p_\parallel\mathrm{d}q_\parallel.\end{aligned} \tag{5.76}$$

The zero helicity flux solutions satisfy,

$$\boxed{E\left(k_\perp,k_\parallel\right)=C_E k_\perp,} \tag{5.77a}$$

$$\boxed{H\left(k_\perp,k_\parallel\right)=C_H k_\perp^2,} \tag{5.77b}$$

which correspond to the thermodynamic spectra found for energy (this can be seen directly from equation (5.70)). For the KZ spectra, we have a family of solutions that meet the following criteria

$$\boxed{x+\tilde{x}=4,} \tag{5.78a}$$

$$\boxed{y+\tilde{y}=1.} \tag{5.78b}$$

The situation is worse than for energy because none of the constant helicity flux solutions (thermodynamic or KZ) can be reached in general because of the presence of the product $s_k s_p$ which, let us recall, prevents the cancellation of the term in the right-hand side of expression (5.76). Only the maximal helicity state allows the existence of these stationary spectra but, as said above, it is not a naturally viable state. (Note that this property found in weak wave turbulence may not be true in strong turbulence.)

In conclusion, the most relevant solutions are the KZ spectra at constant energy flux. In Section 5.8

we will further investigate the corresponding exact solution for $H = 0$ in order to find the direction of the energy cascade and the expression of the Kolmogorov constant. In space plasma physics, we often compare theoretical predictions with the magnetic spectrum E_k^B which is well measured by spacecraft (with the Taylor hypothesis, the frequency is used as a proxy for the wavenumber). In our case, a simple dimensional analysis based on the definition of energy (5.15), leads to the relation $E_k \sim k_\perp^2 E_k^B$. Consequently, we obtain $E_k^B \sim k_\perp^{-9/2}$, which is steeper than the predictions made at scales larger than d_e.

5.6.3 Locality conditions

We have seen that the most interesting exact solutions of the kinetic equations are the KZ spectra at constant energy flux. However, these solutions are only entirely relevant if they satisfy the locality condition. Mathematically, this condition means that the integral must be convergent. If it is not the case, it means that the inertial range is dependent on the largest or smallest scales, where forcing and dissipation are expected. The calculation of the locality condition is highly non-trivial in this anisotropic case. Note that the study of locality is still a subject of investigation [19]. In the absence of helicity, we find the following conditions

$$3 < x + 2y < 4, \tag{5.79a}$$

$$2 < x + y < 4. \tag{5.79b}$$

We obtain a classical result for wave turbulence, in the sense that the power law indices of the KZ spectra fall exactly in the middle of the convergence domain (see Figure 5.4).

The objective is to find the locality domain of the power law solutions at constant energy flux and (for simplicity) in the absence of helicity. In other words, we want to check if the contribution of non-local interactions is not dominant. There are three areas (regions A, B, and C in Figure 5.5) for which the interactions are non-local. To do this, it is convenient to introduce the adimensional wavenumbers $\tilde{p}_\perp \equiv p_\perp/k_\perp$, $\tilde{p}_\parallel \equiv p_\parallel/k_\parallel$, $\tilde{q}_\perp \equiv q_\perp/k_\perp$ and $\tilde{q}_\parallel \equiv q_\parallel/k_\parallel$. We obtain ($H = 0$):

$$\begin{aligned}\frac{\partial E_k}{\partial t} =& \frac{\epsilon^2 C_E^2}{2^{12}\Omega_e} k_\perp^{4-2x} k_\parallel^{-2y} \sum_{s_k s_p s_q} \int_{\Delta_\perp} s_k s_p \frac{\tilde{p}_\parallel}{\tilde{p}_\perp \tilde{q}_\perp^2} \left(s_q \tilde{q}_\perp - s_p \tilde{p}_\perp\right)^2 \left(s_k + s_p \tilde{p}_\perp + s_q \tilde{q}_\perp\right)^2 \sin\alpha_q \\ & \times \tilde{q}_\perp^{-x} \tilde{q}_\parallel^{-y} \left(1 - \tilde{p}_\perp^{-1-x} \tilde{p}_\parallel^{-y}\right) \delta\left(s_k + s_p \frac{\tilde{p}_\parallel}{\tilde{p}_\perp} + s_q \frac{\tilde{q}_\parallel}{\tilde{q}_\perp}\right) \delta\left(1 + \tilde{p}_\parallel + \tilde{q}_\parallel\right) \mathrm{d}\tilde{p}_\perp \mathrm{d}\tilde{q}_\perp \mathrm{d}\tilde{p}_\parallel \mathrm{d}\tilde{q}_\parallel.\end{aligned} \tag{5.80}$$

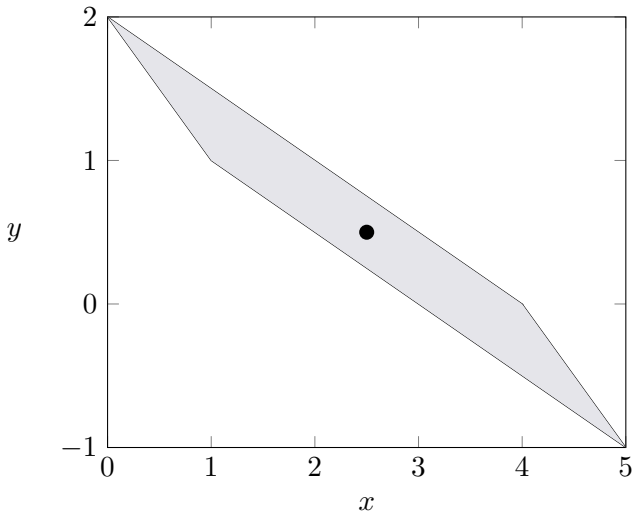

Figure 5.4: Domain of convergence of the energy integral. The black dot at the center of the domain corresponds to the KZ energy spectrum.

This expression can be integrated into parallel directions. We recall the following property,

$$\int_{\mathbb{R}} f(x)\delta\left(g(x)\right)\mathrm{d}x = \sum_i \frac{f\left(x_i\right)}{\left|g'\left(x_i\right)\right|}, \text{ such as } g\left(x_i\right) = 0. \tag{5.81}$$

Then, we have

$$\delta\left(1+\tilde{p}_\parallel+\tilde{q}_\parallel\right) \longrightarrow \tilde{q}_\parallel = -1-\tilde{p}_\parallel, \tag{5.82a}$$

$$\delta\left(s_k + s_p\frac{\tilde{p}_\parallel}{\tilde{p}_\perp} + s_q\frac{\tilde{q}_\parallel}{\tilde{q}_\perp}\right) \longrightarrow \tilde{p}_\parallel = \tilde{p}_\perp\frac{s_k\tilde{q}_\perp - s_q}{s_q\tilde{p}_\perp - s_p\tilde{q}_\perp}. \tag{5.82b}$$

We obtain

$$\begin{aligned}\frac{\partial E_k}{\partial t} =& \frac{\epsilon^2 C_E^2}{2^{12}\Omega_e}k_\perp^{4-2x}\left|k_\parallel\right|^{-2y}\sum_{s_k s_p s_q}\int_{\Delta_\perp} s_k s_p \tilde{q}_\perp^{-x-y-2}\left(s_q\tilde{q}_\perp - s_p\tilde{p}_\perp\right)^2\left(s_k + s_p\tilde{p}_\perp + s_q\tilde{q}_\perp\right)^2 \\ &\times \sin\alpha_q \frac{s_k\tilde{q}_\perp - s_q}{s_q\tilde{p}_\perp - s_p\tilde{q}_\perp}\left|\frac{s_p - s_k\tilde{p}_\perp}{s_q\tilde{p}_\perp - s_p\tilde{q}_\perp}\right|^{-y}\left(1-\tilde{p}_\perp^{-x-y-1}\left|\frac{s_k\tilde{q}_\perp - s_q}{s_q\tilde{p}_\perp - s_p\tilde{q}_\perp}\right|^{-y}\right) \\ &\times \left|\frac{\tilde{p}_\perp\tilde{q}_\perp}{s_p\tilde{q}_\perp - s_q\tilde{p}_\perp}\right|\mathrm{d}\tilde{p}_\perp\mathrm{d}\tilde{q}_\perp,\end{aligned} \tag{5.83}$$

where $\sin\alpha_q = \sqrt{1-\left(1+\tilde{p}_\perp^2-\tilde{q}_\perp^2\right)^2\left(2\tilde{p}_\perp\right)^{-2}}$.

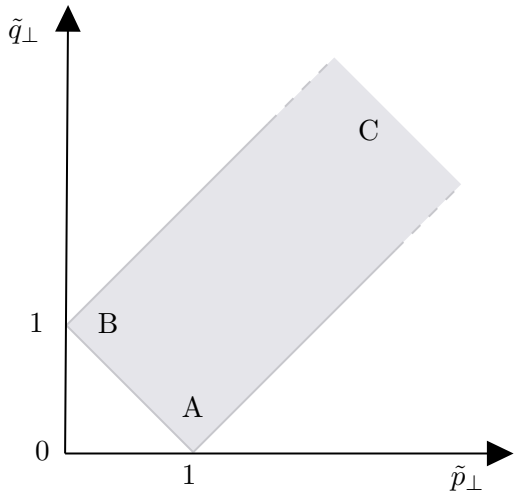

Figure 5.5: The kinetic equations are integrated on a domain verifying $\boldsymbol{k}+\boldsymbol{p}+\boldsymbol{q}=\boldsymbol{0}$. The gray strip corresponds to this domain for the adimensional perpendicular wavevectors. A, B, and C (at infinity) are the non-local regions where the convergence of the integrals must be checked.

Zone A

We define $\tilde{p}_\perp = 1 + r\cos\beta$ and $\tilde{q}_\perp = r\sin\beta$, with $r \ll 1$ and $\beta \in [\pi/4, 3\pi/4]$. Two cases must be distinguished: when $s_k = s_p$ and when $s_k = -s_p$. An evaluation (in leading order) of the different terms of the integral (5.83) is given in Table 1. Note that these evaluations take into account the possible cancellation of the integral due to β symmetry.

	$s_k = s_p$	$s_k = -s_p$
$\frac{s_k\tilde{q}_\perp - s_q}{s_q\tilde{p}_\perp - s_p\tilde{q}_\perp}$	-1	-1
$\left\lvert\frac{s_p - s_k\tilde{p}_\perp}{s_q\tilde{p}_\perp - s_p\tilde{q}_\perp}\right\rvert$	$r\lvert\cos\beta\rvert$	2
$(s_q\tilde{q}_\perp - s_p\tilde{p}_\perp)^2$	1	1
$(s_k + s_p\tilde{p}_\perp + s_q\tilde{q}_\perp)^2$	4	r^2
$\sin\theta$	$r\sqrt{-\cos 2\beta}$	$r\sqrt{-\cos 2\beta}$
$1 - \tilde{p}_\perp^{-x-y-1}\left\lvert\frac{s_k\tilde{q}_\perp - s_q}{s_q\tilde{p}_\perp - s_p\tilde{q}_\perp}\right\rvert^{-y}$	$\propto r^2\cos^2\beta$	$\propto r^2\cos^2\beta$
$\left\lvert\frac{\tilde{p}_\perp\tilde{q}_\perp}{s_p\tilde{q}_\perp - s_q\tilde{p}_\perp}\right\rvert$	$r\lvert\sin\beta\rvert$	$r\lvert\sin\beta\rvert$
$\mathrm{d}\tilde{p}_\perp\mathrm{d}\tilde{q}_\perp$	$r\mathrm{d}r\mathrm{d}\beta$	$r\mathrm{d}r\mathrm{d}\beta$

Table 5.1: Evaluation, in leading order, of the different terms of the integral (5.83) in Zone A.

When $s_k = s_p$, the criterion of convergence of the kinetic equation (5.83) will be given by the following integral

$$\int_0^{R<1} r^{3-x-2y}\mathrm{d}r \int_{\pi/4}^{3\pi/4} |\cos\beta|^{2-y}\sqrt{-\cos 2\beta}\,(\sin\beta)^{-1-x-y}\,\mathrm{d}\beta. \tag{5.84}$$

Therefore, there is convergence if $x + 2y < 4$. When $s_k = -s_p$, we have

$$\int_0^{R<1} r^{5-x-y}\mathrm{d}r \int_{\pi/4}^{3\pi/4} \cos^2\beta\sqrt{-\cos 2\beta}\,(\sin\beta)^{-1-x-y}\,\mathrm{d}\beta \tag{5.85}$$

and the convergence is obtained if $x + y < 6$.

Zone B

We define $\tilde{p}_\perp = r\cos\beta$ and $\tilde{q}_\perp = 1 + r\sin\beta$, with this time $\beta \in [-\pi/4, \pi/4]$. We have two cases: $s_k = s_q$ and $s_k = -s_q$. An evaluation (in leading order) of the different terms of the integral (5.83) is given in Table 2. Note that these evaluations take into account the possible cancellation of the integral due to β symmetry.

	$s_k = s_q$	$s_k = -s_q$
$\frac{s_k\tilde{q}_\perp - s_q}{s_q\tilde{p}_\perp - s_p\tilde{q}_\perp}$	$s_k s_p r^2 \sin^2\beta$	$-2s_k s_p$
$\left\lvert\frac{s_p - s_k\tilde{p}_\perp}{s_q\tilde{p}_\perp - s_p\tilde{q}_\perp}\right\rvert$	1	1
$(s_q\tilde{q}_\perp - s_p\tilde{p}_\perp)^2$	1	1
$(s_k + s_p\tilde{p}_\perp + s_q\tilde{q}_\perp)^2$	4	r^2
$\sin\theta$	$\sqrt{1-\tan^2\beta}$	$\sqrt{1-\tan^2\beta}$
$1 - \tilde{p}_\perp^{-x-y-1}\left\lvert\frac{s_k\tilde{q}_\perp - s_q}{s_q\tilde{p}_\perp - s_p\tilde{q}_\perp}\right\rvert^{-y}$	$1 - (r\cos\beta)^{-x-y-1}\lvert r\sin\beta\rvert^{-y}$	$1 - 2^{-y}(r\cos\beta)^{-x-y-1}$
$\left\lvert\frac{\tilde{p}_\perp\tilde{q}_\perp}{s_p\tilde{q}_\perp - s_q\tilde{p}_\perp}\right\rvert$	$r\lvert\cos\beta\rvert$	$r\lvert\cos\beta\rvert$
$\mathrm{d}\tilde{p}_\perp\mathrm{d}\tilde{q}_\perp$	$r\mathrm{d}r\mathrm{d}\beta$	$r\mathrm{d}r\mathrm{d}\beta$

Table 5.2: Evaluation, in leading order, of the different terms of the integral (5.83) in Zone B.

When $s_k = s_q$, the criterion of convergence of the kinetic equation (5.83) will be given by the following integral

$$\int_0^{R<1} r^{3-x-2y}\mathrm{d}r \int_{-\pi/4}^{+\pi/4} (\cos\beta)^{-x-y}\,\lvert\sin\beta\rvert^{2-y}\sqrt{1-\tan^2\beta}\mathrm{d}\beta. \tag{5.86}$$

Therefore, there is convergence if $x + 2y < 4$. When $s_k = -s_q$, we have

$$\int_0^{R<1} r^{3-x-y}\mathrm{d}r \int_{-\pi/4}^{+\pi/4} (\cos\beta)^{-x-y}\sqrt{1-\tan^2\beta}\mathrm{d}\beta \tag{5.87}$$

and the convergence is obtained if $x + y < 4$.

Zone C

We define $\tilde{p}_\perp = (\tau_2 - \tau_1)/2$ and $\tilde{q}_\perp = (\tau_1 + \tau_2)/2$, with $-1 \leq \tau_1 \leq 1$ and $1 \ll \tau_2$. We have two cases: $s_p = s_q$ and $s_p = -s_q$. An evaluation (in leading order) of the different terms of the integral (5.83) is given in Table 3. Note that these evaluations take into account the possible cancellation of the integral due to τ_1 symmetry. When $s_p = s_q$, the criterion of convergence of the kinetic equation (5.83) will be given by

	$s_p = s_q$	$s_p = -s_q$
$\frac{s_k\tilde{q}_\perp - s_q}{s_q\tilde{p}_\perp - s_p\tilde{q}_\perp}$	$-s_k s_p/2$	$-s_k s_p/2$
$\left\lvert\frac{s_p - s_k\tilde{p}_\perp}{s_q\tilde{p}_\perp - s_p\tilde{q}_\perp}\right\rvert$	$\left\lvert\tau_2\tau_1^{-1}\right\rvert/2$	$1/2$
$(s_q\tilde{q}_\perp - s_p\tilde{p}_\perp)^2$	τ_1^2	τ_2^2
$(s_k + s_p\tilde{p}_\perp + s_q\tilde{q}_\perp)^2$	τ_2^2	$1 + \tau_1^2$
$\sin\theta$	$\sqrt{1-\tau_1^2}$	$\sqrt{1-\tau_1^2}$
$1 - \tilde{p}_\perp^{-x-y-1}\left\lvert\frac{s_k\tilde{q}_\perp - s_q}{s_q\tilde{p}_\perp - s_p\tilde{q}_\perp}\right\rvert^{-y}$	$1 - 2^{x+2y+1}\tau_2^{-x-2y-1}\lvert\tau_1\rvert^y$	$1 - 2^{x+y-1}\tau_2^{-x-y-1}$
$\left\lvert\frac{\tilde{p}_\perp\tilde{q}_\perp}{s_p\tilde{q}_\perp - s_q\tilde{p}_\perp}\right\rvert$	$\tau_2^2\left\lvert\tau_1^{-1}\right\rvert/4$	$\tau_2/4$
$\mathrm{d}\tilde{p}_\perp\mathrm{d}\tilde{q}_\perp$	$\propto \mathrm{d}\tau_1\mathrm{d}\tau_2$	$\propto \mathrm{d}\tau_1\mathrm{d}\tau_2$

Table 5.3: Evaluation, in leading order, of the different terms of the integral (5.83) in Zone C.

the following integral

$$\int_{-1}^{+1}\sqrt{1-\tau_1^2}\,\lvert\tau_1\rvert^{y+1}\,\mathrm{d}\tau_1\int_{\tau>1}^{+\infty}\tau_2^{-x-2y+2}\mathrm{d}\tau_2. \tag{5.88}$$

Therefore, there is convergence if $3 < x + 2y$. When $s_p = -s_q$, we have

$$\int_{-1}^{+1}\left(1+\tau_1^2\right)\sqrt{1-\tau_1^2}\mathrm{d}\tau_1\int_{\tau>1}^{+\infty}\tau_2^{-x-y+1}\mathrm{d}\tau_2, \tag{5.89}$$

and the convergence is obtained if $2 < x + y$.

In conclusion, a solution is local if the following conditions are satisfied

$$\boxed{3 < x + 2y < 4,} \tag{5.90a}$$

$$\boxed{2 < x + y < 4.} \tag{5.90b}$$

We notice that the KZ spectrum for the energy corresponds to $x + 2y = 7/2$ and $x + y = 3$. These values are thus exactly in the middle of the convergence domain.

5.6.4 Domain of validity of inertial electron waves turbulence

The inertial whistler wave turbulence theory presented here is an asymptotic theory that relies on the separation of time scales. Specifically, it assumes that the transfer time is significantly greater than the period of the linear waves. Due to this assumption, the theory does not hold uniformly across the entire $\boldsymbol{k}$-space. To establish the domain of validity, one must begin with the kinetic equation, for which we have obtained the precise KZ solutions. By performing a dimensional analysis of Equation (5.67), we ascertain that the transfer time scales as (with $\Omega_e \sim 1$):

$$\tau_{\rm tr} \sim \frac{1}{\epsilon^2 E_k} k_\perp^{-4} k_\parallel^{-1}. \tag{5.91}$$

By including the KZ solution in the previous equation, we obtain $\tau_{\rm tr} \sim \epsilon^{-2} k_\perp^{-3/2} k_\parallel^{-1/2}$, and simple manipulation of the condition $\tau_1 \ll \tau_{\rm tr}$ leads to the inequality

$$\boxed{\epsilon^{4/3} k_\perp^{5/3} \ll k_\parallel}. \tag{5.92}$$

Equation (5.92) represents the condition for the validity of the IWW/IKAW turbulence theory in the context of three-wave interactions. It is important to highlight that this condition does not contradict the assumption of anisotropy ($k_\parallel \ll k_\perp$) as the small parameter ϵ is present. Hence, there exists a region in $\boldsymbol{k}$-space where the theory remains valid. It is worth noting that in the prohibited region characterized by small $k_\parallel$ or large $k_\perp$, higher-order processes such as four-wave interactions could be considered to accurately describe the system [49, 55, 66].

5.7 Super-local interactions

In this section, we shall study the limit of local triadic interactions (in the perpendicular direction) for which the wave kinetic equations simplify significantly. From the results found in the previous section, we know that it is mainly relevant to study energy only. In the strongly anisotropic limit $k_\parallel \ll k_\perp$, equation (5.67) writes

$$\frac{\partial E_k}{\partial t} = \sum_{s_k s_p s_q} \int T_{\boldsymbol{kpq}}^{s_k s_p s_q} \mathrm{d}p_\perp \mathrm{d}p_\parallel \mathrm{d}q_\perp \mathrm{d}p_\parallel. \tag{5.93}$$

By definition (the small parameter ϵ is absorbed in the time variable)

$$\begin{aligned} T_{\boldsymbol{kpq}}^{s_k s_p s_q} =& \frac{\Omega_e^2}{2^{12}} \frac{s_k s_p k_\parallel p_\parallel}{k_\perp^2 p_\perp^2 q_\perp^2} \left(\frac{s_q q_\perp - s_p p_\perp}{s_k \omega_k} \right)^2 (s_k k_\perp + s_p p_\perp + s_q q_\perp)^2 \sin \alpha_q \\ & \times E_q \left(p_\perp E_k - k_\perp E_p \right) \delta \left(\Omega_{kpq} \right) \delta_{k_\parallel p_\parallel q_\parallel}, \end{aligned} \tag{5.94}$$

is the nonlinear operator which describes the energy transfer between modes which verifies the following symmetry

$$T_{\boldsymbol{kpq}}^{s_k s_p s_q} = -T_{\boldsymbol{pkq}}^{s_p s_k s_q}. \tag{5.95}$$

In the limit of super-local interactions, we can write

$$p_\perp = k_\perp (1 + \epsilon_p) \quad ; \quad q_\perp = k_\perp (1 + \epsilon_q), \tag{5.96}$$

with $0 \ll \epsilon_p \ll 1$ and $0 \ll \epsilon_q \ll 1$. We can introduce an arbitrary function $f\left(k_\perp, k_\parallel\right)$ and integrate the kinetic equation to find

$$\begin{aligned} & \frac{\partial}{\partial t} \int f\left(k_\perp, k_\parallel\right) E_k \mathrm{d}k_\perp \mathrm{d}k_\parallel = \sum_{s_k s_p s_q} \int f\left(k_\perp, k_\parallel\right) T_{\boldsymbol{kpq}}^{s_k s_p s_q} \mathrm{d}k_\perp \mathrm{d}p_\perp \mathrm{d}q_\perp \mathrm{d}k_\parallel \mathrm{d}p_\parallel \mathrm{d}q_\parallel \\ & = \frac{1}{2} \sum_{s_k s_p s_q} \int \left[f\left(k_\perp, k_\parallel\right) - f\left(p_\perp, p_\parallel\right) \right] T_{\boldsymbol{kpq}}^{s_k s_p s_q} \mathrm{d}k_\perp \mathrm{d}k_\parallel \mathrm{d}p_\perp \mathrm{d}p_\parallel \mathrm{d}q_\perp \mathrm{d}p_\parallel. \end{aligned} \tag{5.97}$$

Neglecting the parallel wavenumber contribution (this assumption is fully compatible with the weak cascade along the parallel direction – see arguments based on the resonance condition), for local interactions we have

$$f\left(p_\perp, p_\parallel\right) = \sum_{n=0}^{+\infty} \frac{(p_\perp - k_\perp)^n}{n!} \frac{\partial^n}{\partial k_\perp^n} f\left(k_\perp, k_\parallel\right) = \sum_{n=0}^{+\infty} \epsilon_p^n \frac{k_\perp^n}{n!} \frac{\partial^n}{\partial k_\perp^n} f\left(k_\perp, k_\parallel\right). \tag{5.98}$$

In the main order, we can write

$$\begin{aligned} & \frac{\partial}{\partial t} \int f\left(k_\perp, k_\parallel\right) E_k \mathrm{d}k_\perp \mathrm{d}k_\parallel = \\ & \quad - \frac{1}{2} \frac{\partial}{\partial k_\perp} \left(\sum_{s_k s_p s_q} \int \epsilon_p k_\perp T_{\boldsymbol{kpq}}^{s_k s_p s_q} \frac{\partial}{\partial k_\perp} f\left(k_\perp, k_\parallel\right) \mathrm{d}k_\perp \mathrm{d}k_\parallel \mathrm{d}p_\perp \mathrm{d}p_\parallel \mathrm{d}q_\perp \mathrm{d}p_\parallel \right). \end{aligned} \tag{5.99}$$

Using integration by part, we find the relation

$$\frac{\partial E_k}{\partial t} = \frac{1}{2}\frac{\partial}{\partial k_\perp}\left(\sum_{s_k s_p s_q}\int \epsilon_p k_\perp T_{\boldsymbol{kpq}}^{s_k s_p s_q} \mathrm{d}p_\perp \mathrm{d}p_\parallel \mathrm{d}q_\perp \mathrm{d}p_\parallel\right). \tag{5.100}$$

The asymptotic form of $T_{\boldsymbol{kpq}}^{s_k s_p s_q}$ can be found by using the locality in the perpendicular direction. In particular, we find the relations

$$\begin{aligned}
k_\perp^2 p_\perp^2 q_\perp^2 &= k_\perp^6, && (5.101a)\\
\left(\frac{s_q q_\perp - s_p p_\perp}{s_k \omega_k}\right)^2 &= \frac{k_\perp^4}{\Omega_e^2 k_\parallel^2}\left(s_q - s_p\right)^2, && (5.101b)\\
\left(s_k k_\perp + s_p p_\perp + s_q q_\perp\right)^2 &= k_\perp^2\left(s_k + s_p + s_q\right)^2, && (5.101c)\\
E_q\left(p_\perp E_k - k_\perp E_p\right) &= -\frac{\epsilon_p}{2} k_\perp^4 \frac{\partial}{\partial k_\perp}\left(\frac{E_k}{k_\perp}\right)^2, && (5.101d)\\
\sin\alpha_q &= \sin\pi/3 = \sqrt{3}/2, && (5.101e)\\
\delta_{\Omega_{kpq}} &= \frac{k_\perp}{\Omega_e}\delta\left(s_k k_\parallel + s_p p_\parallel + s_q q_\parallel\right). && (5.101f)
\end{aligned}$$

After simplification, we arrive at

$$\begin{aligned}
T_{\boldsymbol{kpq}}^{s_k s_p s_q} = &-\epsilon_p \frac{\sqrt{3}}{2^{14}}\frac{1}{\Omega_e}\frac{s_p p_\parallel}{s_k k_\parallel} k_\perp^5 \left(s_q - s_p\right)^2\left(s_k + s_p + s_q\right)^2 \frac{\partial}{\partial k_\perp}\left(\frac{E_k}{k_\perp}\right)^2 \\
&\times \delta\left(s_k k_\parallel + s_p p_\parallel + s_q q_\parallel\right)\delta\left(k_\parallel + p_\parallel + q_\parallel\right).
\end{aligned} \tag{5.102}$$

With this form we see that the transfer will be significantly higher when $s_p = -s_q$, therefore we will only consider this type of interaction. Then, the expression of the transfer reduces to

$$T_{\boldsymbol{kpq}}^{s_k s_p - s_p} = -\epsilon_p \frac{\sqrt{3}}{2^{12}}\frac{1}{\Omega_e}\frac{s_p p_\parallel}{s_k k_\parallel} k_\perp^5 \partial_{k_\perp}\left(E_k/k_\perp\right)^2 \delta\left(s_k k_\parallel + s_p p_\parallel - s_p q_\parallel\right)\delta\left(k_\parallel + p_\parallel + q_\parallel\right). \tag{5.103}$$

The resonance condition leads to two possible combinations for the parallel wavenumbers,

$$\begin{aligned}
k_\parallel + p_\parallel - q_\parallel = 0 \qquad &\text{and} \qquad k_\parallel + p_\parallel + q_\parallel = 0, && (5.104a)\\
k_\parallel - p_\parallel + q_\parallel = 0 \qquad &\text{and} \qquad k_\parallel + p_\parallel + q_\parallel = 0. && (5.104b)
\end{aligned}$$

The solution corresponds either to $q_\parallel = 0$ or $p_\parallel = 0$, which means in particular that the strong locality assumption is not allowed for the parallel direction. The second solution cancels the transfer, therefore, we

will only consider the first solution for which we have (with $p_\parallel = -k_\parallel$). We find

$$\frac{\partial E_k}{\partial t} = \frac{1}{2}\frac{\partial}{\partial k_\perp}\left(\int \epsilon_p k_\perp T^{++-}_{\boldsymbol{kpq}} \mathrm{d}p_\perp \mathrm{d}p_\parallel \mathrm{d}q_\perp \mathrm{d}p_\parallel\right) = \frac{\sqrt{3}}{2^{13}}\frac{1}{\Omega_e}\frac{\partial}{\partial k_\perp}\left[k_\perp^8 \frac{\partial}{\partial k_\perp}\left(\frac{E_k}{k_\perp}\right)^2\right]\int_{-\tilde{\epsilon}}^{+\tilde{\epsilon}} \epsilon_p^2 \mathrm{d}\epsilon_p \int_{-\tilde{\epsilon}}^{+\tilde{\epsilon}} \mathrm{d}\epsilon_q. \tag{5.105}$$

We finally obtain the nonlinear diffusion equation

$$\boxed{\frac{\partial E_k}{\partial t} = C\frac{\partial}{\partial k_\perp}\left[k_\perp^7 E_k \frac{\partial}{\partial k_\perp}\left(\frac{E_k}{k_\perp}\right)\right]}, \tag{5.106}$$

where $C = \tilde{\epsilon}^4/\left(2^{10}\sqrt{3}\Omega_e\right)$. This equation has been derived analytically from the kinetic equations in the limit of super-local (perpendicular) interactions and when $H = 0$. It gives the first interesting description of wave turbulence in IEMHD. In particular, the thermodynamic and KZ spectra are exact solutions. We can also prove that the corresponding energy flux is positive, and thus that the cascade is direct.

It is interesting to note that a similar nonlinear diffusion equation has been obtained, in the same approximation of wave turbulence, for EMHD [16, 57] and rotating hydrodynamics [32]. The numerical simulations of this equation reveal the existence of an energy spectrum close to $k_\perp^{-8/3}$ during the non-stationary phase that is steeper than the KZ spectrum. This solution has been understood as a self-similar solution of the second kind (which means it cannot be predicted analytically). It is also shown that once the energy spectrum reaches the dissipative scales, a spectral bounce appears which affects the whole inertial range to finally form the expected KZ spectrum in $k_\perp^{-5/2}$. In the forthcoming chapter, we will establish a connection between the nonlinear diffusion equation and autonomous systems. This link will enable us to accurately determine the energy spectrum exponent during the non-stationary phase, bridging partial and ordinary differential equations and potentially providing an analytical framework to address this unresolved question.

5.8 Direction of the energy cascade and Kolmogorov constant

5.8.1 Direct energy cascade

In this section, we will study the sign of the energy flux from the kinetic equations (5.71) and prove that the cascade in the perpendicular direction is direct. In cylindrical coordinates (see figure 5.6), we have [72]

$$\frac{\partial E(\boldsymbol{k})}{\partial t} = -\boldsymbol{\nabla}\cdot\boldsymbol{\Pi} = -\frac{1}{k_\perp}\frac{\partial\left(k_\perp \Pi_\perp(\boldsymbol{k})\right)}{\partial k_\perp} - \frac{\partial \Pi_\parallel(\boldsymbol{k})}{\partial k_\parallel}, \tag{5.107}$$

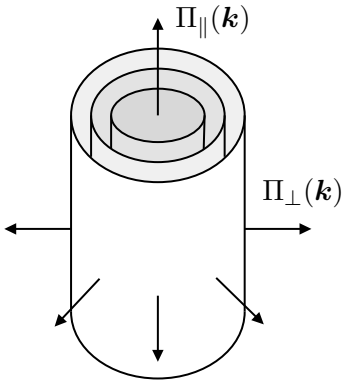

Figure 5.6: Schematic representation of an axisymmetric flux in Fourier space, where each cylindrical shell represents a specific value of $k_\perp$. While in theory, these shells form a continuum, their discrete nature in this illustration helps to provide visual clarity.

where $\boldsymbol{\Pi}$ is the energy flux vector, $\Pi_\perp$, and $\Pi_\parallel$ its perpendicular and parallel components (axisymmetric turbulence is assumed), respectively. Introducing the axisymmetric spectra $E_k \equiv 2\pi k_\perp E(\boldsymbol{k})$, $\Pi_\perp \equiv 2\pi k_\perp \Pi_\perp(\boldsymbol{k})$ and $\Pi_\parallel \equiv 2\pi k_\perp \Pi_\parallel(\boldsymbol{k})$, we obtain

$$\frac{\partial E_k}{\partial t} = -\frac{\partial \Pi_\perp}{\partial k_\perp} - \frac{\partial \Pi_\parallel}{\partial k_\parallel}. \tag{5.108}$$

We now introduce the adimensional variables $\tilde{p}_\perp \equiv p_\perp/k_\perp$, $\tilde{q}_\perp \equiv q_\perp/k_\perp$, $\tilde{p}_\parallel \equiv p_\parallel/k_\parallel$ and $\tilde{q}_\parallel \equiv q_\parallel/k_\parallel$. We seek power-law solutions of the form (5.70) and then obtain

$$\frac{\partial E_k}{\partial t} = \frac{\epsilon^2}{2^{13}\Omega_e}\left[k_\perp^{4-2x}\left|k_\parallel\right|^{-2y} C_E^2 I_E(x,y) + k_\perp^{2-2\tilde{x}}\left|k_\parallel\right|^{-2\tilde{y}} C_H^2 I_H(\tilde{x},\tilde{y})\right], \tag{5.109}$$

where

$$\begin{aligned} I_E(x,y) = \sum_{s_k s_p s_q} \int_{\Delta_\perp} & s_k s_p \frac{\tilde{p}_\parallel}{\tilde{p}_\perp \tilde{q}_\perp^2}\left(s_q\tilde{q}_\perp - s_p\tilde{p}_\perp\right)^2\left(s_k + s_p\tilde{p}_\perp + s_q\tilde{q}_\perp\right)^2 \sin\alpha_q \tilde{q}_\perp^{-x}\left|\tilde{q}_\parallel\right|^{-y} \\ & \times\left(1-\tilde{p}_\perp^{-1-x}\left|\tilde{p}_\parallel\right|^{-y}\right)\left(1-\tilde{p}_\perp^{-5+2x}\left|\tilde{p}_\parallel\right|^{-1+2y}\right) \\ & \times\delta\left(s_k + s_p\frac{\tilde{p}_\parallel}{\tilde{p}_\perp} + s_q\frac{\tilde{q}_\parallel}{\tilde{q}_\perp}\right)\delta\left(1+\tilde{p}_\parallel+\tilde{q}_\parallel\right)\mathrm{d}\tilde{p}_\perp\mathrm{d}\tilde{q}_\perp\mathrm{d}\tilde{p}_\parallel\mathrm{d}\tilde{q}_\parallel, \end{aligned} \tag{5.110}$$

and

$$\begin{aligned} I_H(\tilde{x},\tilde{y}) = \sum_{s_k s_p s_q} \int_{\Delta_\perp} & s_p s_q \frac{\tilde{p}_\parallel}{\tilde{p}_\perp \tilde{q}_\perp^3} \left(s_q \tilde{q}_\perp - s_p \tilde{p}_\perp\right)^2 \left(s_k + s_p \tilde{p}_\perp + s_q \tilde{q}_\perp\right)^2 \sin\alpha_q \tilde{q}_\perp^{-\tilde{x}} \left|\tilde{q}_\parallel\right|^{-\tilde{y}} \\ & \times \left(1 - s_k s_p \tilde{p}_\perp^{-\tilde{x}-2} \left|\tilde{p}_\parallel\right|^{-\tilde{y}}\right) \left(1 - \tilde{p}_\perp^{2\tilde{x}-3} \left|\tilde{p}_\parallel\right|^{2\tilde{y}-1}\right) \\ & \times \delta\left(s_k + s_p \frac{\tilde{p}_\parallel}{\tilde{p}_\perp} + s_q \frac{\tilde{q}_\parallel}{\tilde{q}_\perp}\right) \delta\left(1 + \tilde{p}_\parallel + \tilde{q}_\parallel\right) \mathrm{d}\tilde{p}_\perp \mathrm{d}\tilde{q}_\perp \mathrm{d}\tilde{p}_\parallel \mathrm{d}\tilde{q}_\parallel. \end{aligned} \tag{5.111}$$

Taking the limits, corresponding to the KZ spectra, $(x, y, \tilde{x}, \tilde{y}) \to (5/2, 1/2, 3/2, 1/2)$, thanks to the Hospital rule, we can write

$$\begin{pmatrix} \Pi_\perp^{\mathrm{KZ}} \\ \Pi_\parallel^{\mathrm{KZ}} \end{pmatrix} = \frac{\epsilon^2}{2^{13}\Omega_e} \begin{pmatrix} k_\parallel^{-1} \\ k_\perp^{-1} \end{pmatrix} \left[C_E^2 \begin{pmatrix} I_\perp \\ I_\parallel \end{pmatrix} + C_H^2 \begin{pmatrix} J_\perp \\ J_\parallel \end{pmatrix} \right], \tag{5.112}$$

where

$$\begin{aligned} \begin{pmatrix} I_\perp \\ I_\parallel \end{pmatrix} \equiv \sum_{s_k s_p s_q} \int_{\Delta_\perp} & s_k s_p \frac{\tilde{p}_\parallel}{\tilde{p}_\perp \tilde{q}_\perp^{9/2} \left|\tilde{q}_\parallel\right|^{1/2}} \left(s_q \tilde{q}_\perp - s_p \tilde{p}_\perp\right)^2 \left(s_k + s_p \tilde{p}_\perp + s_q \tilde{q}_\perp\right)^2 \sin\alpha_q \log\left|\begin{pmatrix} \tilde{p}_\perp \\ \tilde{p}_\parallel \end{pmatrix}\right| \\ & \times \left(1 - \tilde{p}_\perp^{-7/2} \left|\tilde{p}_\parallel\right|^{-1/2}\right) \delta\left(s_k + s_p \frac{\tilde{p}_\parallel}{\tilde{p}_\perp} + s_q \frac{\tilde{q}_\parallel}{\tilde{q}_\perp}\right) \delta\left(1 + \tilde{p}_\parallel + \tilde{q}_\parallel\right) \mathrm{d}\tilde{p}_\perp \mathrm{d}\tilde{q}_\perp \mathrm{d}\tilde{p}_\parallel \mathrm{d}\tilde{q}_\parallel, \end{aligned} \tag{5.113}$$

and

$$\begin{aligned} \begin{pmatrix} J_\perp \\ J_\parallel \end{pmatrix} \equiv \sum_{s_k s_p s_q} \int_{\Delta_\perp} & s_p s_q \frac{\tilde{p}_\parallel}{\tilde{p}_\perp \tilde{q}_\perp^{9/2} \left|\tilde{q}_\parallel\right|^{1/2}} \left(s_q \tilde{q}_\perp - s_p \tilde{p}_\perp\right)^2 \left(s_k + s_p \tilde{p}_\perp + s_q \tilde{q}_\perp\right)^2 \sin\alpha_q \log\left|\begin{pmatrix} \tilde{p}_\perp \\ \tilde{p}_\parallel \end{pmatrix}\right| \\ & \times \left(s_k - s_p \tilde{p}_\perp^{-7/2} \left|\tilde{p}_\parallel\right|^{-1/2}\right) \delta\left(s_k + s_p \frac{\tilde{p}_\parallel}{\tilde{p}_\perp} + s_q \frac{\tilde{q}_\parallel}{\tilde{q}_\perp}\right) \delta\left(1 + \tilde{p}_\parallel + \tilde{q}_\parallel\right) \mathrm{d}\tilde{p}_\perp \mathrm{d}\tilde{q}_\perp \mathrm{d}\tilde{p}_\parallel \mathrm{d}\tilde{q}_\parallel. \end{aligned} \tag{5.114}$$

Therefore, the ratio of the two fluxes is

$$\frac{\Pi_\parallel^{\mathrm{KZ}}}{\Pi_\perp^{\mathrm{KZ}}} = \frac{k_\parallel}{k_\perp} \frac{C_E^2 I_\parallel + C_H^2 J_\parallel}{C_E^2 I_\perp + C_H^2 J_\perp}. \tag{5.115}$$

Since it is proportional to $k_\parallel/k_\perp$, we expect $\Pi_\parallel^{\mathrm{KZ}} \ll \Pi_\perp^{\mathrm{KZ}}$, which is in agreement with the analysis based on the resonance condition to find the direction of the cascade. In the absence of helicity, the ratio (5.115) only depends on $k_\parallel/k_\perp \ll 1$ and $I_\parallel/I_\perp$; we numerically find $I_\parallel/I_\perp \simeq 0.73$, then the previous expectation is fulfilled.

We can also find the sign of the energy flux and thus prove the direction of the cascade. Since the perpendicular flux is dominant, we will neglect the parallel flux and only look for the sign of $I_\perp$. A numerical evaluation reveals a positive value, which means that $\Pi_\perp > 0$ and that the energy cascade is direct in the transverse direction.

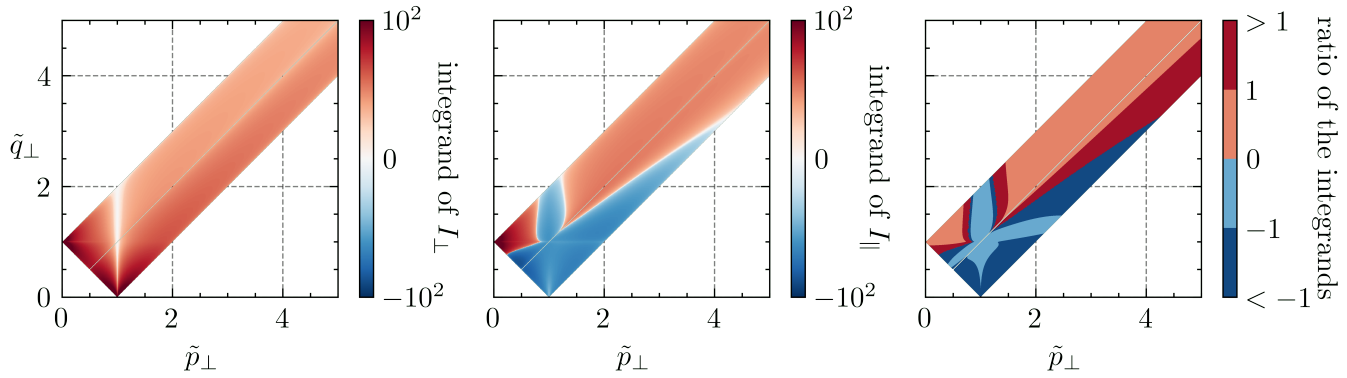

Figure 5.7: Left: integrand of $I_\perp$ which is always positive. Center: integrand of $I_\parallel$ whose sign depends on the perpendicular wavenumbers. Right: integrand of $I_\perp$ divided by the integrand of $I_\parallel$. The blue color corresponds to negative values and the red color to positive values. On the right, the dark colors testify that the integrand of $I_\perp$ is greater than that of $I_\parallel$ in modulus.

In Figure 5.7, we show the sign of the integrands of $I_\perp$ and $I_\parallel$ obtained from a numerical evaluation of expressions (5.113) after integration over the parallel wavenumbers, and for relatively small perpendicular dimensionless wavenumbers (< 5). We see that for $I_\perp$ the integrand is always positive, while for $I_\parallel$ the integrand can be either positive or negative depending on the perpendicular wavenumbers (for large perpendicular wavenumbers it is always positive), but, overall, the positive sign dominates in the sense that the integral $I_\parallel > 0$. Therefore, the parallel cascade is also direct, but it is composed of different contributions, with some triadic interactions contributing to an inverse cascade.

5.8.2 Kolmogorov constant

If we neglect the parallel flux and helicity, we can also obtain the expression of the Kolmogorov constant C_K, for which we can numerically get an estimate. To do so, we take advantage of the Dirac distributions to integrate the parallel wavenumbers. Then, since $I_\perp$ is only defined on the region $\Delta_\perp$, we introduce the change of variable $\tilde{q}_\perp \equiv \xi - \tilde{p}_\perp$ where $\xi \in [1, +\infty[$ and $\tilde{p}_\perp \in \left[\frac{\xi-1}{2}, \frac{\xi+1}{2}\right]$ that confines the integration to this domain (see Figure 5.8). We obtain

$$I_\perp = \int_{a=1}^{a=+\infty} \int_{\tilde{p}_\perp=(a-1)/2}^{\tilde{p}_\perp=(a+1)/2} \sum_{s_k s_p s_q} \mathcal{K}^{s_k s_p s_q}_{\mathbf{1}\tilde{\boldsymbol{p}}\tilde{\boldsymbol{q}}} \mathrm{d}a\mathrm{d}\tilde{p}_\perp, \tag{5.116}$$

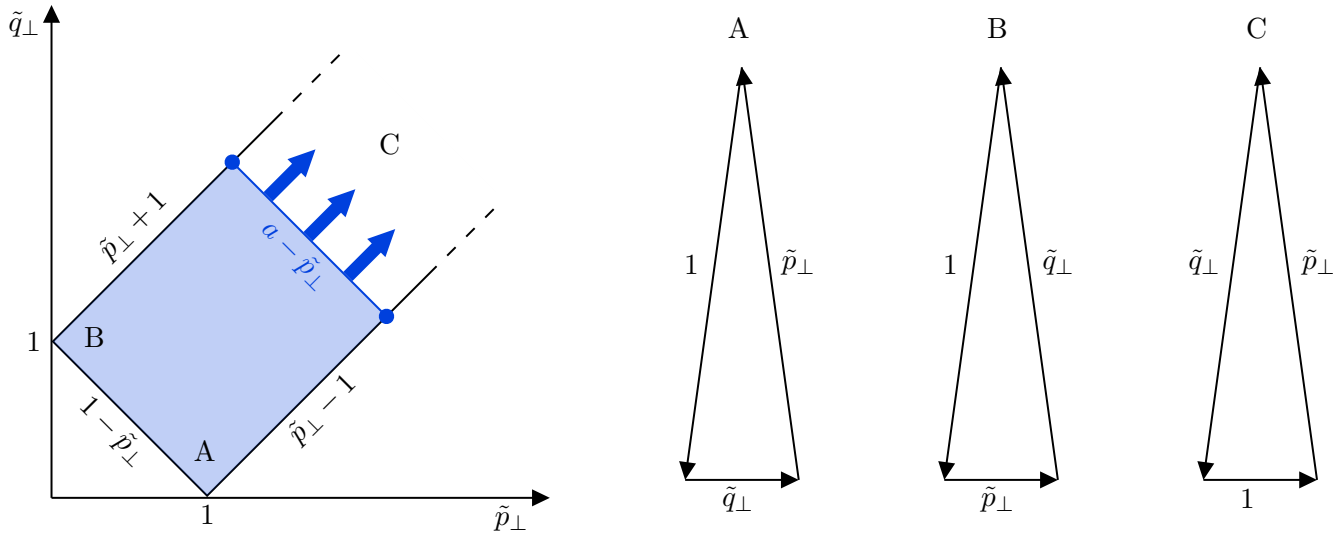

Figure 5.8: Left: The kinetic equation (5.83) is integrated over a domain verifying $\boldsymbol{k}_\perp + \boldsymbol{p}_\perp + \boldsymbol{q}_\perp = \boldsymbol{0}$, which corresponds to an infinite band where the boundaries are flattened triangles. Regions A, B and C (at infinity) are those for which the triadic interactions are non-local. We define $\tilde{q}_\perp = a - \tilde{p}_\perp$, $\forall a \in [1, +\infty[$, to restrict the numerical integration to the domain $\Delta_\perp$. Right: Representation of the non-local triadic interactions for regions A, B and C.

where

$$\mathcal{K}^{s_k s_p s_q}_{\mathbf{1}\tilde{\boldsymbol{p}}\tilde{\boldsymbol{q}}} = \frac{s_k s_p \left|\frac{s_k(a-\tilde{p}_\perp)-s_q}{\tilde{p}_\perp(s_p+s_q)-s_p a}\right|}{(a-\tilde{p}_\perp)^{9/2}\sqrt{\left|\frac{(a-\tilde{p}_\perp)(s_k\tilde{p}_\perp-s_p)}{\tilde{p}_\perp(s_p+s_q)-s_p a}\right|}} \left(s_q\left(a-\tilde{p}_\perp\right)-s_p\tilde{p}_\perp\right)^2 \left(s_k+s_p\tilde{p}_\perp+s_q\left(a-\tilde{p}_\perp\right)\right)^2$$
$$\times \sqrt{1-\frac{\left(a^2-2a\tilde{p}_\perp-1\right)^2}{4\tilde{p}_\perp^2}}\left[1-\tilde{p}_\perp^{-4}\left(\left|\frac{s_q-s_k(a-\tilde{p}_\perp)}{\tilde{p}_\perp(s_p+s_q)-s_p a}\right|\right)^{-1/2}\right]\frac{\log\tilde{p}_\perp}{\left|\frac{s_p}{\tilde{p}_\perp}-\frac{s_q}{a-\tilde{p}_\perp}\right|}, \tag{5.117}$$

is a coefficient with the following symmetries $\mathcal{K}^{s_k s_p s_q}_{\mathbf{1}\tilde{\boldsymbol{p}}\tilde{\boldsymbol{q}}} = \mathcal{K}^{-s_k-s_p-s_q}_{\mathbf{1}\tilde{\boldsymbol{p}}\tilde{\boldsymbol{q}}}$, which reduces by two the number of integrals to compute (four instead of eight). A numerical integration of (5.116) gives finally

$$\boxed{C_K = 64\sqrt{\frac{2}{I_\perp}} \simeq 8.474}. \tag{5.118}$$

The numerical convergence of C_K to this value is shown in Figure 5.9 and, one finds at a given $k_\parallel$,

$$E_k = \sqrt{\Pi_\perp \Omega_e} C_K k_\perp^{-5/2} \tag{5.119}$$

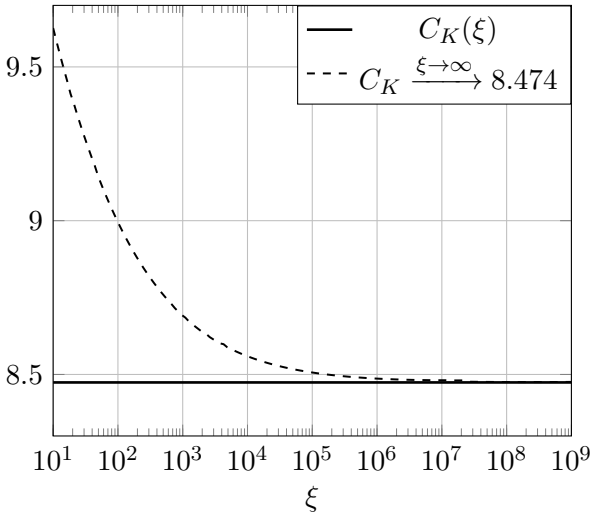

Figure 5.9: Convergence of C_K as a function of ξ.

5.9 Connection with fast rotating hydrodynamics

Interestingly, Equations (5.8) and (5.10) have also been found in the case of hydrodynamics turbulence under fast rotation [38, 47, 50]. The same analysis and results can be obtained for this problem (up to a constant factor). In fact, this work has already been conducted by Galtier [28], except for verifying the locality of the kinetic equations and computing the Kolmogorov constant. Since the equations are exactly the same (up to a constant factor), the locality is also confirmed for fast-rotating hydrodynamics turbulence. The Kolmogorov constant is slightly modified due to the numerical factor associated with the constant, yielding $C_K \simeq 0.749$. Further details can be found in David and Galtier [17].

5.10 Discussion and conclusion

In this chapter, we have developed a wave turbulence theory for inertial electron MHD (i.e., for scales smaller than d_e) mediated by three-wave interactions between inertial whistler waves or between inertial kinetic Alfvén waves. The asymptotic wave kinetic equations are derived for the two quadratic invariants of the system, namely energy, and momentum. The theory is expected to be relevant mainly for ion-electron plasmas such as the Earth's magnetosheath, the solar corona, or the solar wind [47], but also for electron-positron plasmas [45]. We show that this turbulence is mainly characterized by a direct energy cascade in the direction perpendicular to the strong applied magnetic field. The role of the second invariant, the momentum or kinetic helicity, is less important because in general there is no exact solution at constant helicity flux (except for the state of maximal helicity). By converting the exact solution

(Kolmogorov–Zakharov spectrum) into the unit of magnetic field, which is easier to measure in space plasma, we find a magnetic energy spectrum $E^B \sim k_\perp^{-9/2}$. It is interesting to note that this power law is steeper than that observed in the solar wind at sub-MHD scales – satisfying $kd_e < 1$ – with a power law index often close to $-8/3$ [1, 59, 63] (cf., Figure 4.1) whereas, at $kd_e > 1$, power law indices close to $-11/3$ are observed [61, 63] as well as $-9/2$ [62] but in a narrow frequency range. The former matches the strong turbulence prediction [9, 46], while the latter is in adequation with the wave turbulence one. In the absence of helicity, we prove that the energy cascade is direct and numerically estimate the Kolmogorov constant using its analytical expression. We also prove that the Kolmogorov–Zakharov spectrum is in the domain of convergence, showing the relevance of the exact solution.

An interesting point concerns the dynamics of the two-dimensional state (i.e., the slow modes for which $k_\parallel = 0$). We see from the kinetic equation (5.67) that the nonlinear transfer for energy and helicity decreases linearly with $k_\parallel$, and for the value $k_\parallel = 0$ the transfer is exactly null. This means that the dynamics of the slow modes decouple from the three-dimensional state. The slow modes are not described by the wave turbulence theory, which is based on the time scales separation $\tau_{\rm L} \ll \tau_{\rm NL}$ (when $k_\parallel \to 0$ this inequality cannot be satisfied). The possibility that higher-order processes, such as four-wave interactions, could lead to a coupling between two-dimensional and three-dimensional modes has been discussed in the past by [66] in the context of inertial waves in rotating hydrodynamics. Since it is a similar problem, this scenario could also be relevant here.

In the limit of super-local (perpendicular) interactions, we derive a nonlinear diffusion equation that exhibits similarities with the equations found in electron MHD at scales larger than d_e, as well as in the context of inertial wave turbulence (turbulence in fast-rotating fluids). The link is deeper than that, since the two problems share the same kinetic equations (within a factor) with the same dispersion relation (within a factor). This connection is due to a strong asymmetry imposed by a mean magnetic field on the one hand and by the axis rotation on the other hand. It is also due to the helical nature of the waves. This reinforces the bridge between plasma physics and fluid mechanics (see also [32]) and suggests that laboratory experiments [48, 69] can help to better understand space plasma physics at a scale still difficult to detect by current spacecraft.

References

[1] O. Alexandrova, C. Lacombe, A. Mangeney, R. Grappin, and M. Maksimovic, "Solar wind turbulent spectrum at plasma kinetic scales," *The Astrophysical Journal*, vol. 760, no. 2, p. 121, Nov. 2012.

[2] A. Balk and S. Nazarenko, "On the physical realisability of anisotropic kolmogorov spectra of weak turbulence," *Sov. Phys. JETP*, vol. 70, no. 1031, pp. 405–406, 1960.

[3] A. Balk, S. Nazarenko, and V. Zakharov, "On the nonlocal turbulence of drift type waves," *Physics Letters A*, vol. 146, no. 4, pp. 217–221, 1990.

[4] A. Balk, S. Nazarenko, and V. Zakharov, "New invariant for drift turbulence," *Physics Letters A*, vol. 152, no. 5, pp. 276–280, 1991.

[5] D. J. Benney and A. C. Newell, "The propagation of nonlinear wave envelopes," *Journal of Mathematics and Physics*, vol. 46, no. 1-4, pp. 133–139, 1967.

[6] D. J. Benney and A. C. Newell, "Random wave closures," *Studies in Applied Mathematics*, vol. 48, no. 1, pp. 29–53, 1969.

[7] D. Benney and P. Saffman, "Nonlinear Interactions of Random Waves in a Dispersive Medium," *Proc. R. Soc. Lond. A*, vol. 289, no. 1418, pp. 301–320, 1966.

[8] D. Biskamp, E. Schwarz, and J. F. Drake, "Two-Dimensional Electron Magnetohydrodynamic Turbulence," *Phys. Rev. Lett.*, vol. 76, no. 8, pp. 1264–1267, 1996.

[9] D. Biskamp, E. Schwarz, A. Zeiler, A. Celani, and J. F. Drake, "Electron magnetohydrodynamic turbulence," *Phys. Plasmas*, vol. 6, no. 3, pp. 751–758, 1999.

[10] S. V. Bulanov, F. Pegoraro, and A. S. Sakharov, "Magnetic reconnection in electron magnetohydrodynamics," *Phys. Fluids B*, vol. 4, no. 8, pp. 2499–2508, 1992.

[11] C. H. K. Chen and S. Boldyrev, "Nature of kinetic scale turbulence in the earth's magnetosheath," *The Astrophysical Journal*, vol. 842, no. 2, p. 122, Jun. 2017.

[12] J. Cho, "Magnetic Helicity Conservation and Inverse Energy Cascade in Electron Magnetohydrodynamic Wave Packets," *Phys. Rev. Lett.*, vol. 106, no. 19, p. 191 104, 2011.

[13] J. Cho and A. Lazarian, "The anisotropy of electron magnetohydrodynamic turbulence," *The Astrophysical Journal*, vol. 615, no. 1, p. L41, Sep. 2004.

[14] S. Dastgeer, A. Das, and P. Kaw, "Hydrodynamic regime of two-dimensional electron magnetohydrodynamics," *Phys. Plasmas*, vol. 7, no. 5, pp. 1366–1373, 2000.

[15] S. Dastgeer, A. Das, P. Kaw, and P. H. Diamond, "Whistlerization and anisotropy in two-dimensional electron magnetohydrodynamic turbulence," *Phys. Plasmas*, vol. 7, no. 2, pp. 571–579, 2000.

[16] V. David and S. Galtier, "$k_\perp^{-8/3}$ Spectrum in kinetic alfvén wave turbulence: Implications for the solar wind," *The Astrophysical Journal*, vol. 880, no. 1, p. L10, Jul. 2019.

[17] V. David and S. Galtier, "Locality of triad interaction and kolmogorov constant in inertial wave turbulence," *Journal of Fluid Mechanics*, vol. 955, R2, 2023.

[18] L. Deike, C. Laroche, and E. Falcon, "Experimental study of the inverse cascade in gravity wave turbulence," *Europhysics Letters*, vol. 96, no. 3, p. 34 004, Nov. 2011.

[19] G. Dematteis, K. Polzin, and Y. V. Lvov, "On the origins of the oceanic ultraviolet catastrophe," *Journal of Physical Oceanography*, vol. 52, no. 4, pp. 597–616, 2022.

[20] G. Düring, C. Josserand, and S. Rica, "Weak turbulence for a vibrating plate: Can one hear a kolmogorov spectrum?" *Phys. Rev. Lett.*, vol. 97, p. 025 503, 2 Jul. 2006.

[21] S. Dyachenko, A. Newell, A. Pushkarev, and V. Zakharov, "Optical turbulence: Weak turbulence, condensates and collapsing filaments in the nonlinear schrödinger equation," *Physica D: Nonlinear Phenomena*, vol. 57, no. 1, pp. 96–160, 1992.

[22] E. Falcon and N. Mordant, "Experiments in surface gravity–capillary wave turbulence," *Annual Review of Fluid Mechanics*, vol. 54, no. 1, pp. 1–25, 2022.

[23] S. Galtier, *Introduction to modern magnetohydrodynamics*. Cambridge University Press, 2016, p. 288.

[24] S. Galtier and A. Bhattacharjee, "Anisotropic weak whistler wave turbulence in electron magnetohydrodynamics," *Physics of Plasmas*, vol. 10, no. 8, pp. 3065–3076, 2003.

[25] S. Galtier and R. Meyrand, "Entanglement of helicity and energy in kinetic Alfvén wave/whistler turbulence," *J. Plasma Physics*, vol. 81, no. 1, p. 325 810 106, 2015.

[26] S. Galtier, S. V. Nazarenko, A. C. Newell, and A. Pouquet, "A weak turbulence theory for incompressible magnetohydrodynamics," *Journal of Plasma Physics*, vol. 63, no. 5, pp. 447–488, 2000.

[27] S. Galtier and S. Nazarenko, "Direct Evidence of a Dual Cascade in Gravitational Wave Turbulence," *Phys. Rev. Lett.*, vol. 127, p. 131 101, 2021.

[28] S. Galtier, "Weak inertial-wave turbulence theory," *Phys. Rev. E*, vol. 68, p. 015 301, 1 Jul. 2003.

[29] S. Galtier, "Wave turbulence in incompressible hall magnetohydrodynamics," *Journal of Plasma Physics*, vol. 72, no. 5, pp. 721–769, 2006.

[30] S. Galtier, *Physics of Wave Turbulence*. Cambridge University Press, 2022.

[31] S. Galtier, "Fast magneto-acoustic wave turbulence and the iroshnikov–kraichnan spectrum," *Journal of Plasma Physics*, vol. 89, no. 2, p. 905 890 205, 2023.

[32] S. Galtier and V. David, "Inertial/kinetic-alfvén wave turbulence: A twin problem in the limit of local interactions," *Phys. Rev. Fluids*, vol. 5, p. 044 603, 4 Apr. 2020.

[33] S. Galtier and S. V. Nazarenko, "Turbulence of weak gravitational waves in the early universe," *Phys. Rev. Lett.*, vol. 119, p. 221 101, 22 Nov. 2017.

[34] K. Hasselmann, "On the non-linear energy transfer in a gravity-wave spectrum part 1. general theory," *Journal of Fluid Mechanics*, vol. 12, no. 4, pp. 481–500, 1962.

[35] K. Hasselmann, "On the non-linear energy transfer in a gravity wave spectrum part 2. conservation theorems; wave-particle analogy; irrevesibility," *Journal of Fluid Mechanics*, vol. 15, no. 2, pp. 273–281, 1963.

[36] K. Hasselmann, "On the non-linear energy transfer in a gravity-wave spectrum. part 3. evaluation of the energy flux and swell-sea interaction for a neumann spectrum," *Journal of Fluid Mechanics*, vol. 15, no. 3, pp. 385–398, 1963.

[37] P. A. Hwang, D. W. Wang, E. J. Walsh, W. B. Krabill, and R. N. Swift, "Airborne measurements of the wavenumber spectra of ocean surface waves. part i: Spectral slope and dimensionless spectral coefficient," *Journal of Physical Oceanography*, vol. 30, no. 11, pp. 2753–2767, 2000.

[38] K. Julien, E. Knobloch, and J. Werne, "A new class of equations for rotationally constrained flows," *Theoretical and Computational Fluid Dynamics*, vol. 11, no. 3, pp. 251–261, Jun. 1998.

[39] H. Kim and J. Cho, "Inverse Cascade in Imbalanced Electron Magnetohydrodynamic Turbulence," *Astrophys. J.*, vol. 801, no. 2, p. 75, 2015.

[40] R. Kraichnan, "Helical turbulence and absolute equilibrium," *J. Fluid Mech.*, vol. 59, pp. 745–752, 1973.

[41] R. H. Kraichnan, "Inertial ranges in two-dimensional turbulence," *The Physics of Fluids*, vol. 10, no. 7, pp. 1417–1423, 1967.

[42] E. A. Kuznetsov, "Weak magnetohydrodynamic turbulence of a magnetized plasma," *Journal of Experimental and Theoretical Physics*, vol. 93, no. 5, pp. 1052–1064, Nov. 2001.

[43] V. S. L'vov, Y. L'vov, A. C. Newell, and V. Zakharov, "Statistical description of acoustic turbulence," *Phys. Rev. E*, vol. 56, pp. 390–405, 1 Jul. 1997.

[44] J. Laurie, V. S. L'vov, S. Nazarenko, and O. Rudenko, "Interaction of kelvin waves and nonlocality of energy transfer in superfluids," *Phys. Rev. B*, vol. 81, p. 104 526, 10 Mar. 2010.

[45] N. F. Loureiro and S. Boldyrev, "Turbulence in magnetized pair plasmas," *The Astrophysical Journal*, vol. 866, no. 1, p. L14, Oct. 2018.

[46] R. Meyrand and S. Galtier, "A universal law for solar wind turbulence at electron scales," *The Astrophysical Journal*, vol. 721, no. 2, pp. 1421–1424, Sep. 2010.

[47] L. M. Milanese, N. F. Loureiro, M. Daschner, and S. Boldyrev, "Dynamic phase alignment in inertial alfvén turbulence," *Phys. Rev. Lett.*, vol. 125, p. 265 101, 26 Dec. 2020.

[48] E. Monsalve, M. Brunet, B. Gallet, and P.-P. Cortet, "Quantitative experimental observation of weak inertial-wave turbulence," *Phys. Rev. Lett.*, vol. 125, p. 254 502, 25 Dec. 2020.

[49] S. Nazarenko, A. Newell, and S. Galtier, "Non-local mhd turbulence," *Physica D: Nonlinear Phenomena*, vol. 152-153, pp. 646–652, 2001, Advances in Nonlinear Mathematics and Science: A Special Issue to Honor Vladimir Zakharov.

[50] S. V. Nazarenko and A. A. Schekochihin, "Critical balance in magnetohydrodynamic, rotating and stratified turbulence: Towards a universal scaling conjecture," *Journal of Fluid Mechanics*, vol. 677, pp. 134–153, 2011.

[51] S. Nazarenko, *Wave turbulence*. Springer Science & Business Media, 2011, vol. 825.

[52] S. Nazarenko and M. Onorato, "Wave turbulence and vortices in bose–einstein condensation," *Physica D: Nonlinear Phenomena*, vol. 219, no. 1, pp. 1–12, 2006.

[53] S. Nazarenko and M. Onorato, "Freely decaying turbulence and bose–einstein condensation in gross–pitaevski model," *Journal of Low Temperature Physics*, vol. 146, no. 1, pp. 31–46, Jan. 2007.

[54] A. C. Newell and P. J. Aucoin, "Semidispersive wave systems," *Journal of Fluid Mechanics*, vol. 49, no. 3, pp. 593–609, 1971.

[55] A. C. Newell, S. Nazarenko, and L. Biven, "Wave turbulence and intermittency," *Physica D: Nonlinear Phenomena*, vol. 152-153, pp. 520–550, 2001, Advances in Nonlinear Mathematics and Science: A Special Issue to Honor Vladimir Zakharov.

[56] A. C. Newell and B. Rumpf, "Wave turbulence," *Annual Review of Fluid Mechanics*, vol. 43, no. 1, pp. 59–78, 2011.

[57] T. Passot and P. L. Sulem, "Imbalanced kinetic alfvén wave turbulence: From weak turbulence theory to nonlinear diffusion models for the strong regime," *Journal of Plasma Physics*, vol. 85, no. 3, p. 905 850 301, 2019.

[58] T. Passot, P. L. Sulem, and E. Tassi, "Electron-scale reduced fluid models with gyroviscous effects," *Journal of Plasma Physics*, vol. 83, no. 4, p. 715 830 402, 2017.

[59] J. J. Podesta, "Evidence of kinetic alfvén waves in the solar wind at 1 au," *Solar Physics*, vol. 286, no. 2, pp. 529–548, Sep. 2013.

[60] V. Roytershteyn, S. Boldyrev, G. Delzanno, C. Chen, D. Grošelj, and N. Loureiro, "Numerical study of inertial kinetic-alfvén turbulence," *The Astrophysical Journal*, vol. 870, no. 2, p. 103, Jan. 2019.

[61] F. Sahraoui, M. L. Goldstein, P. Robert, and Y. V. Khotyaintsev, "Evidence of a cascade and dissipation of solar-wind turbulence at the electron gyroscale," *Phys. Rev. Lett.*, vol. 102, p. 231 102, 23 Jun. 2009.

[62] F. Sahraoui *et al.*, "Scaling of the electron dissipation range of solar wind turbulence," *Astrophys. J.*, vol. 777, no. 1, p. 15, Oct. 2013.

[63] F. Sahraoui, L. Hadid, and S. Huang, "Magnetohydrodynamic and kinetic scale turbulence in the near-earth space plasmas: A (short) biased review," *Reviews of Modern Plasma Physics*, vol. 4, no. 1, p. 4, Feb. 2020.

[64] C. Savaro *et al.*, "Generation of weakly nonlinear turbulence of internal gravity waves in the coriolis facility," *Phys. Rev. Fluids*, vol. 5, p. 073 801, 7 Jul. 2020.

[65] V. Shrira *et al.*, *Advances in Wave turbulence*. World Scientific, 2013, vol. 83.

[66] L. Smith and F. Waleffe, "Transfer of energy to two-dimensional large scales in forced, rotating three-dimensional turbulence," *Physics of Fluids*, vol. 11, no. 6, pp. 1608–1622, 1999.

[67] L. Turner, "Using helicity to characterize homogeneous and inhomogeneous turbulent dynamics," *J. Fluid Mech.*, vol. 408, no. 1, pp. 205–238, 2000.

[68] F. Waleffe, "The nature of triad interactions in homogeneous turbulence," *Phys. Fluids A*, vol. 4, no. 2, pp. 350–363, 1992.

[69] E. Yarom and E. Sharon, "Experimental observation of steady inertial wave turbulence in deep rotating flows," *Nature Physics*, vol. 10, no. 7, pp. 510–514, Jul. 2014.

[70] V. E. Zakharov and N. N. Filonenko, "Energy spectrum for stochastic oscillations of the surface of a liquid," *Dokl. Akad. Nauk SSSR*, vol. 170, no. 6, pp. 1292–1295, 1966.

[71] V. E. Zakharov and N. N. Filonenko, "Weak turbulence of capillary waves," *J. Appl. Mech. Tech. Phys.*, vol. 8, no. 5, pp. 37–40, 1967.

[72] V. E. Zakharov, V. S. L'Vov, and G. Falkovich, *Kolmogorov spectra of turbulence I: Wave turbulence*. Springer Berlin, Heidelberg, 1992.

[73] V. E. Zakharov and R. Z. Sagdeev, "Spectrum of Acoustic Turbulence," *Soviet Physics Doklady*, vol. 15, p. 439, Nov. 1970.

Chapter 6

Anomalous scaling in wave turbulence

6.1 Introduction

In the previous chapter, we discussed in Section 5.7 the derivation of nonlinear diffusion equations, also referred to as the differential approximation model (DAM). In this chapter, we shall discover that these equations might serve as a crucial milestone in our comprehension of the solar wind at sub-MHD scales. But before, I have to introduce them properly.

The historical development of this type of model can be traced back to the work of Leith [21], who initially applied it to address hydrodynamics questions unrelated to wave turbulence. Subsequently, DAM found application in the study of gravity water wave turbulence by Hasselmann and Hasselmann [15], and it has since been extensively employed to investigate various specific phenomena related to wave turbulence. For instance, the DAM has been utilized to explore the simultaneous presence of strong and weak turbulence components in superfluid [19] as well as phenomena such as reconnections of superfluid vortices [23], Kelvin waves on quantized vortex lines [22], nonlinear Schrödinger equation and optical turbulence [8], Bose–Einstein condensates [6], Alfvén waves in the presence of cross-helicity [10], waves in fuzzy dark matter [28], interacting gravity waves on the surface of deep fluids [31] also, and even for gravitational waves [12, 29].

Basically, direct approximation models can be viewed as a form of non-linear Fourier law, in which the energy flux is expressed as a non-linear function involving the energy spectrum and its spectral derivative. This formulation, with its second-order approximation (involving two spatial derivatives), offers a versatile framework for studying systems that can be described by single conservation laws. It is important to note that second-order models cannot accommodate inverse or dual cascade. To analyze such systems, the implementation of fourth-order models, (involving four spatial derivatives), becomes essential. Nevertheless, one notable advantage of DAM is their ability to exhibit at least two analytical solutions: the thermodynamics one, characterized by a zero energy flux, and the Kolmogorov–Zakharov one, which corresponds to a constant energy flux. A nonlinear combination of the two solutions can also be found and is denoted as a "warm cascade" [6] in which we observe the simultaneous presence of two distinct scalings: the low wavenumbers conform to the Kolmogorov–Zakharov spectrum, while the high wavenumbers align with the thermodynamics solution.

Among the remarkable characteristics, it has been discovered that second-order models with finite capacity (i.e., where the spectrum is integrable at $k \to \infty$ meaning that it contains a finite amount of energy), exhibit a self-similar finite-time blow-up spectrum preceding the KZ one with an anomalous

scaling $x_\star$. In the presence of viscosity, when the energy spectrum reaches the dissipative scales, a distinct bump arises from these scales that modifies the entire spectrum, resulting in a constant energy flux across scales and the emergence of the KZ spectrum. This phenomenon has been observed in a broad range of systems [30], as well as systems displaying inverse cascade behavior [12]. Recent studies have elucidated that these behaviors can be analyzed in terms of self-similar solutions of the second kind [2, 13]. Such solutions manifest self-similar profiles that develop in a finite time but span an infinite range of scales, characterized by a distinct sharp front on one side and an anomalous algebraic decay on the opposite end of the spectral range.

The aim of this chapter is to determine the anomalous scaling $x_\star$ that is linked to the emergence of the self-similar solution. Three options are practicable to tackle this problem. The first one entails embarking upon direct numerical simulations of the exact system, which necessitates a substantial allocation of computational resources in the hopes of achieving a sufficient resolution to make an approximate measurement of the anomalous scaling. The second option involves conducting numerical simulations of the kinetic equations, which allows observation of the anomalous exponent but presents challenges in achieving precise measurements [4, 9, 20]. Alternatively, one can opt for simulations of the DAM, which offers the advantage of accurately observing and quantifying this anomalous scaling, which is independent of the specific closure and initial conditions employed [30].

In the present chapter, we present the analytical known solutions of the DAM, then assuming a self-similar solution, we use an elegant connection between partial differential equations and dynamical autonomous systems (DAS) to probe the anomalous scaling $x_\star$. By doing so, we are going to be able to theoretically bind its value and find a precise method to numerically measure it. Before concluding on the relevance of such models for the solar wind, we will apply this theory to the DAM obtained in the previous chapter (see Equation 5.106). This will allow us to verify if the anomalous exponent $x_\star$, measured via numerical simulation of the DAS, is coherent with the spectrum that appears when we solve numerically the DAM.

6.2 An elegant connection

6.2.1 The differential approximation model

In the general case, we consider the following nonlinear diffusion process in Fourier space for the energy spectrum $E(k,t)$:

$$\frac{\partial E(k,t)}{\partial t} = -\frac{\partial F(k,t)}{\partial k}, \tag{6.1a}$$

$$F(k,t) = -k^m E^n \frac{\partial}{\partial k}\left(\frac{E}{k^{d-1}}\right). \tag{6.1b}$$

In this model, several variables and parameters are involved. Here for wave turbulence systems, F represents the energy flux[1], $d \in \mathbb{N}$ corresponds to the dimension of the system, and $n \in \mathbb{N}^*$ denotes the order of the resonant wave interaction minus two. For example, $n = 1$ for three-wave processes and $n = 2$ for four-wave processes. The constant m depends on the specific type of wave and is typically a positive rational number. For instance, the combination $(d,n,m) = (2,2,19/2)$ represents water gravity waves [24, 31], while $(d,n,m) = (2,1,11/2)$ models water capillary waves. Additionally, Alfvén waves are described by $(d,n,m) = (2,1,19/2)$ [10], while Kelvin waves are characterized by $(d,n,m) = (1,2,6)$ [18]. It is noteworthy that the DAM derived for the IEMHD shares the same formulation as the one used to model inertial waves in fast rotating turbulence, kinetic and whistler Alfvén waves [7, 11, 25]. In this case, it obeys the parameter combination $(d,n,m) = (2,1,7)$.

In turbulence studies, our focus lies on power law solutions. It is therefore logical to seek an energy spectrum represented by the expression $E(k,t) = k^{-x}A(t)$ in the simplest case. By employing this variable separation, we aim to find familiar steady-state analytical solutions that can be derived rigorously from the original equations. Upon substituting this solution into Equations (6.1), we obtain the following expression:

$$\frac{1}{A^{n+1}}\frac{\mathrm{d}A}{\mathrm{d}t} = (x+d-1)(d-m+x+nx)k^{m-d-1-nx}. \tag{6.2}$$

The function $A(t)$ that satisfies this relation is given by:

$$A(t) = n^{-1/n}\left[\frac{A_0^{-n}}{n} - (x+d-1)(d-m+x+nx)k^{m-d-1-nx}t\right]^{-1/n}, \tag{6.3}$$

[1] In the context of wave turbulence, instead of the quantity $E(k,t)$, one may come across the wave action spectrum represented by $N(k,t)$. In this case, F would denote the wave action flux, but it is just a notation issue that does not alter the subsequent analysis and discussion.

where A_0 represents the initial condition. Interestingly, there exist three solutions for which $A(t)$ becomes independent of k:

$$(x_T, x_K, x_F) \equiv \left(1-d,\ \frac{m-d}{n+1},\ \frac{m-d-1}{n}\right). \tag{6.4}$$

The first one x_T corresponds to a zero energy flux and is thus the thermodynamics solution. The second one x_K corresponds to a constant energy flux and is named the Kolmogorov–Zakharov solution. The third one x_F has a non-constant flux and is, so far I know, not predicted by any theoretical analysis of the kinetic equations. The concept of the warm cascade, mentioned earlier, arises when considering a constant energy flux $F(k,t) = F_0$. Under this assumption, we find that the energy spectrum $E(k)$ can be expressed as

$$E(k) = \left(-\frac{F_0}{x_K - x_T} k^{-(n+1)x_K} + c_0 k^{-(n+1)x_T}\right)^{1/(n+1)}, \tag{6.5}$$

where c_0 represents an integration constant. Notably, in the context of finite capacity cascades, where $x_K > 1$, we observe that $x_T < x_K$. This implies that the warm cascade exhibits the KZ spectrum at low wavenumbers k, while conforming to the thermodynamics solutions at higher wavenumbers.

Now that we have identified the main solutions of the DAM, our next step is to propose a self-similar form for the solution of the model. This allows us to delve deeper into the study of anomalous scaling. Our approach involves finding the associated DAS, with the exponent x of the energy spectrum serving as the only free parameter. By doing so, we can establish theoretical bounds for $x_\star$ and numerically determine its precise value by chasing a global bifurcation. This vocabulary will be presented and explained in the upcoming sections.

6.2.2 From DAM to DAS

We are interested in the early evolution of the spectrum, which is initially non-zero only in a finite range of k. As the front of the spectrum propagates toward large k, for the values of k which are much greater than the initial k's the solution tends to be a self-similar solution of the second kind. It is to be found by making in Equation (6.1) substitution in the form $E(k,t) = k_\star^{-x}\phi(\eta)$, with $\eta \equiv k/k_\star$ where $k_\star \equiv (t_\star - t)^{-b}$, and $b(x) \equiv 1/[n(x_F - x)] > 0$. With the new variables, the energy flux becomes

$$F = k_\star^{(n+1)(x_K - x)}\Pi(\eta), \tag{6.6a}$$

$$\Pi(\eta) \equiv -\eta^m \phi^n \frac{\partial}{\partial \eta}\left(\eta^{x_T}\phi\right), \tag{6.6b}$$

and Equation (6.1) can now be written as a bi-dimensional ordinary differential equation:

$$\phi'(\eta) = -x_T\frac{\phi}{\eta} - \Pi\frac{\eta^{1+(n+1)x_K}}{\phi^n}, \tag{6.7a}$$

$$\Pi'(\eta) = b(x)\left[(x-x_T)\phi - \frac{\Pi}{\eta^{(n+1)x_K}\phi^n}\right]. \tag{6.7b}$$

To solve this system, it is crucial to consider the appropriate boundary conditions that capture the desired behavior in both the UV (ultraviolet) and IR (infrared) regimes. Let us examine these boundary conditions in detail: For the UV behavior, characterized by the small scales, we seek algebraic solutions that exhibit a power-law decay. Specifically, we have $\phi(\eta) = A_0\eta^{-x}$ and $\Pi(\eta) = A_0^{n+1}(x-x_T)\eta^{(n+1)(x_K-x)}$. On the other hand, as we approach the IR regime, corresponding to large scales, we require a smooth behavior where the solutions decay faster than a power law. More precisely, both $\phi(\eta)$ and $\Pi(\eta)$ approach zero smoothly as $\eta \to \infty$. Here, "smoothly" implies selecting physically relevant solutions in such a way that the spectrum and the associated flux vanish at the front [29].

We now consider a new change of variable, which allows us to interpret the solution of (6.7) satisfying the boundary conditions prescribed above.

$$f(\eta) = \eta^{x_F}\phi(\eta), \quad p(\eta) = \eta^{x_F-1}\Pi(\eta). \tag{6.8}$$

The correct rescaling is obtained by defining $\tau = \log\eta$ and the system (6.7) becomes now

$$f'(\tau) = \alpha f - \frac{p}{f^n}, \tag{6.9a}$$

$$p'(\tau) = \beta p + b(x)\left[\gamma f - \frac{p}{f^n}\right]. \tag{6.9b}$$

with

$$\alpha \equiv -x_T + \frac{(n+1)x_K - 1}{n}, \tag{6.10a}$$

$$\beta \equiv \frac{(n+1)(x_K-1)}{n}, \tag{6.10b}$$

$$\gamma \equiv x - x_T. \tag{6.10c}$$

It is important to note that $x_K > 1$ because we are examining scenarios with finite capacity, where an explosive cascade occurs. Consequently, both α and β are positive. Concerning the boundary conditions,

now f and p tends to zero when η tends to both zero and infinity: $\lim_{\eta\to 0}(f,p) = \lim_{\eta\to\infty}(f,p) = (0,0)$. In order to apply the standard fixed point analysis, the last step before obtaining the final dynamical autonomous system is to remove the singularity by changing the time variable $\tau \to \theta = \int_{\tau_0}^{\tau} f^{-n}(\tau')\mathrm{d}\tau$ (with arbitrary $\tau_0 > 0$). We finally obtain the following system

$$\boxed{\begin{aligned} f'(\theta) &= \alpha f^{n+1} - p, && \text{(6.11a)}\\ p'(\theta) &= \beta f^n p + b\left(\gamma f^{n+1} - p\right). && \text{(6.11b)}\end{aligned}}$$

6.3 In pursuit of the global bifurcation

As is customary when approaching a problem, our initial focus should be on the behavior of the system at equilibrium. Hence, we need to identify the fixed points of the system to determine when Equations (6.11) do not depend on time by solving the system $(f'(\theta), p'(\theta)) = (0,0)$. This DAS exhibits a rather intricate nature with $n+1$ fixed points. Given the complexity inherent in the general case, we shall consider the specific scenario of $n = 1$, which corresponds to three-wave processes — which is the wave turbulence problem that has piqued our interest. This calculation, for $n = 1$ leads to the finding of two distinct fixed points, denotes P_0 and P_1:

$$P_0 = (0,0) \quad ; \quad P_1 = \left(\frac{b(\alpha-\gamma)}{\alpha\beta}, \frac{b^2(\alpha-\gamma)^2}{\alpha\beta^2}\right). \tag{6.12}$$

The next question is about their stability. Are they stable or not? How an orbit in the phase space will be attracted or repelled by them? This can be determined by computing the trace and the determinant of the Jacobian matrix $\Delta(f,p)$ associated to the fixed points. This matrix is

$$\Delta(f,p) = \begin{pmatrix} 2\alpha f & -1 \\ 2b\gamma f + \beta p & -b + \beta f \end{pmatrix}, \tag{6.13}$$

and the determinants and traces of $\Delta(f,p)$ associated to the fixed points, namely Δ_{P_0} and Δ_{P_1}, are

$$\begin{aligned} \mathrm{Det}\left(\Delta_{P_0}\right) = 0 \quad &; \quad \mathrm{Tr}\left(\Delta_{P_0}\right) = -b, && \text{(6.14a)}\\ \mathrm{Det}\left(\Delta_{P_1}\right) = \frac{b^2(\alpha-\gamma)^2}{\alpha\beta} \quad &; \quad \mathrm{Tr}\left(\Delta_{P_1}\right) = \frac{2b(\alpha-\gamma)}{\beta} - \frac{b\gamma}{\alpha}. && \text{(6.14b)}\end{aligned}$$

The determinant of Δ_{P_0} being zero, it indicates that P_0 is a saddle-node characterized by real eigenvalues with different signs. On the other hand, for P_1, the determinant is positively defined, warranting our attention towards its trace. Remarkably, we find that the trace assumes a positive value when $x > x_H$, a zero value when $x = x_H$, and a negative value when $x < x_H$ where

$$x_H \equiv 1 - d + \frac{2\alpha^2}{2\alpha + \beta} = x_K + \frac{(x_K - 1)^2}{3x_K - x_T - 2}. \tag{6.15}$$

Formally, the point x_H is known as a *Hopf bifurcation*. This denomination, also known as the Poincaré-Andronov-Hopf bifurcation, refers to the occurrence of a local emergence or disappearance of a periodic solution, also known as a self-excited oscillation. By examining the definitions of the trace and the determinant, which are the sum and product of the eigenvalues respectively, and employing the inequality of arithmetic and geometric means, we can establish the relation $\mathrm{Tr}^2\left(\Delta_{P_1}\right) \geq 4\mathrm{Det}\left(\Delta_{P_1}\right)$. In the case where equality holds, we obtain two solutions $x_\pm$, which are:

$$x_\pm = 1 - d + \frac{2\left(\alpha^2 \pm \sqrt{\alpha^3\beta}\right)}{2\alpha + \beta \pm 2\sqrt{\alpha\beta}}. \tag{6.16}$$

Therefore, P_1 is an unstable node (real positive eigenvalues) for $x \leq x_-$, an unstable focus (complex eigenvalues with positive real part) $x_- \leq x \leq x_H$, a stable focus (complex eigenvalues with negative real part) for $x_H \leq x \leq x_+$, and a stable node (real negative eigenvalues) for $x \geq x_+$ (cf., Figure 6.1).

Through the phenomenon of Hopf bifurcation, we have already acquired the necessary elements to establish bounds for the anomalous exponent $x_\star$. Firstly, by definition, x_K always remains smaller than x_H. Secondly, the value of x_H serves as an upper limit for the stability of the fixed point P_1, below which it gives rise to the formation of a limit cycle and above which, all the trajectories in phase space will inexorably converge to the fixed point P_1, leading to a stationary state. As previously mentioned, when the parameter $x \leq x_H$, periodic solutions emerge within the system, allowing for the presence of closely spaced orbits in phase space. This signifies a local bifurcation, whereas our ultimate aim is to identify the value $x_\star$ associated with a global bifurcation. Hence, it is possible to disregard all values of x such that $x_H < x$ for which no bifurcation exists. Thirdly, the lower bound is given by the KZ exponent itself, since it can be proven that no limit cycle exists for this value [13, 14]. A remarkable consequence emerges from the analysis: there always exists an anomalous scaling for direct cascade with finite capacity. This intriguing finding stems from the following considerations. A finite capacity cascade is characterized by

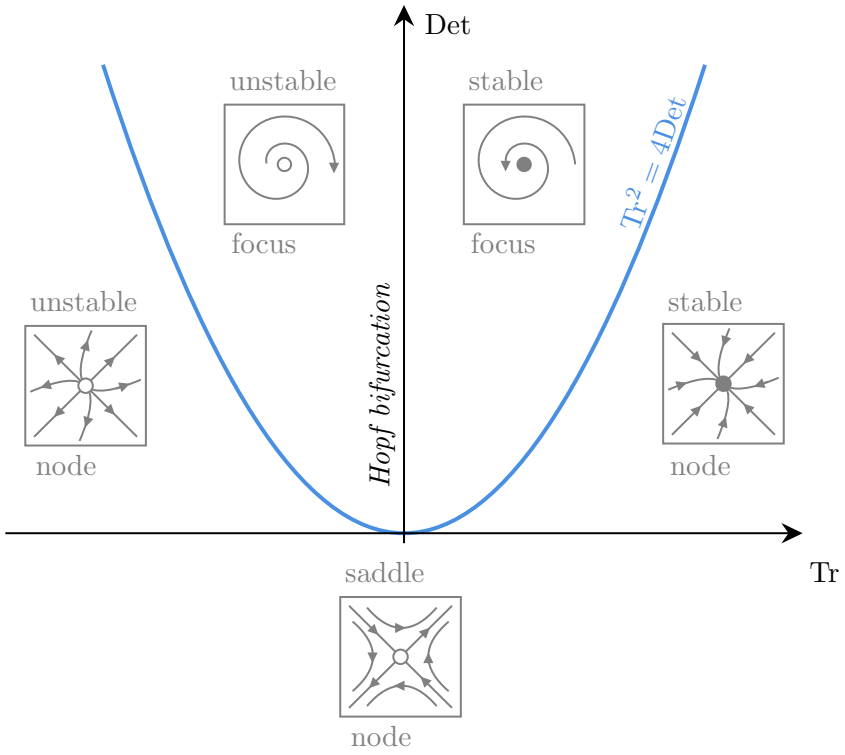

Figure 6.1: Poincaré diagram illustrating the stability of a fixed point in a two-dimensional autonomous system.

a Kolmogorov–Zakharov exponent $x_K > 1$, implying that $m > 1 + d + n$. Conversely, when $x_K = x_H$, we expect the absence of anomalous exponents, as $x_K \leq x_\star \leq x_H$. However, satisfying this condition is equivalent to fulfilling the relation $m = d + 2$ (when $n = 1$), which intriguingly, never occurs in the context of finite capacity cascades[2]. To illustrate this concept, Figure 6.2 provides a visual representation, considering the case of $(d, n) = (2, 1)$, which could correspond to three-wave processes in three-dimensional axisymmetric turbulence. For our specific case of electron MHD with $(d, m, n) = (2, 7, 1)$, the range of potential values for $x_\star$ falls within the interval $[5/2,\ 37/13] \simeq [2.5,\ 2.8462]$.

The final stage of our quest is now to determine the value $x_\star$ at which the limit cycle becomes a global bifurcation. At first glance, the pursuit of such peculiar behavior may seem unconventional. However, upon closer inspection, the rationale becomes apparent. Our objective is to capture the essence of an explosive cascade, where $k \to \infty$ within a finite time. This fundamental characteristic finds its manifestation in our autonomous system through a configuration that exhibits an infinite period in phase space. Remarkably, only global bifurcations possess this unique property, thus providing a compelling explanation for our

[2]The aforementioned statement can be extended to $m = 1+d+n$, irrespective of the specific value of n. This generalization is facilitated by an equivalent DAS derived in Thalabard *et al.* [30], which features only three fixed points, regardless of the particular value of n.

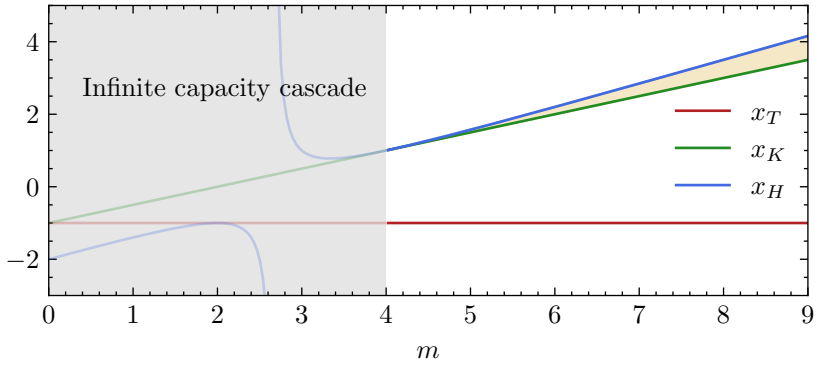

Figure 6.2: Variations of the exponents x related to the thermodynamics solution x_T (red), the Kolmogorov solution x_K (green), and the Hopf bifurcation x_H (blue) for two-dimensional systems ($d = 2$) ruled by three waves process ($n = 1$). In the golden area, the anomalous exponent $x_\star$ can take on values, indicating the region of interest for our analysis.

pursuit of these particular phenomena. Specifically, for three-wave processes ($n = 1$), the only global bifurcation that can occur in the autonomous system (6.11) is a homoclinic cycle. In other words, the emergence of the limit cycle occurs as a result of the Hopf bifurcation taking place at the fixed point P_1, and the collision with the saddle node takes place when the limit cycle connects with the fixed point P_0 (the origin). This global bifurcation is referred to as the homoclinic cycle. Unfortunately, we currently lack an analytical method to predict the exact value of $x_\star$ that produces such a cycle. We must rely on numerical simulations to obtain this information.

6.4 Application to the solar wind

6.4.1 Growth of the limit cycle

To make further progress, numerical simulation becomes necessary. We begin with the knowledge that there exists a homoclinic cycle in the phase space which connects P_0 to P_1 and has an infinite period. When the Hopf bifurcation occurs, the free parameter x takes on the value of x_H, and a limit cycle appears. Subsequently, as we gradually decrease the value of x from $x = x_H$, the area of the limit cycle expands and its period increases until it eventually collides with the origin. This collision allows us to identify the homoclinic cycle at the value $x = x_\star$, which represents the anomalous exponent.

To determine this precise value $x_\star$, we employ numerical continuation algorithms provided by the PyDSTool Python library [5]. Here, we focus on the DAM derived from the IEMHD kinetic equations with $(d, m, n) = (2, 1, 7)$, which is also valid for the EMHD and for strongly rotating nonionized fluids.

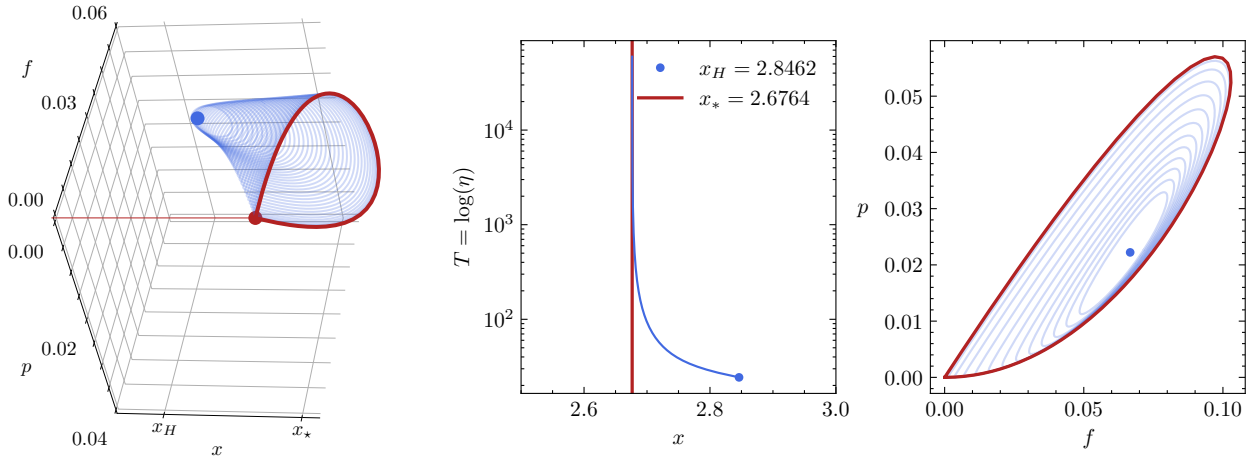

Figure 6.3: Left: A three-dimensional perspective depicting the growth of the limit cycle. Center: Variation of the cycle's period as a function of x. Right: A two-dimensional representation corresponding to the first panel. The limit cycle is attained when the cycle reaches the fixed point P_0 located at the origin. This process determines the formation of the homoclinic cycle.

Consistently to the analytical prediction, we observe a Hopf bifurcation occurring at approximately $x_H \simeq 2.8462$, resulting in the emergence of periodic orbits. Figure 6.3 shows the results obtained through the continuation algorithm. The left panel illustrates that the branch of periodic solutions terminates at $x = x_\star \simeq 2.6764$, coinciding with the collision of the limit cycle with the origin. Furthermore, the central panel demonstrates that the final cycle tends to an infinite period when $x \to x_\star$. Therefore, $x_\star \simeq 2.6764$ represents the sought-after exponent. The right panel is a two-dimensional view of the first one to better visualize the growth of the limit cycle and the final homoclinic cycle.

6.4.2 Comparison with a DAM simulation

To verify the consistency of the anomalous exponent obtained by chasing the homoclinic cycle, we conduct numerical simulations of the Equation (6.1) with $(d, m, n) = (2, 1, 7)$, which corresponds to our specific problem. However, it is important to be aware of the inherent challenges associated with sharp propagating fronts and discontinuous derivatives that arise in such computations. These features often lead to numerical instabilities and blow-ups when conventional differentiation schemes are employed. To overcome these issues, I utilize a numerical code designed by Thalabard *et al.* [29] which employ smooth noise-robust differentiators specifically designed to handle such situations. I opt for a log-discretization approach in the frequency space, which allows us to extend the inertial range and obtain accurate results. This involves discretizing the frequency domain using grid points $k_i = 2^{i/\kappa}$, where i ranges from -1200 to 1200, and $\kappa = 20$ controls the frequency binning. To stabilize the system, no viscosity is introduced. Instead, we rely

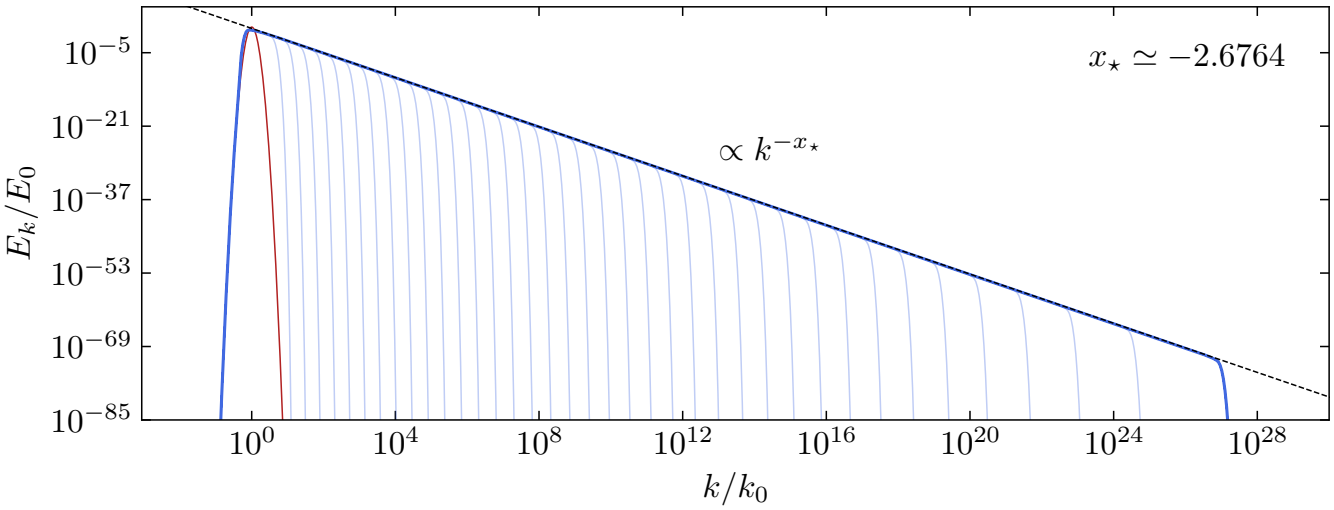

Figure 6.4: Direct numerical simulation of the DAM. The red curve corresponds to the initial condition. As time goes on, the spectrum develops and exhibits a power law fitting the anomalous exponent $x_\star$ determined with the limit cycle.

on the smooth noise-robust differentiators [16], which enable us to compute derivatives in the k-space and effectively regulate the dynamics of the system. The derivative is computed using the expression:

$$D(f,i) = \frac{42\delta_1 + 48\delta_2 + 23\delta_3 + 8\delta_4 + \delta_5}{512hk_i}, \tag{6.17}$$

where $\delta \equiv f_{i+k} - f_{i-k}$ and $h = \ln 2^{1/\kappa}$. To advance in time, we employ the second-order Adams-Bashforth scheme. The time step Δt is determined by the CFL condition:

$$\Delta t = \mu \times \min_k \frac{E+\epsilon}{|D_t E + \epsilon|}, \tag{6.18}$$

where $\epsilon = 10^{-50}$ and $\mu = 10^{-2}$. The initial condition for the energy is a Gaussian centered at $k_0 = 10^{-14}$ with an amplitude of 10^{25} and variance of 0.1.

In Figure 6.4, we observe the time evolution of the energy spectrum. As anticipated, a prominent direct cascade emerges, accompanied by a remarkably extensive inertial range that extends across more than 25 decades. The power law exponent precisely aligns with the one derived from our pursuit of the homoclinic cycle, thus providing compelling evidence for the equivalence we posited between DAM and DAS.

6.4.3 Comparison with reality

Solar wind turbulence at sub-proton scales is characterized by a magnetic energy spectrum with a power law index close to -8/3, as depicted in Figure 4.1, and has posed a significant challenge in the field of space plasma physics [1, 26, 27]. This scaling law defies the predictions of classical turbulence theories, which rely on different types of model equations and wave behaviors, either with or without anisotropy. For years, it seemed impossible to reconcile these observations with existing turbulence theories, marking this problem as one of great importance. Some attribute it to coherent structures, while others propose kinetic effects as the cause (here "kinetic" denotes phenomena that are not described by a fluid model, such as wave-particle interactions, and Landau dumping, to name a few).

Here, we have taken a different approach by considering a nonlinear diffusion model, which incorporates only local interactions. By relaxing the assumption of stationarity, commonly employed in turbulence predictions, we discovered a self-similar solution of the second kind that aligns with the observed magnetic energy spectrum. Remarkably, this non-stationary phase exhibits no viscous dissipation, which is a crucial departure from fluid turbulence. It is important to acknowledge that the absence of viscous dissipation is a more appropriate approach when addressing the solar wind turbulence, since it is a collisionless plasma. However, we must explore the implications and consequences of this assumption. Notably, we should not expect kinetic dissipation at these scales to behave similarly to hydrodynamics, as demonstrated by phenomena like Landau damping [3]. Hence, a pertinent question emerges: why do we persist in our quest for stationary solutions? Based on these considerations, this seemingly anomalous exponent has nothing of anomalous.

Our interpretation of the results suggests the presence of kinetic dissipation that does not significantly impact the inertial range, which is a departure from fluid turbulence behavior. However, it is worth noting that kinetic dissipation may still play a role in plasma heating, as it could explain the slow variation of ion temperature with respect to heliocentric distance (cf., Figure 1.8), or justify the presence of wave turbulence at EMHD scales (cf., Chapter 4). Additionally, we suggest that the presence of a spectral index close to -8/3 in the solar wind can be attributed to the cascade of weak turbulence at sub-proton scales, where the absence of significant dissipation prevents the cascade to converge to a state with a constant energy flux. This would provide an explanation for the observed spectral index close to -8/3 instead of -5/2, as demonstrated in our study. Furthermore, why not coin this phenomenon as *collisionless wave turbulence*? This concept captures the idea of energy dissipation occurring through collisionless processes,

such as kinetic effects, rather than relying on viscous or resistive dissipation mechanisms.

6.5 Conclusion

Differential approximation models are useful to probe specific turbulence features because it allows fine predictions both numerically since it does not require a huge amount of numerical resources, contrary to DNS of the exact equations from where they are derived, and theoretically as we demonstrated in this chapter. In order to precisely determine the anomalous scaling which appears when considering a direct cascade with a finite amount of energy, we took advantage of the bridge that exists between differential approximations models and dynamical autonomous systems. In the general case of second-order models, we were able to bound the anomalous exponent $x_\star$ which is greater than the KZ solution but lower than the exponent associated with the Hopf bifurcation. To pursue the analysis, we had to perform numerical experiments by finding the x value associated with the homoclinic cycle of the system, and in the case of IEMHD (or EMHD or inertial waves turbulences), we found that value to be equal to $x_\star \simeq 2.7674$ which is a very tiny correction ($\sim 7\%$ steeper than the KZ solution). We solved numerically the original DAM and verified that this anomalous scaling coincides with the observed spectrum.

However, it is important to note a caveat regarding the relevance of the second-order models discussed here when applied to systems exhibiting an inverse or dual cascade. In such cases, these models may be less applicable, and it becomes necessary to consider fourth-order models which accurately capture and account for the behavior associated with inverse or dual cascades. Although the analysis becomes more intricate, the underlying approach remains the same. This extension has been developed by Thalabard *et al.* [29], who thoroughly addresses the strengths and limitations of second-order models and conducts a similar analysis, but specifically for fourth-order models. It is worth noting that while fourth-order models prove useful in dealing with systems featuring an inverse or dual cascade, they do not benefit from certain theorems that ensure the existence of a global bifurcation, as is the case for second-order models [13].

What motivated us to delve deeply into the determination of this small correction is the remarkable observation that in the solar wind, dissipative mechanisms like viscosity or resistivity are entirely negligible, yet we consistently observe a scaling behavior close to $-8/3$ for the magnetic spectrum at sub-proton scales [1, 17, 26, 27]. While the DAM relies on several assumptions derived from kinetic equations (considering only super-local interactions, balanced turbulence, and neglecting interactions between counter-propagating waves), the fact that the anomalous exponent remains independent of any closure or initial conditions, and

closely matches the observed exponent in the solar wind, presents either a remarkable coincidence or a compellingly elegant and simple explanation to account for the in situ observations. Together with the findings presented in Chapter 4, these results strongly support weak turbulence as a plausible scenario for the behavior of the solar wind at sub-proton scales. Exploring other systems that lack viscosity and allow for experimental investigations, such as superfluids, could be an intriguing research. If the anomalous exponent predicted by the analyses presented here aligns with the one measured experimentally in superfluids, it would prompt us to seriously consider the relevance of these seemingly simple models. Perhaps their derivation retains the essential components necessary to investigate the question of anomalous scaling? In any case, such studies would undoubtedly shed light on the relevance and applicability of these models, offering valuable insights into the underlying mechanisms at play.

References

[1] O. Alexandrova, C. Lacombe, A. Mangeney, R. Grappin, and M. Maksimovic, "Solar wind turbulent spectrum at plasma kinetic scales," *The Astrophysical Journal*, vol. 760, no. 2, p. 121, Nov. 2012.

[2] G. I. Barenblatt and Y. B. Zel'dovich, "Self-similar solutions as intermediate asymptotics," *Annual Review of Fluid Mechanics*, vol. 4, no. 1, pp. 285–312, 1972.

[3] A. Barnes, "Collisionless Damping of Hydromagnetic Waves," *The Physics of Fluids*, vol. 9, no. 8, pp. 1483–1495, Aug. 1966.

[4] W. J. Bos, C. Connaughton, and F. Godeferd, "Developing homogeneous isotropic turbulence," *Physica D: Nonlinear Phenomena*, vol. 241, no. 3, pp. 232–236, 2012, Special Issue on Small Scale Turbulence.

[5] L. M. Clewley R Sherwood W and G. JM, *Pydstool, a software environment for dynamical systems modeling*, 2007.

[6] C. Connaughton and Y. Pomeau, "Kinetic theory and bose–einstein condensation," *Comptes Rendus Physique*, vol. 5, no. 1, pp. 91–106, 2004, Bose-Einstein condensates: recent advances in collective effects.

[7] V. David and S. Galtier, "$k_\perp^{-8/3}$ Spectrum in kinetic alfvén wave turbulence: Implications for the solar wind," *The Astrophysical Journal*, vol. 880, no. 1, p. L10, Jul. 2019.

[8] S. Dyachenko, A. Newell, A. Pushkarev, and V. Zakharov, "Optical turbulence: Weak turbulence, condensates and collapsing filaments in the nonlinear schrödinger equation," *Physica D: Nonlinear Phenomena*, vol. 57, no. 1, pp. 96–160, 1992.

[9] S. Galtier, S. V. Nazarenko, A. C. Newell, and A. Pouquet, "A weak turbulence theory for incompressible magnetohydrodynamics," *Journal of Plasma Physics*, vol. 63, no. 5, pp. 447–488, 2000.

[10] S. Galtier and É. Buchlin, "Nonlinear diffusion equations for anisotropic magnetohydrodynamic turbulence with cross-helicity," *The Astrophysical Journal*, vol. 722, no. 2, p. 1977, Oct. 2010.

[11] S. Galtier and V. David, "Inertial/kinetic-alfvén wave turbulence: A twin problem in the limit of local interactions," *Phys. Rev. Fluids*, vol. 5, p. 044 603, 4 Apr. 2020.

[12] S. Galtier, S. V. Nazarenko, É. Buchlin, and S. Thalabard, "Nonlinear diffusion models for gravitational wave turbulence," *Physica D: Nonlinear Phenomena*, vol. 390, pp. 84–88, 2019.

[13] V. N. Grebenev, S. V. Nazarenko, S. B. Medvedev, I. V. Schwab, and Y. A. Chirkunov, "Self-similar solution in the leith model of turbulence: Anomalous power law and asymptotic analysis," *Journal of Physics A: Mathematical and Theoretical*, vol. 47, no. 2, p. 025 501, Dec. 2013.

[14] V. N. Grebenev, S. V. Nazarenko, and S. B. Medvedev, "Complementary remarks to properties of the energy spectrum in leith's model of turbulence," *ZAMM - Journal of Applied Mathematics and Mechanics / Zeitschrift für Angewandte Mathematik und Mechanik*, vol. 97, no. 6, pp. 664–669, 2017.

[15] S. Hasselmann and K. Hasselmann, "Computations and parameterizations of the nonlinear energy transfer in a gravity-wave spectrum. part i: A new method for efficient computations of the exact nonlinear transfer integral," *Journal of Physical Oceanography*, vol. 15, no. 11, pp. 1369–1377, 1985.

[16] P. Holoborodko, *Smooth noise-robust differentiators*, 2015.

[17] K. H. Kiyani, K. T. Osman, and S. C. Chapman, "Dissipation and heating in solar wind turbulence: From the macro to the micro and back again," *Philosophical Transactions of the Royal Society A: Mathematical, Physical and Engineering Sciences*, vol. 373, no. 2041, p. 20 140 155, 2015.

[18] V. S. L'vov and S. Nazarenko, "Spectrum of kelvin-wave turbulence in superfluids," *JETP Letters*, vol. 91, no. 8, pp. 428–434, Apr. 2010.

[19] V. S. L'vov, S. V. Nazarenko, and O. Rudenko, "Gradual eddy-wave crossover in superfluid turbulence," *Journal of Low Temperature Physics*, vol. 153, no. 5, pp. 140–161, Dec. 2008.

[20] R. Lacaze, P. Lallemand, Y. Pomeau, and S. Rica, "Dynamical formation of a bose–einstein condensate," *Physica D: Nonlinear Phenomena*, vol. 152-153, pp. 779–786, 2001, Advances in Nonlinear Mathematics and Science: A Special Issue to Honor Vladimir Zakharov.

[21] C. E. Leith, "Diffusion Approximation to Inertial Energy Transfer in Isotropic Turbulence," *The Physics of Fluids*, vol. 10, no. 7, pp. 1409–1416, Jul. 1967.

[22] S. Nazarenko, "Differential approximation for kelvin wave turbulence," *Journal of Experimental and Theoretical Physics Letters*, vol. 83, no. 5, pp. 198–200, May 2006.

[23] S. Nazarenko, "Kelvin wave turbulence generated by vortex reconnections," *JETP Letters*, vol. 84, no. 11, pp. 585–587, Feb. 2007.

[24] S. Nazarenko, "Sandpile behaviour in discrete water-wave turbulence," *Journal of Statistical Mechanics: Theory and Experiment*, vol. 2006, no. 02, p. L02002, Feb. 2006.

[25] T. Passot and P. L. Sulem, "Imbalanced kinetic alfvén wave turbulence: From weak turbulence theory to nonlinear diffusion models for the strong regime," *Journal of Plasma Physics*, vol. 85, no. 3, p. 905 850 301, 2019.

[26] J. J. Podesta, "Evidence of kinetic alfvén waves in the solar wind at 1 au," *Solar Physics*, vol. 286, no. 2, pp. 529–548, Sep. 2013.

[27] F. Sahraoui *et al.*, "Scaling of the electron dissipation range of solar wind turbulence," *Astrophys. J.*, vol. 777, no. 1, p. 15, Oct. 2013.

[28] J. Skipp, V. L'vov, and S. Nazarenko, "Wave turbulence in self-gravitating bose gases and nonlocal nonlinear optics," *Phys. Rev. A*, vol. 102, p. 043 318, 4 Oct. 2020.

[29] S. Thalabard, S. Medvedev, V. Grebenev, and S. Nazarenko, "Inverse cascade anomalies in fourth-order leith models," *Journal of Physics A: Mathematical and Theoretical*, vol. 55, no. 1, p. 015 702, Dec. 2021.

[30] S. Thalabard, S. Nazarenko, S. Galtier, and S. Medvedev, "Anomalous spectral laws in differential models of turbulence," *Journal of Physics A: Mathematical and Theoretical*, vol. 48, no. 28, p. 285 501, Jun. 2015.

[31] V. E. Zakharov and A. N. Pushkarev, "Diffusion model of interacting gravity waves on the surface of deep fluid," *Nonlinear Processes in Geophysics*, vol. 6, no. 1, pp. 1–10, 1999.

Chapter 7

General conclusion

In this manuscript, we have embarked on a journey through the intricacies of plasma turbulence, exploring various scales and dynamics. While the path may at times seem elusive, we can distill our findings into a coherent summary.

7.1 MHD scales

Our exploration began at the MHD scales, where we grappled with the challenge of defining energy dissipation. We employed a powerful tool called anomalous dissipation, originally developed for the Euler and Navier-Stokes equations [2]. This methodology, tailored for systems with infinite Reynolds numbers, aligns remarkably well with the solar wind, characterized by its lack of viscosity and resistivity. Inspired by the Onsager conjecture, which asserts that the lack of smoothness in fields leads to energy dissipation [3, 5], we unraveled the intricate interplay between anomalous dissipation and the Zeroth law of turbulence. In Chapter 2, we delved into a low-dimensional model known as the Yanase model. Through this model, we not only demonstrated the Zeroth law of turbulence, but also confirmed its profound connection with anomalous dissipation. Moreover, leveraging the insights gained from this model, we successfully applied the concept of anomalous dissipation to measure the heating generated by shocks. Remarkably, we obtained a single, elegant analytical formula, rendering the computation of anomalous dissipation unnecessary for quantifying shock-induced heating.

We then moved to the general case, with the study of three-dimensional incompressible MHD. While we were unable to prove the Zeroth law – which would have secured the coveted million-dollar prize from the Clay Institute [4] – we employed the anomalous dissipation to estimate turbulent heating in the solar

wind. By comparing our findings with the PP98 exact law, which requires signal homogeneity, we revealed the superiority of anomalous dissipation. This remarkable tool extends the scope of the PP98 law by enabling its application to discontinuous data and facilitating the tracking of dissipation at each moment of measurement. Moreover, we made a notable discovery regarding the ability of anomalous dissipation to differentiate between different flows. In Chapter 3, we used the anomalous dissipation to theoretically distinguish shocks from fluctuations and viscous flows. Additionally, our investigation into switchbacks, observed near the Sun, uncovered a scaling $\ell^{-3/4}$ in the evolution of anomalous dissipation across scales ℓ when switchbacks occur. This finding suggests that anomalous dissipation not only provides a more precise estimation of energy dissipation, but also serves as a tool for detecting and characterizing switchbacks. Moreover, it has the potential to identify specific plasma regions where dissipative mechanisms play a significant role.

In summary, our exploration of anomalous dissipation has yielded remarkable insights into energy dissipation and its applications in differentiating flows, detecting switchbacks, and identifying dissipative regions within the plasma. While the proof of the Zeroth law remains an elusive goal, we have successfully demonstrated the intimate connection between it and the concept of anomalous dissipation in the Yanase model, suggesting that is an interesting way to overcome this long-time-standing challenge.

7.2 EMHD scales

In our exploration beyond MHD scales, as described in Chapter 4, we encountered a new range of scales ruled by EMHD, that posed intriguing questions. Contrary to the behavior observed in MHD, the analysis of in-situ solar wind data at sub-proton scales revealed a distinct phenomenon: the magnetic fluctuations exhibited no intermittency. To unravel this difference, we performed high-resolution three-dimensional DNS of the reduced EMHD equations, specifically investigating weak and strong wave turbulence regimes. Our simulations led to a significant finding: only the weak wave turbulence regime could accurately reproduce the observed scale-invariance in the data. The presence of weak turbulence at those scales may be attributed to the helicity barrier that arises in the context of imbalanced turbulence [1]. When the helicity is nonzero, heating occurs through ion cyclotron resonance at the ion scale, which weakens the turbulent cascade at sub-proton scales. As a result, the regime transition to weak turbulence provides a compelling explanation for the observations.

Another intriguing aspect we addressed was the observation of the -8/3 power law in the magnetic

spectrum at these scales. In Chapter 6, which encompassed weak turbulence at both EMHD and IEMHD scales, we tackle this problem by turning to the direct approximation model derived from the kinetic equations, selectively emphasizing super-local interactions. By adopting this model, we look for self-similar non-stationary solutions, as no dissipative force was introduced to the equations. This deviation from the conventional approach, which typically predicts a stationary solution, allowed us to gain deeper insights into the true behavior of the solar wind. Our investigations yielded remarkable results: a manifestation of anomalous scaling with an exponent close to $k_\perp^{-8/3}$ in the energy spectrum during the non-stationary phase. These findings further bolstered the notion that the interactions at play are predominantly local and, given the collisionless nature of the plasma, it concurred with the theory that the observed magnetic spectrum, by in situ data, originates from a non-stationary phase. In other words, it arises from a non-viscous regime or collisionless wave turbulence.

7.3 IEMHD scales

The final model we looked at is the IEMHD, where the electron inertia has to be taken into account. In Chapter 4, we developed a weak wave turbulence theory within this regime in the presence of a relatively strong and uniform external magnetic field. We derived the kinetic equations that capture the three–wave interactions between inertial whistler or inertial kinetic Alfvén waves. Astonishingly, we discovered a striking parallel between these kinetic equations and those describing inertial wave turbulence in non-ionized fluids undergoing rapid rotation (albeit differing by a constant). We showed that for both invariants, energy, and momentum, the transfer is anisotropic with a direct energy cascade mainly in the direction perpendicular to the mean magnetic field and the exact stationary solutions reveal a magnetic energy spectrum $\sim k_\perp^{-9/2}$, which is steeper than the EMHD prediction where electron inertia is neglected. The profound interconnection between inertial wave turbulence and turbulence in IEMHD sheds light on the striking similarities between these seemingly disparate topics. This revelation holds profound implications, as it invites us to explore laboratory investigations of turbulence at these scales—a domain that remains beyond the current reach of spacecraft.

7.4 Perspectives

Leaving aside my perspective to rob a central bank and disappear on a lost and paradisiacal island, I can distinguish three questions that pique my curiosity.

The first one revolves around the turbulent dynamics at sub-proton scales and the quest to uncover the underlying physics governing the magnetic spectrum within this domain. Through our investigations, we have demonstrated, in Chapter 4, that weak turbulence successfully captures the observed phenomena. We have also discussed the presence of a potential helicity barrier in the solar wind that could give rise to this regime. An intriguing avenue of exploration lies in the application of anomalous dissipation to the region where the helicity barrier manifests itself. By quantifying the energy dissipation within this domain, we have the potential to gain insights into the amount of energy that persists at sub-proton scales. Through careful observation, it might even be possible to establish an empirical relationship between the intensity of the helicity barrier, as characterized by the amount of helicity present, and the residual energy beyond this barrier.

The second point concerns the stationary solutions derived from theoretical frameworks that may not accurately reflect the true nature of the system due to the lack of dissipation. To advance our understanding, a key questions emerge: While direct approximation models, as demonstrated in Chapter 6, provide reliable measurements, can transformations of kinetic equations (such as Kolmogorov–Zakharov) be found to directly predict non-stationary solutions? Additionally, like the transition from MHD to EMHD scales, could there exist another helicity barrier between the EMHD and IEMHD ranges? This last question converges into a more fundamental inquiry: What are the consequences arising from the interplay of the invariants, namely energy, and helicity? Could there exist a helicity barrier, or its equivalent, at every transition between different scales? In other words, might we encounter such a barrier between MHD and EMHD scales, followed by another between EMHD and IEMHD scales, and so forth?

My last perspective centers around the connection between rotating turbulence and IEMHD. We have observed that the two systems of equations are identical up to a constant. This prompts an intriguing question: Can we rely on mathematical consistency (which I have great faith in) to bridge the gap and explore turbulence at IEMHD scales using fast-rotating water tanks? While we acknowledge that there are differences between the systems and the solar wind may exhibit kinetic effects at IEMHD scales, from a turbulence standpoint, the essence appears to be the same. Therefore, I propose an unconventional approach: Why not save resources and conduct experiments using this proxy to investigate turbulence at its core before to launch spacecraft?

References

[1] T. A. Bowen *et al.*, "Mediation of collisionless turbulent dissipation through cyclotron resonance," *arXiv*, 2023.

[2] J. Duchon and R. Robert, "Inertial energy dissipation for weak solutions of incompressible euler and navier-stokes equations," *Nonlinearity*, vol. 13, no. 1, pp. 249–255, Dec. 2000.

[3] G. L. Eyink, *Review of the onsager "ideal turbulence" theory*, 2018.

[4] C. M. Institute, *The millenium prize problems: Navier-stokes equation*, 2000.

[5] L. Onsager, "Statistical hydrodynamics," *Il Nuovo Cimento*, vol. 6, 2 1949.

Chapter 8

Synthesis (in French)

Le vent solaire est un plasma turbulent mesuré *in situ* par des sondes telles que Voyager/NASA, PSP/NASA ou THEMIS/ESA. Les mesures révèlent des fluctuations du champ magnétique sur une large gamme de fréquences, avec un changement de pente autour de 1 Hz, indiquant une transition du comportement mono-fluide MHD du plasma vers un état où ions et électrons ont une dynamique distincte. Une seconde transition est observée vers 50 Hz, au-delà de laquelle le spectre magnétique se raidit davantage, marquant un changement de physique où les effets d'inertie des électrons deviennent importants. L'étude de cette turbulence est étroitement liée à la compréhension de l'origine du chauffage local, caractérisé par une décroissance lente de la température ionique en fonction de la distance héliosphérique. Cette décroissance est interprétée comme la signature d'un chauffage résultant du transfert d'énergie des grandes échelles vers les petites échelles par la turbulence. L'objectif de cette thèse est d'étudier la turbulence du vent solaire à des échelles allant de la MHD aux échelles inertielles électroniques.

Dans un premier temps, nous utilisons la loi zéro de la turbulence pour mesurer la dissipation d'énergie aux échelles MHD. Cette loi qui stipule que la dissipation d'énergie par unité de masse tend vers une limite non nulle appelée dissipation anomale lorsque les viscosité/résistivité diminuent. Selon la théorie de Kolmogorov de 1941, cette dissipation anomale conduit à la dérivation de la loi 4/5 pour l'hydrodynamique incompressible et peut être généralisée à d'autres fluides incompressibles ou compressibles. Une forme locale de la loi exacte de Kolmogorov fut dérivée en s'appuyant sur la conjecture d'Onsager, puis généralisée à la MHD Hall, obtenant ainsi un équivalent local des lois exactes de la MHD et de la MHD de Hall. Cette découverte est cruciale pour les plasmas spatiaux, car elle permet l'examen de la dissipation locale, étant donné que la dissipation anomale ne nécessite pas de moyenne d'ensemble. Une forme locale de la loi exacte de Kolmogorov est donc utilisée dans les données THEMIS et PSP, pour montrer que le chauffage

calculé avec la dissipation anomale peut être significativement plus élevé que celui déduit de la loi exacte de la MHD. De plus, l'utilisation de la dissipation anomale permet de prouver la loi zéro dans un modèle simplifié de la MHD. Son application aux données Voyager 2 révèle que le chauffage généré par les chocs présents aux abords de Jupiter domine celui provenant des fluctuations turbulentes.

Dans un deuxième temps, nous nous intéressons aux échelles sous-MHD (fréquences entre 1 et 50 Hz). Les mesures *in situ* révèlent un comportement monofractal des fluctuations magnétiques, alors qu'aux échelles MHD un comportement (standard) multifractal est observé. Pour étudier cette différence, des simulations numériques directes tridimensionnelles et haute résolution des équations de l'électron MHD réduite sont menées dans les régimes de turbulence d'ondes faible et forte. Ces simulations montrent que seule la turbulence faible peut reproduire la monofractalité. Jointe à des travaux récents, ce résultat suggère qu'aux échelles électroniques le vent solaire est dans un régime de turbulence d'ondes d'Alfvén cinétique faible et sans collision. Une autre question concerne l'observation de la loi de puissance -8/3 du spectre magnétique à ces échelles. Les équations de la turbulence faible de la MHD électronique, dans la limite des interactions super-locales, se simplifient en une équation de diffusion non linéaire qui peut être facilement simulée numériquement, révélant un spectre d'énergie en -8/3 pendant la phase non stationnaire de la cascade d'énergie. Cela suggère que les interactions sont principalement locales, et compte tenu de la nature non collisionnelle du plasma, cela est conforme à la théorie selon laquelle nous observons le spectre magnétique dans une phase non stationnaire, résultant de l'absence de collisions.

Enfin, une théorie de la turbulence d'ondes (faible) pour la MHD électronique inertielle en présence d'un fort champ magnétique externe est développée. Ce régime est pertinent lorsque l'inertie des électrons est prise en compte. Nous avons dérivé les équations cinétiques qui décrivent les interactions à trois ondes entre les ondes whistler inertielles ou les ondes d'Alfvén cinétiques. Nous montrons que, pour les deux invariants, l'énergie et la quantité de mouvement, le transfert est anisotrope avec une cascade d'énergie directe principalement dans la direction perpendiculaire au champ magnétique moyen, et les solutions stationnaires exactes (i.e. spectre de Kolmogorov—Zakharov) révèlent un spectre d'énergie magnétique plus raide que la prédiction de la MHD électronique où l'inertie des électrons est négligée. De manière remarquable, ces équations sont identiques (à une constante près) à celles décrivant la turbulence d'ondes inertielles dans les fluides non ionisés en rotation rapide. Ce lien fort souligne l'importance des expériences en laboratoire pour étudier la turbulence à ces échelles, actuellement difficilement accessibles aux satellites.

Ces travaux permettent d'obtenir une vision globale du comportement turbulent du vent solaire tant d'un point de vue observationnel, que numérique ou théorique.

Appendix A

Published papers

The first two articles were published during my internships, while the rest were published during my Ph.D.

• $k_{\perp}^{-8/3}$ Spectrum in Kinetic Alfvén Wave Turbulence: Implications for the Solar Wind,

V. David, S. Galtier., *Astrophys. J. Lett.* ***880****, L10, 6 pages (2019)*

• Inertial/Kinetic-Alfvén wave turbulence: a Twin Problem in the Limit of Local Interactions,

S. Galtier, **V. David**., *Phys. Rev. Fluids* ***5****, 44603, 1-14, 14 pages (2020)*

• Proof of the Zeroth Law of Turbulence in 1D Compressible MHD and Shock Heating,

V. David, S. Galtier., *Phys. Rev. E* ***103****, 063217, 7 pages (2021)*

• Energy Transfer, Discontinuities, and Heating in the Inner Heliosphere Measured with a Weak and Local Formulation of the Politano-Pouquet Law,

V. David, S. Galtier, F. Sahraoui, L. Z. Hadid., *Astrophys. J.* ***927****, 200, 10 pages (2022)*

• Wave Turbulence in Inertial Electron MHD,

V. David, S. Galtier., *J. Plasma Physics* ***88****, 905880509, 32 pages (2022)*

• Locality of Triad Interaction and Kolmogorov Constant in Inertial Wave Turbulence,

V. David, S. Galtier., *J. Fluid Mech. Rapids* ***955****, R2, 11 pages (2023)*